Ternary chalcogenides and their composites with titanium dioxide for photocatalytic applications

A thesis submitted for the award of

Doctor of Philosophy

Submitted to the Institute of Technology

Sligo, Ireland

By

Priyanka Ganguly

Under the supervision of

Prof. Suresh C. Pillai and Dr. Ailish Breen

April 2021

To my beloved parents and Riyanka

DECLARATION

I hereby declare that the thesis entitled **"Ternary chalcogenides and their composites with titanium dioxide for photocatalytic applications"** is a bona fide thesis submitted for the fulfilment of Doctor of Philosophy in Department of Environmental Sciences, Institute of Technology Sligo, under the supervision of Prof. Suresh C. Pillai and Dr. Ailish Breen. No part of this thesis has been presented earlier for any degree or diploma of any other university.

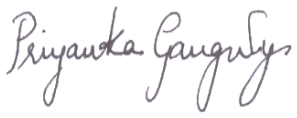

Priyanka Ganguly

Prof. Suresh C. Pillai

Dr. Ailish Breen

April 2021

“First principle: never to let one’s self be beaten down by persons or by events.”- Marie Skłodowska-Curie

“I don't have a feeling of inferiority. Never had. I'm as good as anybody, but no better.”- Katherine Johnson

ACKNOWLEDGEMENTS

I would like to acknowledge the Institute of Technology Sligo for providing financial support, in the form of the IT Sligo President's Bursary (grant no: PPRES052) while completing this research. I would like to thank my supervisors Prof. Suresh C. Pillai and Dr. Ailish Breen, who have provided constant support, advice, encouragement and guidance throughout this work. Suresh had always remained the backbone to my entire journey, where he gave me the liberty to pursue my work based on my interest. His Thursday meetings resulted in a structured mentoring and guidance to finish the entire thesis as well as my work completion in an organised timeframe.

I would like to appreciate the efforts of Dr. Laura Clarizia of Università di Napoli Federico II, p. le V. Tecchio, Napoli, Italy for completing the water splitting tests. I would like to thank Dr. Steven Hinder at the University of Surrey, UK, for completing XPS analysis. I would also acknowledge the access to Raman Spectroscopy and PL spectroscopy at Centre for Research in Engineering Surface Technology (CREST), FOCAS Institute, Technology University Dublin, Kevin Street. Moreover, I would like to acknowledge for the TEM imaging, which was carried out at the Advanced Microscopy Laboratory (AML) at the AMBER Centre, CRANN Institute, Trinity College Dublin, Ireland. I would also like to thank Dr. Akinlolu Akande and PhD researcher Mr. Syam Kumar for completing the theoretical investigation. I am also thankful to Dr. Manu Jose for the JCPDS files. I am grateful to all the IT Sligo technicians and lecturers who had supported in completing all experiments. I am thankful to Dr. John Bartlett (Head of research), Ms. Mary Mcloughlin, Ms. Veronica Cawley and Ms. Ursula Cox for being an excellent research support system.

I am thankful to Ms. Saoirse Dervin and Dr. Ciara Byrne for being there with me in my initial days to this new country. I am grateful to my colleagues, especially Ms. Snehamol Mathew who has been with me in long and sleepless nights in the lab. I am thankful to Dr. Vignesh Kumaravel for his kind input throughout the project. I am grateful to all my friends in Sligo, who made my

journey extremely beautiful. I am thankful to Syam for bearing with me in these last four years and being with me in all the ups and downs of my journey. I am grateful to my college buddies Deepti, Surbhi, Liya, Swati and Ishita for their love and support through this journey. My parents have been the most significant asset and champion of my strength and intellect. This thesis is dedicated to my grandparents, my parents, and my lovely twin sister Riyanka. In the last lap of my journey, the presence of my fiancé Dr. Bharadwaj Vijaysarathy has led to completion of this marathon to a wonderful finish. My supportive in-laws became the fresh champion of my work and intellect. Finally, everything until this moment is because of the Almighty Lord, without his blessings, this journey would not have been possible.

ABSTRACT

This thesis addresses the preparation of semiconductor nanomaterials and their composites with ternary chalcogenides (TC) for photocatalytic applications. Rapid depletion and ever-increasing demand for fossil fuels have posed some grave challenges. Rising global temperature and population are the key elements of concern to the energy shortage and environmental pollution. Heterogeneous photocatalysis, in the past decade, has deemed to be an effective route for producing greener energy and environmental remediation. Ternary chalcogenides (TC) with remarkable visible light absorption, are identified as an ideal candidate to form heterostructure with classical semiconductors such as TiO_2. In the present investigation, heterostructure nanocomposite of $AgBiS_2$-TiO_2, $AgInS_2$-TiO_2, $AgBiSe_2$-TiO_2 and $AgInSe_2$-TiO_2 composites are synthesised utilising two-step calcination and solvothermal technique. The study also contributes to the process optimisation of the TC nanoparticles synthesis.

Computational analysis was utilised to study the structural, electronic and optical properties of the pristine parent samples. This aided in validating the results obtained experimentally as well as to understand the charge transfer mechanism within the heterojunction creation. The XRD results confirm the formation of the parent TC nanoparticles of different crystal structure and anatase phase of titania. The minor shift in binding energies in XPS, red shift observed in Raman spectra, and the TEM results illustrate the successful heterostructure formation. The UV-DRS pattern for all the composites shows enhanced visible light absorption due to the coupling of TC. The band gap of the composites decreased with increased doping levels.

Moreover, these materials were studied for their photocatalytic efficiency, by photocatalytic degradation of Doxycycline, photocatalytic hydrogen generation and photocatalytic antimicrobial disinfection. The composite samples illustrated more than 95% degradation results within 180 minutes and showed about 5 log reductions of bacterial strains (*E. coli* and *S. aureus*) within 30 minutes of irradiation.

The hydrogen production results were promising as all the composites samples displayed higher efficiencies compared to their parent samples. The PL measurement also validated the enhanced activity exhibited by the composite structures, as the intensity of the composite samples gets dampened compared to pristine TiO_2, which suggests the decreased rate of recombination. A mechanism for the enhanced photocatalytic activity is proposed based on scavenging experiments and theoretical analysis.

Keywords; Ternary chalcogenides; Photocatalysis; Water splitting; Antimicrobial disinfection; Degradation.

TABLE OF CONTENTS

LIST OF SYMBOLS AND ABBREVIATIONS

Electrons	e^-
Holes	h^+
Reactive Oxygen Species	ROS
Doxycycline	DC
Partial Density of States	PDOS
Diffuse Reflectance Spectroscopy	DRS
Transmission Electron Microscopy	TEM
X-ray Diffraction	XRD
Transient Absorption	TA
X-ray Photoelectron Spectroscopy	XPS
Fourier-Transform-Infrared Spectroscopy	FTIR
Time-Resolved Microwave Conductivity	TMRC
Photoluminescence Spectroscopy	PL
Conduction Band	CB
Valence Band	VB
Ternary Chalcogenides	TC
Density Functional Theory	DFT
Heyd-Scuseria-Ernzerhof	HSE06
Electron Affinity Model	EAM
Photoelectrochemical	PEC
Solar to H_2 Conversion Efficiency	STH
Quantum Yield	QY
Apparent Quantum Yield	AQY

LIST OF FIGURES

LIST OF TABLES

CHAPTER 1

INTRODUCTION

Nanotechnology arguably is one of the defining technologies of the 21st century. Nanomaterials typically of dimensions between 1 nm and 100 nm are the key ingredients to this successful technology. The present body of work encompasses the synthesis of novel classes of nanomaterials for their use in energy and environmental applications. The prime focus of the thesis is engaged towards the synthesis of ternary chalcogenides (TC) and their photocatalytic applications. Inorganic or organic semiconductors, metal complexes, biomolecules and supramolecular complexes are some of the various class of nanomaterials that act as potential solar harvesting centres. These materials, along with other charge carriers mediate in several photo /electrocatalytic applications. TC materials are an exciting class of nanomaterials that display fascinating optical and electronic properties. The formation of heterojunction composites with traditional semiconductor nanomaterials such as titania opens doorways to their multifunctional photocatalytic applications. The following chapter reviews the basic features of titania, TC and gives a brief understanding of the photocatalytic mechanisms. This shall be followed with an understanding of photocatalytic water splitting and degradation of Doxycycline (DC). Finally, a comprehensive review of various photocatalytic antimicrobial disinfection mechanisms is presented.

1.1. BRIEF INTRODUCTION ON TITANIUM DIOXIDE (TiO_2)

TiO_2 is a semiconductor metal oxide that has received enormous attention in the last three decades because of its large band gap energy, chemical stability, low toxicity and photocatalytic activity.[1-3] This has resulted in its use in wide

varieties of applications in the cosmetic industry, textile industry, paint pigments, batteries and in catalysis.[4-6] The ease of synthesis and the interesting structural and temperature properties make them an exciting material used for multifunctional applications. Titania occurs in nature in three major polymorphs, these are anatase (tetragonal, a=b=3.785Å, c=9.54Å), brookite (a=5.143Å, b=5.456Å, c=9.182Å) and rutile (a=b=4.593Å, c=2.959Å).[7-10] The octahedra of $[TiO_6]^{2-}$ make the different phases of the structure.[3, 4, 7-17] Anatase phase is the low temperature metastable phase with eight octahedra shared between the corners leaving larger interstitial voids compared to rutile. [3, 15, 18] This phase of titania has a band gap of 3.25 eV with a density value of 3.894 g/cm^3 and a refractive index of 2.5. [3, 15] The alignment of the octahedral geometry in rutile phase is spatially different from that of the anatase. The ten octahedra in this phase are shared amongst the edges and is obtained on calcination at higher temperature.[3, 15] The measured optical band gap of rutile is 3.05 eV with a density value of 4.26 g/cm^3. [3, 15] It is the most stable phase at all temperatures and pressures and has a high refractive index of 2.7. [3, 15] This results in its application in sunscreens and paint pigments due to the high light scattering ability and UV absorptivity. The lesser known phase of titania is the brookite phase. This phase is rarely found in nature and could be synthesised synthetically at very defined experimental conditions. It is also a metastable phase which transforms to rutile at higher calcination temperature. However, the thermodynamically stable phase is only attained at a precise crystal dimension of 11-35 nm.[3, 15] The octahedra of titania crystals are connected both along the edges and the corners of the crystal structure. Brookite has a refractive index of 2.63, the density of 4.11 g/cm^3, with an optical band gap of 3.11 eV and an indirect band gap of 2.85 eV. The synthesis of a pure phase of brookite is still considered as a hurdle to overcome.[3, 17, 19-21]

Amongst all these phases, anatase is reported to be the photocatalytically active phase. The high crystallinity and large specific surface area contribute to the enhanced photocatalytic efficiency. The rutile phase has a smaller direct

band gap energy compared to the higher indirect band gap energy of anatase, which results in quicker charge carrier recombination compared to the anatase structure. The anatase phase of TiO_2, although having the enhanced photocatalytically active phase amongst its other structural peers suffers several disadvantages. The larger band gap energy and low visible light utilisation which results in faster exciton recombination. Thus, in order to improve the photocatalytic efficiency of TiO_2, there are several methods employed such as doping with metal and non-metal atoms, making heterostructure composites with several other semiconductor nanomaterials (ZnO, V_2O_5, and WO_3 *etc.*), morphological alterations by synthesising nanotubes and nanosheets, the introduction of voids by creating different types of cationic and anionic vacancies. The introduction of any kind of structural and chemical changes in the structure of the titania results in enhanced visible light absorption, delayed charge carrier recombination and an efficient increase in photocatalytic applications.[1, 3, 8, 16, 22]

1.2. BRIEF INTRODUCTION ON TERNARY CHALCOGENIDES (TC)

Semiconductor nanomaterials display different characteristic absorptions. Continuous absorption in the ultraviolet region, visible and some instances of the near-infrared region. [23-25] Metal chalcogenides have shown interesting applications across photochemistry. However, the search for new, less toxic, narrow band gap semiconductor materials has resulted in the formation of ternary and even quaternary combination of elements to form multi class chalcogenide compounds.[26, 27] The presence of multiple probabilities for chemical substitutions amongst the three-element combination and the structural modifications (formation of rods, needles, tubes and flowers *etc.*) provides substantial opportunity to tune the essential properties for the desired applications. TC are a fascinating class of semiconductor nanomaterials with narrow band gaps suitable for light harvesting ability in the entire domain of visible and small region of infrared band of the electromagnetic spectrum. These nanocrystals are used at present in various

applications such as in photovoltaics, photodetectors, light-emitting diodes, sensors *etc*. TC could be broadly classified into three groups (1) A-B (III)-X; (2) A-B (IV)-X and (3) A-B (V)-X, where X denotes the chalcogens (S, Se and Te), B denotes the lattice forming elements with their oxidation states denoted beside and A is a variable metal.[28] The first class of material A-B(III)-X, the lattice elements are In/Ga and in much rare case Al/B. The chalcogens in this combination remain to be S/Se/Te, while the A, variable metal could be of +1 (Cu/Ag) or +2 (Zn/Cd) oxidation states resulting in the formation of ABX_2 or AB_2X_4 compounds respectively. The second group of materials A-B (IV)-X, the lattice element is comprised of Sn in general and in the rare presence of Ge. The chalcogen elements remains the same while the variable element could be a bivalent (Cu^{2+}/Zn^{2+}) or trivalent (In^{3+}) element making ABX_3 or A_4BX_8 compounds respectively. The final class of materials A-B (V)-X, the lattice elements are Sb or Bi and rarely As. The chalcogen elements remains the same with variable elements with monovalent oxidation states (Cu^{1+}/Ag^{1+}) making ABX_2 compounds.[23-25]

Along with the versatility of stoichiometric compositions, the TC also exhibits a vast range of stable and metastable nanocrystalline compounds. In general, the TC crystallises in stable chalcopyrite which is derived from the zinc blende structure of metal chalcogenides; substitution of bivalent metal atoms from the metal chalcogenides with a combination of monovalent/trivalent (A^{1+}/B^{3+}) or bivalent/tetravalent (A^{2+}/B^{4+}). Similarly, the wurtzite structure of the metal chalcogenide could result in the formation of several combinations of metastable phases.[29] The stoichiometric composition as well as the size of the nanoparticles of the TC influences the broad variability of the light absorption. The quantum size modifies the optical properties affects, which results in enhanced absorption. Numerous approaches such as solid-state reaction, solid solution technique, flux technique, microwave-assisted method, hydro/solvothermal procedure, polyol route and sonochemical techniques are used to synthesise TC.[27, 30-32] Reports of the use of these multicomponent elemental compounds as potential materials for

heterojunction formation with traditional semiconductor nanomaterials such as metal oxides and other two-dimensional nanomaterials is relatively new. The narrow band gap of these compounds with a combination of wide band gap semiconductors has resulted in efficient heterostructures for multifunctional applications.

1.3. FUNDAMENTALS OF PHOTOCATALYSIS

Photocatalysis was first discovered over 90 years ago; however, it got a significant interest only after the discovery of photocatalytic splitting of water by Fujishima and Honda in 1972.[33-37] Since then, extensive studies into photocatalysis and improving the efficiency of photocatalysts have been performed.[34]

Light is used to initiate the photocatalysis by bombarding photons on the surface of the photocatalyst.[34, 38] Irradiation of light with compatible wavelength (higher than the band gap of the photocatalytic material) on the photocatalytic surface excites the electrons (e^-) from the conduction band of the photocatalyst, see **Figure 1**.[16, 36, 38] When the e^- leaves the valence band and is absorbed onto the conduction band (e^-_{CB}), a positive hole is formed on valence band (h^+_{VB}) (**Equation 1** and **Figure 1**).[16, 39-41]

$$Photocatalyst + hv \rightarrow h^+_{VB} + e^-_{CB} \quad (Equation\ 1)$$

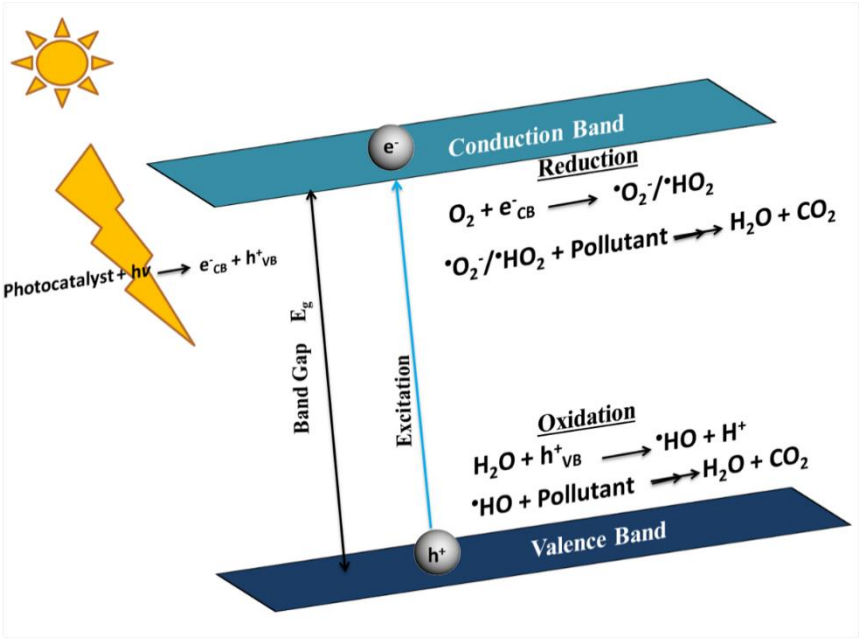

Figure 1. Semiconductor Photocatalytic Mechanism.

In the conduction band (e^-_{CB}), the e^- reacts with oxygen (O_2) and it leads to the formation of superoxide radicals ($\bullet O_2^-$), or hydroperoxide radicals ($\bullet HO_2$) (**Figure 1** and **Equation 2**).[39, 42, 43] The pollutants are photodegraded by the reactive oxygen species (ROS) into water (H_2O) and carbon dioxide (CO_2).[44, 45] Further degradations can occur by using the superoxide radicals.[46] Simultaneously, at the positive hole (h^+_{VB}), the oxidation of water takes place.[39] The oxidation reaction generates hydroxyl radicals ($^{\bullet}OH$) and hydrogen ions (H^+) (**Equation 3**).[39] H_2O and CO_2 are formed when the pollutants react with the hydroxyl radicals.

$$e^-_{CB} + O_2 \rightarrow O_2^- \ (Equation\ 2)$$

$$h^+_{VB} + H_2O \rightarrow *OH + H^+ (Equation\ 3)$$

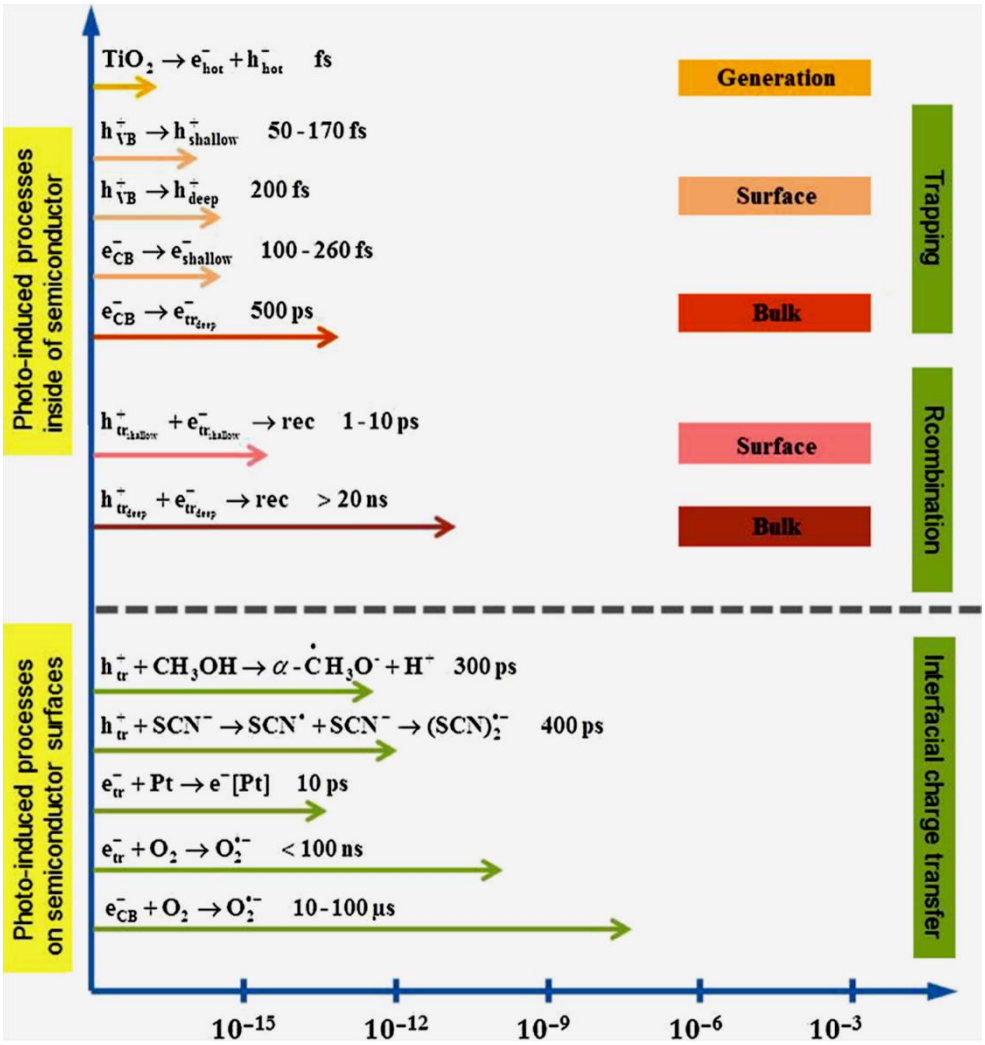

Figure 2. Steps involved in the TiO_2 photocatalysis process.[47, 48] Reprinted with permission of Etacheri *et al.* (2015). Full details are given in the respective publication.

While the exact mechanism of photocatalysis may vary depending on the materials used and the pollutants being examined, the technology generally follows a redox reaction of electrons and holes.[48-51] **Figure 2** shows the possible pathways taken during photocatalysis inside and on the surface of TiO_2. The photocatalysis process begins on the surface of a semiconductor when photons are absorbed.[47, 48, 51-55] The electrons from the valence band (VB) become 'excited' from these photons to the conduction band (CB) when the energy is higher than that of the band gap. The photocatalytic reaction is

shown in **Figure 1**, while **Figure 2** shows the time scale that this reaction occurs. Spectroscopic analysis, such as transient absorption (TA) spectroscopy, transient diffuse reflectance (TDR) spectroscopy, and time-resolved microwave conductivity (TMRC) measurements, can be used to detect photogenerated charge carriers.[51, 52, 56-67] These instruments use the fact that electron-hole pairs absorb light in the visible and near IR regions and free electrons absorb light in the IR or microwave regions.[51, 57, 68-73]

Serpone *et al.* examined TA analysis for TiO_2 sols that had been 'excited' by a 30-ps-width UV laser.[58] Based on the spectra from a 30 ps laser pulse, they concluded the time for trapping electrons and holes should take approx. ≤ 1–10 ps. [58] In 2001, Yang *et al.* examined TiO_2 nanoparticles using femtosecond TA spectroscopy and proposed that hole trapping takes ~50 fs and electron trapping takes ~260 fs. [51, 74]

rous TiO_2 films for the electron-hole trapping.[75, 76] They found that it took 100 fs to generate trapped electrons-holes that were shallow in depth, while it took 150 fs and 200 fs for deeply trapped electrons and holes, respectively.[75, 76] Tamaki *et al*. stated that it took 100 ps for trapped holes to go from shallow to deep traps and that it took the electrons 500 ps to go from the shallow traps to the deep traps. They concluded that the electrons-holes should be trapped and not free charge carriers.[51, 75, 76]

Yamakata *et al.* used time-resolved infrared absorption to examine the decay of free electrons prompted by water and oxygen environments.[64] With commercial P25 TiO_2; they found that the oxygen captured the electrons and there was an increase of the decay rate of 10-100 μs, while in less than 2 μs there was a reaction between the water vapour and the holes. [51, 64] Furube *et al.* examined the charge recombination kinetics for Pt/TiO_2 and found that on top of finding the normal charge recombination there was a new decay component (a few ps) when excited at 390 nm.[61] Increasing the amount of Pt present, the more it affected the migration of electrons was observed. [64] They determined the migration of the electrons between TiO_2 and Pt caused the increase in the decay process. [51, 64] Iwata *et al.* also examined the decay

process with Pt-TiO_2. As with Furube *et al.*, Iwata *et al.* also stated that the electrons are transferring from TiO_2 and Pt and they found the decay rate of 2.3 ps.[63] They propose that a small portion of the electrons remain on TiO_2 as there is still signal present after some time (100s of ps).[51, 63]

Fujishima and Zhang proposed three points based on the research examined. Firstly, they speculated that the recombination during photocatalysis is a slow process as a result of efficient charge trapping.[51] Secondly, they hypothesised that the charge transfer process competes with charge recombination.[51] Finally, they concluded that it could take μs to ms for photocatalysis to occur once the electron-hole pair created. This suggests that under low-intensity UV irradiation (1 mW cm^{-2}, ~1015 photons s^{-1} cm^{-2}), the electron-hole pair is generated and has already gone through reaction or charge recombination before the photocatalyst absorbs a photon. [51]

Recent studies have examined the ability of a photocatalyst to utilise visible light or natural light.[36] There has also been increasing investigations into non-titania photocatalysts. [36, 77-84] Most of these were first examined for photocatalytic water splitting but have now been tested for several other applications such as water/air treatment.[36] Due to the vast volume of studies exploring photocatalysts, they have been divided into two categories; oxide photocatalysts and non-oxide photocatalysts (**Figure 3**). How the valance and conduction bands are affected by the change in pH is one of the significant differences between the two categories. [36, 77-79]

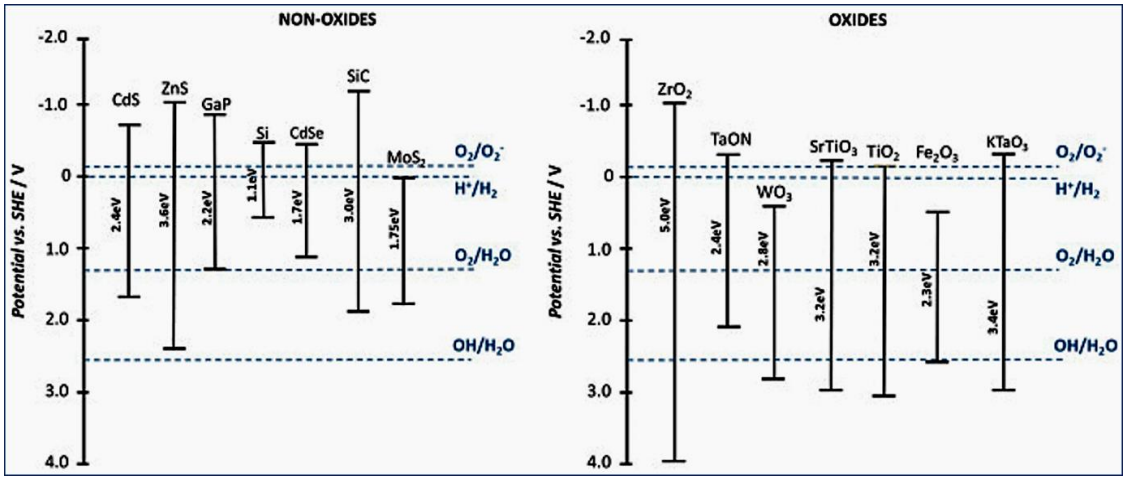

Figure 3. The band gaps of non-oxide photocatalysts (left) and oxide photocatalysts at a pH of 7 (right). Reprinted with permission of Waldmann *et al.* (2016). Full details are given in the respective publication. [36, 77-79]

Using two photocatalysts to form heterojunctions has also been examined in recent years.[36] The e^- are transferred between the two photocatalysts, this reduces or stops recombination.[36] This increases the charge separation and affects the rate of photodegradation. [36, 85] There are different classes of heterojunctions such as (a) semiconductor-semiconductor, (b) semiconductor-metal, (c) semiconductor-non-metal and (d) semiconductor-multicomponent. The selection of an appropriate semiconductor to create a heterojunction with TiO_2 is extremely important. This junction creation not only enhances the visible light absorption ability but also tailors the carrier migration and enhances the separation time period of the excitons. These factors are critical to undertake any photocatalytic reactions.[86-90]

In the semiconductor universe, heterojunctions are the building blocks. It is defined as a semiconductor structure, where the change in position determines the chemical composition. The formation of a heterojunction supports the migration of charge carriers and the alteration of band edge positions. When two semiconductor materials are joined, the difference in the band gap energy between the materials results in small discontinuities at the interface. The VB and CB edge positions of both semiconductors determine the performance of heterojunction photocatalyst. The surface morphology or any defects created in the process is assumedly neglected.[90] These listed properties determine the type of heterojunctions; the band offset of the semiconductors, work function and the electron affinity.[90]

Several models were proposed to calculate the band offset values of heterojunctions. The electron affinity model (EAM) defined the process to calculate the band offset values, assuming the absence of any potential developed at the interface. However, the offset value is determined by the charge transfer process as an interface dipole is created in the process as

defined in the models explaining the concepts of Schottky barriers. Based on the alignment of energy levels, heterojunctions are classified as Type I (straddling gap), Type II (staggered gap), Type III (broken gap), Z-scheme, and Schottky junction. [86-90]

In a type, I heterojunction (**Figure 4A**) the CB of semiconductor X is higher than that of semiconductor Y. The VB of X is also higher to that of Y, creating a straddling band alignment.[91] Hence both the offsets of Y lies in between of X. In this case, the charge carriers generated on individual semiconductor surface accumulate all on the site of semiconductor Y. This kind of heterojunction displays poor photocatalytic efficiency compared to the other heterojunctions. The overall photogenerated charge carriers of the heterojunction are accumulated in one semiconductor surface. Thus, the whole charge carrier separation process is impaired, and it results in a higher rate of charge carrier recombination. In a type II heterojunction, (**Figure 4B**), the CB and semiconductor X is higher than that of Y. The VB of semiconductor X is lower than that of Y. Therefore, the photoelectrons of X flow towards the CB of Y, while the photogenerated holes of Y migrate towards the VB of X, creating staggered band alignment. This kind of charge transfer process makes the type II heterojunction as an ideal photocatalyst for various applications.[92] The chances of exciton recombination are delayed to several folds. The type III heterojunction (**Figure 4C**) is one of the extreme cases of a type II heterojunction.[89, 93] In this case, the energy levels of semiconductor X is extremely farther than Y, thus making the driving force of the charge transfer much higher.[90, 94]

The type II band alignment is the ideal case as the enhanced charge carrier migration results in high efficiency. However, the overall transfer of the excitons is to lower potential values, as the electrons and holes migrate to the lower CB and VB potentials, respectively. Consequently, the overall oxidation and reduction potentials could be lower. Another class of heterojunctions known as the Z-scheme are reported to evade the shortcoming as mentioned above. There are two types of Z-schemes, as shown in **Figure 4D**

(semiconductor-semiconductor Z- scheme) and **Figure 4E** (semiconductor-conductor-semiconductor Z-scheme). These heterojunctions could serve as an excellent candidate for charge carrier separation, and the excitons in the corresponding semiconductors have strong redox ability. In semiconductor-semiconductor Z-scheme, the electrons from the less CB potential (Y) interacts with the holes of the VB of X with low VB potential. The electrons and holes in the higher CB and VB of X and Y participate in the oxidation and reduction reactions. On the other hand, the semiconductor-conductor-semiconductor heterojunction, the conductor component at the interface is such materials as graphene or metal nanomaterials (Ag, Au, Cu, *etc.*). The presence of a conductor in between the two semiconductors eases out the interaction process of the electrons and holes of the opposite semiconductor process. This could enhance the charge migration and increases the overall reaction kinetics. The presence of metal nanoparticles in the heterojunction could improve the efficiency through the surface plasmon resonance (SPR) effect under light illumination.[90, 95]

Apart from having two semiconductors to form different types of heterojunctions; type I, II, III or a Z-scheme, another kind of combination is to have a semiconductor-metal combination to create a Schottky junction (**Figure 4F**).

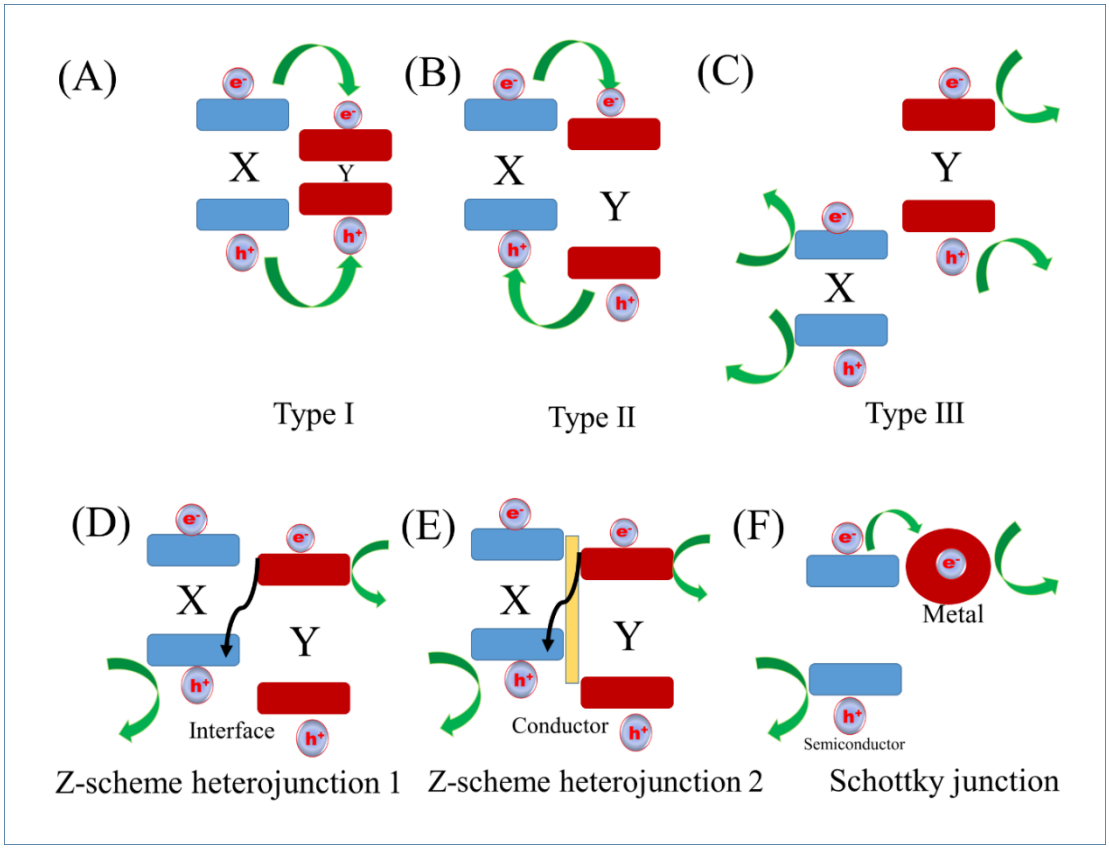

Figure 4. Schematic illustration of different types of heterojunctions. (A) Type I, (B) Type II, (C) Type III, (D) Z-scheme heterojunction 1, (E) Z-scheme heterojunction 2 and (F) Schottky junction.

The metals could function as a co-catalyst to drive the charge carriers and provide more active reaction sites (**Figure 5**). The work function (ϕm) of the metal is the energy required to move the electron from the Fermi level to the vacuum. The δs is the difference in the energy of CB and the vacuum energy of semiconductor. The fermi levels of metal ($E_{Fermi\ M}$) are usually lower as compared to that of semiconductor ($E_{Fermi\ S}$) (**Figure 5A**). Thus, the electron flow is always in the direction from semiconductor to metal in this case. The electron flow is continued until the Fermi level of the semiconductor reaches in equilibrium to that of the metal resulting in a uniform Fermi level for both the components. This process results in the accumulation of electrons from the metal to the junction and a positive charge layer or depletion layer below

the semiconductor to maintain the neutral domain at the interface. This leads to the band bending or known as the Schottky junction (**Figure 5B**). Thus, the formation of Schottky junction serves as an electron sink in the metal and prevents the reverse flow towards the semiconductor. Hence, it could expand the lifetime of the photogenerated electrons from recombination to participate in photochemical processes.[90, 96]

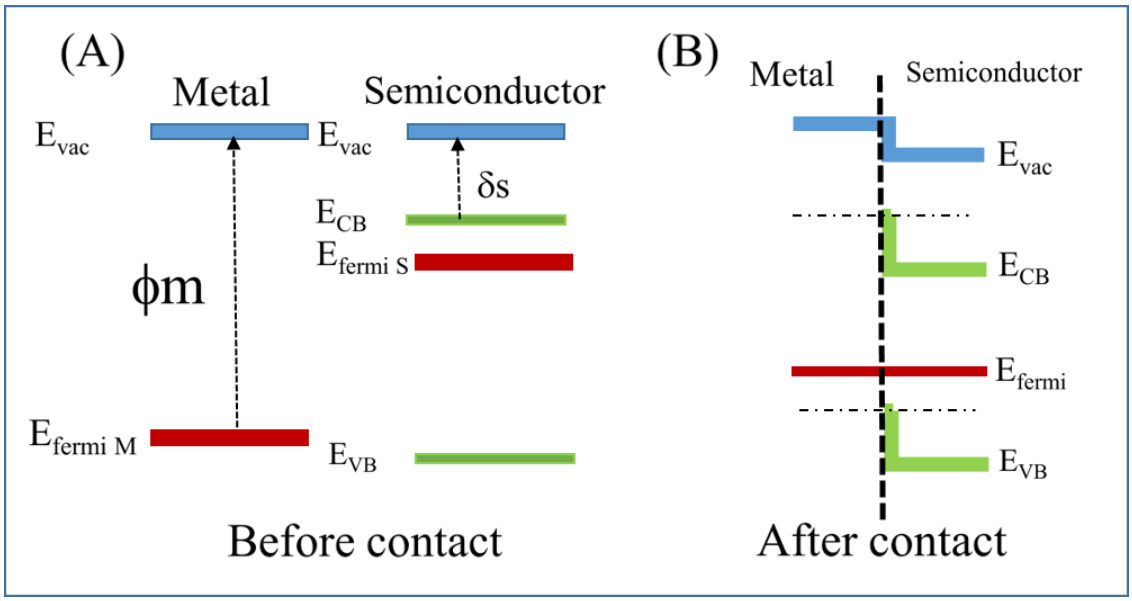

Figure 5. Schottky junction formation between a semiconductor and a metal (A) before and (B) after contact.

1.4. FUNDAMENTALS OF PHOTOCATALYTIC HYDROGEN EVOLUTION REACTION (HER)

In a critical perspective by Amal and co-workers, the authors outlined the fundamental demand of a functioning photocatalytic system. Firstly, with the ability to provide better charge transfer mobility, secondly incorporating facile synthetic process with efficient reaction mechanism. Finally, the importance of photons to impend the nanoarchitectures to reach the photoactive sites.[97] In this section, the primary knowledge of hydrogen production is discussed.

The search for optimal H_2 evolution catalyst initiated in 1958. Parsons *et al.* found that the catalytic evolution is directly related to the heat of formation of H_2 on the catalyst surface.[98] Moreover, using computational chemistry Norskov and co-workers established the ability to predict the binding energies which in turn helped in understanding the efficiency of H_2 production.[99]

The water splitting reaction involves two sets of essential reactions, the hydrogen evolution (HER) and the oxygen evolution reaction (OER). (**Figure 6**)

$$2H^+ + 2e^- \rightarrow H_2 \quad E^0 = -0.41\ V \ (Equation\ 4)$$

$$2H_2O \rightarrow O_2 + 4H^+ + 4e^- \quad E^0 = +0.82\ V (Equation\ 5)$$

$$H_2O \rightarrow H_2 + \frac{1}{2} O_2 \quad E^0 = 1.23\ V \ and\ \Delta G^0 = +237.2\ kJ\ per\ mol (Equation\ 6)$$

Hence, the whole strategy is to find out photocatalytic surfaces which have the potential to absorb light and generate electron-hole pairs. These electrons and holes can then proceed in the HER and OER reaction on the catalyst surface. However, to achieve this target, the conduction band edge (CB) of the catalyst must be more negative than the reduction potential of H^+ to H_2 (-0.41 V). In comparison, the valence band edge of the surface (VB) should exceed the oxidation potential of H_2O to O_2 (0.82 V). In summation, the band gap value of the semiconductor is estimated to be 1.23 eV. Still, due to thermal lossage, the broader approximation or suitable semiconductor band gap is in-between 1.5 to 2.5 eV.

The hydrogen production presently is established by steam reforming. In this process, methane reacts with steam, in the presence of a catalyst at elevated temperature and pressure to convert carbon monoxide and hydrogen gas is produced. The CO generated in this step is utilised again to react with surplus steam to attain CO_2 and more H_2.

$$CH_4 + H_2O \rightarrow CO + 3H_2 \ (Equation\ 7)$$

$$CO + H_2O \rightarrow CO_2 + H_2 \ (Equation\ 8)$$

The use of solar energy for water splitting reaction to generate H_2 is one of the eco-friendliest techniques. However, the use of solar energy for H_2O splitting is categorised into three types;

1. Thermochemical water splitting: In the process, high temperature drawn from solar energy or waste nuclear heat is utilised to initiate a chemical reaction on the surface of a catalyst to produce hydrogen and oxygen. The high temperature (500 °C- 2000 °C) is drawn using large concentrators or using waste heat generated from advanced nuclear reactors. The water splitting process occurs in two different methods. One is the 'direct' way which utilises two step processes; on the other hand, a more complicated process is the 'hybrid' process. This hybrid process involves multiple steps, but the operating temperature is comparatively lower than the direct method and involves less radiative loss.[100-102]

2. Photobiological water splitting: Microorganisms like cyanobacteria and green algae are utilised in the presence of sunlight to generate hydrogen from water. The microorganisms like cyanobacteria absorb light through pigments present in 2 photosystems. Later, the absorbed light is transferred to the chlorophyll reaction centres, where the charge separation occurs to form different reductants and oxidants.[103-105] These reductants and oxidants react in the photosystems to generate electrons and holes which further participate in the water-splitting process. The demerit of this process is the low levels of hydrogen produced and the low solar to hydrogen efficiency. Hence this process is commercially unviable; however, in near future searches for a zero fossil fuel society, the utilisation of the tiniest form of energy is advantageous.[106]

3. Photoelectrochemical water splitting: Honda and Fujishima were the first people to report the use of TiO_2 electrodes for H_2 generation under UV light illumination.[107] Henceforth, this idea was extended towards the particulate system in heterogeneous photocatalysis by Bard *et al*.[108] All through the previous 50 years, significant advances have been made in this quickly rising field. The photoelectrochemical (PEC) activity of hydrogen

production occurs inside a PEC cell under light irradiation. It consists of a working photoanode, which is made up of the synthesised semiconductor materials for oxygen evolution and secondly there is a counter photocathode for hydrogen evolution. These electrodes are placed inside an electrolyte solution with a wire connecting the current loop, in-between the electrodes to complete the circuit. Semiconductors with bandgap less than 1.23 eV can be used as photoelectrodes for hydrogen generation. This can provide an external bias to enable the reaction. However, the use of additional bias often leads to partial depletion of electrons in the semiconductor photoactive surface. This depletion results in the formation of surface space layer and the associated band bending. This process necessarily decreases the rate of recombination and increases the lifespan of the charge carriers.[109]

Reports of the use of 2D structures for electrochemical hydrogen generation are also extensively stated in past few years.[110] The photocatalytic electrochemical activity and the photocatalytic water splitting reactions are measured by evaluating the amount of hydrogen or oxygen emanated from the reactions. It is generally measured in μmol h^{-1} $g^{-1}$and photocurrent density (mA cm^{-2}). The wavelength and intensity of the irradiated light are a few of the other parameters of concern. However, every reaction setup is different, and yields varied results. Therefore, to compare the results, two different terms are used known as quantum yield (QY) or apparent quantum yield (AQY).[111]

$$QY\% = \frac{Number\ of\ reacted\ electrons}{Number\ of\ adsorbed\ photons} \times 100 (Equation\ 9)$$

$$AQY\% = \frac{Number\ of\ reacted\ electrons}{Number\ of\ incident\ photons} \times 100 (Equation\ 10)$$

$$= \frac{Number\ of\ evolved\ hydrogen\ molecules \times 2}{Number\ of\ incident\ photons} \times 100 (Equation\ 11)$$

4. Photocatalytic water splitting: In this process, a high yield of H_2 is generated on irradiating the catalyst surface with sunlight or visible light. The catalyst or more categorically defined as photocatalysts are the semiconductor materials aid in the water-splitting reactions without being transformed or consumed in this procedure. It is a more reliable process compared to the previous options because of the substantial solar to H_2 efficiency, low cost and effortless operation approach. In general, a semiconductor surface on being irradiated with appropriate energy, the electrons from the valence band travel to the conduction band. The electron hole pairs are quite unstable and tend easy recombination. However, structural or electronic manipulation aid in transporting the charge carriers to initiate a chemical reaction on the catalyst surface. The number of electron hole pair created and recombined should be equal to prevent the structural deformation of the catalyst. Apart from using the quantum efficiency values, both the photoelectrochemical and photocatalytic water splitting reactions utilises another parameter solar to H_2 conversion efficiency [STH] (**Equation 12**) under 1.5 global (AM 1.5G) illumination.[111]

$$STH\% = \left(\frac{output\ energy\ of\ hydrogen}{Energy\ of\ the\ incident\ solar\ light}\right) A.M_{1.5G} \times 100 (Equation\ 12)$$

$$= \left(\frac{mmoles\ of\ hydrogen\ per\ second \times 237\ KJ\ per\ mole}{P_{total}(mW\ per\ cm^2) \times Area\ (cm^2)}\right) A.M_{1.5G} \times$$

$100\ (Equation\ 13)$

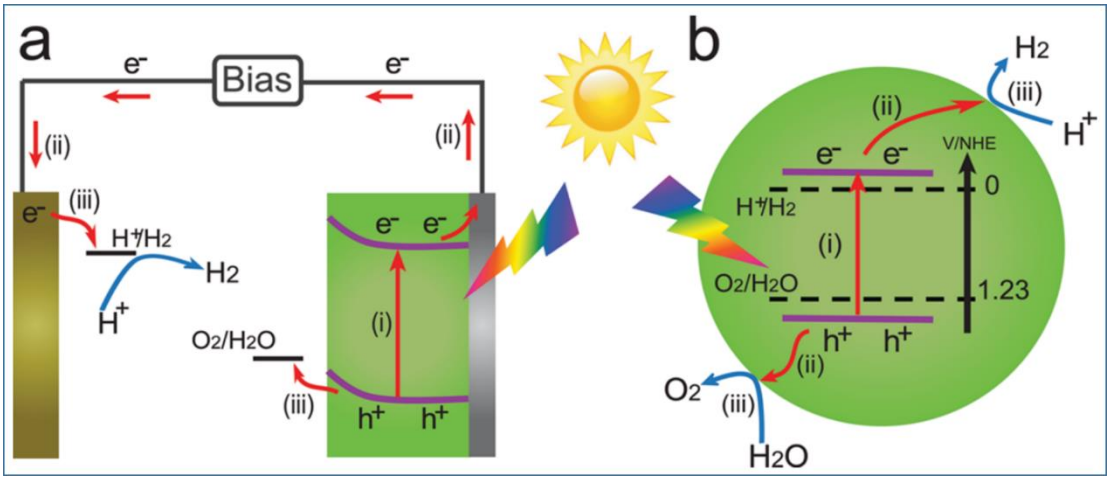

Figure 6. Schematic diagram highlighting the principle and the primary process of a) photoelectrochemical and b) photocatalytic hydrogen generation from water splitting. Reproduced with permission of ref 69 Copyright 2011 Wiley publishers.[109]

1.5. PHOTOCATALYTIC DISINFECTION MECHANISMS OF MICROORGANISMS

The understanding of the bacterial inactivation process is essential to underlay the effective development of novel composites for photocatalytic disinfection mechanisms.[112, 113] Matsunaga *et al.* were the first to demonstrate the light induced inactivation process and proposed that the degradation of coenzyme A by potential ROS generated in the reaction process as the likely mechanism for bactericidal activity. The denaturation of the enzyme resulted in a possible inhibition of respiratory activity, which further led to the cause of death.[114] However, researchers soon found that cell death was prompted by the disruption of the cell wall membrane. Leakage of potassium ions and the subsequent flow of cellular components such as RNA and protein resulted in the complete destruction of these cells. Saito *et al.* were among the first to confront these results; the Transmission Electron Microscopy (TEM) images illustrated the total destruction of these cells.[115] Kikuchi *et al.* evaluated the role of the ROS in the reaction process, by the addition of hydroxyl radical

scavenger. [116] It was observed that the addition of the scavenger reduced the bactericidal activity, but the activity did not cease. The authors proposed the presence of more reactive hydrogen peroxide as the reason for continued bactericidal activity. Hence the antimicrobial activity is a cooperative effect of all the ROS intermediates formed in the reaction process.[116] Advances in defining the plausible mechanism for photocatalytic disinfection of microbes led researchers to understand the reasons for the destruction of the cell wall. Jacoby *et al.* finally found the evidence of complete mineralisation of the damaged cells. Scanning Electron Microscopy (SEM) micrographs were used to observe the disappearing colonies of bacteria and ^{14}C radioisotope labelling was used to analyse the carbon content. [117] Manes *et al.* found that the peroxidation of the phospholipid component of the cellular wall due to the potential ROS attack leads to its disruption.[118] Furthermore, Sokmen *et al.* quantified the lipid peroxidation by quantifying the formation of Malondialdehyde. The by-products of lipid peroxidation were reported at a very early stage. It was found that continuous irradiation resulted in complete degradation of Malondialdehyde into simpler products like Carbon Dioxide (CO_2) and water (H_2O).[119] The formations of these by-products were monitored by Gas chromatography mass spectrometry (GC/MS).[120] Later, Kiwi *et al.* investigated the peroxidation mechanism of the bacterial cell wall on the TiO_2 surface. The cell wall destruction mechanism was monitored by Fourier Transform Infrared spectroscopy with an Attenuated Total Reflection accessory (FTIR-ATR). The h^+ formed in the reaction process competes with the oxidation of the lipid polysaccharide layer or the recombination reaction of h^+ and e^- the authors claim this as the first step towards the complete disintegration process.[121]

Remy *et al.* investigated the bacterial targets and assessed the bacterial cultivability along with its cell wall integrity under dark and visible light irradiation. The authors found that the titania particles exhibited potential bactericidal behaviour way before the light irradiation. The increase in titania content decreased the bacterial cells cultivability. The particles caused

damage to cell wall integrity which further contributed to the increased bactericidal nature. On the other hand, the cell wall permeability was not affected in the presence of silica nanoparticles. The electrostatic charge difference between the particles and the cell wall was found to be the prime reason. In a more in-depth understanding, the RNA and the DNA of the bacterial cells were found to be the bacterial targets of the oxidative attacks induced by the ROS generated during the photocatalytic disinfection mechanism.[122] Wang *et al.* investigated the dominant ROS responsible for the visible light induced disinfection mechanism against *E. coli* using B and Ni co-doped titania microspheres. The hydrogen peroxide (H_2O_2) generated in the system was identified to be the most predominant species. The hydroxyl radical present in the bulk solution and on the surface of the catalyst contributed to the H_2O_2 production.[123] Matai *et al.* studied the antibacterial mechanism of Ag-ZnO composite and adequately defined plausible routes of inactivation (**Figure 7**).[124]

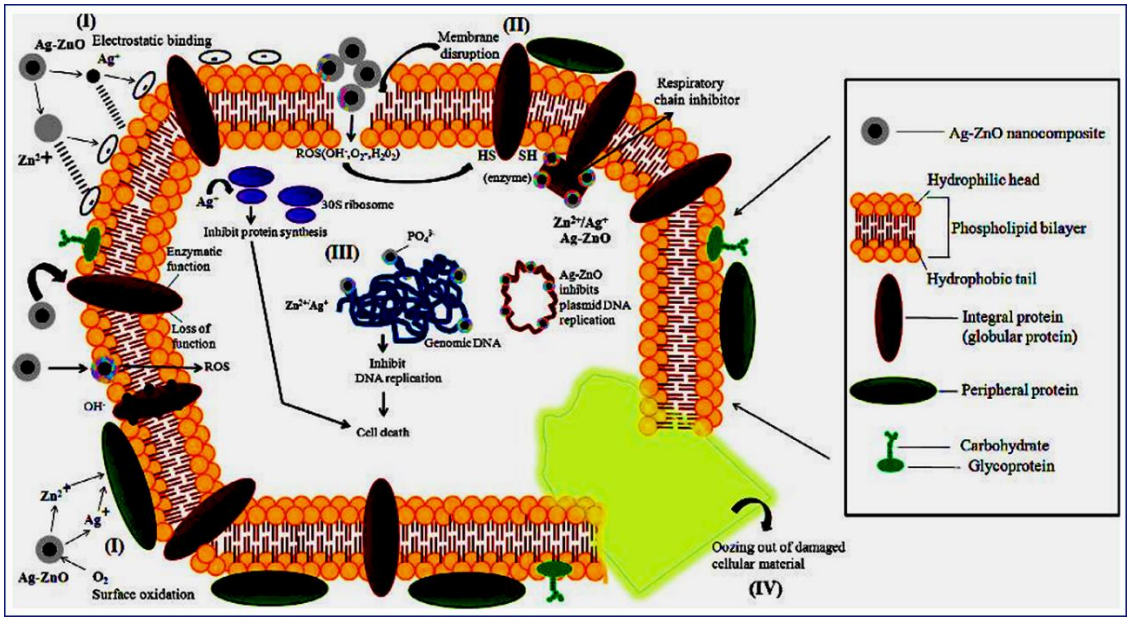

Figure 7. Schematic representation of the antibacterial mechanism of Ag–ZnO nanocomposite. Reprinted with permission of Matai *et al.* (2014). Full details are given in the respective publication.[124]

The first route depicted is the direct interaction of the composite with the bacterial cell. This could happen by the surface oxidation, which will result in the dissolution of the Ag and Zn ions. The possible interaction might also be attained by direct contact of the composite particles with the bacterial cell wall by electrostatic interaction. The second possible method is by the disruption of the bacterial cell wall by potential ions or attack by the ROS generated. The third way of inactivation is the alteration/inhibition of the DNA replication by the interaction of the ions or the ROS with sugar-phosphate groups causing gene alteration, thus altering the protein expression responsible for cellular functioning. Finally, the potential disruption of the membrane leads to the release of the intracellular materials, which eventually leads to cell lysis.[124] **Table 1** provides a summarised glimpse of the mechanisms defined to access the antimicrobial behaviour of the photocatalyst.

Table 1: Summarised analysis of the plausible mechanisms defined in recent years.

Mechanism Defined	Reference
Degradation of coenzyme A	Matsunaga *et al.* [114]
Disruption of the cell wall membrane observed in TEM images	Saito *et al.* [115]
Production of H_2O_2	Kikuchi *et al.* [116]
SEM micrographs and C^{14}labelling to illustrate the disappearing colonies	Jacoby *et al.* [117]
Peroxidation of the phospholipid component of the cellular wall	Manes *et al.* [118]
Quantified the lipid peroxidation by measuring the Malondialdehyde formed	Sokmen *et al.* [120]
Defined the toxic nature of the nanoparticles and found the nuclear material as the potential targets of the bactericidal function.	Remy *et al.* [122]
Identified the influential ROS species and found hydroxyl radicals as a prominent contributor	Wang *et al.* [123]

1.6. PHOTOCATALYTIC DEGRADATION OF DOXYCYCLINE

The Tetracycline (TC) family, which was discovered in the 1940s is a family of antibiotics that inhibit protein synthesis. Doxycycline (DC) is a semisynthetic antimicrobial that belongs to tetracycline class, exhibiting activity against a wide range of gram positive, gram negative bacteria's and against disease causing organisms as Chlamydia, Mycoplasmas and Rickettsia and Protozoan parasites. Pharmaceutical products, such as antibiotics are consumed to mitigate any risk or infection associated with bacterial strains. [125] They are an effective potential cure against several infectious diseases in humans and animals. [126] The use of antibiotics has resulted in a significant decline in

mortality rates amongst humans and animals. [127] However, the irrational use and dumping of pharmaceutical products by different sectors of human services result in alteration of the therapeutic effect of the antibiotics consumed. [128] The bacterial response changes on the consumption of the same medicines, and hence the growth of bacterial colonies remains unaltered. [129] This makes it harder to kill them compared to non-resistant bacteria [130]. This is defined as antibiotic resistance and is a major threat for global health and food security. [131] The rise in cases of antibiotic resistances impacts the overall economy of the country. [125, 132] This increases the duration of medical care, which enhances the average medical cost of the population. [133] It also jeopardizes the life of modern medicines which are vital for several day to day critical treatment such as organ transplant, chemotherapy *etc.* [134] The scope of this issue arises from many folds of society. Countries with preferred guidelines for treatment often tend to overuse prescribed drugs. [134] Improper vaccination and hygiene practices are some of the individual choices made, which contributes to the chances of hosting antibiotic resistant bacteria. [128] Moreover, the growing pharmaceutical industries across developing countries with improper secondary treatment plants, discharge off effluents that result in conventional water pollution [135]. The pharmaceutical effluent leads in leaving residue in water bodies that affect the aquatic ecosystem. [136] The use of these contaminated water sources for irrigation or even human consumption of aquatic bodies results in bioaccumulation in the higher order of the food chain. [137] Urban waste water treatment plants are the major site for antibiotics concentrated in water effluents and hence strategizing routes to degrade antibiotic residues and even disinfection of antibiotic resistant bacteria is critical. [138] Photocatalysis is one of such vital process that projects to be a cost effective, green and sustainable technology against drug resistance and pharmaceutical effluent. [139]

The photocatalytic degradation and the possible intermediates (polar and non-polar) forms of DC have been identified using GC-MS and HPLC-MS [140].

Based on the chromatograms obtained Zhu *et al*. proposes a degradation pathway (**Figure 8**).[140]

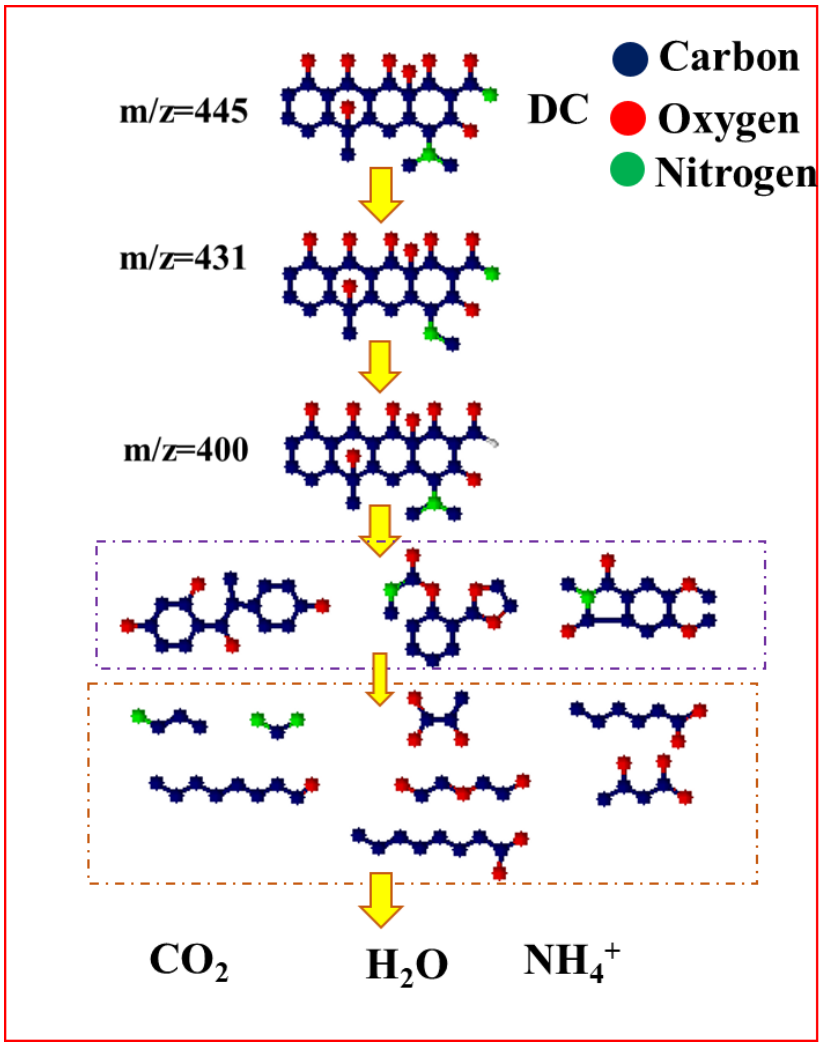

Figure 8. Schematic illustration of a plausible photocatalytic degradation pathway of Doxycycline.[140, 141]

The holes generated in the process accepts electrons from the pollutant molecules and results in the formation of intermediate products. The loss of the N-methyl group was observed at the very beginning, which resulted in an anion species of m/z 431. Further degradation results in the formation of intermediates at m/z 400. Additional mineralisation after a prolonged irradiation results in the breakdown of the DC structure and results in the

generation of smaller fragments of complex structures. Further oxidation of these intricate structures leads to the generation of shorter organic compounds such as acids and alcohols.[140-142]

1.7. OBJECTIVE AND THESIS OUTLINE

The growth led after the industrial revolution in the past century improved the quality of living of the average human being. However, the unaccounted rise in global population and environmental pollution has equally increased the demand for energy and a cleaner environment. Amongst various possibilities for sustainable development, photocatalysis has emerged to be a leading technology. Heterogeneous photocatalysis, in general, is deemed to be an effective solution to the energy crisis and environmental remediation.

However, as with any process there exist certain disadvantages.[143] The search for an effective catalyst that could be commercialised in large scale for various photocatalytic applications is yet to be learnt.[144] Quicker recombination, poor light-harvesting ability and recovery of the catalyst after use are some of the significant challenges. Hence, this gives researchers cause to seek out new generation materials to enhance the reported efficiency.[145] Semiconductor photocatalysis has become an exciting venture lately, as reports of new hybrids and nanoarchitectures has resulted in several functional applications, such as sensors, CO_2 reduction, hydrogen generation, degradation, antimicrobial disinfection *etc*.[146] These nanomaterials display different characteristic absorptions, continuous absorption in the ultra-violet region, visible and some instances of the near-infrared region.[24, 147] Semiconductor materials such as titania is stable, non-toxic, easy to synthesise. However, these materials have a wide band gap which results in absorption of light at the UV region of the electromagnetic spectrum. The absorption of the UV light which accounts only a small portion is a severe concern to these traditional semiconductor nanomaterials. In contrast, metal chalcogenides have shown exciting applications across photochemistry. However, the search for new, less toxic, narrow band gap semiconductor materials has resulted in the

formation of ternary and even quaternary combination of elements to form multi-class chalcogenide compounds.[148-150]

Hence, the main objectives of this research are;

- To prepare novel heterostructure composites of semiconductor nanomaterials and ternary chalcogenides.
- To identify the crystallinity, phase identification and the purity of the as prepared composites using X-ray Diffraction (XRD). The additional characterisation for phase analysis is to be performed for the samples using Raman spectroscopy for some samples.
- To understand the structural, electronic, and dielectric properties through the theoretical study of the parent samples.
- To identify the chemical state and the elemental composition of each sample is identified using X-ray Photoelectron Spectroscopy (XPS) analysis.
- To understand the morphology and to visualise composite creation by TEM image capture of the samples. To study the optical properties and calculate the band gap of the samples using UV-Vis DRS spectroscopy and Photoluminescence spectroscopy.
- Finally, these composites with reduced band gap and enhanced visible light absorption will aid in different photocatalytic applications; to study as prepared composites for their photocatalytic degradation of Doxycycline, photocatalytic water splitting and photocatalytic antimicrobial disinfection.

The following information provides a summary of each chapter in this thesis and how each of the above objectives was achieved.

Chapter 2 defines the materials and the methods of essential characterisation performed for the as prepared composites and their parent samples. The methods for characterising the nanomaterials were XRD, Raman spectroscopy, XPS, TEM, UV-VIS DRS, and PL. Moreover, the chapter provides a detailed description of the synthesis process of the TiO_2, TC and its

composite nanomaterials. It also details the experimental processes of light induced disinfection, degradation and hydrogen evolution process.

Chapter 3 elaborates the formation of novel heterojunctions of the $AgBiS_2$-TiO_2 composite were synthesised using a solvothermal technique. Computational analysis was utilised to study the electronic and optical properties of the pristine parent samples. The XRD results show the formation of the cubic phase of $AgBiS_2$ and TiO_2 is in tetragonal phase. The XPS and TEM results illustrate the heterostructure formation. The UV-DRS pattern for all the composites shows enhanced visible light absorption due to the coupling of TC. The band gaps of the composites were decreased with increased doping levels. These materials were further studied for their photocatalytic efficiency, by photocatalytic degradation of Doxycycline, photocatalytic hydrogen generation and photocatalytic antimicrobial disinfection. The composite samples illustrated more than 95% degradation results within 180 min and showed about 3 log reductions of bacterial strains (*E. coli* and *S. aureus*) within 30 min of irradiation. The hydrogen production results were interesting as the $AgBiS_2$ based composites illustrated a 1000-fold enhanced output. The enhanced photocatalytic activity is attributed to the decreased rate of recombination of the photogenerated excitons, as validated in the PL measurements. The scavenging experiments along with the theoretical analysis are used to define a plausible photocatalytic mechanism

Chapter 4 describes the preparation of $AgInS_2$-TiO_2 composites using a modified sol–gel method. The experimental results reveal that these nanocomposites display enhanced visible light absorption and effective charge carrier separation compared to their pristine parent samples ($AgInS_2$ or TiO_2). 0.5 wt % AgInS2 loading was found to be the optimum concentration for photocatalytic applications. More than 95% of doxycycline degradation was achieved within 180 min of solar light illumination. Similarly, the dopant concentrations at lower values (<2 wt %) exhibited 300 times higher H_2 generation rate under visible light irradiation compared to $AgInS_2$ and TiO_2. The microbial strains (Escherichia coli and Staphylococcus

aureus) showed a 99.999% reduction within half an hour of simulated solar light illumination. The computational investigation was employed to understand the structural, electronic, and the dielectric properties of $AgInS_2$ and TiO_2 composites. The improved photocatalytic results are explained as a result of the decreased rate of exciton recombination. The current investigation opens new insights into the use of novel ternary heterostructure nanocomposites for improved visible light activity.

Chapter 5 details the formation of $AgBiSe_2$-TiO_2 composites and demonstrate the results obtained for the composite structure for various photocatalytic applications. The theoretical study of the pristine parent samples showed the creation of the hexagonal phase of $AgBiSe_2$ and tetragonal phase of TiO_2, which corroborated to the experimentally synthesised structures. $AgBiSe_2$-TiO_2 composites displayed enhanced visible light absorption and reduced band gap in the UV-DRS patterns. An indirect band gap was estimated for TiO_2 and $AgBiSe_2$. The XPS results exhibited a shift in binding energy values and indicated the formation of heterojunctions. The as synthesised materials were studied for their photocatalytic efficiency, by hydrogen generation, degradation of Doxycycline, and antimicrobial disinfection (*E. coli* and *S. aureus*). The composite samples illustrated more than 95% degradation results within 180 minutes and showed 5 log reductions of bacterial strains within 30 minutes of irradiation. The $AgBiSe_2$ based composites displayed an increase of hydrogen generation about 180 folds. The enhanced photocatalytic efficiency displayed is attributed to the delayed charge recombination of the photogenerated electron-hole pairs in the $AgBiSe_2$-TiO_2 interface. Hence, a *p-n* nano heterojunction for $AgBiSe_2$-TiO_2 composite is formed.

Chapter 6 defines the preparation of $AgInSe_2$-TiO_2 novel composites were prepared using a two-step solvothermal synthesis process. The computational study of the pristine parent samples showed the formation of the tetragonal phases of $AgInSe_2$ and TiO_2, which validated the experimentally synthesised structures. $AgInSe_2$-TiO_2 composites displayed enhanced visible

light absorption and reduced band gap in the UV-DRS patterns. An indirect band gap was estimated for TiO_2 while a direct band gap was observed for $AgInSe_2$. The XPS results exhibited a shift in binding energy values and indicated the formation of heterojunctions. The as synthesised materials were studied for their photocatalytic efficiency, by hydrogen generation, degradation of Doxycycline, and antimicrobial disinfection (*E. coli* and *S. aureus*). The composite samples illustrated more than 95% degradation results within 180 minutes and showed 5 log reductions of bacterial strains within 30 minutes of irradiation. The hydrogen production outcomes were significantly improved as the $AgInSe_2$ based composites illustrated a 250-fold enhanced output compared to their parent samples. The improved photocatalytic efficiency displayed is attributed to the delayed charge recombination of the photogenerated electron-hole pairs in the $AgInSe_2$-TiO_2 interface. Hence, type II heterojunction for $AgInSe_2$-TiO_2 composite is formed. **Chapter 7** provides the overall conclusions of all the chapters. It discusses the optimum samples obtained for various photocatalytic applications. Besides, possible future work which includes the formation of different heterostructure units with several novel class of two-dimensional materials are discussed.

CHAPTER 2

EXPERIMENTAL PROCEDURES

2.1. CHEMICALS AND REAGENTS

All the materials used were of analytical grade and used without further purification. Silver nitrate ($AgNO_3$), Indium nitrate ($In(NO_3)_3$), Bismuth(III) nitrate pentahydrate ($Bi(NO_3)_3{\cdot}5H_2O$), Thiourea (CH_4N_2S), Selenium tetrachloride ($SeCl_4$), Titanium(IV) isopropoxide ($C_{12}H_{24}O_4Ti$), Ethanolamine ($NH_2CH_2CH_2OH$), Benzoquinone ($C_6H_4O_2$), Isopropanol ($(CH_3)_2CHOH$), Ethanol (CH_3CH_2OH), Methanol (CH_3OH), Doxycycline hyclate ($C_{22}H_{24}N_2O_8{\cdot}HCl{\cdot}0.5H_2O{\cdot}0.5C_2H_6O$) were purchased from Sigma-Aldrich. Triethanolamine ($C_6H_{15}NO_3$) was bought from PanReac AppliChem ITW reagents. Distilled water was used in all experiments. For antimicrobial studies, strains of *Staphylococcus aureus* (ATCC-25923) and *Escherichia coli* (ATCC-25922) were purchased from LGC Standards. Agar nutrient, Nutrient broth No.2, and 90 mm Petri dishes were bought from Cruinn Diagnostics. Phosphate-buffered saline tablets were supplied from VWR.

2.2. SYNTHESIS

TiO_2 was synthesized using a sol-gel method. The required amount of titanium isopropoxide (TTIP) was stirred in isopropanol for 15 min. The water was added dropwise to the previous solution under vigorous stirring. The ratio of water and isopropanol was kept constant (1:1) and the resultant solution was kept for gelation for 2 h. Furthermore, the gel was dried in an oven at 100 °C for 12 h, followed by calcination at 500 °C, at a ramp rate of 10 °C/min for 2 h.

The $AgBX_2$-TiO_2 heterostructure composites were prepared by a simple one-pot solvothermal technique. Where B are the lattice forming elements (In or Bi) and X are the chalcogens (S or Se). In this process, a definite amount of $AgNO_3$, $In(NO_3)_3$. H_2O or $Bi(NO_3)_3.5H_2O$ (the sources of the B metal component) and thiourea or $SeCl_4$ (sources of the chalcogen) at a ratio of 1:1:2 was weighed and mixed in 30 mL of ethanolamine under vigorous stirring. After an hour of stirring, the as-synthesised TiO_2 was added into the above mixture and ultra-sonicated for another 30 mins, such that the final composites resulted in the ratio of 0.5/1/2 & 5 wt % $AgBX_2$ with remaining TiO_2. The above mixture solution was placed in a 50 mL steel Teflon vessel (from Parr instruments) and heated up to `different temperatures for varying time period for different ternary chalcogenide titania ($AgBX_2$-TiO_2) composites. **Table 2** summarises the optimised experimental parameters for the synthesis of various ternary chalcogenides. The resultant solid product was washed multiple times with water and ethanol to remove the solvent residue and later dried overnight at 60 °C. The dried powder obtained was used for further characterisation and applications. The same protocols were used for synthesising various parent samples without adding TiO_2.

Table 2. The summarised glance of the optimised experimental parameters for ternary chalcogenides.

Ternary chalcogenides	Temperature (°C)	Time (in hours)
$AgBiS_2$	180	24
$AgInS_2$	180	12
$AgInSe_2$	200	12
$AgBiSe_2$	200	12

2.3. DFT/ COMPUTATIONAL CALCULATIONS

The all-electron code, based on full-potential and efficient basis sets, Fritz Haber Institute Ab Initio Molecular Simulations (FHI-AIMS) [151] has been used

for the structural, electronic and dielectric properties of TiO_2, $AgBiS_2$, $AgInS_2$ within the Density Functional Theory (DFT). The calculations are performed at the generalised gradient approximation (GGA) exchange correlation level as implemented by Perdew, Burke and Ernzerhof. [152] In all calculations, we employ the Tkatchenko and Scheffler (TS) van der Waals (vdW) correction scheme to consider the long-range vdW interactions. Geometrical relaxations for both the atomic positions and the lattice vectors are performed by the Broyden-Fletcher-Goldfarb-Shanno (BFGS) algorithm.[153, 154] An 8x8x8 Γ-centered k-point mesh for the Brillouin zone integration and the 'tight' all-electron basis sets provided by the FHI-AIMS package are used for high accuracy. The convergence thresholds set on the eigenvalues, total energies and forces were 10^{-3}, 10^{-4} eV and 10^{-3} eV/Å respectively. The Spin-Orbit Coupling (SOC) effect was included in the calculation of the electronic and dielectric properties of the systems to take into consideration the relativistic impacts. Moreover, the absorption spectra for $AgInS_2$ and TiO_2 are calculated using the independent particle approximation in the range of 0−7.5 eV input light. The computational calculations of $AgBiSe_2$, $AgInSe_2$ were performed using the Vienna Ab initio Simulations Package (VASP) based on Density Functional Theory (DFT).[155] Standard generalized gradient approximation (GGA) within the Perdew-Burke-Ernzerhof (PBE) was used as the exchange-correlation functional to relax the geometries of TiO_2, $AgInSe_2$ and $AgBiSe_2$.[156] It is known that PBE reproduces these structures well, but at the same time, it is affected by the self-interaction correction leading to the systematic underestimation of the band gap of these materials.[157] The projector-augmented wave (PAW) method with the plane-wave basis-set cut-off of 520 eV and a Monkhorst-Pack (MP) grid of 8x8x5 k-points were used.[158-160] The convergence criterion is that the forces on individual atoms are less than 0.001 eV/ Å and the total energy of $1x10^{-7}$ eV per atom. The ground-state electronic structure calculations have been carried out using 4x4x3 MP k-grid and the hybrid Heyd-Scuseria-Ernzerhof (HSE06) exchange-correlation functional.[161, 162] HSE06 is nonlocal, range separated, screened Coulomb

potential density functional that provides accurate the electronic properties that match the experimental results.[163] The initial geometries of TiO_2, $AgBiS_2$, $AgInS_2$, $AgInSe_2$ and $AgBiSe_2$ were extracted from the Materials Project Library.[164]

2.4. CHARACTERISATIONS

X-ray diffraction (XRD) was used to analyse the crystallinity and phase of the prepared samples. In Siemens D500 X-ray powder diffractometer, the diffractograms were produced using Cu Kα radiation (λ= 0.15418 nm) at 40 kV and 30 mA. The diffraction was examined in the range of 10°- 80° with the constant scan rate at 0.2°/s.

The phase transformation was analysed using Raman spectroscopy (Horiba Jobin Yvan LabRAM HR 800) with a grating of 300 gr/mm. A solid-state diode laser (660 nm) standard bandwidth version with double edge filter upgrade was used with the acquisition time of 3 seconds.

The bonding interactions and oxidation state of elements were studied with the help of X-ray photoelectron spectroscopy. Samples were analysed on an XPS, Thermo Fisher Scientific, (East Grinstead, UK) K-Alpha$^+$ spectrometer, which has an XR3 twin anode X-ray source (Al Kα/Mg Kα) and an Alpha 110 analyser. The twin anodes Al Kα X-ray source (hν = 1486.6 eV) was used at 300 W (15 kV x 20 mA) for analysis of all samples. For all survey spectra, a Pass Energy of 200 eV and a step size of 0.4 eV was used. In order to acquire C 1s, O 1s and Ti 2p high resolution spectra a Pass Energy of 20 eV and a step size of 0.2 eV were used.

The characteristic absorptions of the as prepared samples were measured using a Perkin- Elmer Lambda 35 UV-Vis Spectrophotometer equipped with reflectance measuring attachment. Barium sulphate ($BaSO_4$) was used as a reference, and slit width was set to 1 nm. Band gaps were calculated using

both Kubelka-Munk function and Tauc equation. Where Kubelka-Munk function F(R);

$$F(R) = \frac{(1-R)^2}{2R} \text{ (Equation 14)}$$

Where R is the absolute reflectance of the sample.

And the Tauc equation is;

$$(h\vartheta\alpha)^{1/n} = A(E - E_g) \text{ (Equation 15)}$$

Where A = Constant depending on the properties of the material.

E = Energy of the incident photon.

Eg = Band gap of the material.

h = Planck's Constant.

ν = Frequency of the incident photon.

n = Constant that depends on the type of electronic transition, where;

n= ½ for permitted direct transition

n = 3/2 for prohibited direct transition

n = 2 for permitted indirect transition

n = 3 for prohibited indirect transition.

The obtained diffused reflectance of the sample is converted to Kubelka-Munk function as F(R) is proportional to the absorption coefficient. The α in the Tauc equation is substituted with F(R). Hence, the equation becomes; [165]

$$(h\vartheta F(R))^{1/n} = A(E - E_g) \text{ (Equation 16)}$$

The morphology and microstructure of the samples were imaged using a JEOL 2100 Transmission Electron Microscope (TEM) at an accelerating voltage of 200 kV with Lanthanum Hexaboride emission source. The TEM samples were prepared by ultrasonication of samples in 5 mL of acetone for 10 minutes and

was later drop casted on copper mesh. The samples were left to be air dried overnight and later used for imaging.

Photoluminescence spectra (PL) were obtained using a Perkin-Elmer LS55B luminescence spectrometer with a pulsed Xenon discharge lamp. The measurements were recorded using an excitation wavelength set at 320 nm, and emission measured from 330 nm to 800 nm. The excitation wavelength was determined based on the absorption measurements obtained for the samples. The spectra reported is not normalised as the intensity of the emission spectra was critical in assessing the recombination rate.

The photocatalytic degradation of Doxycycline and microbial disinfection experiments were performed inside a weathering and corrosion photo-reactor from Q-Labs (Q-sun Xe-1-S) using a Xenon lamp source (500 W), equipped with a window glass filter. The irradiation intensity is fixed at 1.1 $W/m^{2,}$ and the chamber temperature was maintained at 38 °C.

2.5. PHOTOCATALYTIC DEGRADATION REACTION

The photocatalytic activities of as-synthesized $AgBX_2$-TiO_2 composites were evaluated by photodegradation of doxycycline (DC) under visible light illumination using a photo chamber unit. In a typical photocatalytic experiment, 0.08 g of the photocatalyst was dispersed in 80 ml of aqueous DC (10^{-5} M) solution. Before irradiation, the resultant suspension was magnetically stirred for 60 min in the dark to attain absorption-desorption equilibrium. After every 15 minutes of illumination period, aliquots were withdrawn to measure the concentration of DC with a UV-Vis spectrophotometer in the spectral range of 200 to 800 nm. Doxycycline exhibits strong characteristic absorption peaks at 278 and 357 nm. The peak at 357 nm is considered to be the main absorption peak. The reduction in the intensity of the peak at 357 nm is monitored with time for the degradation profiles. The data obtained are not normalised further and plotted against the time. For a complete assessment of the degraded solution, a calibration curve

is plotted for DC using a standard solution of 10^{-3} M. Serial dilution of the solution to 10^{-4}, 10^{-5} and 10^{-6} M is prepared in order to plot the standard calibration curve (Absorbance versus concentration) and the typical R^2 value is obtained to be ~0.988. For comparative assessment, photocatalytic degradation of pristine parent samples (TiO_2, $AgBiS_2$ and $AgInS_2$) were also carried out under identical conditions. After every experiment, the photocatalysts were centrifuged, washed, dried, and reused to evaluate the recyclability of the samples. The equation calculated the degradation ratios;

$$\%DC\ degraded = \left(\frac{C_0 - C_t}{C_0}\right) \times 100 \text{ (Equation 17)}$$

where C_0 (mg L^{-1}) and C_t (mg L^{-1}) correspond to the DC concentration at the initial and after contact time t (min) respectively. The experiments were performed three times and the best results attained are reported hereafter in each chapter.

Scavenging Experiment

In order to evaluate the reactive oxygen species generated in the reaction system, different scavenger tests were performed. 10 mM isopropanol [a quencher of hydroxyl radicals (OH^-)], 6 mM $AgNO_3$ (a quencher of the electron), 6 mM benzoquinone [a quencher of superoxide radicals (O_2^-)] and 10 mM triethanolamine (a quencher of holes) are added respectively in 4 different photocatalytic systems, with 0.08 g of photocatalyst dispersed in 80 ml of aqueous DC (10^{-5} M) solution. These systems were further subjected to light irradiation for 180 mins, prior to the illumination they were kept for 60 min in the dark to achieve the adsorption-desorption equilibrium. Aliquots after every 15 min were taken and estimated for DC concentration as explained above for the photocatalytic experiments.

2.6. PHOTOCATALYTIC HYDROGEN GENERATION

With the aim of evaluating the photocatalytic competence, the synthesised composites of TiO_2 were investigated for H_2 generation. Visible light induced water splitting and photoreforming of organic species in aqueous solution is considered as a crucial process to convert solar to chemical energy. The use of sacrificial organic agents helps to obtain higher photoefficiency due to the oxidation of organic species by photogenerated positive holes, with the simultaneous production of H^+ ions. Photogenerated electrons on the surface of the catalyst encounter with hydrogen ions to produce hydrogen gas. Therefore, merging organic wastewater supervision and H_2 generation *via* sunlight might be a promising sustainable approach to tackle environmental and energy issues.

Photocatalytic runs were performed in an annular glass batch reactor (V =300 mL) covered with a layer of aluminium foil. On the top of the reactor, an inlet allowed feeding reactants and nitrogen gas, and an outlet was used to collect liquid and gaseous samples at different reaction times.

The reactor was endowed with a high-pressure mercury vapour lamp by Helios Italquartz (power input: 125 W) and a high-pressure sodium vapour lamp by (power input: 150 W), both of which are from Helios Italquartz. The reactor was cooled at 25 °C during each run utilizing a thermostatic bath (Falc GTR 90).

The pH of the solution was monitored employing an Orion 420Aþ pH-meter (Thermoscientific).

In order to avoid the undesired reaction of dissolved oxygen with photogenerated electrons, before starting the photocatalytic runs, a nitrogen stream was bubbled into the solution for 30 minutes for removing atmospheric oxygen. Moreover, throughout the experiments, nitrogen was continuously fed at a flow rate (Q_{N_2}) of 0.3 L/min to prevent any entrance of air into the reactor. For each run, fixed amounts of catalyst and methanol were

added to 300 mL of aqueous solution; the resulting suspension was fed into the batch reactor under magnetic stirring.

The liquid samples, collected at different reaction times, were quickly filtered on regenerated cellulose filters (pore diameter 0.20 μm, Scharlau) and the filtrate was used to measure pH. The gaseous samples were recovered from the reactor outlet in Tedlar gas sampling bags and then used to evaluate hydrogen concentration.

Hydrogen concentration was measured by a gas chromatograph (Agilent 7820A) equipped with an HP–PLOT Molesieve 5A column (Agilent) and a TCD detector using argon as a carrier gas.

During the experiments, the radiation emerging from the reactor was measured on the external walls of the reactor by means of proper radiometers (not shown in **Figure 9**) in the wavelength ranges of 315-400 nm and 400-1100 nm.

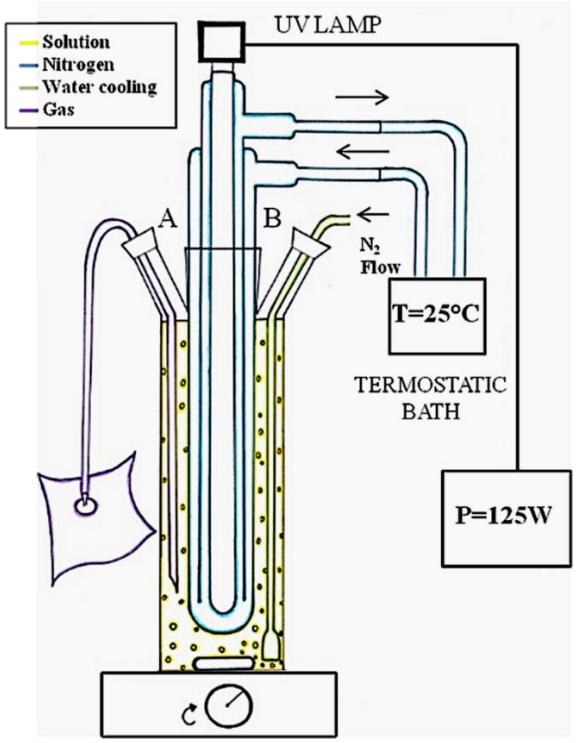

Figure 9. Schematic illustration of the photocatalytic reactor (A) outlet and (B) inlet.

In the same experimental runs, at a fixed reaction time (60 minutes) a solution of sodium nitrite (1 M) was introduced inside the cooling jacket for controlling the temperature (25°C) and for cutting-off UVA radiation emitted by the lamp (λ < 400 nm). The amount of evolved hydrogen is given by the pressure and can be calculated from the ideal gas law. Where V_m is the molar volume of hydrogen, $n(H_2)$ is the obtained moles of hydrogen, p is the pressure, R is the ideal gas constant, T is the reaction temperature, V_{total} is the total volume of the setup, and V_{liquid} is the volume of the reaction solution.

$$V(H_2) = V_m n(H_2) = V_m \frac{p(V_{total} - V_{liquid})}{RT} \text{ (Equation 18)}$$

2.7. PHOTOCATALYTIC ANTIMICROBIAL ACTIVITY

All the glassware used for the photocatalytic disinfection experiments were autoclaved prior to their use. Two strains of bacteria, one gram-negative (*E. coli*) and the other gram-positive (*S. aureus*) were utilised to evaluate the light induced disinfection ability of the as prepared $AgBX_2$-TiO_2 composites and further compared with their pristine parent samples (TiO_2, $AgBiS_2$, $AgInS_2$, $AgInSe_2$ and $AgBiSe_2$). 25 g of nutrient broth No.2 (10 g peptone, 5.0 g NaCl, 10 g beef extract) was dissolved in 1 L of distilled water to make the nutrient broth cultural medium, which is further sterilized at 121 °C using an autoclave. 28 g nutrient agar (5.0 g peptone, 8.0 g NaCl, 3.0 g beef extract, Agar No.2) was dissolved in 1 L of distilled water and further autoclaved at 121 °C for 15 mins and later poured into 90 mm agar plates. The strains were inoculated in 20 mL of nutrient broth and incubated for 24 h at 37 °C. A particular volume of the expanded culture was transferred to the cylindrical glass vessel to make the working solution of 10^4 CFU/mL (colony forming unit/ml). The reaction suspension was placed inside the photo test chamber for visible light illumination. The photocatalyst concentration was fixed at 1 g/L and illuminated for an overall 3 h. Additionally, aliquots of 1 mL were removed out from the reaction suspension at a regular time interim of 15 mins. In order to achieve a countable CFU, the bacterial solution was diluted

once in 9 mL PBS solution, and later 100 μL of the diluted solution was plated. Lastly, the plates were incubated at 37 °C for 24 h. The colonies developed on the agar plates were calculated and recorded as CFU/mL. Control experiments were also performed in the absence of the photocatalyst. The same sets of samples were tested simultaneously under dark conditions to understand the importance of light in the experiment. The antimicrobial efficiency was calculated using 2 methods; i) log reduction and ii) N/N_0% vs time. Where,

$$\text{log reduction} = log_{10}\frac{(A)}{(B)} \Rightarrow \log_{10}(A) - \log_{10}(B) \quad \text{(Equation 19)}$$

Where A = initial number of viable microorganisms

B = number of viable microorganisms at any time "t".

Now, $\log_{10}(A) \rightarrow N_0$, $\log_{10}(B) \rightarrow N$ for any time "t".

Triplicate set of experiments were performed, and the best results attained are reported hereafter in each chapters.

CHAPTER 3

THEORETICAL AND EXPERIMENTAL INVESTIGATION OF VISIBLE LIGHT RESPONSIVE $AgBiS_2$-TiO_2 HETEROJUNCTIONS FOR ENHANCED PHOTOCATALYTIC APPLICATIONS

3.1. INTRODUCTION

Recent advances have seen novel semiconductor materials such as ternary chalcogenide (TC) compounds utilised to improve visible light absorption.[166, 167] TC are an exciting class of materials, these multicomponent chalcogenides have garnered enough attention in recent years for their effective electro-optical properties, and used for potential applications in biomedical imaging, photovoltaic devices, LEDs, phase change memory devices.[168-170] Among them, the family of I-V-VI has gained significant interest because of their wide band gap and high visible light absorption.

$AgBiS_2$ (I-V-VI), a ternary semiconductor material is a very common mineral sulfbismuthide in nature (matildite). It exists in two phases, namely, the low-temperature phase β-$AgBiS_2$ with a hexagonal structure and the elevated temperature phase α-$AgBiS_2$ with a cubic structure. The phase transition temperature is 195 °C.[171] The nanocrystals of $AgBiS_2$ are reportedly synthesised through various methods such as solid-state reaction, solid solution technique, flux technique, microwave-assisted method,

hydro/solvothermal procedure, polyol route and sonochemical techniques.[172-177] The narrow band gap and the high visible light absorption benefits different functional applications. However, these semiconductor exhibit low quantum efficiency and strong light etching which restricts its large-scale applications.[178, 179]

In order to promote the separation of photogenerated excitons, the visible light absorption alone cannot promote high photocatalytic efficiency, thereby there requires possible structural or morphological manipulation.[180] Hence, heterostructure formation with other classical semiconductors such as TiO_2 can possibly aid in delaying the excitons recombination.[179] TiO_2 due to its high structural and photostability along with facile synthesis process, makes it an ideal photocatalytic candidate.[181] However, the poor visible light absorption and wide band gap decrease their catalytic efficiency.[182, 183] Therefore, the formation of heterostructure composite with $AgBiS_2$ could potentially increase the photocatalytic efficiency by reducing the composite bandgap and by enhancing the charge transfer. Finally, the challenge to overcome the lack of exciton population on the photocatalytic surfaces could be possibly evaded by structural manipulations.[184] The staggered band alignment of a possible heterostructure would promote the delaying of the photogenerated electron-hole pair recombination, which effectively enhances the interfacial charge transfer.[181, 185]

$AgBiS_2$-TiO_2 heterostructure for solar cell application has been reported. Zhou *et al.* reportedly synthesised $AgBiS_2$ quantum dots (QDs) and assembled onto TiO_2 nanorods film for QD-sensitized solar cell (QDSSC).[186] However, there exists a definite paucity in correlating the theoretical concepts on the structural details of the semiconductor materials with the experimental process. There are no reports of these novel composites with a complete understanding and evaluation of their photocatalytic behaviour by various functional applications.

Therefore, in this present study, a solvothermal technique was utilised to synthesize $AgBiS_2$-TiO_2 composite. Stable and visible light improved effective heterojunctions of $AgBiS_2$- TiO_2 at different weight percent loading were developed (0.5, 1, 2 and 5 wt%) and further evaluated for photocatalytic degradation of Doxycycline, photocatalytic hydrogen generation and photocatalytic antimicrobial disinfection. Computational analysis of the structural, electronic and optical properties of the pristine parent samples (TiO_2 and $AgBiS_2$) were studied. The as prepared composites illustrated homogeneous distribution as observed in TEM images and showed composite formation through Raman and XPS analysis. The composites of $AgBiS_2$-TiO_2 displayed 1000-fold enhanced photocatalytic H_2 production compared to $AgBiS_2$ and TiO_2 samples. Similar results were also observed for bacterial disinfection activity, where the $AgBiS_2$-TiO_2 exhibited better results compared to its pristine counterparts. Furthermore, the degradation results were also impressive as the composites exhibited more than 95% activity within 180 mins of visible light irradiation. A plausible photocatalytic mechanism based on the computational results, PL measurements and the scavenger experiments have been proposed.

The synthesis process and the process optimisation of the composites are explained in **section 2.2**.

3.2. RESULTS AND DISCUSSION

3.2.1 Computational analysis

The crystal structures of TiO_2 and $AgBiS_2$ have been fully relaxed. TiO_2 crystallises into the tetragonal crystal structure as shown in **Figure 10**. Ti and O are connected to each other in octahedral molecular geometry, and the octahedra are connected by the alternate edge and corner sharing. The lattice parameters of the relaxed structure of tetragonal TiO_2 crystal are a = b = 10.1621 Å, c = 2.9605 Å and $\alpha = \beta = \gamma = 90^{\circ}$.

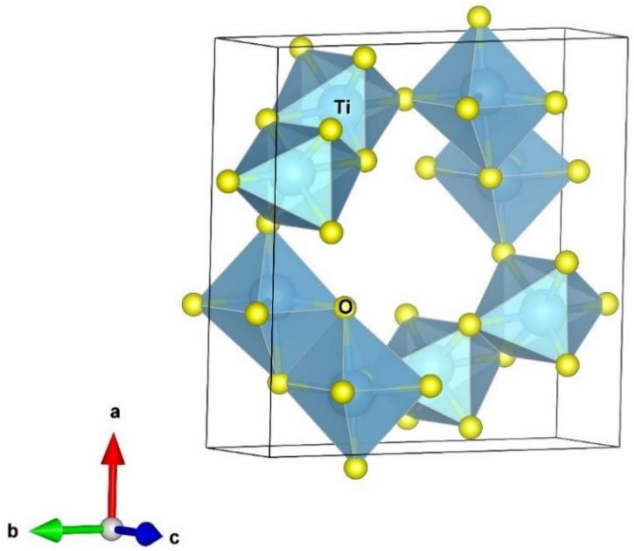

Figure 10. (Colour Online) Optimised structure of TiO_2. Fully relaxed tetragonal crystal structure of TiO_2. Colour code: blue = Ti and yellow = O. Data generated courtesy of Dr. Syam Kumar.

$AgBiS_2$ is layered and found to be stable in a trigonal crystal structure and is given in **Figure 11**. BiS_6 octahedra are separated by AgS_6 tetrahedra in its unit cell.

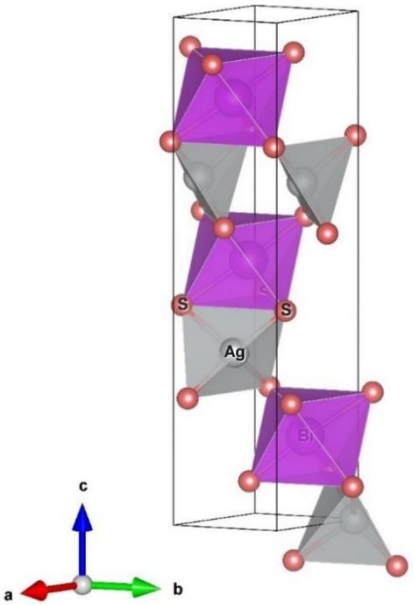

Figure 11. (Colour Online) Optimised structure of Silver Bismuth Sulphide ($AgBiS_2$). Fully relaxed trigonal structure of $AgBiS_2$. Colour code: grey = Ag, light pink = Bi, red = S. Data generated courtesy of Dr. Syam Kumar.

In the relaxed structure, the lattice parameters of trigonal $AgBiS_2$ are a = b = 4.0817 Å, c = 19.3362 Å, $\alpha = \beta = 90^{\circ}$ and $\gamma = 120^{\circ}$. The optimised lattice constants of TiO_2 and $AgBiS_2$ are within approximately 2% deviation from the experimental data as provided in the **section 3.2.2**.

The band structure and the partial density of state (PDOS) of TiO_2 are shown in **Figure 12**. The system has a computed indirect band gap of ~ 2.7 eV. The valence band maxima (VBM) lies between Z and P k-points and the conduction band minima (CBM) lie between the Γ and X k-points in the reciprocal space. The upper valence band (UVB) is dominated by O p-states, and the lower conduction band (LCB) is dominated by Ti d-states. There is the presence of Ti p-states also near the UVB.

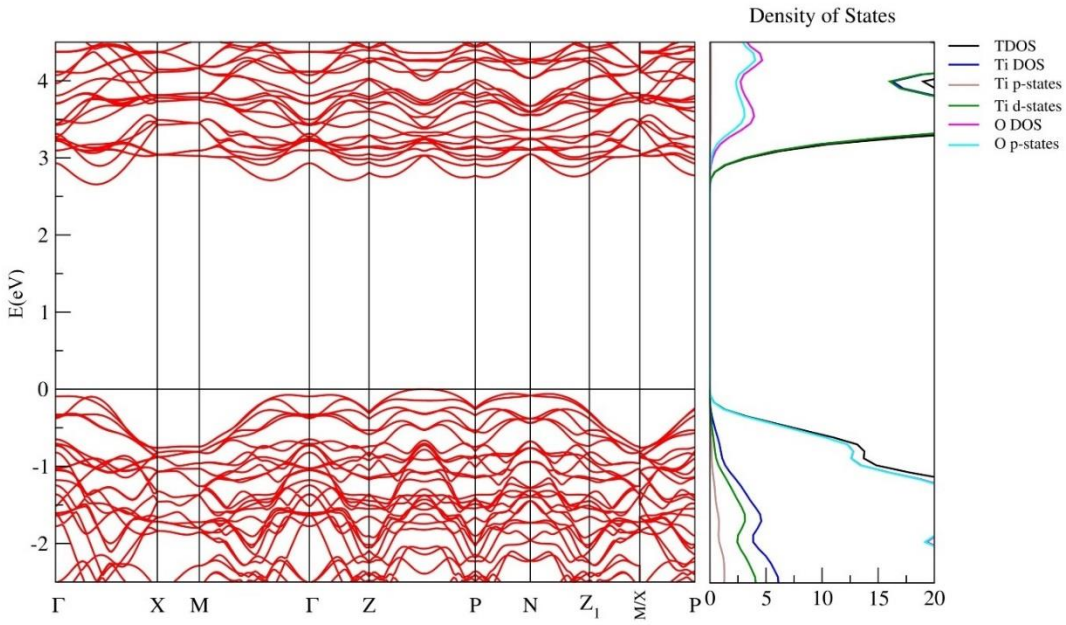

Figure 12. Optimised electronic structure of TiO_2. Calculated band structure for TiO_2. The valence band top is aligned at 0 eV (horizontal line) with the corresponding PDOS. Data generated courtesy of Dr. Syam Kumar.

Figure 13 shows the computed band structure and the PDOS of $AgBiS_2$. The system has an indirect bandgap of ~0.7 eV. The VBM lies between the H and A k-points, and the CBM lies between the Γ and A k-points of the Brillouin zone. The calculated electronic structure around UVB can be attributed to the electronic states of AgS_4 tetrahedra and the region around the LCB can be attributed to the electronic states of BiS_6 octahedra. The S p-orbitals and Ag d-orbitals dominate the UVB, and the Bi and S p-states dominates the LCB, respectively. As mentioned earlier, the forbidden transitions hints that the actual energy required for the electron to move from the VB to CB will be more than the computed bandgap value.

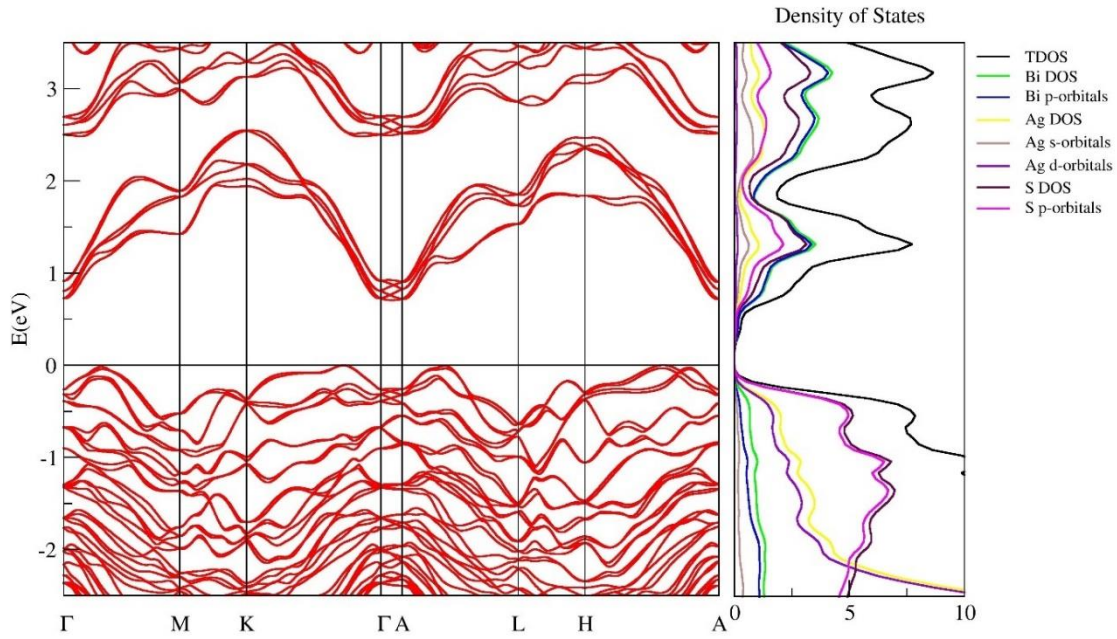

Figure 13. Optimised electronic structure of Silver bismuth sulphide. Calculated band structure for $AgBiS_2$. The valence band top is aligned at 0 eV (horizontal line) with the corresponding PDOS. Data generated courtesy of Dr. Syam Kumar.

The imaginary part of the dielectric function was calculated using PBE-GGA to find out the energy value at which the actual electron transition starts. The calculations carried out using FHI-AIMS package were for an input light of energy range 0 to 7.5 eV that includes the infrared, visible and ultraviolet region of the electromagnetic spectrum. The first peak of the imaginary part of the dielectric spectra gives us the energy value at which the actual absorption takes place. The first peaks in the imaginary part of the dielectric function of TiO_2 and $AgBiS_2$ were found at 3.87 eV and 2.57 eV respectively and are shown in **Figure 14a** and **Figure 14b**, respectively. In the case of TiO_2 and $AgBiS_2$, the light absorption spectrum is isotropic along the x and y directions.

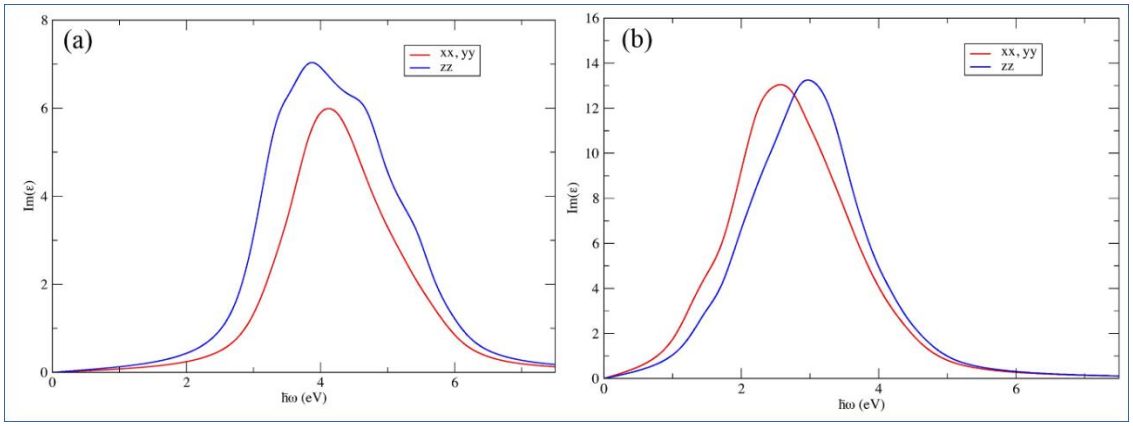

Figure 14. Imaginary part of the frequency-dependent dielectric function of (a) TiO_2, (b) $AgBiS_2$. Optical isotropy was found in the case of TiO_2 and $AgBiS_2$. Data generated courtesy of Dr. Syam Kumar.

3.2.2 X-ray diffractogram (XRD)

The crystal structure of as synthesised $AgBiS_2$-TiO_2 composites was examined using XRD. **Figure 15** shows the formation of the cubic phase of $AgBiS_2$ with a lattice constant of a= 5.64 Å is distinctly observed without the formation of any impurity phase.[187]

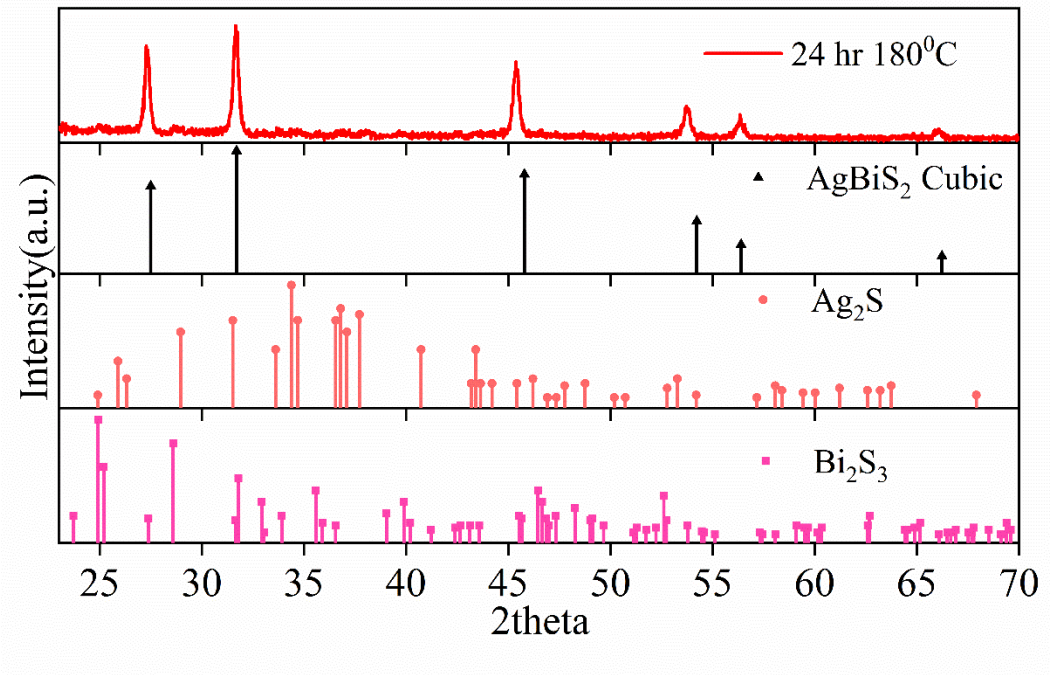

Figure 15. XRD of as prepared $AgBiS_2$ with other standard peaks of $AgBiS_2$ cubic, Ag_2S and Bi_2S_3.

Well defined peaks at 27.5°, 31.70°, 45.79°, 54.2°, 56.4°, 66.22° corresponding to (111), (200), (220), (311), (222) and (400) respectively is observed [ICDD-00-004-0699]. **Figure 15** also compares the as prepared $AgBiS_2$ with other standard peaks of Bi_2S_3 [ICDD - 00- 017-0320] and Ag_2S [ICDD - 00-033-0624]. This confirms the formation of a pure phase of silver bismuth sulphide without any impurities.

In order to understand the optimum parameters for the solvothermal synthesis of $AgBiS_2$ different temperature and time studies were completed. **Figure 16a** and **16b** illustrate the diffractograms obtained after synthesis at different temperatures and time, respectively. As observed, in **Figure 16a** the crystallinity of the signature peak of $AgBiS_2$ at 31.7° increases with increase in temperature from 160 °C to 180 °C for a time of 24 h. The intensity of the same peak dampens on enhancing the temperature beyond 180 °C (at 200°C). Similarly, in **Figure 16b** shows a similar pattern, on synthesising at 180 °C for different time periods, on increasing the time from 6 h to 24 h, the signature peak emerges gradually, while increasing it up to 48 h, decreases the crystallinity. The optimum solvothermal synthesis parameter for $AgBiS_2$ is 180 °C at 24 h.

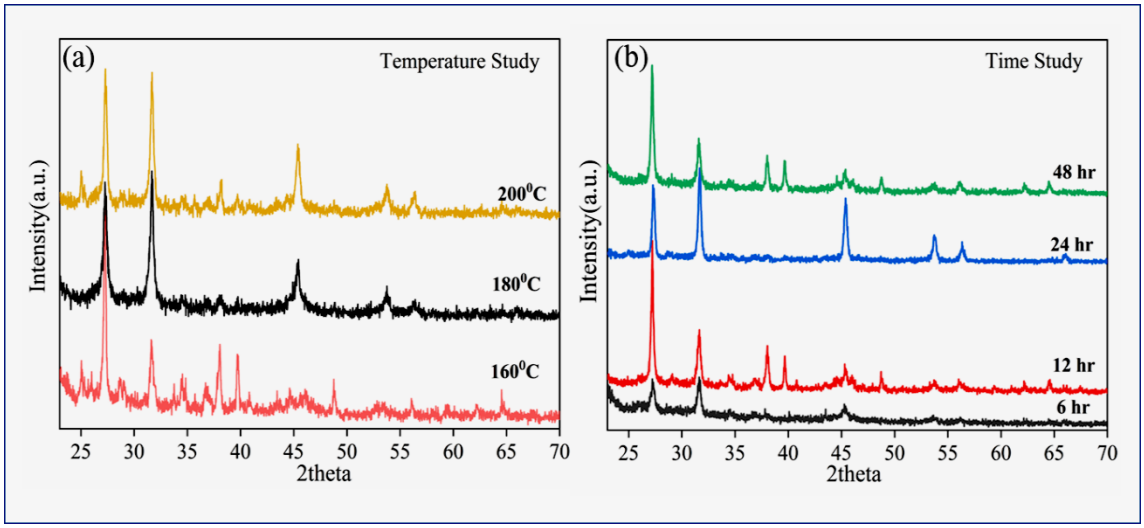

Figure 16. (a) Temperature study for 24 h and (b) time study of $AgBiS_2$ at 180 ˚C of solvothermal synthesis.

Figure 17 exhibits the formation of pristine anatase phase of TiO_2 [a=b= 3.7821 Å and c= 9.5 Å] with sharp peaks at 25.4˚, 38.5˚, 48.0˚, and 55.0˚ owing to (101), (112), (200) and (211) respectively.[188] **Table 3** summarises the lattice parameters experimentally calculated with the reported values in literature.

Table 3. Summarised lattice parameters of TiO_2 and $AgBiS_2$.

Compound	Parameter	a(Å)	b(Å)	c(Å)	α(°)	β(°)	γ(°)	**Ref**
TiO_2	Experimental	3.78	3.78	9.50	90.00	90.00	90.00	
	From Literature	3.80	3.80	9.60	90.00	90.00	90.00	188
$AgBiS_2$	Experimental	5.64	5.64	5.64	90.00	90.00	90.00	
	From Literature	5.66	5.66	5.66	90.00	90.00	90.00	187

The figure also illustrates the diffractograms of $AgBiS_2$-TiO_2 composites. As observed the peaks of $AgBiS_2$ is not evident at lower dopant percent (0.5 to 2 wt %). However, a small peak at 31.7˚ is observed in the case of a 5 wt% $AgBiS_2$-TiO_2 composite.

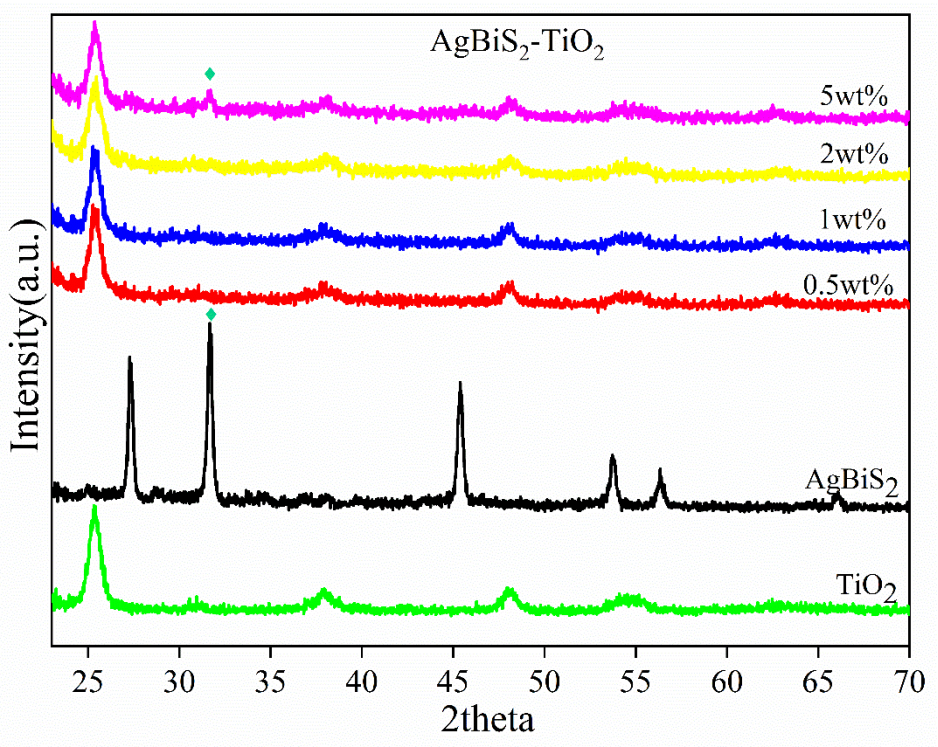

Figure 17. XRD patterns of as prepared TiO_2, $AgBiS_2$ and $AgBiS_2$-TiO_2 composites.

The most notable fact about the composite structures as observed in **Figure 17** is that on the introduction of TiO_2 by solvothermal synthesis to form a possible heterojunction did not tamper the anatase phase of the sample, and the crystallinity of the composite remained unaltered. The lattice constant obtained for pristine parent samples showed good agreement to the theoretically calculated values.

Similarly, as observed from the XRD diffractograms, the formation of the metastable cubic phase of $AgBiS_2$ could be attributed to the choice of solvent used in the synthesis process. Ethanolamine (EA), with a single amine and N-chelating atom, has been used as a potential structure directing agent.[189] The inbuilt pressure and the appropriate temperature supports the formation of such unique phases. The growth mechanism of $AgBiS_2$ in a solvothermal technique could be explained as below;

$$AgNO_3 + xEA \rightarrow Ag(EA)_x^+ + NO_3^- \text{ (Equation 20)}$$

$$Bi(NO_3)_3 + yEA \rightarrow Bi(EA)_y^{3+} + 3NO_3^- \text{ (Equation 21)}$$

The use of EA as a solvent results in coordination with Ag^+, and Bi^{3+} ions to form a covalent complex as in **equation 20** and **21** (where x and y are positive integers).[190, 191] Furthermore, these complexes react with thiourea (TH) to form complexes as;[192]

$$Ag(EA)_x^+ + xTH \rightarrow [Ag(TH)_x]^+ + xEA \text{ (Equation 22)}$$

$$Bi(EA)_y^{3+} + yTH \rightarrow [Bi(TH)_y]^{3+} + yEA \text{ (Equation 23)}$$

The solvent ethanolamine in the reaction aids in the formation of complexes in the first half of the reaction and preserves thiourea from dissociation to form any free radicals of S^{2-}. This mechanism prevents the formation of any other impurity phases (binary compounds) such as Bi_2S_3 or Ag_2S. As the temperature enhances, the stability of the thiourea decreases to yield $AgBiS_2$, since the ternary chalcogenide is the more stable phase in that reaction atmosphere. In the meantime, thiourea in the reaction mixture plays a dual role in forming a complex and also being the source of sulphur.[193, 194]

$$[Ag(TH)_x]^+ + [Bi(TH)_y]^{3+} \rightarrow AgBiS_2 \text{(Equation 24)}$$

The 2 wt% $AgBiS_2$-TiO_2 composite illustrated the best photocatalytic results (discussed in the later sections) among their parent and sister samples (or other dopant %) and hence hereafter are used for further characterisations unless otherwise stated.

3.2.3 Raman Spectroscopy

Figure 18 illustrates the Raman peaks of TiO_2, $AgBiS_2$ and $AgBiS_2$-TiO_2. In the case of $AgBiS_2$, a peak around 147 cm^{-1} is observed, which is attonated to the Ag lattice vibrations. A small peak at 238 cm^{-1} is attributed to the Ag-S lattice vibrations.[195, 196] Meanwhile, the typical active modes for anatase are observed at 147, 197, 396, 516 and 638 cm^{-1} for A1g, 2B1g and 3Eg

respectively.[197] On the other hand, for the composite samples, the peaks of anatase appear to be sharp and symmetric. A minor red shift is observed (as given in the inset of **Figure 18**), as the peak maxima for the composite sample shift towards lower wavenumbers. This is considered to be the positive note of successful composite formation.[198, 199]

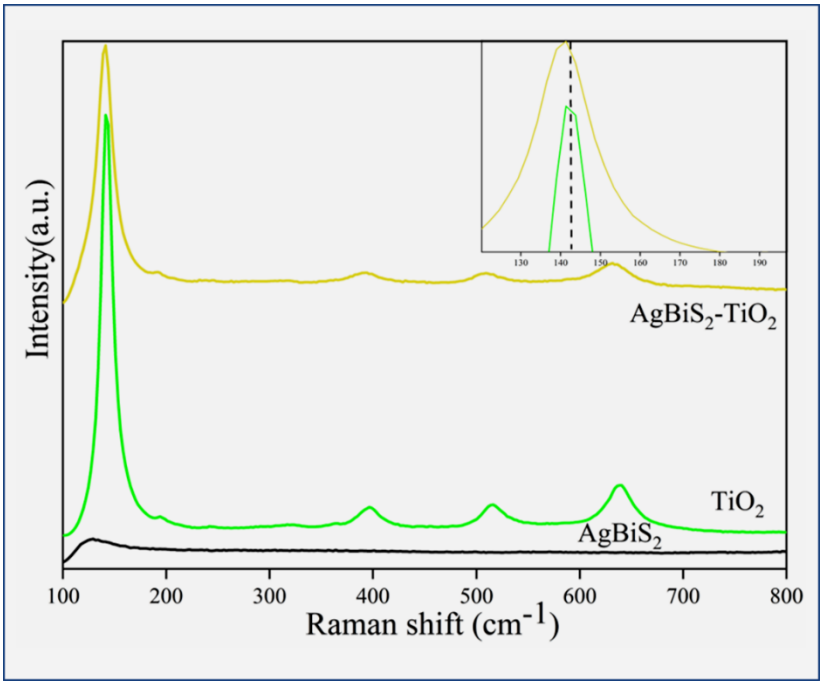

Figure 18. Raman spectra of TiO_2, $AgBiS_2$ and 2 wt% $AgBiS_2$ –TiO_2 composite.

3.2.4 X-ray Photoelectron Spectroscopy (XPS)

XPS detects the chemical states and the nature of the bonds. The survey spectra of TiO_2 and $AgBiS_2$-TiO_2 are given in **Figure 19**.

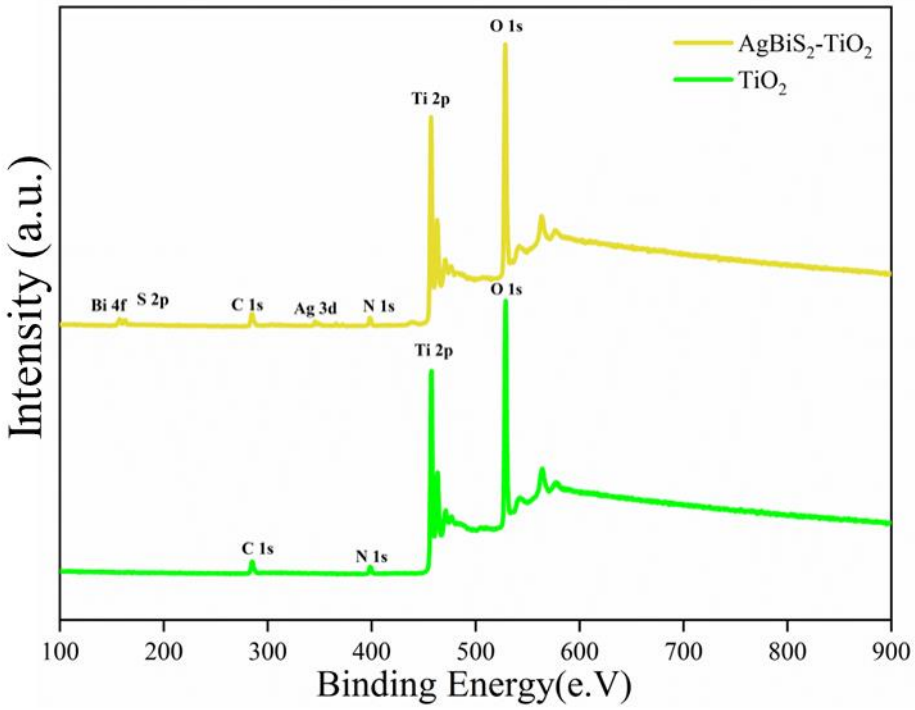

Figure 19. Survey spectra of TiO_2, and 2 wt% $AgBiS_2$-TiO_2. Data generated courtesy of Dr. Steven Hinder.

Peaks of Ti 2p and O 1s are observed for TiO_2. Additional peaks of Ag 3d and Bi 4f are observed in $AgBiS_2$-TiO_2. Small peaks of C 1s and N 1s are also observed in all the samples which are presumably contaminants acquired during the synthesis or characterisation process.

Figure 20A shows the Ti 2p spectra of TiO_2 and the composite sample. As observed, the Ti 2p spectrum illustrates peaks of Ti $2p_{3/2}$ at 557.8 eV, which is consistent with Ti being in the +4 oxidation state. Similarly, **Figure 20B** illustrates the O 1s spectra of TiO_2 and composite sample. Peaks at 528.59 eV and 530.40 eV corresponding to the crystal lattice oxygen (O-Ti^{4+}) and for hydroxyl molecules respectively are observed. There is no evident shift in peaks of Ti 2p and O 1s of the composite sample.[17, 188, 200] **Figure 20C** exhibits the high-resolution spectra of Ag 3d. Characteristic peaks of Ag $3d_{3/2}$ and Ag $3d_{5/2}$ are observed at 373.9 eV and 367.9 eV respectively for $AgBiS_2$.[201, 202] A shift of approximately -1.8 eV is observed in the peaks of Ag $3d_{3/2}$ and Ag $3d_{5/2}$

[372.03 eV and 366.04 eV respectively] of $AgBiS_2$–TiO_2 composite sample. Similarly, **Figure 20D** illustrates the high-resolution spectra of Bi 4f and S 2p for $AgBiS_2$ and the composite structure. The characteristic peaks at 163.66 eV and 158.28 eV corresponding to the Bi $4f_{5/2}$ and Bi $4f_{7/2}$ respectively are observed for $AgBiS_2$ samples with a doublet separation of 5.38 eV.[201-203] The S 2p peaks of the pristine $AgBiS_2$ sample is attonated at 161.12 eV.[171, 201] The composite sample illustrates the presence of Bi in +3 and elemental oxidation states. The peaks at 155.24 eV and 160.60 eV corresponds to the Bi in elemental state, while the peaks at 157.13 eV and 162.57 eV corresponds to the Bi in +3 oxidation states of $AgBiS_2$.[203, 204] The doublet splitting remained consistent (~5.4 eV) for both the oxidation states. Moreover, as in the case of Ag 3d, the peaks of Bi 4f of the composite also exhibited a considerable shift of -1.1 eV. The summarised glance of the position of all the elements is tabulated in **Table 4**.

As observed in the case of the composite structure, the shift in the peaks of Ag and Bi compared to their pristine samples is evident. The binding energy shifts of the heterostructure components is explained by the strong interaction between $AgBiS_2$ and TiO_2. The increase in electron concentration due to strong electron screening effect results in the decrease in binding energy. Whereas the decreased electron concentration by the weakened electron screening effect leads to an increase in binding energy. Therefore, in the current aspect, the increase in electron concentration due to the interfacial charge transfer between heterostructure components result in the shift of the peak observed.[205-208]

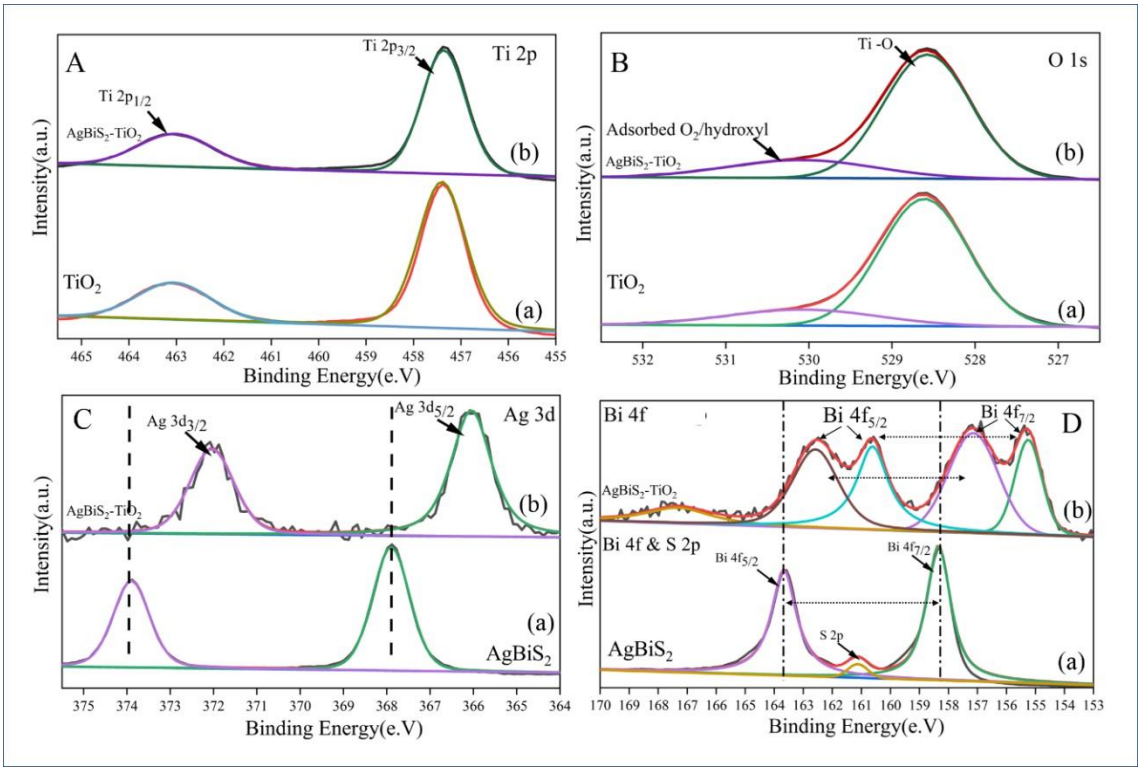

Figure 20. Deconvoluted spectra (A) high resolution spectra of Ti 2p (a) TiO_2 and (b) 2 wt% $AgBiS_2$-TiO_2; (B) high resolution spectra of O 1s (a) TiO_2 and (b) 2 wt% $AgBiS_2$-TiO_2; (C) high resolution spectra of Ag 3d (a) $AgBiS_2$ and (b) 2 wt% $AgBiS_2$-TiO_2 and (D) high resolution spectra of Bi 4f and S 2p (a) $AgBiS_2$ and (b) 2 wt% $AgBiS_2$-TiO_2. Data generated courtesy of Dr. Steven Hinder.

Table 4. A summarised glance of all the peak position of different elements $AgBiS_2$ and 2 wt% $AgBiS_2$-TiO_2 (in eV).

Sample	**Ag $3d_{3/2}$**	**Ag $3d_{5/2}$**	**Bi $4f_{5/2}$**	**Bi $4f_{7/2}$**
$AgBiS_2$- TiO_2	372.030	366.040	162.570	157.130
$AgBiS_2$	373.900	367.900	163.660	158.289

3.2.5 UV-Vis absorption and bandgap estimation

The optical absorption, corresponding electron transition and the band gap of the as prepared samples were studied using UV-Vis spectra. On exposing

semiconductor material with photons having energy more significant than its band gap, an electron from the valence band transfers to the conduction band. Hence, we observe an increase in absorbance at a corresponding wavelength (λ). The nature of the absorption coefficient (α), with the incident light, depends on the electronic transitions. During the electron transfer, if the momentum of the electron is conserved, then it is defined as a direct band semiconductor. While, if the momentum of the electron is not conserved, then there involves phonon in the process and is defined as indirect band semiconductor.[58, 209]

On plotting $[h\nu F(R)]^{1/n}$ against $h\nu$, the tangent line is drawn along the slope of the spectra which intersects the horizontal axis provides the band gap value Eg. However, it should be noted that absorption is determined by low and high energies when the photon energy is greater to the band gap (Eg) of the semiconductor, the absorption increases linearly with increase in photon energy.[210] While, the photon energy is lower than Eg, then the absorption observed deviates from linearity and exhibits photonic absorption corresponding to the defect levels present in between the valence band and conduction band of sample.[211]

Figure 21 shows the diffuse reflectance spectra and band gap estimation of TiO_2 and $AgBiS_2$-TiO_2 composites. A sharp absorption at UV region (350 nm) is observed by TiO_2 while a significant enhancement in the visible light absorption is observed for the composite samples (**Figure 21a**). As observed, all the composite samples exhibit the absorption shoulder at 380 nm, the signature peak of TiO_2, but the absorption edge of all the spectra are enhanced up to 800 nm. This shows the improved visible light absorption observed in composites samples at very small addant levels. Meanwhile, **Figure 21b** illustrates the corresponding indirect band gap energies of the samples. As perceived, the band gap values of TiO_2, and $AgBiS_2$- TiO_2 is estimated as 3.18 eV and further decreases with increase in $AgBiS_2$ content (as given in the inset of **Figure 21b**).

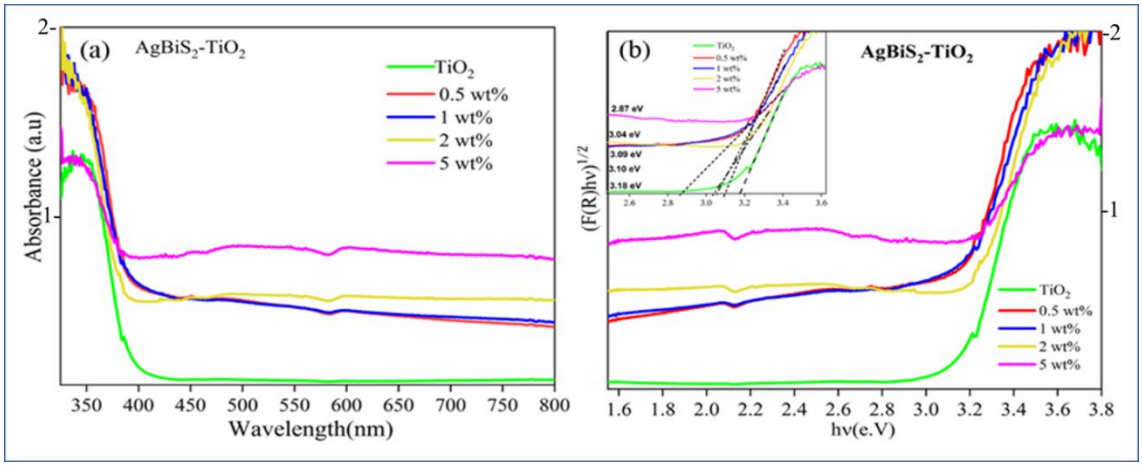

Figure 21. (a) DRS spectra and (b) band gap estimation of TiO_2 and $AgBiS_2$-TiO_2 composites.

In the case of pristine $AgBiS_2$, a defined absorption peak is observed around 380 nm (**Figure 22a**). Apart from that, **Figure 22b** illustrates the direct band gap calculated from the Kubelka-Munk plot.[212]

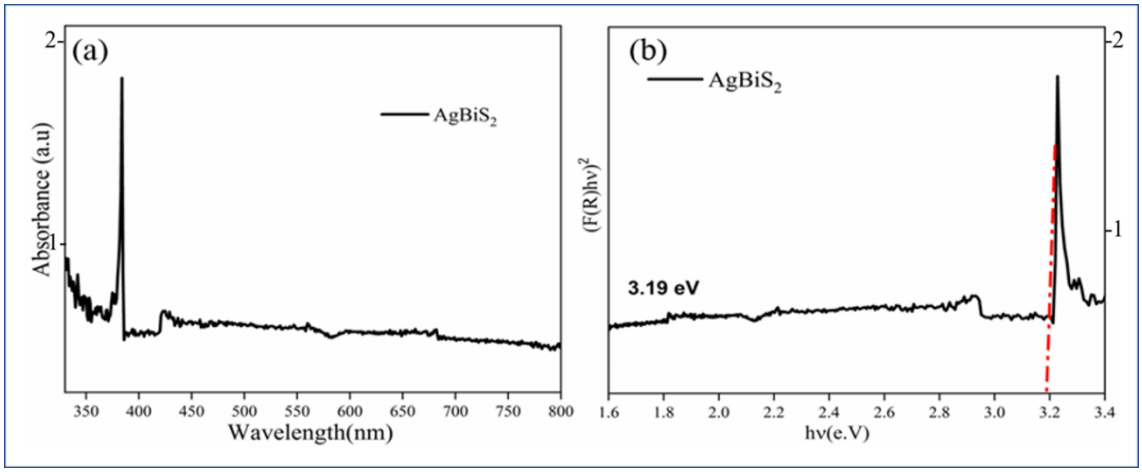

Figure 22. (a) DRS spectra and (b) band gap estimation of $AgBiS_2$.

Table 5 tabulates the obtained band gap values of TiO_2 and $AgBiS_2$-TiO_2 composites.

Table 5. Band gap values of TiO_2 and $AgBiS_2$-TiO_2 composites.

Sample	**TiO_2**	**$AgBiS_2$**	**0.5 wt%**	**1 wt%**	**2 wt%**	**5 wt%**

Band gap (eV)	3.18	3.19	3.10	3.09	3.04	2.87

The absorption edge of the pristine TiO_2 nanoparticles in the DRS spectra is observed around 415 nm while the $AgBiS_2$ shows an absorption edge around 400 nm. However, a strong visible light absorption extending up to 800 nm is seen in the case of $AgBiS_2$. The composite samples exhibit strong absorption of TiO_2 and illustrate an enhanced absorption edge garnered by the increased visible light absorption due to the coupling with $AgBiS_2$. It is in good agreement with the change in colour of the composite sample from white (TiO_2) to dark grey (2 wt% $AgBiS_2$-TiO_2). As observed in XPS results, the strong interaction between the heterostructure components leads to interfacial electron transfer which results in the enhanced absorption edge and decrease in the overall band gap.[205, 207, 208] **Table 6** summarises the experimentally attained band gap value and the reported values in literature.

Table 6. Band gap values of TiO_2 and $AgBiS_2$-TiO_2 composites.

Sample	**Band gap (eV)**	**From Literature**	**Band gap type**	**Ref**
TiO_2	3.18	3.20	Indirect	[248]
$AgBiS_2$	3.19	3.00	Direct	[212]

3.2.6 Transmission Electron Microscopy (TEM)

The morphology and the details of the microstructure formed are evaluated using transmission electron microscopy (TEM). **Figure 23a** illustrates the TEM image of TiO_2 and its SAED pattern. The nanoparticles where spheroidal in nature and were of average size of 25 to 40 nm. The anatase phase of the nanoparticles formed is evident from the *d* spacing values calculated for different zones.[213] The TEM image of $AgBiS_2$ is observed in **Figure 23b**; these nanoparticles also appeared to be spheroidal. The lattice fringes of planes

(111), (200) and (220) with corresponding d- values of 0.324 nm, 0.282nm and 0.198 nm is observed.[214] Meanwhile, **Figure 23c** and **23d** show the TEM images of $AgBiS_2$-TiO_2 composite. The image shows the presence of irregular particles identified as $AgBiS_2$ (through lattice fringe identification).[187] The low dopant ratio of the ternary chalcogenides makes them difficult to be observed. However, the presence of the $AgBiS_2$ nanoparticles demonstrates the successful integration with the TiO_2 nanoparticles firmly and hence forming heterojunction structures.

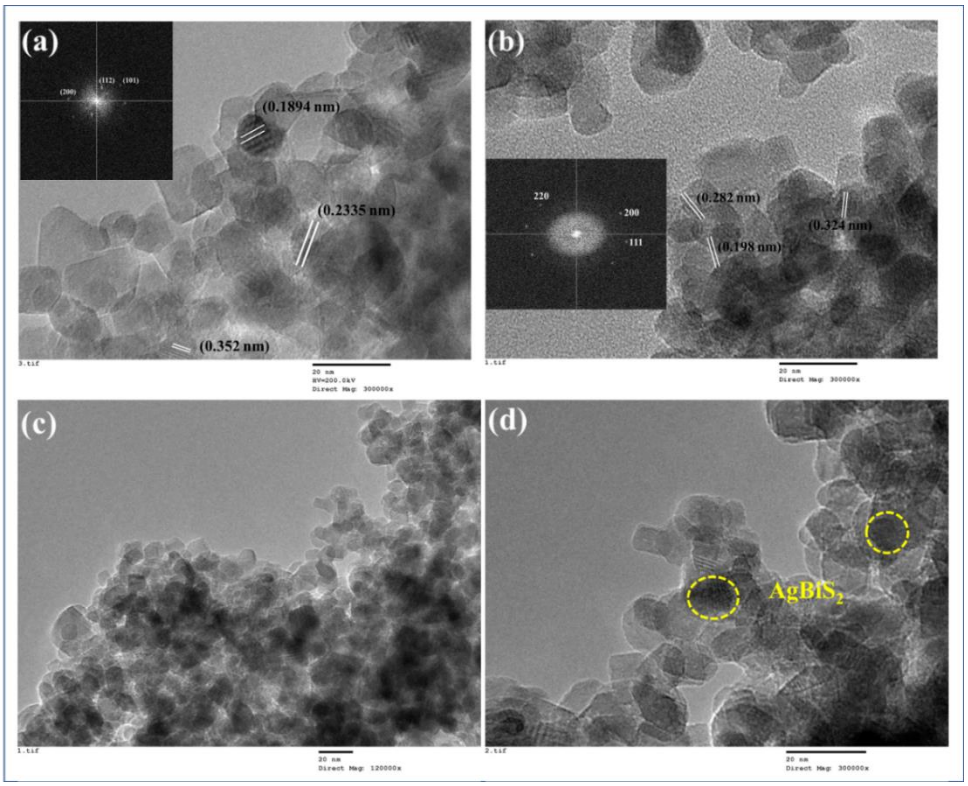

Figure 23. TEM images of (a) TiO_2; (b) $AgBiS_2$; (c) and (d) 2 wt% $AgBiS_2$-TiO_2 composite.

Figure 24 displays some additional TEM images of $AgBiS_2$-TiO_2 composite structure.

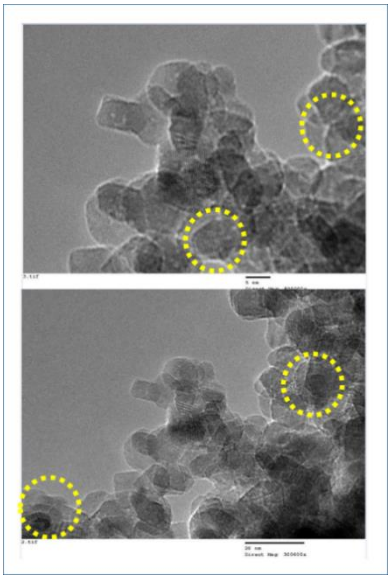

Figure 24. TEM images of 2 wt% $AgBiS_2$-TiO_2 composite structure. Yellow highlights indicate the sites for possible heterojunctions.

3.2.7 Photodegradation

The photocatalytic efficiency of the as synthesised TC composites with TiO_2 was evaluated by degradation of Doxycycline (DC) as a modal pollutant and compared with their pristine parent samples. The photocatalytic experiments were conducted under dark and light illumination, respectively. The composites and their parent samples did not show any adsorption activity in all the cases. **Figure 25** illustrates the degradation profile of $AgBiS_2$-TiO_2 composites by showing the change in concentration of DC with time [C/C_0 % vs time].

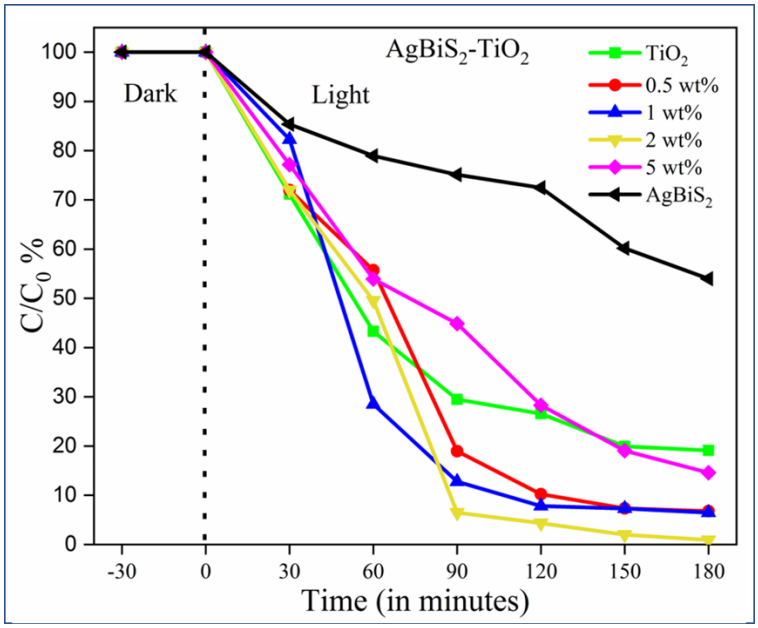

Figure 25. Change in concentration of DC with time TiO_2, $AgBiS_2$ and $AgBiS_2$-TiO_2 composites.

As observed, the parent samples $AgBiS_2$ and TiO_2 with higher band gap values show the least activity. On the other hand, the composites samples show more than 94% degradation within 180 min of irradiation. The 5 wt% composite exhibited the least, and the 2 wt% composite showed the best degradation activity among the entire composite sample. This proves that the composites show better results only at lower dopant levels, and the activity decreases as the loading levels go higher than 2 wt%. a bandgap value of 1.95 eV was not efficient to show improved activity. This could be attributed to the high recombination of the photogenerated electron-hole pairs. These results could be further validated by the H_2 production results, as discussed in the later section.

The photocatalysts after every single photocatalytic study were washed, dried and reused to evaluate the recyclability of the efficiency of the samples. **Figure 26a** illustrates the recyclability profiles of 2 wt% $AgBiS_2$-TiO_2. As observed, the efficiency of the samples remains consistent even after 4 cyclic runs. The scavenging experiment was also performed to evaluate the potential reactive

oxygen species involved in the degradation process by adding $AgNO_3$, triethanolamine, benzoquinone and IPA in the reaction mixture. **Figure 26b** compares the degradation percent of all the 4 sets of systems with 2 wt% $AgBiS_2$-TiO_2 in the reaction mixture on exposed for 180 min of light irradiation.

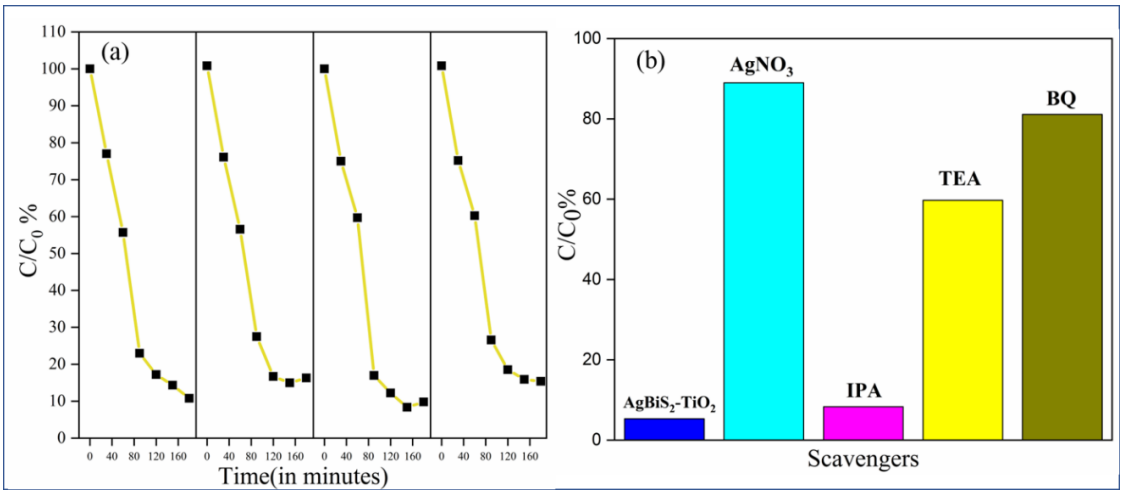

Figure 26. (a) Recyclability profiles and (b) Results of species trapping experiment of 2 wt% $AgBiS_2$-TiO_2.

Electrons and holes are found to be the significant reactive species in this case, as the reduction activity was affected significantly on the addition of $AgNO_3$ and benzoquinone (BQ). However, the system with IPA showed a slight reduction, which proves that hydroxyl radicals did not have a much significant role in the degradation reaction. Hence, electron and holes could be found as the dominant species for $AgBiS_2$-TiO_2.

3.2.8 Photocatalytic H_2 production

In order to evaluate the photocatalytic efficiency, the as prepared composites of TC with TiO_2 is studied for hydrogen production. The hydrogen production rate of $AgBiS_2$-TiO_2 composite samples along with their pristine parent materials was evaluated in the presence of methanol ([CH_3OH] =10 vol.%) as sacrificial species. As it is clear from the figure illustrated (**Figure 27a**), all the catalysts tested show almost negligible hydrogen production in the first 60

minutes of reaction, during which the UVA-component of the light source has been cut off by means of a proper sodium nitrite filter, as reported in **Section 2.6**. After removing the UVA-cut off the filter, the highest values of hydrogen production rate for the $AgBiS_2$-TiO_2 materials have been recorded overweight percentages of 0.5, 1 and 2 wt%. Lower values of hydrogen production rate have been recorded for the 5 wt% $AgBiS_2$-TiO_2 sample, and this shows that on increasing the doping levels beyond 2%, the efficiency of the process decreases. The composite structures at lower weight percent exhibited H_2 production as high as 1310 μmole/min, compared to almost 0 μmole/min observed in case of the parent pristine samples ($AgBiS_2$ and TiO_2). As regards to the solution pH, no significant changes have been recorded for the $AgBiS_2$-TiO_2 samples throughout the reaction time, except for the 2 wt% $AgBiS_2$-TiO_2 sample, for which a moderate pH decrease has been observed after removing the UVA-cut off filter (**Figure 27b**).

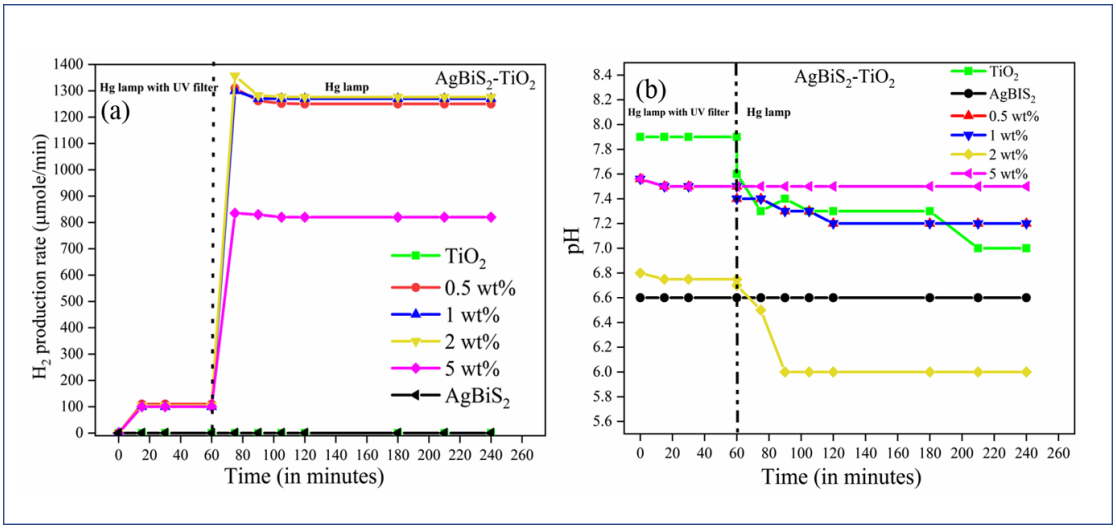

Figure 27. (a) The H_2 production rate and (b) pH of the solution at varying weight percentage of $AgBiS_2$-TiO_2 catalysts. [CH_3OH] =10 vol.%; Catalyst load=500 ppm; T=25°C; P=1 atm. Data generated courtesy of Dr. Laura Clarizia

While **Figure 28a** shows the irradiance, values recorded in the UV range (λ=315÷400 nm) on the external wall of the reactor in the first 60 minutes of reaction are almost negligible due to the presence of the UVA-cut off the filter.

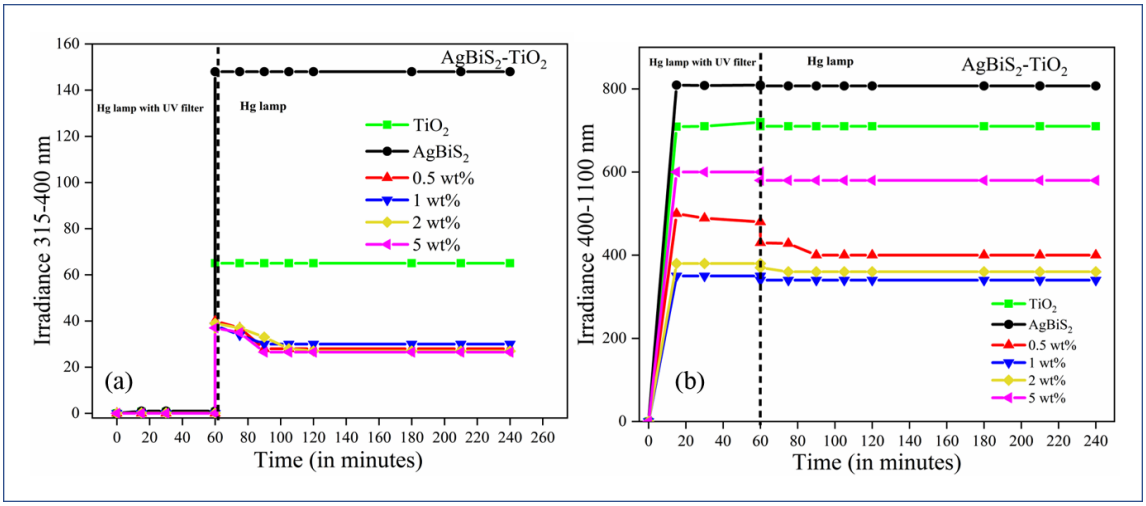

Figure 28. Irradiance measured on the external walls of the reactor between (a) 315-400 nm and (b) 400-1100 nm at varying weight percentage of $AgBiS_2$-TiO_2 catalysts. [CH_3OH] =10 vol.%; Catalyst load=500 ppm; T=25°C; P=1 atm. Data generated courtesy of Dr. Laura Clarizia

After removing the UVA-cut off the filter, an instant increase in the irradiance values has been recorded, which has been followed by a moderate lowering at t=90 min probably due to the photocatalysts activation resulting into a higher suspension absorption. No significant changes before and after removing the UVA-cut off filter have been observed for the irradiance values collected on the external walls of the reactor in the visible range (λ=400÷1100 nm) as shown in **Figure 28b**. The higher values recorded for the 5 wt % $AgBiS_2$-TiO_2 sample indicate its lower capacity to absorb the light irradiation in the visible range.

3.2.9 Photocatalytic antimicrobial studies

The evaluation of photocatalytic bacterial inactivation of *E. coli* and *S. aureus* to $AgBiS_2$-TiO_2 samples was carried out by suspension test. The solutions of

catalyst were prepared in distilled water, inoculated with bacterial strains and further subjected to dark and light conditions, respectively. Control samples were made without the addition of catalysts. The obtained data were also compared with their parent samples. Exposing the bacterial cells with catalysts (1 g/L) under visible light showed different results. The composite structure displayed a superior photocatalytic efficiency than that of pristine samples [$AgBiS_2$ & TiO_2], under light irradiation. In the absence of photocatalysts, the growth of both strains was the same under light and dark conditions. Graphical representation of the test results of $AgBiS_2$-TiO2, $AgBiS_2$ & TiO_2 against *E. coli* and *S. aureus* is given in the above **Figure 29**.

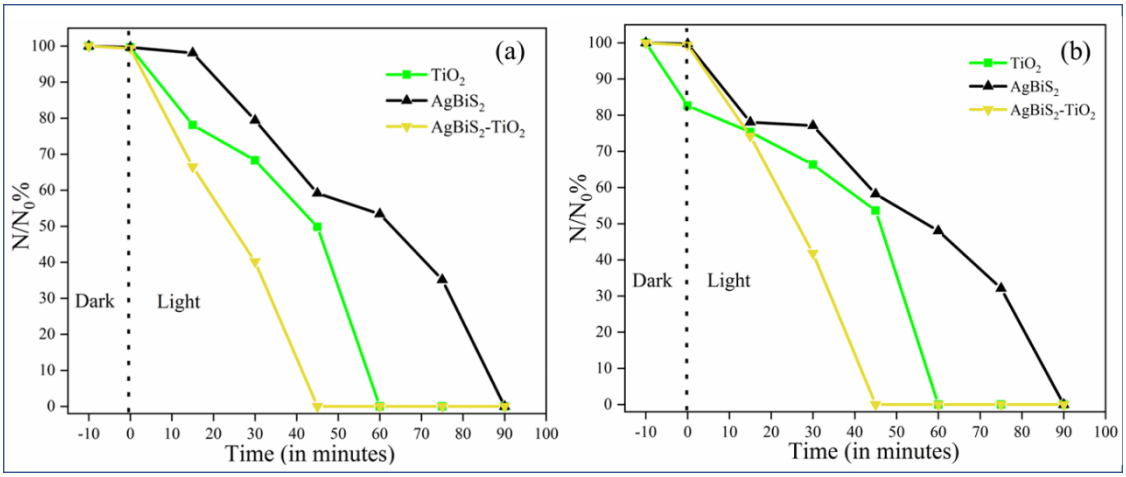

Figure 29. Photocatalytic inactivation of (a) *E. coli* and (b) *S. aureus* with TiO_2, $AgBiS_2$ and 2 wt% $AgBiS_2$-TiO_2.

For both the strains, all the catalysts exhibited a similar pattern of photocatalytic activity. In the case of $AgBiS_2$-TiO_2, a visible decrease was observed in the bacterial growth for both the strains. Log 3 reduction was attained within 45 min of irradiation (**Figure 30**).

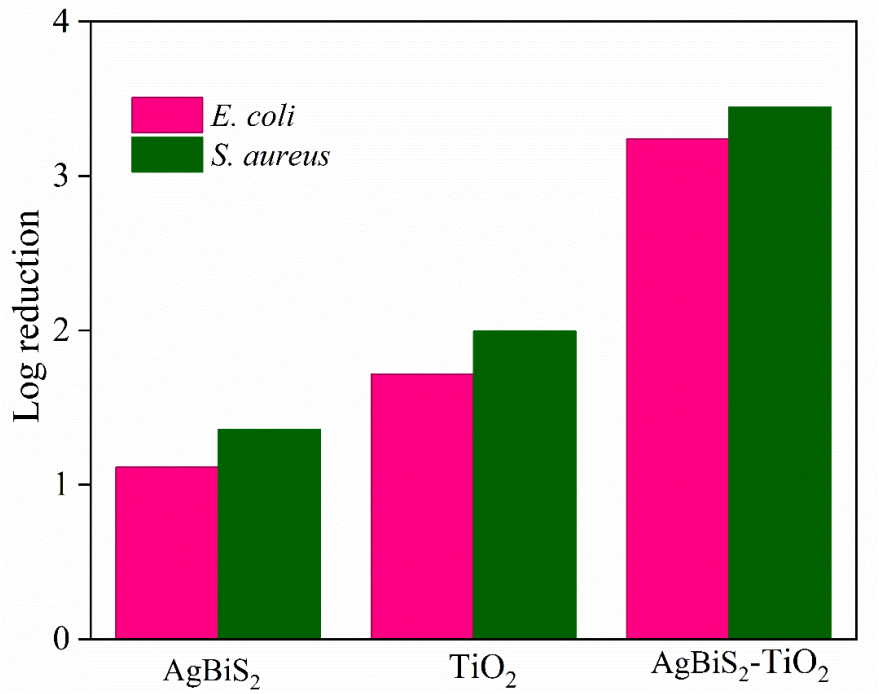

Figure 30. Log reduction of all the samples against *E. coli* and *S. aureus*.

While, for pristine $AgBiS_2$, it required 90 mins of exposure to achieve the same result. **Figure 31** illustrates the images of bacterial colonies grown on agar plates on various time intervals for $AgBiS_2$-TiO_2. The close interface developed in the composite structure aided to the delayed charge recombination. Thus, promoting the inactivation efficiency amongst the composite sample when compared to their parent samples. The charge carriers result in the formation of potential reactive oxygen species which tampers the bacterial cell wall integrity. This results in an outflow of intracellular materials and cell lysis. Moreover, the reactive species created in the photocatalytic process can cause gene alteration by oxidation of the DNA. Alteration in the genetic expression would affect the cellular functioning and could lead to cell lysis. [182, 215]

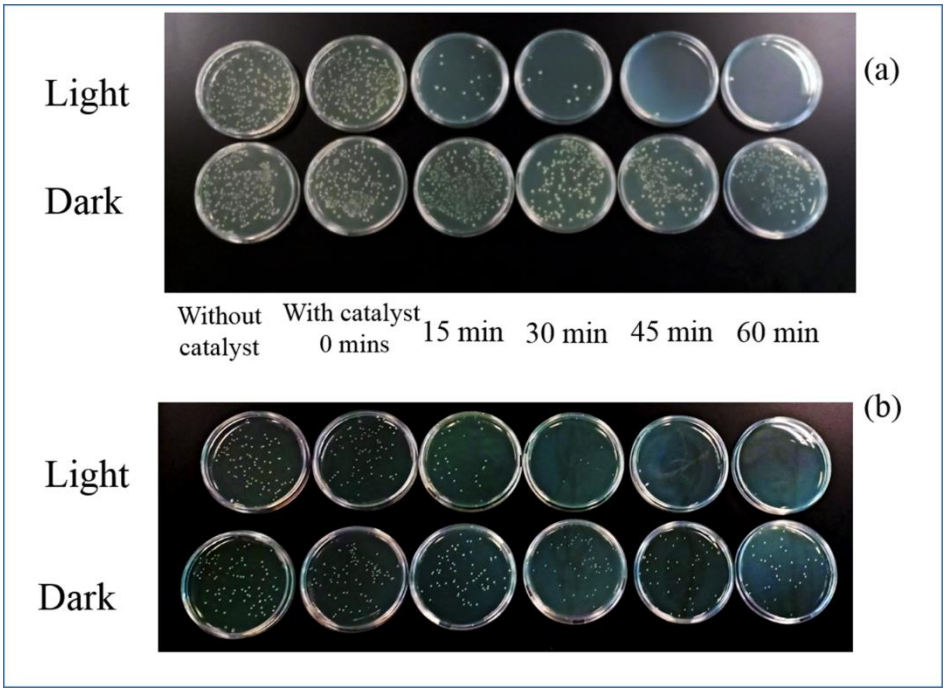

Figure 31. Images of (a) *E. coli* colonies and (b) *S. aureus* colonies on agar plates after various time intervals of 2 wt% $AgBiS_2$-TiO_2.

3.2.10 Photoluminescence analysis

The mass normalised photoluminescence spectrum of TiO_2 and composites of $AgBiS_2$-TiO_2 is presented in **Figure 32**. It is used to demonstrate the effect of heterojunction formation on the exciton recombination rates. The emission peak of $AgBiS_2$-TiO_2 shows dampened intensity compared to TiO_2. The lower PL intensity indicates the lower recombination of electron-hole pairs. The recombination of the excitons was inhibited by the heterostructure formation, resulting in high photocatalytic efficiency. On the other hand, the strong fluorescence signals observed in the case of TiO_2 is due to the higher rate of recombination, which further explains the lower photocatalytic activity observed.

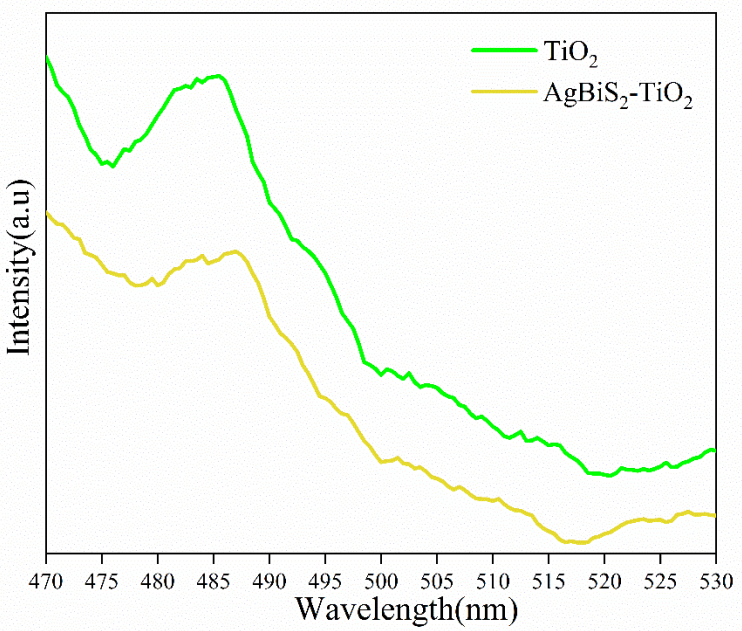

Figure 32. The photoluminescence spectra of TiO_2 and composites of 2 wt% $AgBiS_2$-TiO_2.

3.3. PHOTOCATALYTIC MECHANISM

All the above applications demonstrated that the composite architecture of ternary chalcogenide with TiO_2 showed impressive results compared to their pristine parent samples. The theoretical study was important to understand the electronic and optical properties of this ternary chalcogenide along with TiO_2. The TC exists in polymorphic states, as discussed in the introduction and found in theoretical studies. The computational analysis reveals the stability of trigonal crystal structure of $AgBiS_2$, while positive formation energy is observed in the case of the cubic phase of the sample. The use of solvent like ethanolamine, as explained in **section 3.2.2**, plays a crucial role instability as well as the formation of such metastable phases. Moreover, the band structure and PDOS analysis reveal that the valence band of TiO_2 is dominated by Ti 3d orbital and the conduction band is governed by the 2p orbital of oxygen. On visible light irradiation on $AgBiS_2$-TiO_2 composites, the electrons travel from the Ag 4d and S 3p orbitals to the Bi 3p orbital of $AgBiS_2$ respectively, and further to the O 2p orbital of TiO_2.

The XPS results highlight the shift of the TC peaks in the composite structure to lower binding energies. The strong interaction between the heterostructure components resulted in the shift. However, the peaks of TiO_2 remained unaltered, when compared with the parent and the composite sample. In the composite sample, the presence of a peak at 457.8 eV is the direct measure of the Ti in +4 state. It also indicates the absence of any increase in anionic oxygen vacancies in the heterostructure formed. The strong Ti^{4+} state reiterates the anatase phase of the sample in the composite architecture, which effectively contributes to the photocatalytic process.[17, 184] Apart from that, it is further observed in all the application results that the TC at lower dopant ratio effectually contributes to the degradation/disinfection and the H_2 production output. However, on enhancing the dopant concentration beyond an optimised limit, results in suppression of the effective interfacial charge transfer, as these dopant sites start to behave as potential recombination centres.[216-218]

Based on the theoretical study, scavenger experiments, band gap values from UV-DRS and the PL results, a likely photocatalytic mechanism is illustrated for $AgBiS_2$-TiO_2. In order to understand the separation of photogenerated e-hole pairs over the two different nanocomposites, it is vital to calculate the conduction band (CB) and valence band (VB) potentials of the components. The energy levels are calculated using the following empirical equations;[165, 219, 220]

$$E_{VB} = \chi - E^e + 0.5\, E_g \quad \text{(Equation 25)}$$

$$E_{CB} = E_{VB} - E_g \quad \text{(Equation 26)}$$

Where, χ= Mulliken's electronegativity

E^e= Energy of a free electron on hydrogen scale (ca. 4.5 eV)[221]

Eg= Band gap of the semiconductor

E_{VB}= Valence band potential of the semiconductor

E_{CB}= Conduction band potential of the semiconductor

Now, according to Mulliken's electronegativity theory, electronegativity (χ) of any element is the arithmetic mean of the first ionisation energy (I.E) and the electron affinity (E.A) of an element:[222, 223]

$$\text{so, } \chi = \frac{1}{2}[I.E + E.A] \text{ (Equation 27)}$$

and χ of any polyvalent molecule say $A_aB_aC_c$ is given as;

$$\chi_{AaBbCc} = [(\chi_A)^a \times (\chi_B)^b \times (\chi_C)^c]^{\frac{1}{a+b+c}} \text{ (Equation 28)}$$

where a, b and c are the number of atoms of A, B and C respectively.

Thus, to estimate the E_{CB} and E_{VB} values of TiO_2 and $AgBiS_2$, it is important to estimate the χ_{TiO2} and χ_{AgBiS2}. In order to do so, the E.A and the I.E values of constituent elements are provided in **Table 7**.

Table 7. I.E and E.A values of elements.

Elements	I.E (eV)	E.A (eV)
Ti	6.820	0.079
O	13.618	1.460
Ag	7.576	1.301
Bi	7.289	0.945
S	10.360	2.070

Hence, using **equation 28**, the χ values of TiO_2 and $AgBiS_2$ are calculated. **Table 8** summarises the χ values calculated and the Eg values obtained from the UV-DRS plot in **section 3.2.5**.

Table 8. χ values and Eg values.

Semiconductor	χ (eV)	Eg (eV)

TiO_2	5.8050	3.18
$AgBiS_2$	5.1533	3.19

Hence using **equation 25** and **26**, the E_{CB} and E_{VB} of the bare samples are estimated. **Table 9** summarises the values as obtained after calculation.

Table 9. E_{VB} and E_{CB} values**.**

Semiconductor	**E_{CB} (eV)**	**E_{VB} (eV)**
TiO_2	-0.2850	2.895
$AgBiS_2$	-0.9417	2.248

Thus, using the above-calculated values, a possible photocatalytic mechanism is proposed below. In **Figure 33**, illustrates the band edge position of the CB and VB potentials of $AgBiS_2$ and TiO_2, before and after the formation of a possible $AgBiS_2$-TiO_2 nanocomposite heterojunction. The Fermi levels of $AgBiS_2$ and TiO_2 is located at 0.65 eV and -0.1 eV respectively (**Figure 33a**). As the heterojunction is created, the Fermi levels of both the semiconductors reach a consistent level (**Figure 33b**).[224, 225] In this case, the band positions of $AgBiS_2$ is altered as it is in low dopant levels, so the Fermi level of $AgBiS_2$ reaches -0.1 eV, which is identical to that of TiO_2. **Figure 33b** shows the new band edge positions for $AgBiS_2$ as the VB and CB moves to +1.49 and -1.6917 eV. In this type-II heterostructure, on visible light illumination, electron hole pairs are generated on the surface of TiO_2 and $AgBiS_2$. The holes from the valence band of TiO_2 migrate to the VB of $AgBiS_2$, and the electrons migrate to the conduction band of titania. As explained, the difference in the electronegativity between titania and $AgBiS_2$ nanoparticles and the band alignment in the heterojunction promotes the transfer of the flow of electrons to the CB of TiO_2. These electrons react with the oxygen adsorbed in the catalyst surface to form superoxide radicals, and the holes participate in the

reaction process directly. This explains the role of different ROS species, as suggested in the results observed in scavenger experiments. The scavenging results illustrate the superior role of superoxide radicals, electrons and holes in the enhanced photocatalytic applications. The ROS generated further undergoes the photocatalytic process.

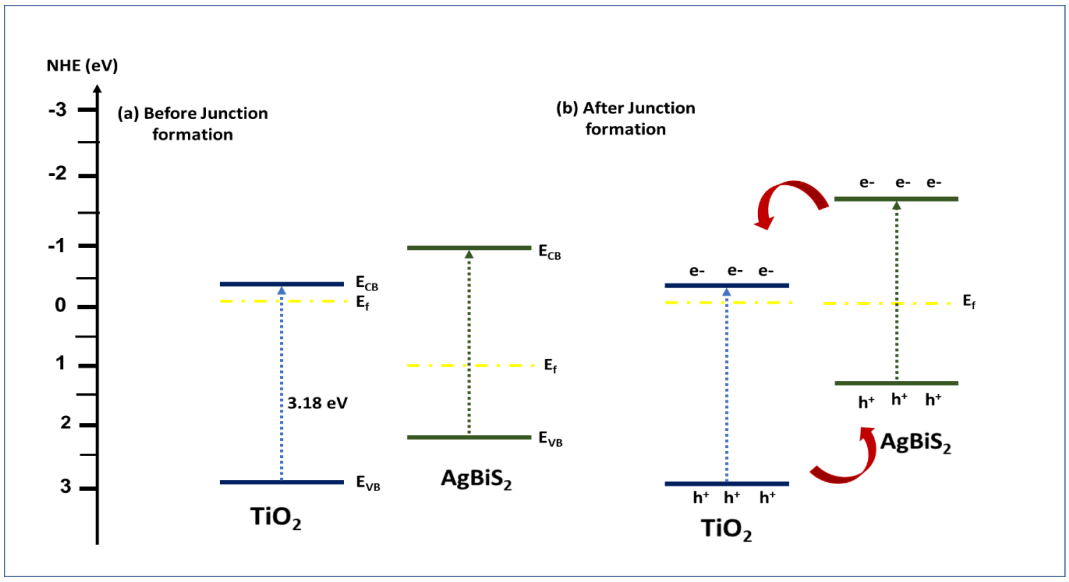

Figure 33. The photocatalytic mechanism for $AgBiS_2$-TiO_2 (a) before the junction and (b) after junction formation.

3.4. CONCLUSIONS

In this study, we successfully synthesised $AgBiS_2$-TiO_2 using a one-pot solvothermal technique. The as prepared composite structure with a small dopant level was efficient in improved visible light absorption. The band gap of the composites decreased with the increase in the dopant levels. Moreover, the XPS analysis demonstrated the shift in the peaks corresponding to the change in the local environment of the composite structure. The degradation results of the composites showed improved efficacy.

Similarly, a significant improvement for the light induced hydrogen generation is also observed. A log 3 bacterial reduction was attained within 30 minutes of visible light illumination. A plausible mechanistic

understanding is proposed based on computational analysis, scavenger experiments and the band gap values derived from the DRS plot. Thus, the present study demonstrated the successful formation of heterostructure and details the multifunctional applications.

CHAPTER 4

TERNARY METAL CHALCOGENIDE HETEROSTRUCTURE ($AgInS_2$-TiO_2) NANOCOMPOSITES FOR VISIBLE LIGHT PHOTOCATALYTIC APPLICATIONS

4. 1. INTRODUCTION

Discovering light absorbing materials with semiconducting properties is not enough. But then again, the critical attribute lies on tailoring materials to enhance their interfacial charge transfer effectively and decreasing the rate of recombination. Various procedures such as band-gap modulation, defect formation, dimensionality alteration, pore texture alteration, surface sensitization, heterojunction creation *etc.* are attempted to reduce the recombination rate and enhance the visible light absorption.[91, 226]

Amid all, $AgInS_2$ (I-III-VI), a ternary semiconductor crystallises into two different polymorphs; a room temperature stable tetragonal chalcopyrite structure and the other high-temperature orthorhombic wurtzite structure.[227] The phase transition occurs at 620 °C, and these nanocrystals are known to be synthesised using different liquid phase reactions.[178, 228-230] The orthorhombic $AgInS_2$ has been reported for various photocatalytic applications.[231] The small band gap and excellent photon absorption in the visible region of the electromagnetic spectrum aids in several efficient processes. Nevertheless, these materials display reduced quantum efficiency and strong light etching that confines its significant application.[179] Yin and Cui *et al.* reported the synthesis of $AgInS_2$ nanoparticles sensitised TiO_2 nanotube arrays and $AgInS_2$ cluster films on TiO_2/FTO substrate, respectively. These

composites were investigated for their photoelectrochemical properties.[232, 233] Similarly, Liu *et al.* effectively studied the same composite and illustrated the degradation of 1,2 dichlorobenzene.[179] Similar heterostructural composites such as $AgBiS_2$-TiO_2 were also previously reported.[234] However, there still exists the significant potential of these materials for their various functional applications, which remains unexplored. Studies of these composites for photocatalytic hydrogen production, doxycycline degradation and antibacterial disinfection has not yet been reported.

Hence, in the current investigation, we outlined the optimal solvothermal synthesis parameters of $AgInS_2$ and developed a staggered heterostructure composite of TiO_2 at different wt% (0.5, 1, 2 and 5). These as prepared composites illustrate positive heterostructure formation in the Raman and the XPS results. Moreover, the UV-DRS spectra demonstrate the enhanced visible light absorption by the composite samples. The decreased band gap of the material enabled in illustrating 300 times increased hydrogen output, 5-log bacterial inactivation within 30 minutes of illumination and more than 95% degradation of Doxycycline (DC) within 3 hours of irradiation. The introduction of even a low dopant ratio of $AgInS_2$ effectually harnessed the efficiency of the incoming light and decreased the recombination rate. A plausible photocatalytic mechanism and the interfacial charge transfer is discussed.

The synthesis process and the process optimisation of the composites are explained in **section 2.2**.

4. 2. RESULTS AND DISCUSSION

4.2.1 Computational analysis

In this section, computational results concerning the structural properties, the electronic structure, the projected density of states (PDOS) and dielectric properties of TiO_2 and $AgInS_2$ are presented. This helped to understand the

underlying photocatalytic mechanism. The initial structures of TiO_2 and $AgInS_2$ were obtained from the Materials Project library. The initial geometry of $AgInS_2$ had the lattice constants, a = 6.81 Å, b = 7.15 Å, c = 8.35 Å and the angles were α=β=γ= 90°. After the structural optimisation, there were no changes in the lattice angles, but the lattice constants slightly changed upon volume relaxation to a = 6.75 Å, b = 7.05 Å and c = 8.25 Å. The volume was relaxed by 3.5% in the case of orthorhombic $AgInS_2$. The XRD pattern of the orthorhombic phase of $AgInS_2$ obtained theoretically is also given in **Figure 34**.

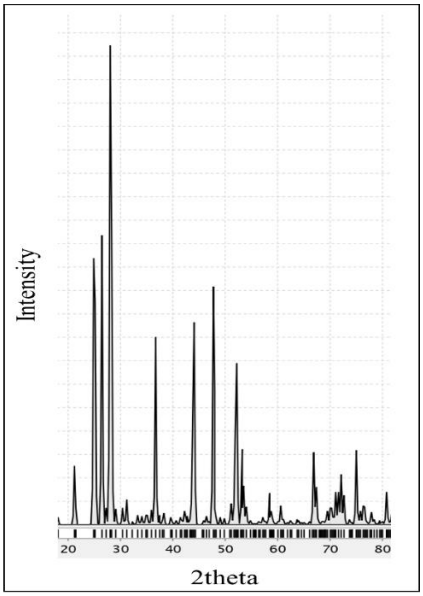

Figure 34. XRD pattern of the orthorhombic phase of $AgInS_2$ obtained theoretically. Data generated courtesy of Dr. Syam Kumar.

Both the Ag and In cations have tetrahedral coordination with S. The AgS_4 and InS_4 tetrahedra are connected to one another at the corners (see polygons diagrams in **Figure 35**).

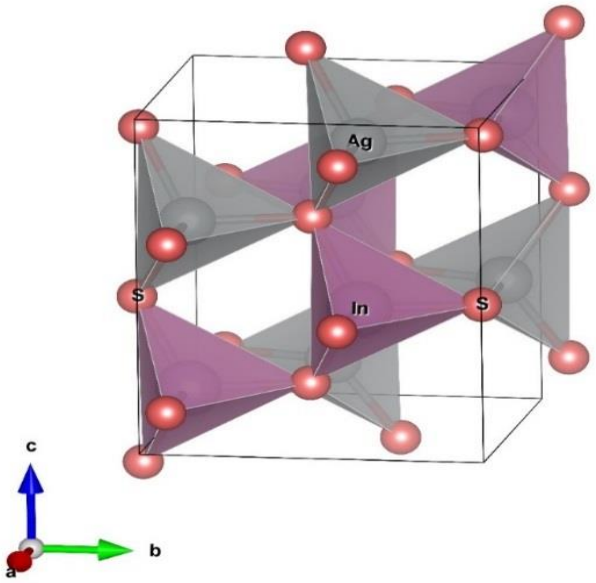

Figure 35 (Colour Online) Optimised crystal structure of $AgInS_2$. Colour code: grey = Ag, light red = In, red = S. Data generated courtesy of Dr. Syam Kumar.

TiO_2, on the other hand, had lattice constants a = b = 10.16 Å and c = 2.96 Å, and the lattice angles α=β=γ= 90° at the end of the geometry relaxation where the volume was reduced by 3.77% from the initial structure. The initial structure of TiO_2 had the lattice parameters a = b = 10.32 Å and c = 2.98 Å, and angles α=β=γ= 90°. The Ti cations and O anions are connected to each other in octahedral coordination. Alternate edge and corner sharing connect these octahedra to each other, as seen in **Figure 36**.

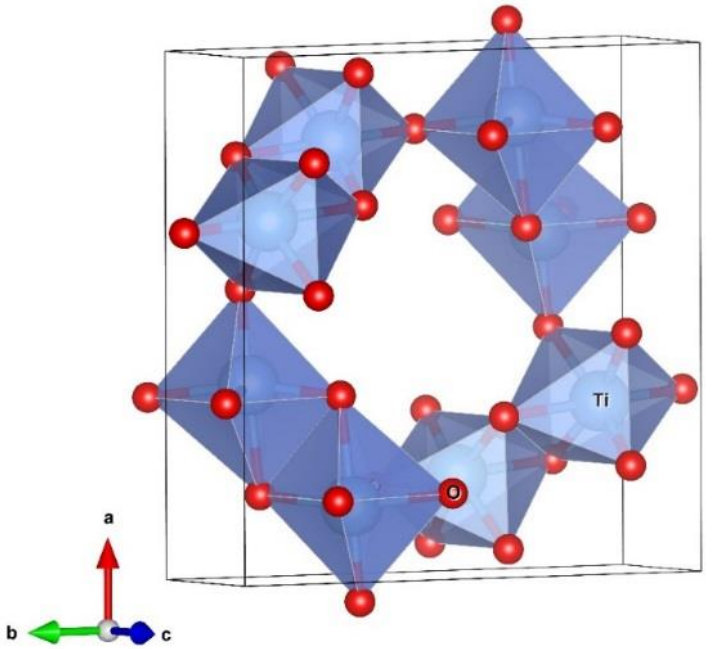

Figure 36. (Colour Online) The crystal structure of TiO_2 in the tetragonal phase. Colour code: blue = Ti and red = O. Data generated courtesy of Dr. Syam Kumar.

There is an underestimation in the bandgap value with respect to the experimentally observed value even though the computed lattice parameters fall within 1% error with respect to the experimental ones. This is not unexpected as the Generalised Gradient Approximation (GGA) functional used is well known to underestimate the band gap.[235] In the calculation of the band structure, the Perdew-Burke-Ernzerhof (PBE) functional under GGA was used owing to its computational speed. This functional is known to contain unphysical Coulomb repulsion which leads to an inadequate description of the band gap.[236] There are works that reports the PBE band gap of well-known compounds which are shown to underestimate the experimentally observed bandgap[3]. In fact, there are many insulators (nonzero bandgap) such as FeO and GaSb that were estimated as metals (zero band gap) upon the usage of PBE functional.[237] The band structure of $AgInS_2$ is presented in **Figure 37a** and shows a direct band gap of ~ 0.5 eV. Both the valence band maxima (VBM)

and the conduction band minima (CBM) lies on the Γ point in the Brillouin zone. The upper valence band (UVB) is dominated by S *p*-orbitals and Ag *d*-orbitals, and the lower conduction band (LCB) by the In *s*-orbitals and S *p*-orbitals. Energy larger than the computed band gap value is expected for the electrons to transfer from VB to CB due to the *p*-*p* forbidden transitions. In the current work, the experimentally observed bandgap of $AgInS_2$ is 1.95 eV (**Figure 46b**), and the PBE bandgap is 0.5 eV which is within an error of 74.36%. The band structure and partial density of states (PDOS) plots were only used as a tool to illustrate the orbital occupancies near the band edges.

Percentage errors calculated using the equation,

$$\% \text{ error} = \left|\frac{\text{PBE bandgap} - \text{Experimental bandgap}}{\text{Experimental bandgap}}\right| \times 100 \quad \text{(Equation 29)}$$

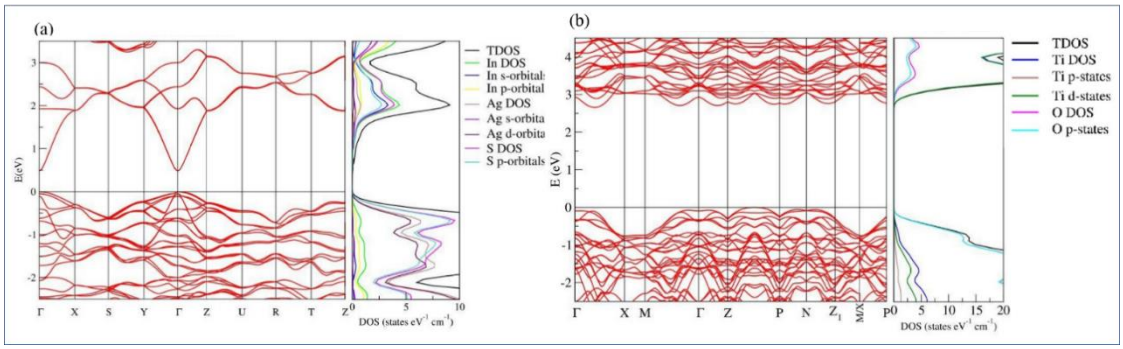

Figure 37. Calculated band structure of (a) $AgInS_2$ and (b) TiO_2 with the corresponding PDOS. The top of the valence band (horizontal line) is aligned at 0 eV. Data generated courtesy of Dr. Syam Kumar.

TiO_2, on the other hand, is an indirect band gap material with a band gap of ~ 2.7 eV. The band structure and the PDOS of TiO_2 are shown in **Figure 37b**. The VBM lies between Z and P points, and the CBM lies between the Γ and X points of the Brillouin zone. The O *p*-states dominates the UVB, and the Ti *d*-states dominates the LCB. The Ti *p*-states were also present at the UVB of TiO_2.

Absorption spectra for $AgInS_2$ and TiO_2 are calculated in the independent particle approximation and plotted in **Figure 38** in the range of 0 to 7.5 eV

input light. The first peak of the imaginary part of the dielectric function, which indicates the energy value at which the actual electron transition starts, of $AgInS_2$ and TiO_2, was found to be 2.04 eV and 3.43 eV, respectively.[238] $AgInS_2$ is optically anisotropic, but along the x and y directions, the light absorption spectrum is isotropic for TiO_2.

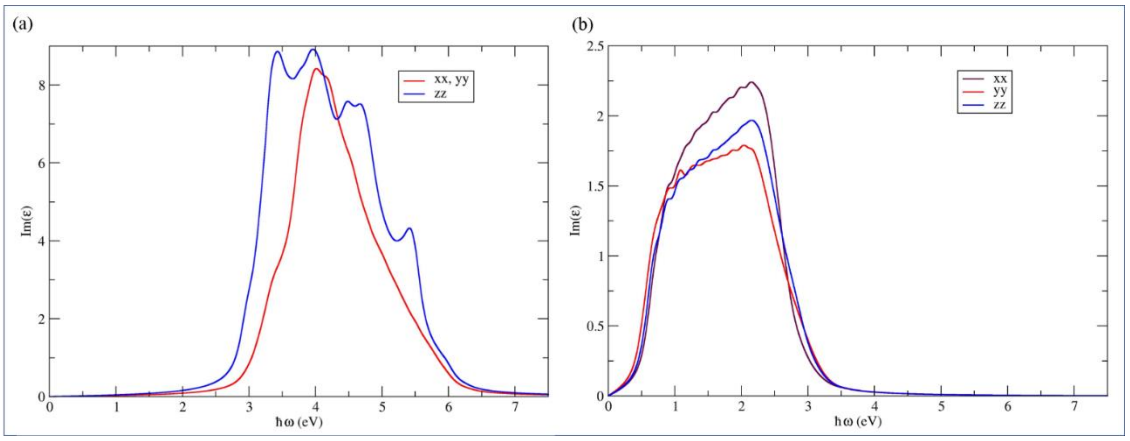

Figure 38. The imaginary part of the dielectric function (Im(ε)) of (a) TiO_2 and (b) $AgInS_2$ calculated infrared, visible and ultraviolet region. Data generated courtesy of Dr. Syam Kumar.

The band gap and the optimised crystal structure of $AgInS_2$ in the tetragonal phase were also calculated (**Figure 39**). The geometry was obtained from the Materials Project library with the lattice parameters a = b = 5.93 Å and c = 11.52 Å, and the angles α=β=γ= 90°. After relaxation, the volume of the cell was reduced by 3.3%, and the lattice constants were obtained as a = b = 5.85 Å and c = 11.42 Å without changing its angles. The band gap of $AgInS_2$ in tetragonal phase was found to be 0.36 eV.

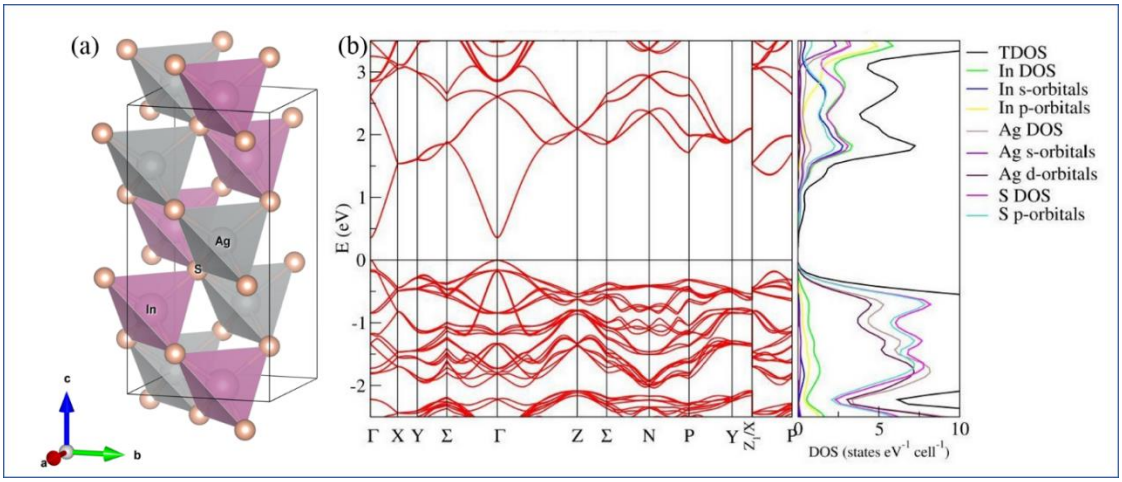

Figure 39. (a) (Colour Online) Optimised crystal structure of tetragonal $AgInS_2$. Colour code: grey = Ag, light red = In, red = S. and (b) Calculated band structure of tetragonal $AgInS_2$. Data generated courtesy of Dr. Syam Kumar.

The crystal structure of $AgInS_2$ attained *via* experimental synthesis exists in an orthorhombic phase. Hence the computational conclusions drawn for the orthorhombic phase is discussed hereafter, except otherwise identified.

4.2.2 X-ray diffractogram (XRD)

The synthesis process of $AgInS_2$-TiO_2 is illustrated in **Figure 40**. Typically, the TiO_2 nanoparticles prepared by the sol-gel method undergoes a solvothermal process resulting in the *in situ* formation of the $AgInS_2$ nanoparticles.[179] This results in a uniform distribution of the dopant particles and formation of close intimate heterojunctions as discussed in the latter sections. The challenges of synthesising these semiconductor nanostructures are their stability, controlling the stoichiometric composition and the crystal structure.[239-241] As similar to other bulk materials, the nanoparticles of the ternary compounds exhibit interesting electronic and optical properties compared to their bulk counterparts.[242] The formation of low temperature stable orthorhombic structure of $AgInS_2$ could be ascribed to the solvent picked for the reaction and the balanced use of the two cationic precursors used in the synthesis process. The appropriate reaction temperature and time aid in tuning the reactivity of Ag and In precursors (as observed in the diffractograms of time

and temperature study of $AgInS_2$). As Ag^+ is a soft Lewis acid, therefore appropriate Lewis base such as Ethanolamine (EA) is used as suitable ligand required for the complexation process. Moreover, the presence of lone nitrogen chelating atoms on an amine molecule makes EA, a potential structure forming mediator. [193, 194]

The formation of $AgInS_2$ nanoparticles using a solvothermal technique could be explained as followed;

$$AgNO_3 + \mathrm{x}EA \rightarrow Ag(EA)_x^+ + NO_3^- \text{ (Equation 30)}$$

$$In(NO_3)_3 + \mathrm{y}EA \rightarrow In(EA)_y^{3+} + 3NO_3^- \text{ (Equation 31)}$$

At the beginning of the reaction, the Ag^+ and In^{3+} ions form covalent complexes as given above (where x and y are positive integers), due to the use of EA as a solvent. [190, 191] Additionally, these complexes react with thiourea (TH) resulting in the formation of complexes as;

$$Ag(EA)_x^+ + xTH \rightarrow [Ag(TH)_x]^+ + \mathrm{x}EA \text{ (Equation 32)}$$

$$In(EA)_y^{3+} + yTH \rightarrow [In(TH)_y]^{3+} + \mathrm{y}EA \text{ (Equation 33)}$$

The formation of any free radicals of S^{2-} from thiourea is proposed to be prevented to some extent, due to the use of EA as a solvent. This mechanism averts the creation of any additional binary impurity phases, for example, In_2S_3 or Ag_2S. The stability of thiourea falls on enhancing the temperature and eventually results in the formation of more stable ternary chalcogenide phase to yield $AgInS_2$. Meanwhile, the thiourea in the reaction plays a dual nature partly by aiding in the formation of complex and also as a source of sulphur other than thiourea. [189 192]

$$[Ag(TH)_x]^+ + [In(TH)_y]^{3+} \rightarrow AgInS_2 \ (Equation\ 34)$$

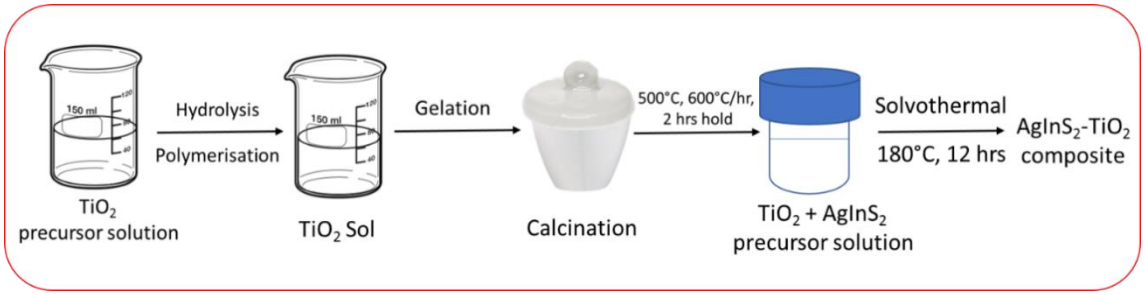

Figure 40. Schematic illustration of the synthesis mechanism of $AgInS_2$-TiO_2 composites.

The structure and the crystallinity of the as synthesised $AgInS_2$-TiO_2 composites were investigated using X-ray diffractogram (XRD). **Figure 41** displays the formation of the as prepared $AgInS_2$ and $AgInS_2$–TiO_2 composites. Orthorhombic phase of $AgInS_2$ [a=7.00 Å, b= 8.28 Å, c=6.69 Å and α = β = γ = 90˚] with peaks defining at 24.90˚, 25.40˚, 26.80˚, 28.50˚, 36.70˚, 43.67˚, 44.78˚, 48.23˚ and 51.80˚ owing to (120), (200), (002), (121), (122), (040), (320), (203) and (042) respectively is observed [ICDD -00-025-1328]. [231] The XRD peak intensity at 26.8° of (002) plane shows higher intensity. Although the primary peak in the given case might reflect the formation of the tetragonal phase. However, the presence of prominent peaks at 24.9°, 25.4°and 28.5° prove otherwise. The tetragonal phase of the $AgInS_2$ does not exhibit any peaks at <26° (2Θ value). **Table 10** summarises the lattice parameters experimentally calculated with the reported values in literature.

Table 10. Summarised lattice parameters of TiO_2 and $AgInS_2$.

Compound	Parameter	a(Å)	b(Å)	c(Å)	α(°)	β(°)	γ(°)	**Ref**
TiO_2	Experimental	3.78	3.78	9.50	90.00	90.00	90.00	
	From Literature	3.80	3.80	9.60	90.00	90.00	90.00	188
$AgInS_2$	Experimental	7.00	8.28	6.69	90.00	90.00	90.00	
	From Literature	7.00	8.27	6.70	90.00	90.00	90.00	244

The slightly widened peaks could be attributed to the decreased nanocrystal size as observed in the TEM images (**Figure 51**) and also observed in the previous reports.[243-245] Moreover, the Raman results to aid in confirming the orthorhombic phase as the peaks at 264 cm^{-1} and 316 cm^{-1}corresponds to the orthorhombic wurtzite structure while the peaks of tetragonal only appear at 240 cm^{-1} and 345 cm^{-1}which are absent in this case (inset of **Figure 47**).[229, 231, 246, 247]

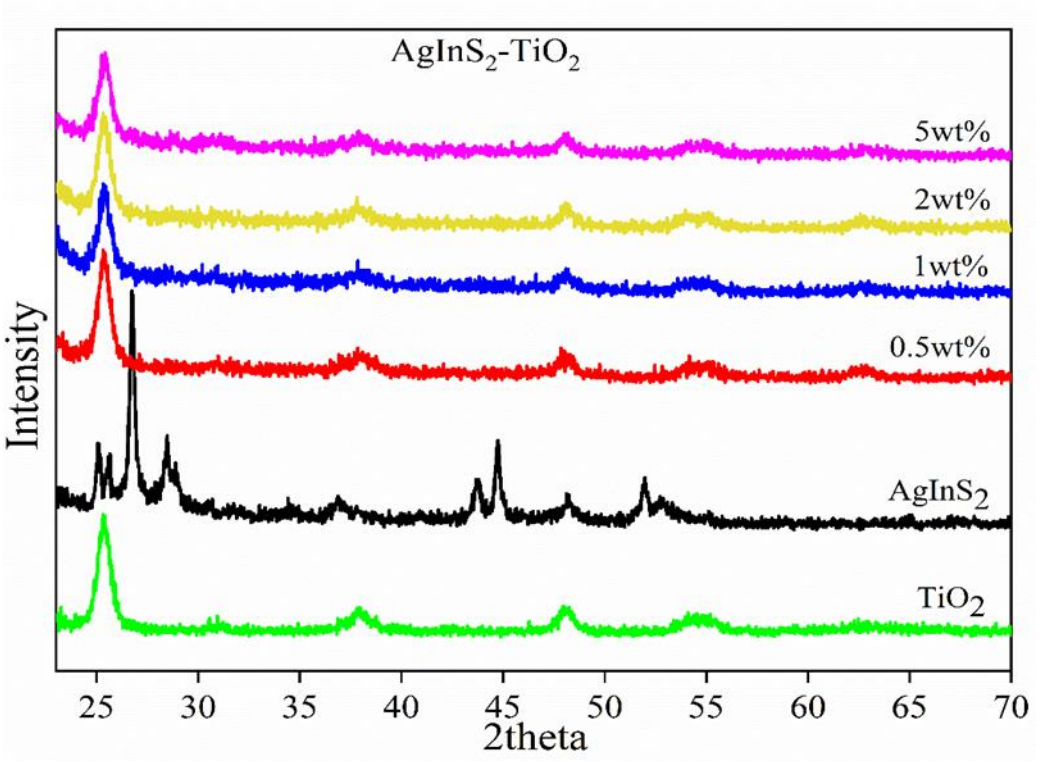

Figure 41. X-ray diffractograms of $AgInS_2$, TiO_2 and $AgInS_2$-TiO_2 composites.

The diffractograms in **Figure 42** compares the as synthesized $AgInS_2$ with other peaks of Ag_2S [ICDD 00-014-0072], In_2S_3 [ICDD 00-033-0624], $AgIn_5S_8$ [ICDD 00-026-1477] and $AgInS_2$ tetragonal [ICDD 00-025-1330]. It displays the orthorhombic $AgInS_2$ formation, deprived of any impurity.

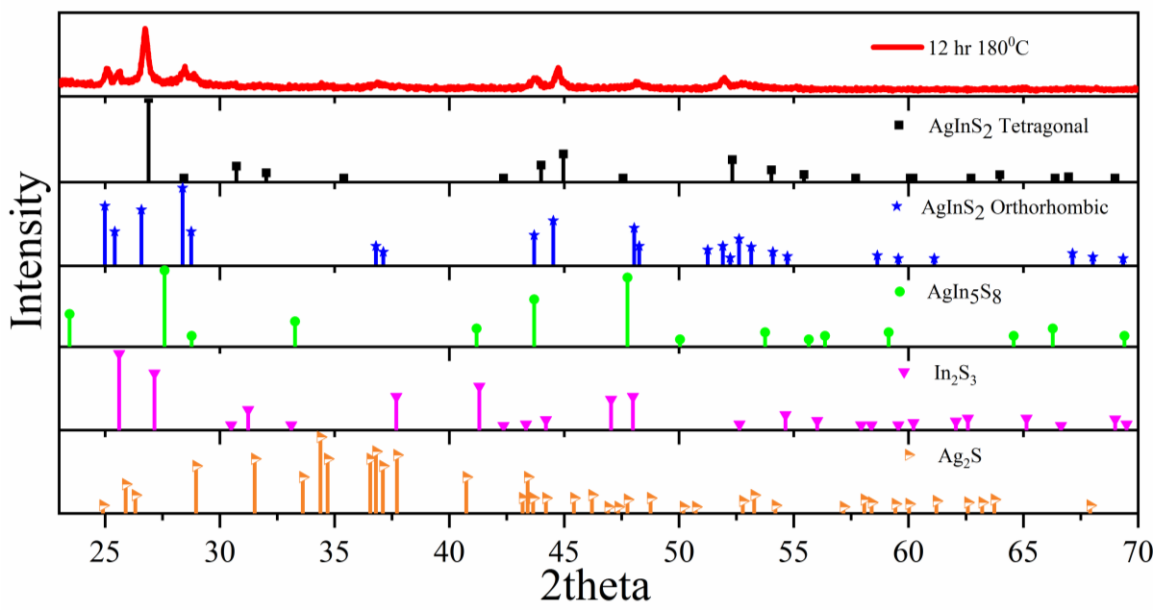

Figure 42. XRD of as prepared $AgInS_2$ with other standard peaks of $AgInS_2$ orthorhombic $AgInS_2$ tetragonal, Ag_2S and In_2S_3.

The temperature and time studies were accomplished, to optimise the reaction parameters for solvothermal synthesis. **Figure 43a** illustrates the temperature study of $AgInS_2$ at altered temperatures (150 ˚C to 250 ˚C) for 12 h. The crystallinity of the sample increases with the rise in temperature from 150 ˚C to 180 ˚C (the peak observed at 26.80˚). The intensity of the identical peak declines on increasing the temperatures after 200 ˚C to 250 ˚C. Therefore, 180 ˚C was applied as an ideal temperature for further assessing the time period for this solvothermal synthesis. **Figure 43b** exhibits the outcome of time study, which demonstrates the surge in the crystallinity of the peak at 26.10˚ on enhancing the time duration from 6 h to 12 h. The intensity of the peak at 26.80˚ decreases on assessment up to 72 h of synthesis period. Therefore, 180 ˚C for 12 h is reflected as the optimum solvothermal parameters for $AgInS_2$.

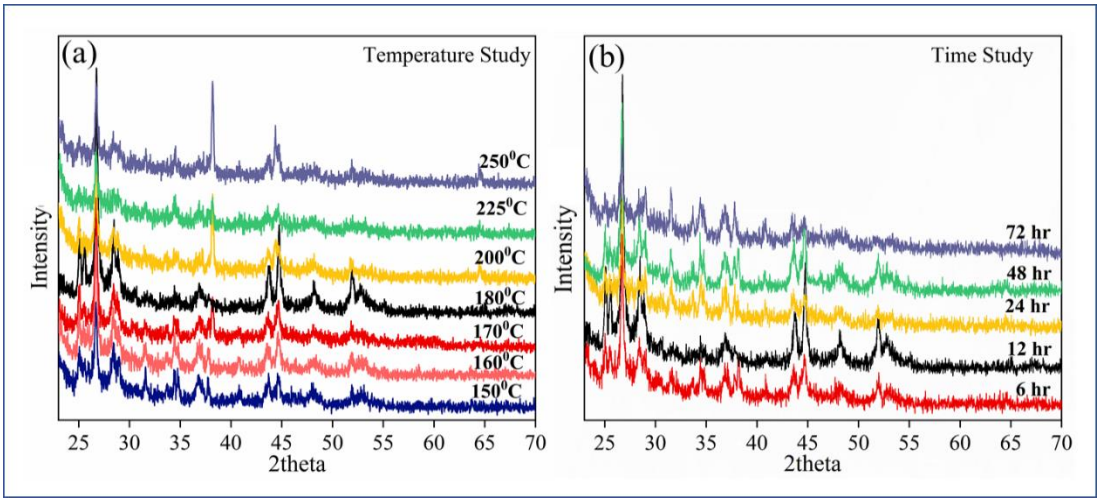

Figure 43. (a) Temperature study for 12 h and (b) time study of $AgInS_2$ 180 ˚C of solvothermal synthesis.

Figure 41 also exhibits the diffractograms of TiO_2 and its composites with $AgInS_2$. Peaks corresponding to $AgInS_2$ are not observed in the current diffractogram, which is endorsed to the high crystallinity of the TiO_2 nanoparticles and the small doping amount of $AgInS_2$. Sharp peaks of TiO_2 [a=b= 3.78 Å and c= 9.50 Å] at 25.40˚, 38.50˚, 48.00˚, and 55.00˚ to (101), (112), (200) and (211) correspondingly are likewise displayed in the diffractogram.[197, 248]

The composites structures as exhibited in **Figure 41** neither showed any change in crystallinity, nor there is any indication of rutilation (impurity phase) of TiO_2. Moreover, the lattice constant acquired for the bare samples presented a decent agreement to the computationally obtained values. The 0.5 wt% $AgInS_2$-TiO_2 composite demonstrated the top photocatalytic outcomes (as shown in the latter segments) amid their parent and other dopant % samples. Therefore, henceforward it is used for additional characterisations except otherwise identified.

4.2.3 Optical properties

To examine the optical absorption behaviour of the as synthesised materials, UV–vis diffuse reflectance spectroscopy (DRS) spectra were employed.

Figure 44 shows the diffused reflectance spectra of titania and $AgInS_2$-TiO_2 composites. TiO_2 exhibits a maximum at 350 nm (UV region), which corroborates the computationally obtained the first peak of the imaginary part of the dielectric spectra at 3.8 eV. Whereas a substantial improvement in the absorption in the visible region is detected in $AgInS_2$-TiO_2 materials.[248] The composite samples exhibited the signature sharp hump of TiO_2 at 380 nm. However, the absorption edge is extended up to 800 nm.

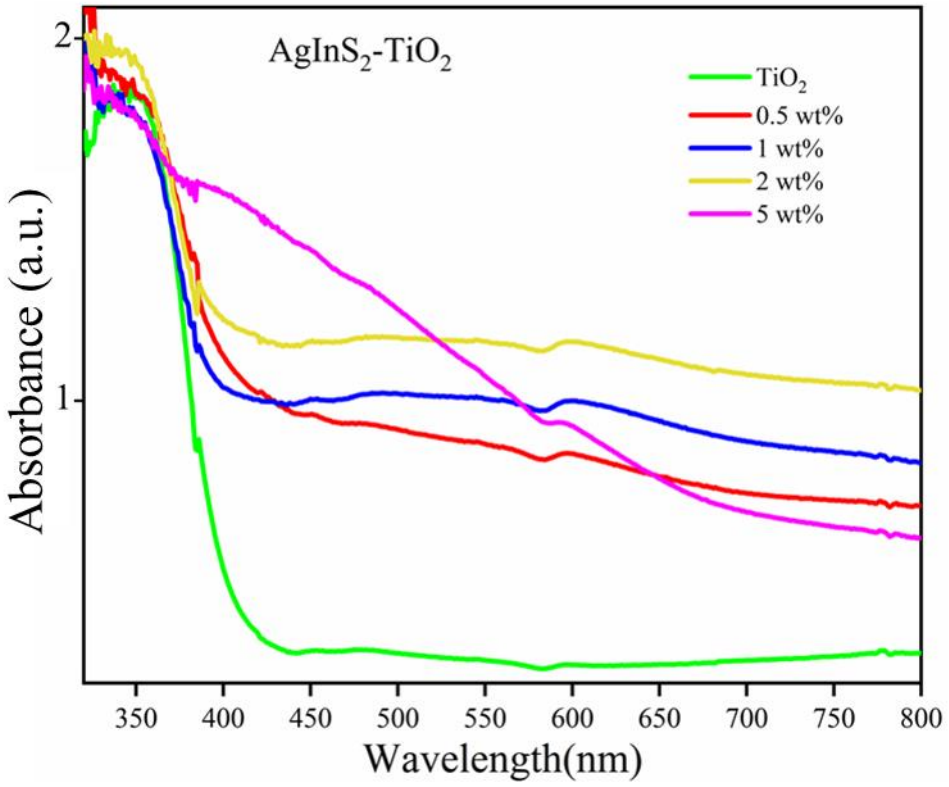

Figure 44. DRS spectra of TiO_2 and $AgInS_2$-TiO_2 composites.

The indirect bandgap measurements of the composite samples and titania are assessed, as shown in **Figure 45**. Thus, this substantiates the results computed theoretically (**Figure 37b** and **Figure 38a**). The composite samples show decreased band gap value with increase in $AgInS_2$ content. This conclusively proves the successful doping of the sample and the formation of

the heterostructure. [179] **Table 11** summarises the band gap of the composite samples and the parent materials.

Table 11. Band gap values of TiO_2 and $AgInS_2$-TiO_2 composites.

Sample	**TiO_2**	**$AgInS_2$**	**0.5 wt%**	**1 wt%**	**2 wt%**	**5 wt%**
Band gap (eV)	3.18	1.95	3.14	3.04	2.94	2.58

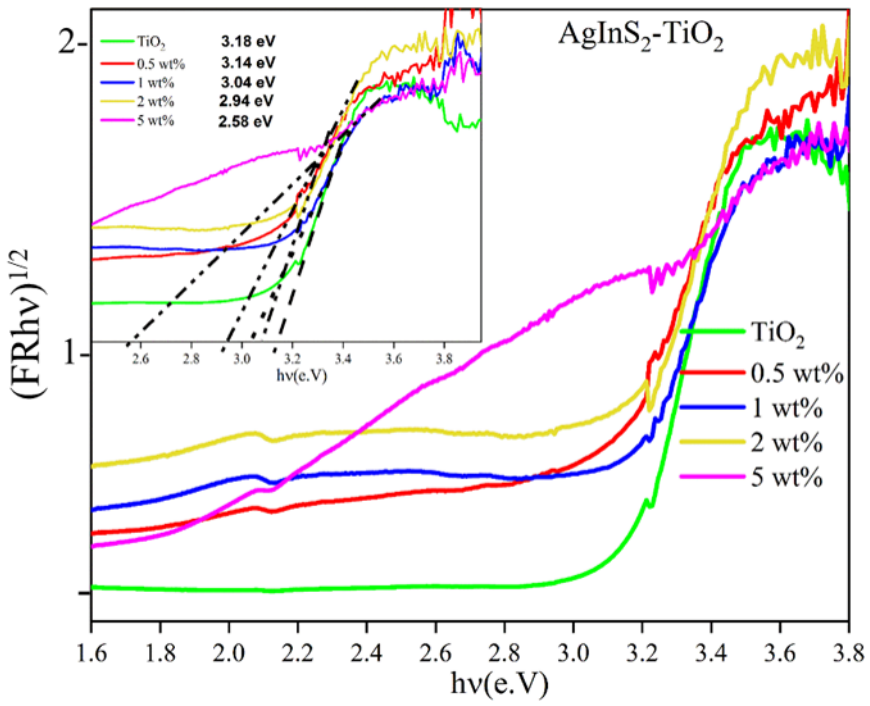

Figure 45. Band gap estimation of titania and $AgInS_2$-TiO_2 composites

Figure 46a illustrates the DRS spectra of $AgInS_2$, it shows an enhanced visible light absorption, and the edge extending up to 800 nm. The corresponding band gap is also calculated and displayed in **Figure 46b**.

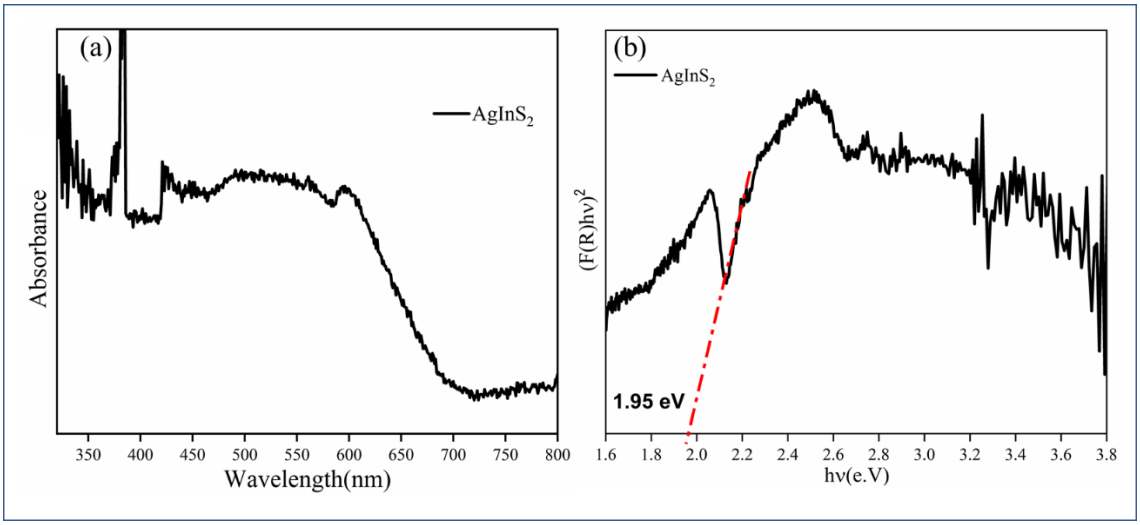

Figure 46. (a) DRS spectra of $AgInS_2$ (b) Band gap estimation of $AgInS_2$.

As observed through the absorption spectra, a high visible light absorption resulted in a small band gap of 1.95 eV, which is consistent with the theoretically computed results as discussed in an earlier section (**Figure 37a** and **Figure 38b**). The first peak of the imaginary part of the dielectric spectra obtained at 2.04 eV restates the experimental findings of absorption maxima observed at 600 nm (**Figure 38b**). **Table 12** summarises the experimentally attained band gap value and the reported values in literature.

Table 12. Band gap values of TiO_2 and $AgInS_2$-TiO_2 composites.

Sample	Band gap (eV)	From Literature	Band gap type	Ref
TiO_2	3.18	3.20	Indirect	[248]
$AgInS_2$	1.95	1.98	Direct	[231]

The Raman analysis of titania, $AgInS_2$ and $AgInS_2$-TiO_2 are illustrated in **Figure 47**. Characteristic vibrational peaks of the wurtzite structure of $AgInS_2$ are observed at 264 cm^{-1} and 316 cm^{-1}(as shown in the inset).[229, 231] Apart from that, characteristic bands for titania are detected at 147, 197, 396, 516

and 638 cm^{-1} for A1g, 2B1g and 3Eg correspondingly attributed to the anatase phase. [197, 249]

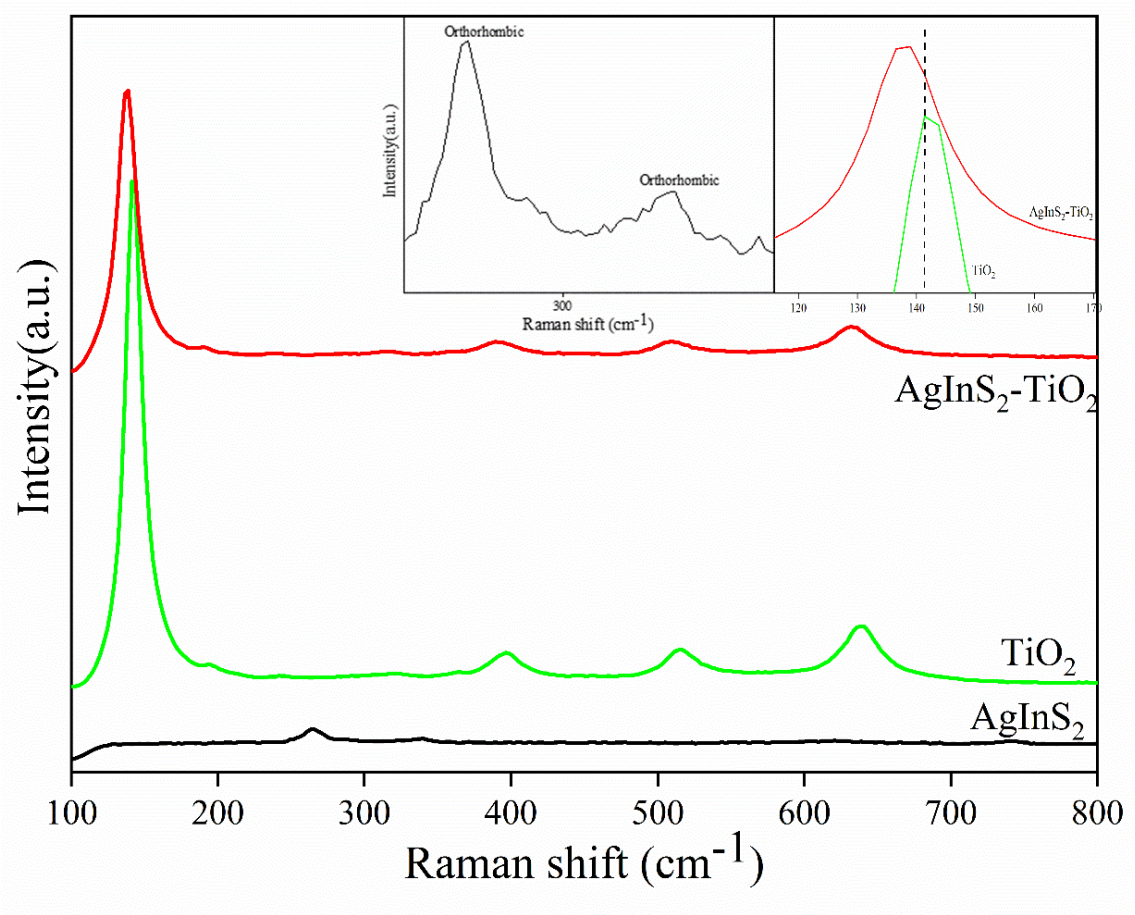

Figure 47. Raman analysis of $AgInS_2$, TiO_2, and 0.5 wt% $AgInS_2$-TiO_2 composites.

Sharp and symmetric peaks of anatase appear in the case of the composite sample, and a red shift is also detected for the composite maxima (as specified in the inset of **Figure 47**), this successfully proves the efficient doping of the TC atoms into the TiO_2 host material. Moreover, the Raman spectra of the composite do not show the existence of any other impurity peaks, which corroborates to the inferences observed in XRD. [198, 199]

The recombination rate of the solar light generated electron-hole pair, is evaluated using the photoluminescence (PL) measurement. The PL spectrum

of $AgInS_2$-TiO_2 and TiO_2 is displayed in **Figure 48** (mass normalised). The emission peak intensity of $AgInS_2$-TiO_2 is reduced compared to TiO_2. The lesser PL intensity specifies the reduced rate of recombination of electron-hole pairs. This suggests that the introduction of $AgInS_2$ results to retardation in the recombination rate of the excitons, which overwhelmingly improves the photocatalytic efficiency.

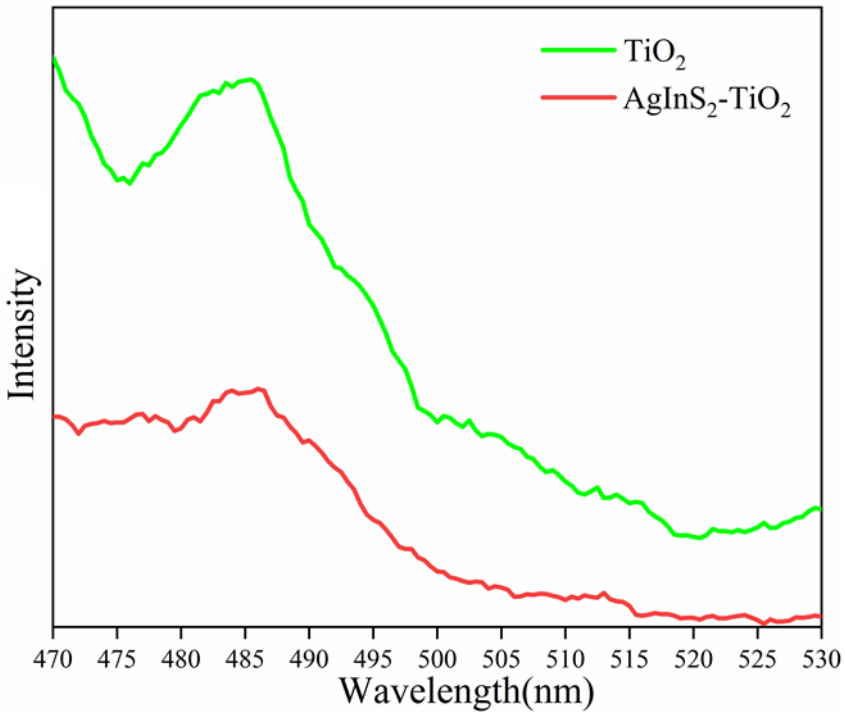

Figure 48. The Photoluminescence spectra of 0.5 wt% $AgInS_2$-TiO_2 and TiO_2

4.2.4 Chemical composition analysis

The chemical environment and the bonding characteristics are analysed using X-ray Photoelectron Spectroscopy (XPS). The survey spectra exhibit the presence of Ti 2p and O 1s in spectra of TiO_2. Peaks of Ti 2p, O 1s, Ag 2d, In 3d and S 2p were observed for $AgInS_2$-TiO_2 composites. Very low intensity peaks of C 1s and N 1s are also detected amongst all the materials which might be acquired through the experimental or analysis procedure (**Figure 49**).

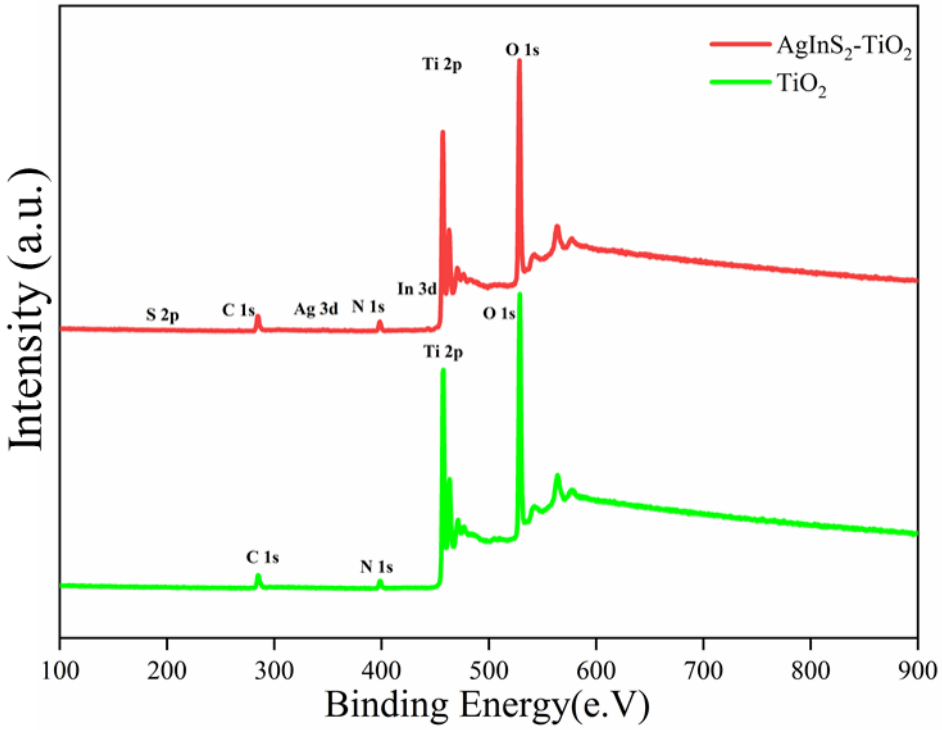

Figure 49. Survey spectra of TiO_2 and 0.5 wt% $AgInS_2$-TiO_2. Data generated courtesy of Dr. Steven Hinder.

Figure 50A illustrates the Ti 2p spectra of titania (a) and the composite of $AgInS_2$-TiO_2 (b). Peaks of Ti $2p_{3/2}$ are observed at 457.8 eV, assigned to Ti^{+4}. The Ti 2p peaks remained unaltered in both cases. Moreover, the O 1s spectra illustrated in **Figure 50B** shows no change in the values of 528.59 eV and 530.40 eV consistent to crystal lattice oxygen of (O-Ti^{4+}) and adsorbed O_2 molecules correspondingly in TiO_2 (a) and $AgInS_2$-TiO_2 (b) sample. [17, 188, 200] The Ag 3d high resolution spectra for both $AgInS_2$ (a) and $AgInS_2$-TiO_2 structure (b) is displayed in **Figure 50C**.

The signature points of Ag $3d_{3/2}$ and Ag $3d_{5/2}$ is detected at 372.73 eV and 366.72 eV correspondingly for $AgInS_2$ sample. [201, 202] The peak shifts slightly to 372.1 eV and 366.1 eV for $AgInS_2$-TiO_2 sample. [230] Nevertheless, the doublet separation of Ag 3d oxidation state remained unaltered (6 eV).[250] A similar shift in peaks is observed for In 3d peaks at 451.52 eV and 443.97 eV

corresponding to In $3d_{3/2}$ and In $3d_{5/2}$ respectively to 451.24 eV and 443.63 eV for $AgInS_2$-TiO_2 (**Figure 50D**). The doublet separation of 7.55 eV was observed for the In 3d peaks, consistent with previous literature.[251]

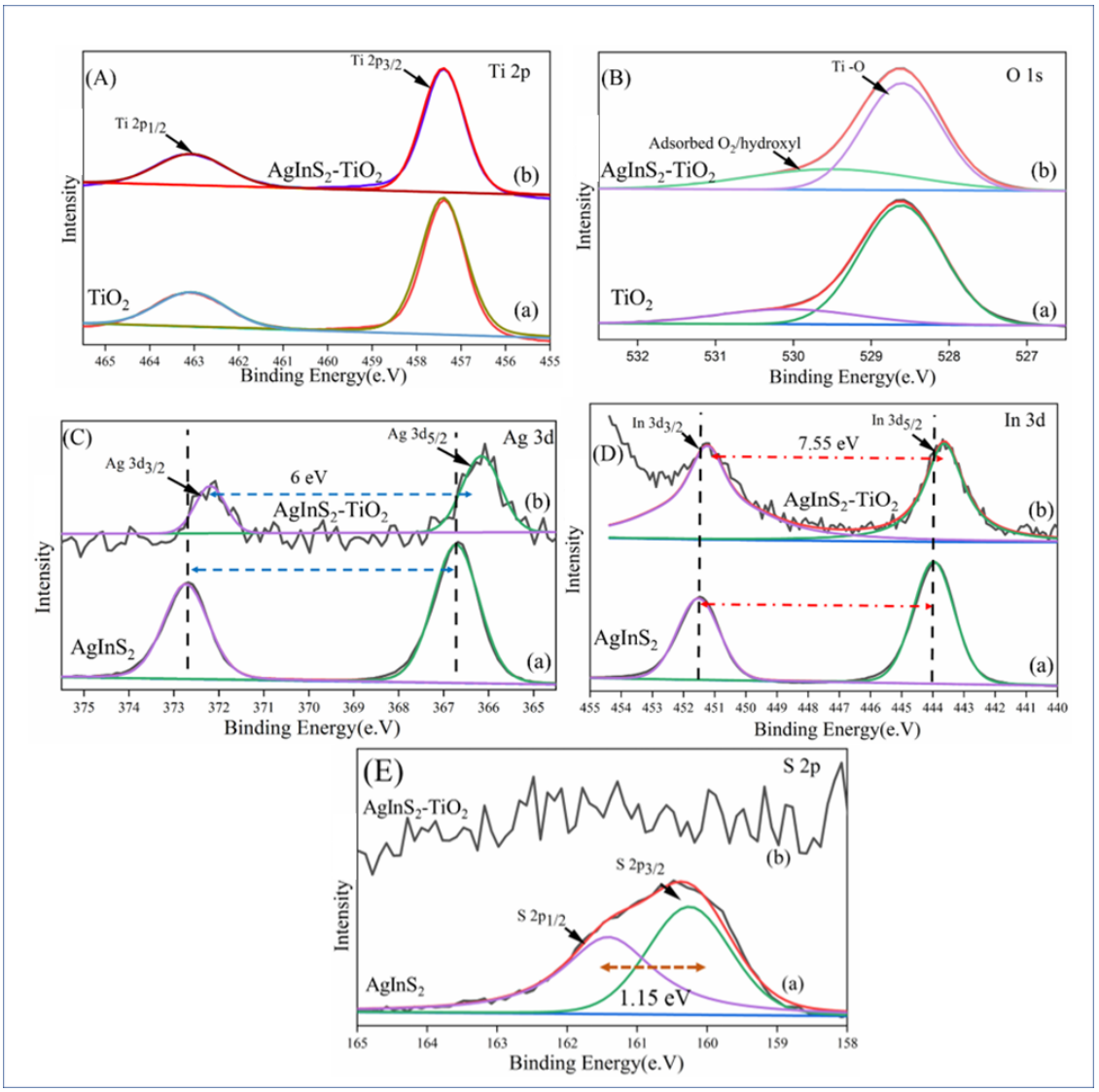

Figure 50. High resolution deconvoluted spectra of (A) Ti 2p (a) titania and (b) $AgInS_2$-TiO_2; (B) O 1s (a) TiO_2 and (b) 0.5 wt% $AgInS_2$-TiO_2; (C) Ag 3d (a) $AgInS_2$ and (b) 0.5 wt% $AgInS_2$-TiO_2 and (D) In 3d (a) $AgInS_2$ and (b) 0.5 wt% $AgInS_2$-TiO_2 and (E) S 2p (a) $AgInS_2$ and (b) 0.5 wt% $AgInS_2$-TiO_2. Data generated courtesy of Dr. Steven Hinder.

Figure 50E illustrates the high resolution spectra of S 2p. Peaks at 161.41 eV and 160.26 eV corresponds to the S $2p_{1/2,}$ and S $2p_{3/2}$ respectively are observed for $AgInS_2$ samples (doublet splitting of 1.15 eV).[252] Apparently, significant peaks of Sulphur were not detectable in that same region, however broad peak around 161.4 eV is noticed. The peak location of all the elements is summarised in **Table 13**.

Table 13. A summarised glance of all the peak position of different elements in $AgInS_2$ and 0.5 wt% $AgInS_2$-TiO_2 (in eV).

	Ag $3d_{3/2}$	**Ag 3d $_{5/2}$**	**In $3d_{3/2}$**	**In $3d_{5/2}$**	**S $2p_{1/2}$**	**S $2p_{3/2}$**
$AgInS_2$-TiO_2	372.10	366.10	451.24	443.63	161.48	-
$AgInS_2$	372.73	366.72	451.52	443.97	161.41	160.26

Thus, the effective interaction amid the heterostructure elements results in the rise in electron concentration which leads to the interfacial charge transfer causing the shift of the peak detected. The effective electron screening results in the increase in electron concentration leading to a decrease in binding energy. [205-208]

4.2.5 Transmission Electron Microscopy (TEM)

Transmission electron microscopy (TEM) was employed to evaluate the morphology and microstructure of the samples prepared. The TEM of titania and its Selected area diffraction (SAED) pattern is demonstrated in **Figure 51a**. The nanoparticles exhibited ovular features, and the typical size was observed to be around 25 to 40 nm. The interplanar spacing (*d)* values obtained for diverse areas of the image confirm the formation of the anatase phase of the nanoparticles.[213] **Figure 51b** illustrates the TEM image of

pristine orthorhombic $AgInS_2$. The nanoparticles likewise displayed ovular nature, and the bright lattice fringes were identified of (002) and (121) planes with respective interplanar spacing values of 0.314 nm, and 0.176 nm is observed. In the meantime, **Figure 51c** and **51d** show the TEM images of $AgInS_2$-TiO_2 composites. The presence of asymmetric particles identified as $AgInS_2$ in TiO_2 is observed.

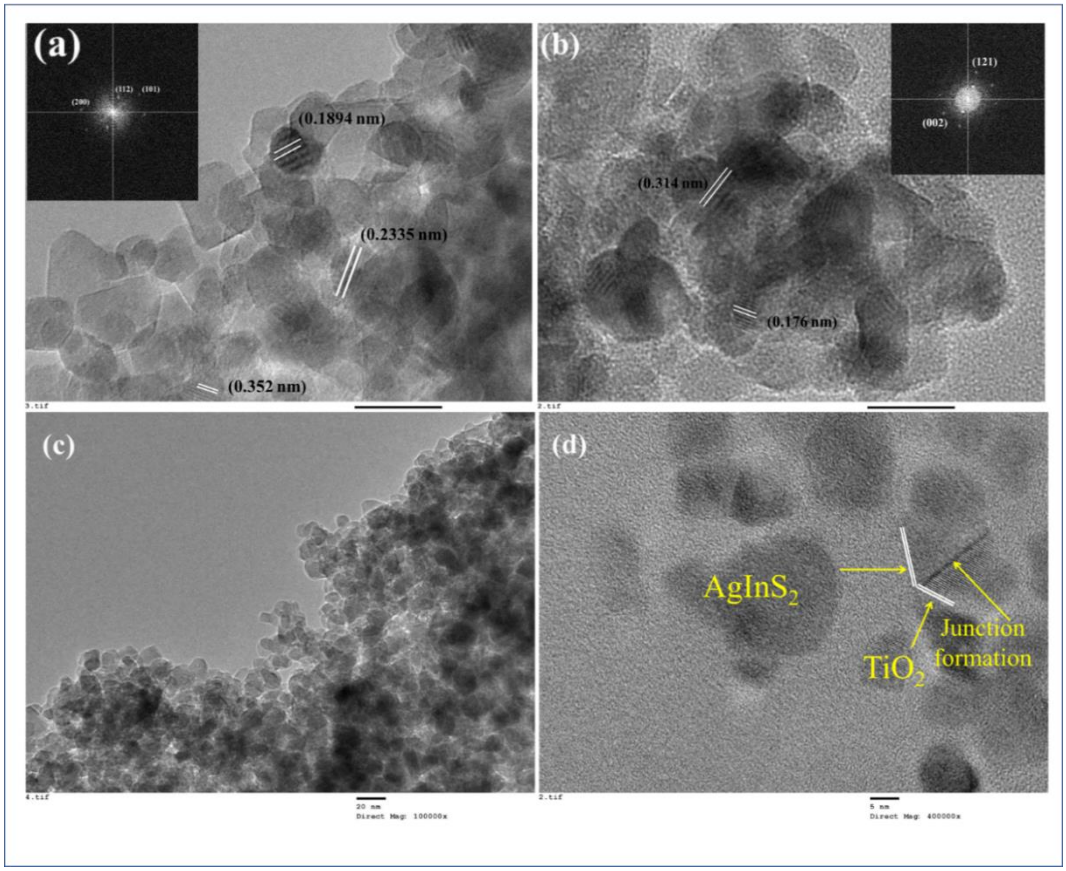

Figure 51. TEM pictures of (a) Titania; (b) $AgInS_2$; (c) & (d) 0.5 wt% $AgInS_2$-TiO_2.

However, the existence of the nanoparticles demonstrates that both $AgInS_2$ results in intimate integration with the TiO_2 nanoparticles, and thus results in the formation of the heterostructure. [179, 253] HRTEM images of the composites are further provided in **Figure 52**.

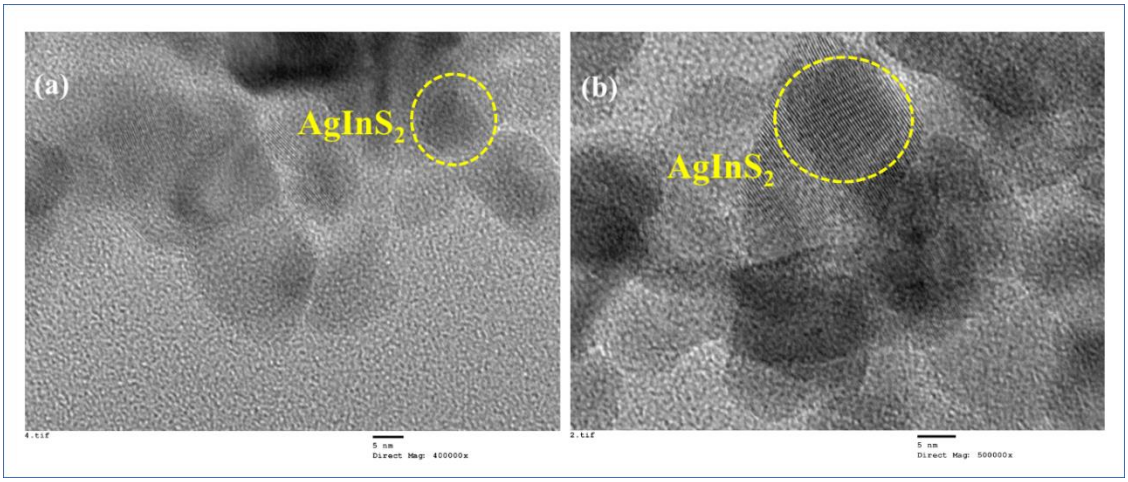

Figure 52. (a) and (b) HRTEM Images of 0.5 wt% $AgInS_2$-TiO_2.

4.2.6 Photodegradation

Pharmaceutical effluent has grown to be a major contaminant source in river and groundwater. The rise in contamination shall result in the growth of antibiotic resistant bacteria in the water bodies. Hence, effective secondary wastewater treatment has resulted in being an imperative solution to this crisis. The photocatalytic trials were done under dark and solar light illumination correspondingly.[254] **Figure 53** demonstrates the degradation pattern of $AgInS_2$-TiO_2 materials by presenting the variation in DC amount (in concentration) with time [C/C_0 % vs time]. As illustrated in **Figure 53**, the pristine parent and the composite sample displayed no adsorption activity. Moreover, the DC solution (blank sample) exposed under the same condition did not report any change in profile and thus nullified any possibility of photodecomposition.

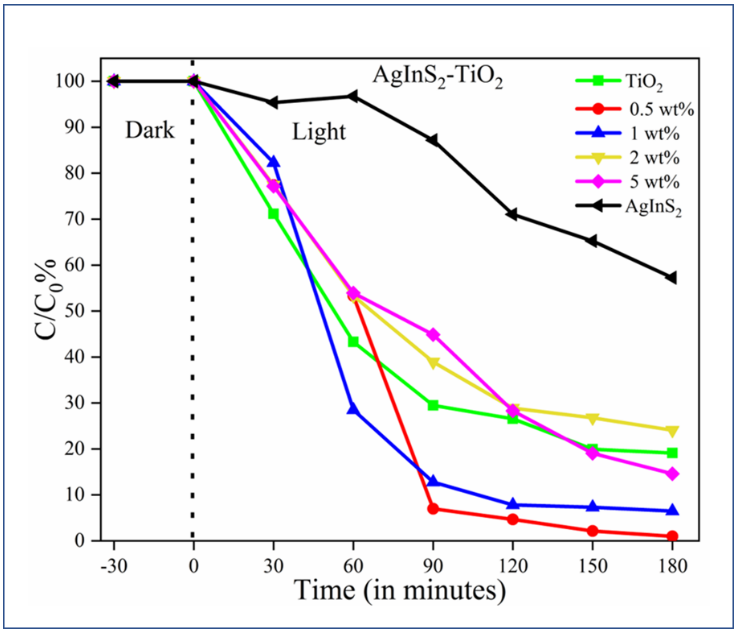

Figure 53. The concentration changes of DC with time with TiO_2, $AgInS_2$ and $AgInS_2$-TiO_2 composites.

Under visible light irradiation, the $AgInS_2$-TiO_2 composites exhibit remarkable photocatalytic efficacy as compared to the TiO_2 and $AgInS_2$ exposed under the same condition. The pristine TiO_2 and $AgInS_2$ presented the least activity compared to the composite samples. The $AgInS_2$, even though having a lower bandgap value, is not enough to display enhanced results. This might be ascribed to the higher recombination of the photogenerated excitons (e-h pairs). Although all the composites unveiled remarkable degradation profiles, the 0.5 wt% material showed the best, and the 5 wt% of $AgInS_2$-TiO_2 composite presented the lowest activity within 180 min of irradiation. Henceforth, it could be said that the composites display the best outcomes solely at lesser addant ratios. These effects might be additionally confirmed by the hydrogen generation outcomes as conferred in the later section.

To assess the reusability competence of the materials, the used sample was washed, dried and reused after every single photocatalytic study. The C/C_0 % vs time graph of 0.5 wt% $AgInS_2$-TiO_2 is illustrated in **Figure 54a**. The degradation profile remained unaltered even after 4 cyclic runs, and this

illustrates the efficiency and the stability of the catalyst prepared. The scavenging experiment was also completed to clarify the contribution of the potential reactive oxygen species associated in the degradation phenomenon. Scavenger chemicals; $AgNO_3$, triethanolamine (TEA), benzoquinone (BQ) and Isopropyl Alcohol (IPA) were added to the degradation system. As observed in **Figure 54b**, it compares the degradation profiles of 0.5 wt% $AgInS_2$-TiO_2 with the 4 sets of systems in the reaction mixture on irradiated, under the same irradiation condition. The decrease in activity was considerably altered on the introduction of Silver nitrate and BQ. Thus, electrons and holes are observed to be the major active entities in the reaction mixture. Moreover, the IPA added reaction mixture also exhibited a nominal decrease, which outwardly demonstrates that hydroxyl radicals are not the key players in the photocatalytic activity. Therefore, electron and holes might be established as the key reactive oxygen elements for $AgInS_2$-TiO_2. Moreover, Liu *et al.* and Zhang *et al.* studied $AgInS_2$-TiO_2 for various applications. They verified the results of the scavenging experiments by EPR technique. The composite samples did not display any signal under dark while on light irradiation the $AgInS_2$-TiO_2 displayed 4 peak intensity for DMPO-O_2^*. The DMPO-OH^- exhibits a fragile signal intensity; hence substantiating to the results observed in the scavenging experiments.[179, 255]

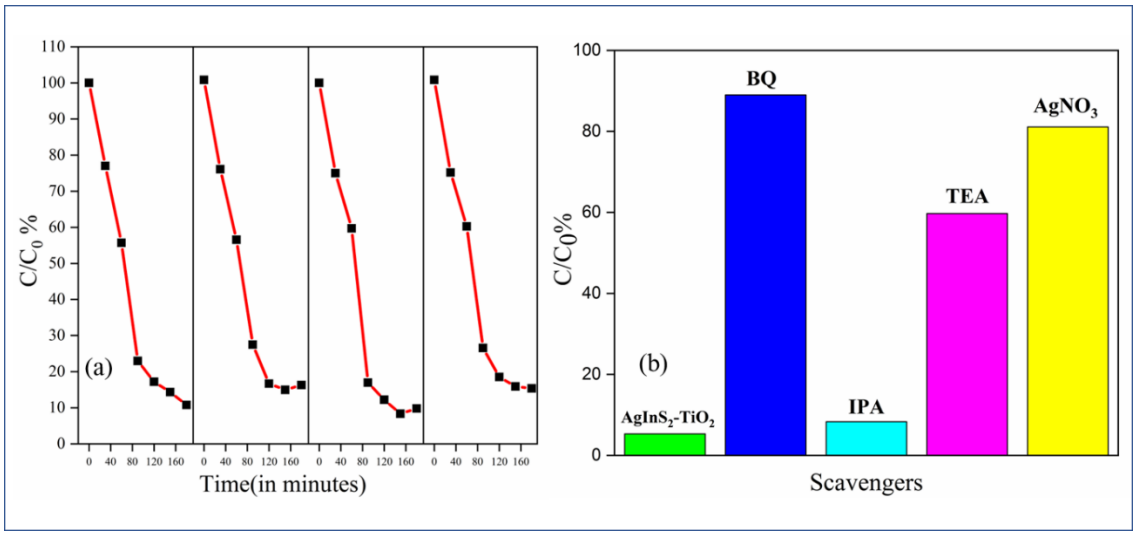

Figure 54. (a) Cyclic study and (b) Results of species trapping experiment of 0.5 wt% $AgInS_2$-TiO_2.

Nevertheless, earlier results of EPR on TiO_2 and $AgInS_2$ parent samples indicates the formation of superoxide radicals. He *et al.* studied the primary reactive species generated on visible light irradiation on $AgInS_2$ nanoparticles.[256] Weak signals of hydroxyl and singlet oxygen were observed, however, superoxide radicals exhibited strong signals which concluded it as the major species in the study. Similarly, anatase TiO_2, illustrate weak signals for hydroxyl and singlet oxygen for UV light irradiation and strong peaks were observed for superoxide radicals. The visible light illumination also left weak signals for all the three major species. [257, 258]

4.2.7 Photocatalytic H_2 production

The H_2 generation rate of $AgInS_2$-TiO_2 synthesised materials together with their bare samples ($AgInS_2$ and TiO_2) was measured. Methanol ([CH_3OH] =10 vol.%) as a sacrificial agent was utilised in this experimental process. As shown in **Figure 55a**, all the catalysts tested show appreciable hydrogen production for 0.5, 1 and 2 wt% for all over the photocatalytic runs. The composite at low dopant % exhibited H_2 output as high as 310 µmole/min. On the contrary, the pristine parent samples ($AgInS_2$ and TiO_2) showed 0 µmole/min. The composite structure exhibits efficient output at lower wt% (up to 2), on increasing the dopant value to 5 wt%, decreases the photocatalytic efficiency. Concerning the starting pH values of the solution, no noteworthy variations have been logged for the $AgInS_2$-TiO_2 composite materials during the illumination duration (**Figure 55b**).

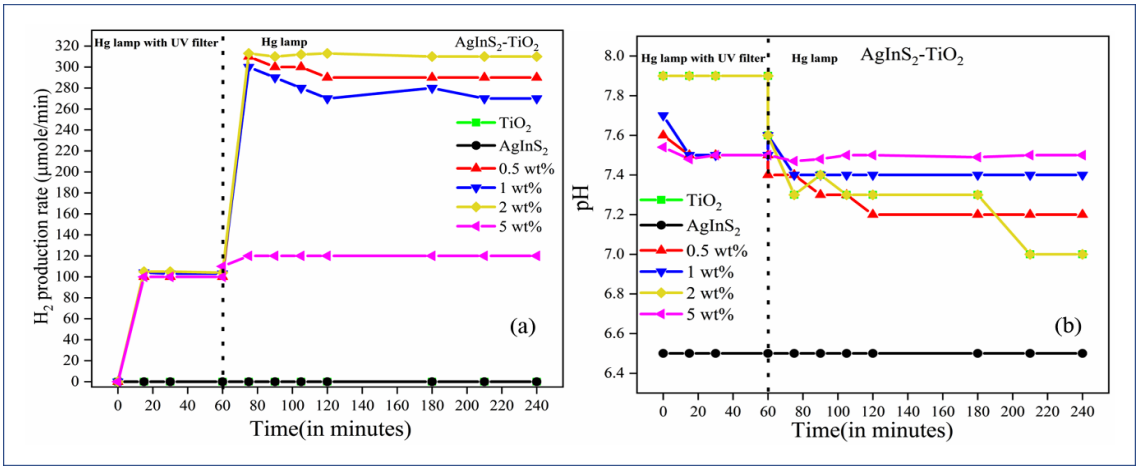

Figure 55. (a) The H_2 production rate and (b) pH of the solution at varying weight percentage of $AgInS_2$-TiO_2 catalysts. [CH_3OH] =10 vol. %; Catalyst load=500 ppm; T=25°C; P=1 atm. Data generated courtesy of Dr. Laura Clarizia.

The irradiance values recorded in the UV and the visible wavelength range on the external wall of the reactor for the various the $AgInS_2$-TiO_2 samples tested are reported in **Figure 56a** and **56b**, respectively.

Subsequently eliminating the Ultra-violet A filter, a quick surge to the UV illuminance measure has been logged. The higher illuminance values herein logged for the $AgInS_2$ material indicating a lesser suspension absorption, thus resulting in the absence of photocatalytic hydrogen generation. The illumination measures obtained from the outer walls of the reactor did not exhibit any prominent alteration at the visible region. On comparing the irradiance values with hydrogen production rates in the visible region for samples with different composition in weight percentage. It can be stated that higher radiation absorption values (i.e., lower irradiance values recorded on the photoreactor walls) result in slightly improved hydrogen generation rates. In accordance with pecking order of irradiance values in the visible region, the photocatalytic activity had the following sequence: 2%$AgInS_2$-TiO_2 > 1%$AgInS_2$-TiO_2 ≈ 0.5%$AgInS_2$-TiO_2 >> 5%$AgInS_2$-TiO_2. Comparable irradiance values have been recorded in such range for all $AgInS_2$-TiO_2 samples,

irrespective of their different composition in weight percentage. The composites of TC with TiO_2 exhibited improved H_2 production output compared to their parent samples. These composites with unique asymmetric band gap result in efficient charge transfer, which effectively reduced the recombination and enhanced the photocatalytic efficiency. The overall bandgap of the composites is decreased, as explained in the UV-DRS section.

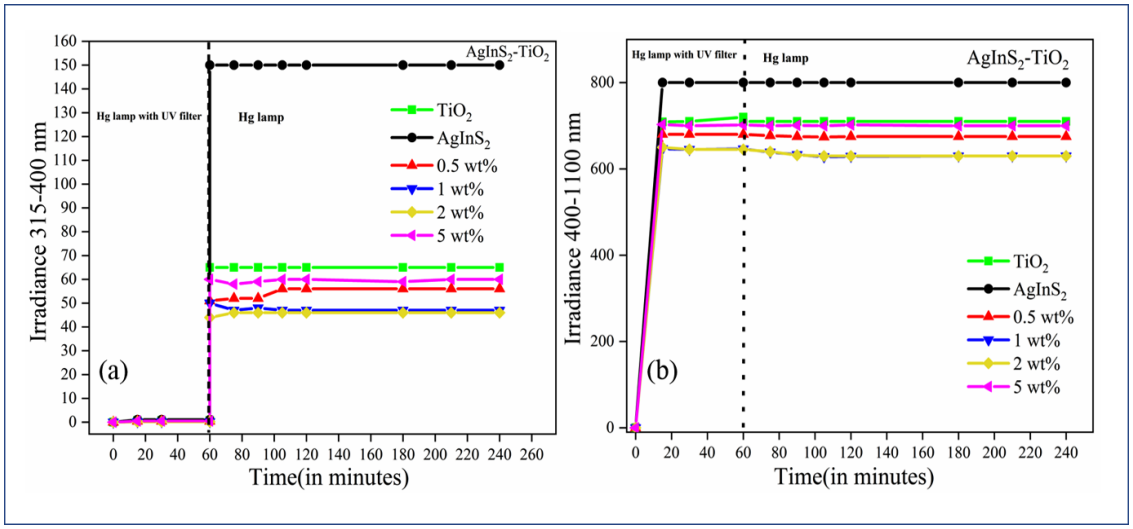

Figure 56. Irradiance measured on the external walls of the reactor between (a) 315-400 nm and (b) 400-1100 nm at varying weight percentage of $AgBiS_2$-TiO_2 catalysts. [CH_3OH] =10 vol. %; Catalyst load=500 ppm; T=25°C; P=1 atm. Data generated courtesy of Dr. Laura Clarizia.

4.2.8 Photocatalytic antimicrobial studies

The photocatalytic efficacy of $AgInS_2$-TiO_2 sample with their pristine parent samples was also studied by light induced bacterial inactivation of *E. coli* and *S. aureus* using a suspension test. A sample mixture with bacterial inoculate and catalyst was subjected to dark and light conditions, respectively. Additionally, control samples were prepared without the presence of any catalysts. As illustrated in **Figure 57**, on irradiating bacterial cells with catalysts (1 g/L) under visible light, showed that the $AgInS_2$-TiO_2 displayed a superior photocatalytic efficiency than that of their parent samples.

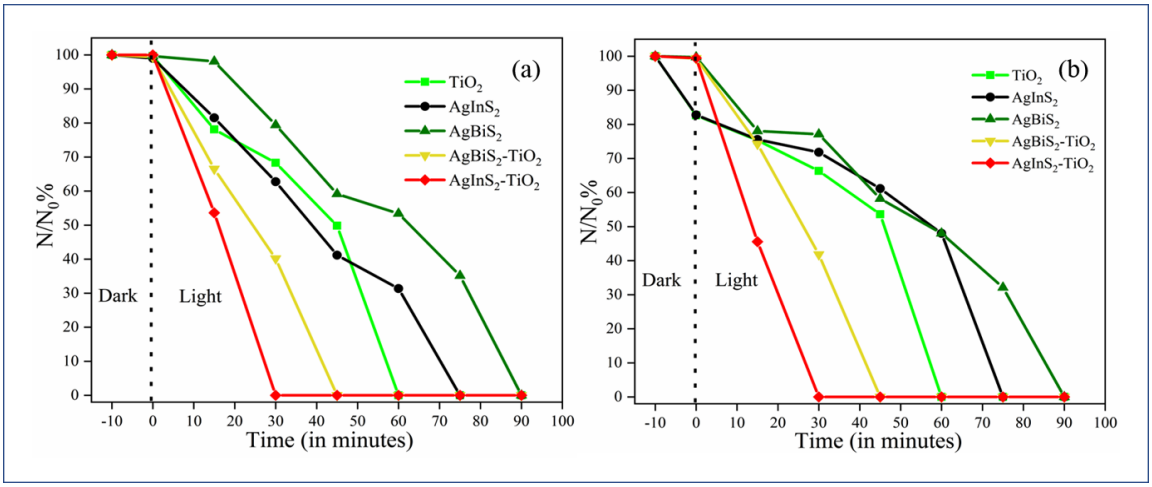

Figure 57. Photocatalytic inactivation of (a) *E. coli* and (b) *S. aureus* with TiO_2, $AgInS_2$ and $AgInS_2$-TiO_2.

More than 5- log reduction was attained within 30 min of irradiation (**Figure 58**).

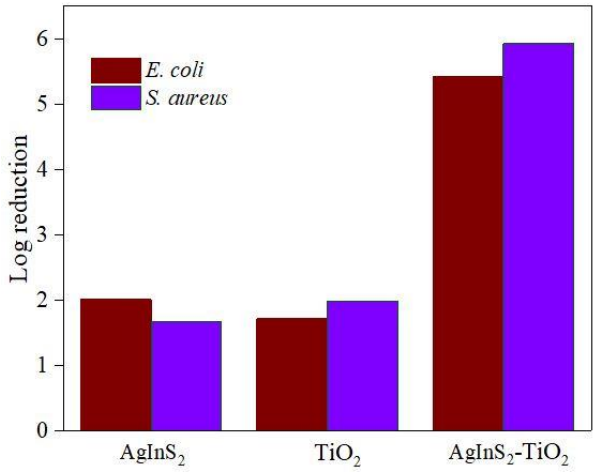

Figure 58. Log reduction of all the samples against *E. coli* and *S. aureus*.

Nonetheless, the growth of both strains was constant under light and dark conditions in the absence of photocatalysts. The bacterial growth of $AgInS_2$ parent sample displayed a complete antibacterial efficiency only after 80 min. In the case of pristine TiO_2, the total bacterial inactivation for both the strains was reached only after 60 min of light illumination.

The images of bacterial colonies on agar plates on various time intervals for $AgInS_2$-TiO_2 is given in **Figure 59**. All the composite samples were more active than their parent samples. This could be attributed to the enhanced photocatalytic efficiency of the composite sample. None of the test samples showed any bacterial disinfection property under dark conditions.

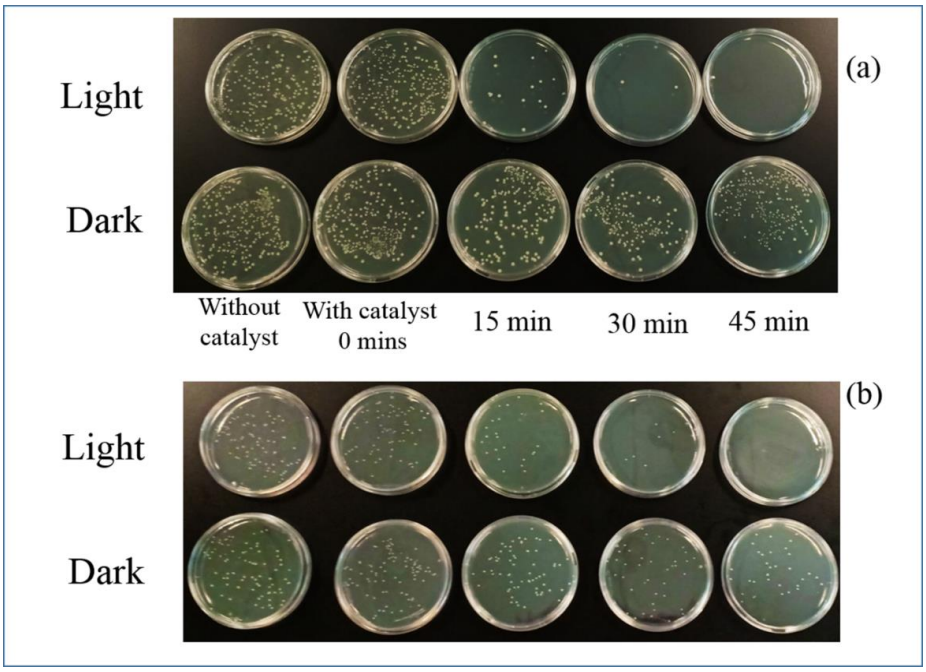

Figure 59. Images of (a) *E. coli* colonies and (b) *S. aureus* colonies on agar plates after various time intervals of 0.5 wt% $AgInS_2$-TiO_2.

4.3 PHOTOCATALYTIC MECHANISM

The composite architecture of $AgInS_2$ with TiO_2 showed remarkable photocatalytic performance compared to their pristine parent samples. The computational results of the electronic and optical properties of $AgInS_2$ and TiO_2 helped in corroborating with the experimentally obtained orthorhombic and tetragonal phases, respectively. Additionally, the band structure and PDOS analysis reveal that the valence band of TiO_2 is dominated by Ti 3d orbital and the conduction band is governed by the 2p orbital of oxygen. Also, the conduction band minima of $AgInS_2$ are dominated by the In-S interaction, while the valence band maxima are determined by the Ag-S interaction.

Hence, on visible light irradiation on $AgInS_2$-TiO_2 composites. The electrons travel from the Ag 4d and S 3p orbitals to the In 5s orbital of $AgInS_2$ and further to the O 2p orbital of TiO_2.[179, 259]

In accordance with the theoretical study, trapping experiments and the band gap values from UV-DRS; a likely photocatalytic and interfacial electron transfer mechanism for $AgInS_2$-TiO_2 heterojunction is illustrated in **Figure 60**. The conduction band (CB) and valence band (VB) potentials of the heterostructure components ($AgInS_2$ and TiO_2) is vital to understand the separation of photogenerated e-hole pairs over the nanocomposites. The energy levels are calculated using **equations 25** and **26**.

Therefore, the evaluation of χ_{TiO2} and χ_{AgInS2} is essential to estimate the E_{CB} and E_{VB} values of TiO_2 and $AgInS_2$. Thus, the E.A and the I.E values of constituent elements are provided in **Table 14**.

Table 14. I.E and E.A values of elements

Elements	I.E (eV)	E.A (eV)
Ti	6.820	0.079
O	13.618	1.460
Ag	7.576	1.301
In	5.786	0.299
S	10.360	2.070

Hence, **equation 27** and **equation 28** is used to calculate the χ values of TiO_2 and $AgInS_2$. **Table 15** tabulates the χ values calculated and the Eg values obtained from the UV-DRS plot (**Table 11**).

Table 15. χ values and Eg values.

Semiconductor	χ (eV)	Eg (eV)
TiO_2	5.805	3.180

$AgInS_2$	4.777	1.950

Hence using **equation 25** and **26**, the E_{CB} and E_{VB} of the bare samples are estimated. **Table 16** summarises the values as obtained after calculation.

Table 16. E_{VB} and E_{CB} values.

Semiconductor	E_{CB} (eV)	E_{VB} (eV)
TiO_2	-0.285	2.895
$AgInS_2$	-0.698	1.252

Therefore, utilizing the above-calculated values, a likely photocatalytic mechanism is proposed below. In **Figure 60**, illustrates the band edge position of the CB and VB potentials of $AgInS_2$ and TiO_2, before and after the formation of a possible $AgInS_2$-TiO_2 nanocomposite heterojunction. The Fermi levels of $AgInS_2$ and TiO_2 is positioned at 0.27 eV and -0.1 eV respectively (**Figure 60a**). The Fermi levels of both the semiconductors reach a uniform level, as the heterojunction is created (**Figure 60b**). The band positions of $AgInS_2$ is altered as it is in low dopant levels, so the Fermi level of $AgInS_2$ reaches -0.1 eV.[179] The new band edge positions for $AgInS_2$ as the VB and CB moves to +0.825 eV and -0.625 eV, as shown in **Figure 60b**. On visible light illumination, electron hole pairs are generated on the surface of TiO_2 and $AgInS_2$. The holes on the valence band of TiO_2 and the holes in the VB of $AgInS_2$ participate in the reaction process individually.[260] While the electrons from the CB of $AgInS_2$ migrate to the conduction band of titania. The electrons react with the oxygen adsorbed in the catalyst surface to form superoxide radical. As observed in the result of the trapping experiments, the electrons, superoxide radicals and the holes played the predominant species. These radicals further engaged in the photocatalytic reactions.

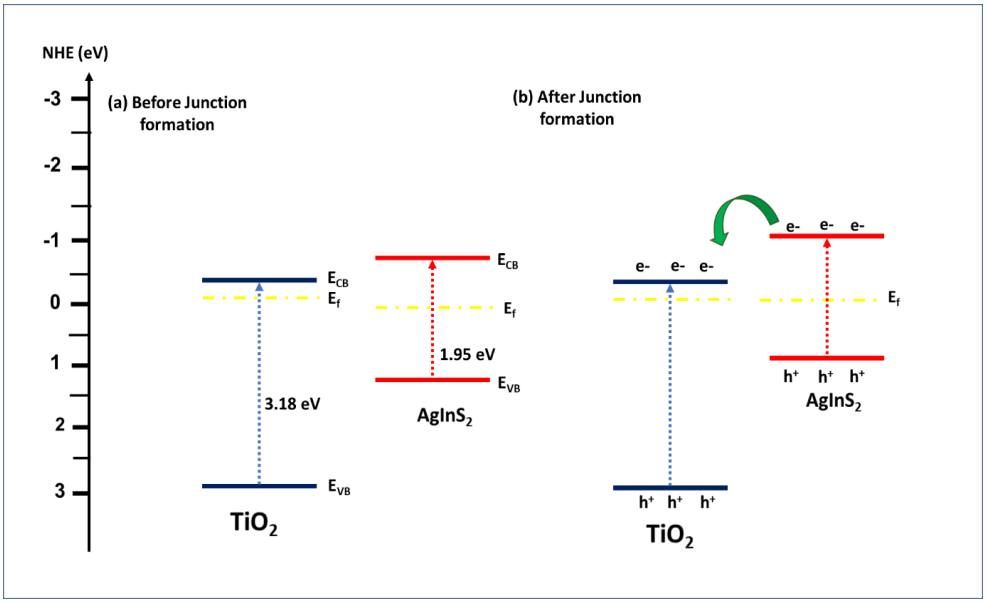

Figure 60. The photocatalytic mechanism for $AgInS_2$-TiO_2 heterojunction(a) before the junction and (b) after junction formation.

4.4 CONCLUSIONS

In summary, the current study reported the fabrication of ternary metal chalcogenide heterostructure nanocomposites of Titania. The composite material showcased a dramatic improvement in visible light absorption. The increase in the dopant percent in the composite ensued in narrowing of the band gap. Furthermore, the shift in the peak signals of XPS suggested an alteration in the chemical surroundings of the heterostructure. Importantly the degradation outcomes illustrated the enhanced efficiency and comparable results were observed in the case of the light induced hydrogen generation. The composite structure displayed a 300 times enhanced hydrogen production output when matched with their bare sample materials. A log 5 microbial inactivation was accomplished in 30 minutes of light irradiance. A possible interfacial electron transfer and the photocatalytic mechanism is offered based on the computational analysis, species trapping experiment also the bandgap value estimation from the absorbance plot. Therefore, the

current investigation details the positive composite preparation and highlights the multifunctional photocatalytic applications.

CHAPTER 5

EXPERIMENTAL AND DFT INSIGHTS OF $AgBiSe_2$-TiO_2 COMPOSITES FOR EFFICIENT CHARGE TRANSFER

5.1 INTRODUCTION

Metal chalcogenides have shown exciting applications across photochemistry. The search for new, less toxic, narrow band gap semiconductor materials has resulted in the formation of ternary and even quaternary combination of elements to form multi-class chalcogenide compounds.[148-150] Ternary chalcogenides (TC) are a fascinating class of semiconductor nanomaterials with narrow band gaps suitable with light-harvesting ability in the entire domain of visible and small region of infrared band of the electromagnetic spectrum. The family of I-V-VI has gained significant interest because of their wide band gap and high visible light absorption.

$AgBiSe_2$ exists in three crystalline phases. The commonly synthesised crystal structure is the hexagonal phase (space group $Pm\bar{3}1$), transitions to a rhombohedral phase (space group $R\bar{3}m$). The rhombohedral phase is the intermediate phase (transition at 137 °C) which finally leads into a cubic phase at 297 °C (space group $Fm\bar{3}m$).[261] In the rhombohedral phase, the silver and the bismuth cations occupy ordered positions, while in the cubic phase, these atoms get disordered. The hexagonal and the rhombohedral nanomaterials are narrow band gap semiconductors, whereas the cubic phase behaves as metal. Studies on heterostructure formation with $AgBiSe_2$ nanoparticles are yet to be reported.

Hence, in this chapter, a new novel composite of $AgBiSe_2$-TiO_2 is prepared using a facile two-step synthesis technique. The theoretical study of the pristine parent samples showed the formation of the hexagonal phase of $AgBiSe_2$, and tetragonal phase of $AgInSe_2$, which corroborated to the experimentally synthesised structures. $AgBiSe_2$-TiO_2 composites displayed enhanced visible light absorption and reduced band gap in the UV-DRS patterns. An indirect band gap was estimated for both TiO_2 and $AgBiSe_2$. The XPS results exhibited a shift in binding energy values and indicated the formation of heterojunctions. The as synthesised materials were studied for their photocatalytic efficiency, by hydrogen generation, degradation of Doxycycline, and antimicrobial disinfection (*E. coli* and *S. aureus*). The composite samples illustrated more than 95% degradation results within 180 minutes and showed 5 log reductions of bacterial strains within 30 minutes of irradiation. The hydrogen production outcomes were significantly improved as the $AgBiSe_2$ based composites displayed an increase of hydrogen generation about 180 folds. The enhanced photocatalytic efficiency displayed is attributed to the delayed charge recombination of the photogenerated electron-hole pairs in the $AgBiSe_2$-TiO_2 interface. Hence, a *p-n* nano heterojunction for $AgBiSe_2$-TiO_2 composite is formed.

The synthesis process and the process optimisation of the composites are explained in **section 2.2**.

5.2 RESULTS AND DISCUSSION

5.2.1 Computational analysis

After the structural optimization, the space groups of anatase TiO_2 and $AgBiSe_2$ were found to be $I4_1/amd$ (space group number: 141), and $P\bar{3}m1$(space group number: 164), respectively. TiO_2 was found to crystallize into a body centred tetragonal crystal system upon relaxation, and the optimized structures are presented in **Figure 61**. Octahedral molecular geometry connects Ti and O in the case of anatase TiO_2. These octahedra are

connected to each other by edge sharing at the centre of the unit cell and corner sharing elsewhere in the unit cell. There are two different Ti-O bond lengths present in the compound. The in-plane Ti-O bond length was found to be 1.94 Å, and the out-of-plane Ti-O bond length was 2.00 Å which are well consistent with the ones that could be obtained from the literature.[157, 262]

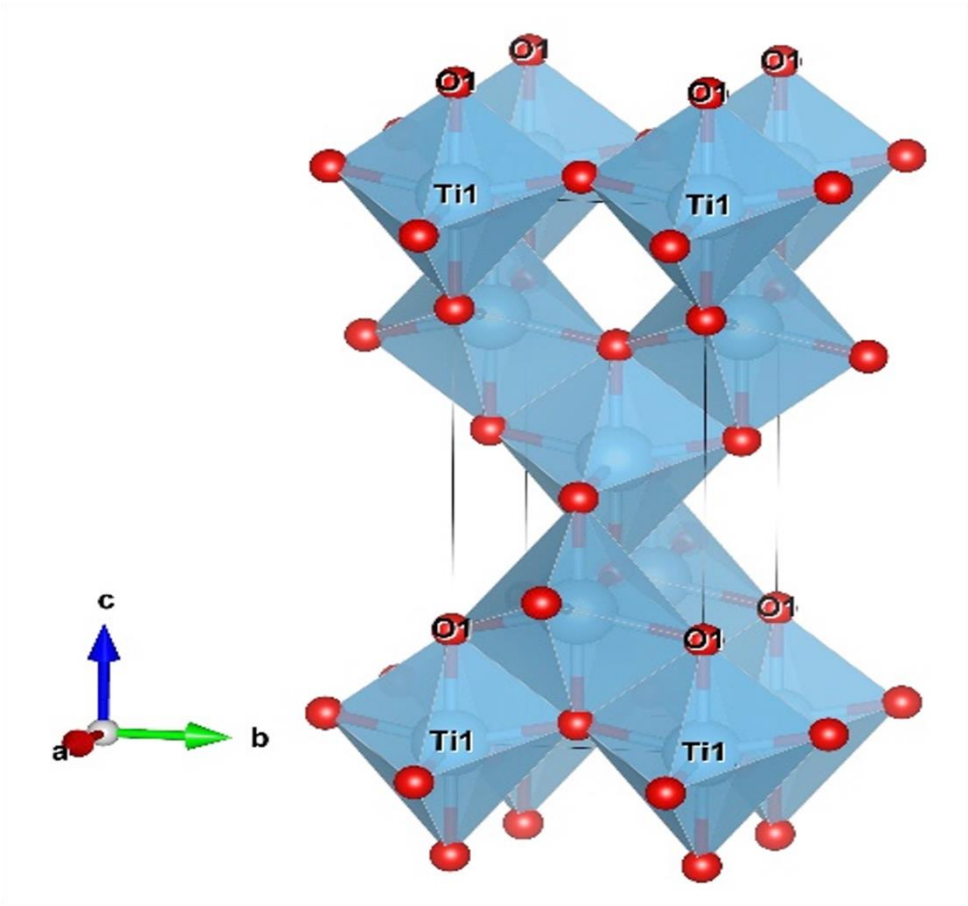

Figure 61. (Colour online) The optimised structures of TiO_2. Data generated courtesy of Dr. Syam Kumar.

While $AgBiSe_2$ was found to be stable in a hexagonal lattice upon relaxation, the optimized structures are presented in **Figure 62**. $AgBiSe_2$ is a layered material where Ag intercalates the Bi-Se octahedra. The Bi-Se bond length is found to be 2.99 Å and is isotropic within the octahedral molecular geometry. The octahedra are connected to each other through edge sharing.

The lattice parameters and volume of the two compounds obtained after structural optimization are tabulated in **Table 17**. The lattice parameters of these compounds obtained after structural optimization are consistent with the reported ones and are well within the expected error range when compared to the experimental values observed in **section 5.2.3**.[157, 263, 264]

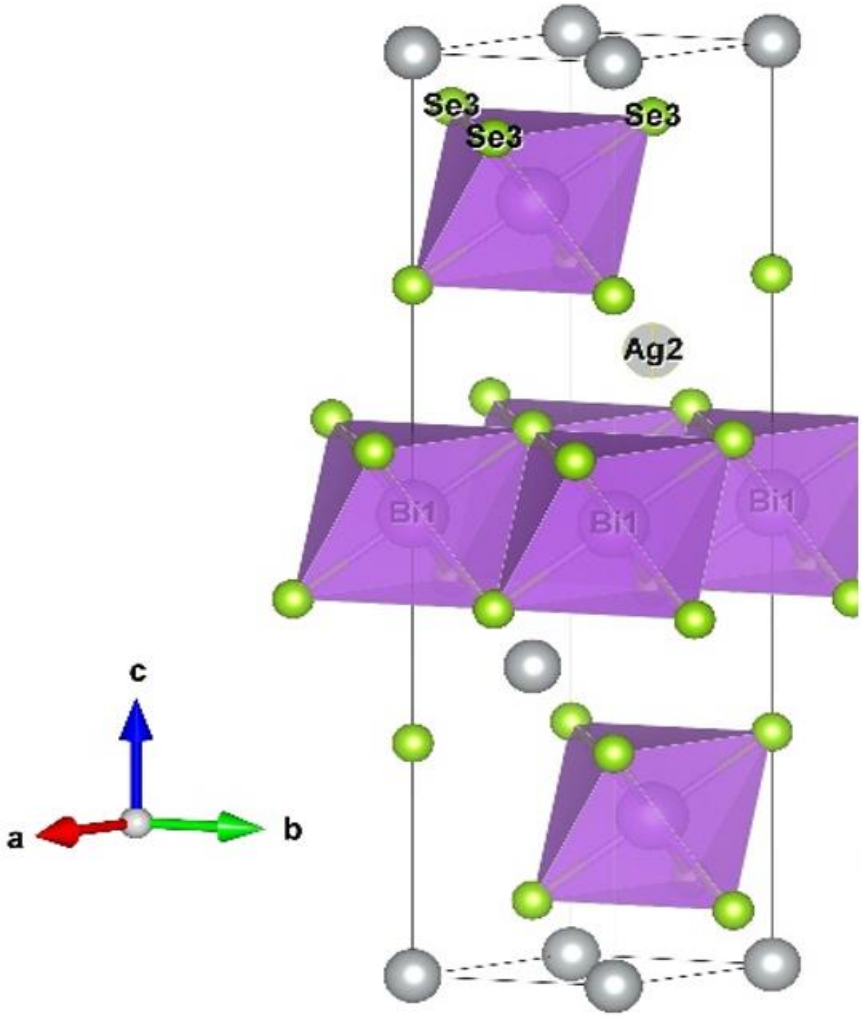

Figure 62. (Colour online) The optimised structures of $AgBiSe_2$. Data generated courtesy of Dr. Syam Kumar.

Table 17: The DFT optimised lattice parameters of TiO_2 and $AgBiSe_2$, and the percentage deviations from the observed experimental values.

Compound	Parameter	a(Å)	b(Å)	c(Å)	V(Å^3)	a(°)	b(°)	g(°)
TiO_2	Experimental	3.78	3.78	9.43	135.06	90.00	90.00	90.00
	DFT	3.80	3.80	9.75	141.10	90.00	90.00	90.00
	Deviation (%)	0.53	0.53	3.26	4.47	0.00	0.00	0.00
$AgBiSe_2$	Experimental	4.17	4.17	19.76	298.04	90.00	90.00	120.00
	DFT	4.20	4.20	19.91	304.49	90.00	90.00	120.00
	Deviation (%)	0.68	0.68	0.77	2.17	0.00	0.00	0.00

5.2.2 Electronic properties

Since the HSE has been known to reproduce the electronic properties of materials accurately, it has been adopted to investigate the electronic properties of these compounds. Starting with anatase TiO_2, its band structure and its corresponding partial density of states (PDOS) are presented in **Figure 63**. Ti d-orbitals dominate the lower CB while the O p-orbitals are found to dominate the upper VB of TiO_2. The HSE06 calculation returns the bandgap of 3.35 eV for TiO_2, which is consistent with the experimentally observed value (**Section 5.2.4**) and in the reported literature.[157, 262] Anatase TiO_2 is an indirect bandgap material with its CBM positioned at the centre of the Brillouin zone, Γ and the VBM between P and Y.

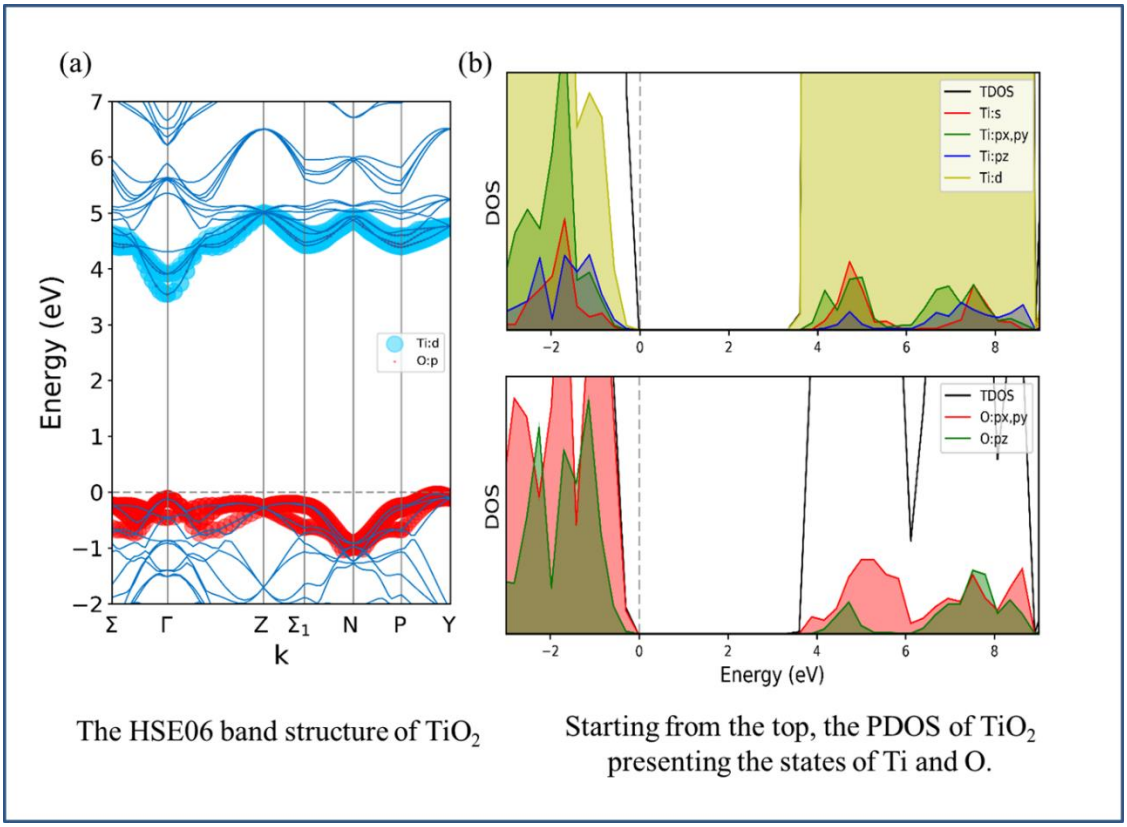

Figure 63: (Colour online) The HSE06 (a) band structure and (b) PDOS of anatase TiO_2. The PDOS plot is split into two to describe the Ti and O states separately. Data generated courtesy of Dr. Syam Kumar.

Ti 3*d* states are clearly dominating the lower CB while the O $2p_x$ and $2p_y$ states are dominating the upper VB. $AgBiSe_2$ presents a bandgap of 0.55 eV, which is slightly less than 0.6-0.8 eV reported in the literature.[263, 265] The HSE06 band structure and PDOS are presented in **Figure 64**. $AgBiSe_2$ is an indirect bandgap material with its CBM placed at the high symmetry point, A and the VBM between K and Γ of the Brillouin zone. The upper VB is dominated by the Ag 4*d* and Se 4*p* states. The lower CB of $AgBiSe_2$ is dominated by the combination of Bi 6p and Se 4p states.

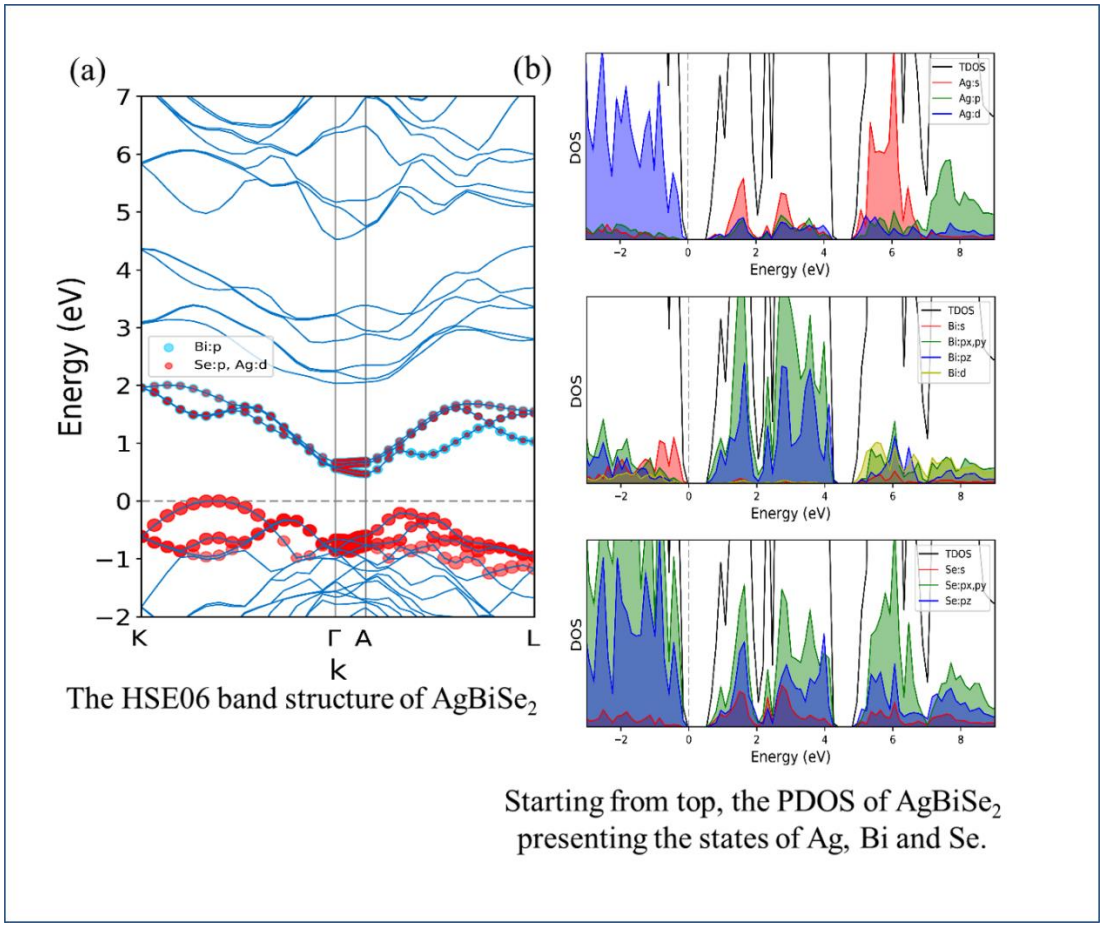

Figure 64: (Colour online) The HSE06 (a) band structure and (b) PDOS of $AgBiSe_2$. The PDOS plot is split into two to describe the Ag, Bi and Se states separately. Ag 4*d* and Se 4*p* states dominate the upper VB while the Se 4*p* and Bi 6*p* states are dominating the lower CB. Data generated courtesy of Dr. Syam Kumar.

The band edge values of TiO_2 and $AgBiSe_2$ are presented in **Table 18**. The reference scale was NHE which keeps the hydrogen evolution reaction (HER) potential at 0 eV and the oxygen evolution reaction (OER) potential at 1.23 eV. Looking into the band edge positions of the pristine compounds, it could be observed that $AgBiSe_2$ as its own fails to aid either of the reaction paths.

Table 18. The band edge positions obtained experimentally and using HSE06 calculations for the pristine TiO_2 and $AgBiSe_2$.

Compound	Determination	Valence Band Edge (eV)	Conduction Band Edge (eV)
TiO_2	HSE06	2.98	-0.36
	Experimental	2.90	-0.29
$AgBiSe_2$	HSE06	0.960	0.408
	Experimental	1.134	-0.096

5.2.3 Synthesis and structural analysis by X-ray diffraction

$AgBiSe_2$ nanoparticles are synthesised using a solution-based technique. Organic solvents such as oleylamine, diethanolamine has been used previously to produce various types of TC. In this study, ethanolamine is used as the solvent for the solvothermal synthesis. Ethanolamine has a high boiling point and acts as a stabilising agent in the synthesis process, hence making it a perfect choice of solvent. Unlike the sintering technique, where long annealing time and there is the need for high temperature, in the solvothermal process, this is easily evaded. Amine based solvent usually lowers the temperature for thermal decomposition of the precursors and aid in the formation of nanoparticles at a lower temperature.[266] They are often used as a potential reagent for anisotropic growth of nanoparticles as well as surfactants for a possible stabilising agent.[28] At the start, the Ag^+ and Bi^{3+} ions react with the solvent molecules (ethanolamine) to form a covalent complex as given below (where x and y are positive integers).[190, 191]

$$AgNO_3 + xEA \rightarrow Ag(EA)_x^+ + NO_3^- \text{ (Equation 35)}$$

$$Bi(NO_3)_3 + yEA \rightarrow Bi(EA)_y^{3+} + 3NO_3^- \text{ (Equation 36)}$$

Furthermore, the silver complexes react with the Se^{2-} ions to form binary compound; [192]

$$Ag(EA)_x^+ + Se^{2-} \rightarrow Ag_2Se + xEA \text{ (Equation 37)}$$

As explained by Bai *et al.,* the initial species formed in the process are the orthorhombic phase of Ag_2Se spherical nanoparticles.[267] The fluid-like nature of the silver and fast conducting behaviour of silver chalcogenides result in the creation of various cationic vacancies in the orthorhombic crystal structure. This results in rapid diffusion of Bi^3 to form heterostructures of $AgBiSe_2$-Ag_2Se. As the synthesis progresses, the diffusion phenomenon continues, until all the Ag_2Se seeds are exhausted. This could also be observed in the temperature and the time study graphs of the TC (**Figure 65**). The peaks of Ag_2Se are present at lower reaction time and temperature, and as the reaction progresses the intensity of the peak starts to diminish, leaving a residue of a small percent of impurity.[28, 267, 268]

$$Ag_2Se + Bi(EA)_y^{3+} \rightarrow AgBiSe_2 + yEA \text{ (Equation 38)}$$

Ethanolamine (EA), with a single amine and N-chelating atom, act as a potential structure directing agent.[189] The inbuilt pressure and the appropriate temperature supports the formation of unique phases and morphology. This results in the formation of spherical nanoparticles of $AgBiSe_2$ in hexagonal phase.[266]

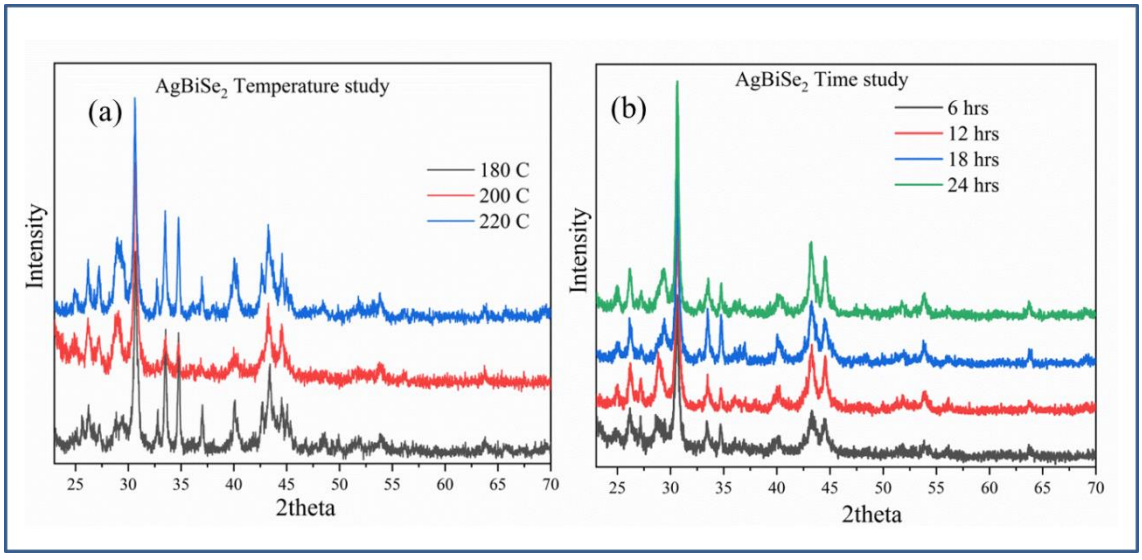

Figure 65. The XRD patterns of the solvothermal (a) temperature study for 12 h and (b) time study of $AgBiSe_2$ at 200 ˚C.

Figure 65 illustrates the temperature and time study for $AgBiSe_2$ solvothermal synthesis. The 100% intensity peak of $AgBiSe_2$ is found at 30.62°. Furthermore, ICDD card is utilised to match up the remaining smaller peaks as well as identify the phase of the nanoparticles prepared at varying time and temperature. As displayed, varying the temperature from 180 °C to 220 °C for 12 h showed a varying change in the crystallinity, as well as many additional peaks, were detected. Thus, 200 °C was found to be the optimal synthesis temperature. Hence, using the same temperature, the influence of time was studied from 6 to 24 h. It was observed that all the diffractograms displayed a similar pattern. However, for the 12 h time study, the crystallinity was observed to be maximum. Hence, 200 °C for 12 h is the controlled solvothermal parameter for the synthesis of $AgBiSe_2$.

The nanoparticles ($AgBiSe_2$) and the composites with titania were examined using X-ray diffraction. Formation of hexagonal phase $AgBiSe_2$ nanoparticles was observed in **Figure 66** [ICDD card no: 04-010-1589]. The influence of the solvothermal duration and the temperature to identify the optimised experimental parameters was also performed (**Figure 65**). As observed, the intensity (100%) of the peaks at 30.62° for $AgBiSe_2$ is found to be sharp and well defined. This infers the formation of crystalline structures at 200 °C and 12 h of solvothermal duration. Hence 200 °C and 12 h is the optimal temperature and time for the synthesis process and henceforth used for composite preparation with titania nanoparticles. The sol-gel synthesis of TiO_2 and its further calcination at 500 °C leads in the formation of the anatase phase. Defined peaks at 25.1° corresponding to the tetragonal structure of the anatase phase are observed [ICDD card no: 00-021-1272]. The lattice parameter of the parent samples were estimated to be; hexagonal phase of $AgBiSe_2$ with a = b = 4.17 Å, c = 19.72 Å and $\alpha = \beta = 90^{\circ}$ and $\gamma = 120^{\circ}$. These values are similar to the values obtained through the computational study, as

explained in **section 5.2.1**. **Table 19** summarises the lattice parameters experimentally calculated with the reported values in literature.

Table 19. Summarised lattice parameters of TiO_2 and $AgBiSe_2$.

Compound	Parameter	a(Å)	b(Å)	c(Å)	α(°)	β(°)	γ(°)	**Ref**
TiO_2	Experimental	3.78	3.78	9.50	90.00	90.00	90.00	
	From Literature	3.80	3.80	9.60	90.00	90.00	90.00	188
$AgBiSe_2$	Experimental	4.17	4.17	19.72	90.00	90.00	120.00	
	From Literature	4.18	4.18	19.67	90.00	90.00	120.00	263

Figure 66 further displays the composites prepared at various weight ratios. Peaks at 25.1° of titania in the anatase phase are observed for all the composite structures irrespective of the weight ratios. The broadening of the peaks demonstrates that the crystalline size of the sample is minimal. Peaks of TC are not observed prominently in any of the diffractograms, except for the 5wt% $AgBiSe_2$-TiO_2, where a small peak at 30.6° is detected. The incorporation of TC in minimal weight ratios and the crystalline nature of the titania nanoparticles makes it difficult to observe any distinct peaks of TC in the diffractograms. Furthermore, it also validates that the structure of TiO_2 remains unaltered even after the solvothermal reaction for the composite formation.

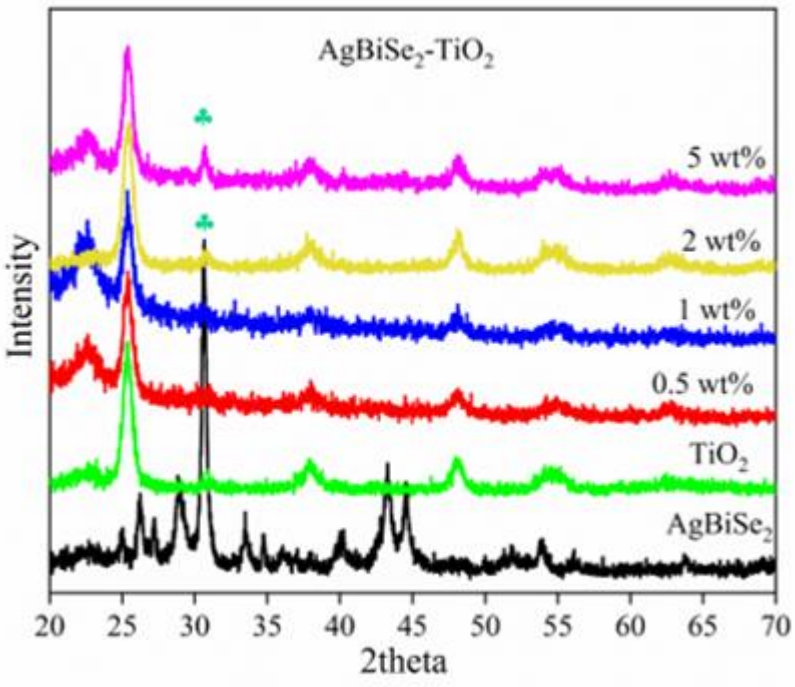

Figure 66. The XRD patterns of TiO_2, $AgBiSe_2$, $AgBiSe_2$-TiO_2 composites.

5.2.4 Absorption properties

UV-vis DRS measurements were taken of the as prepared samples to study their light absorption characteristics. As shown in **Figure 67**, the pristine TiO_2 displays its signature absorption at 320 nm in the UV region, and the absorption edge steeps at 400 nm. **Figure 67** also displays the absorption spectra of the $AgBiSe_2$-TiO_2 composites. The absorption pattern displays a combination of both the parent samples. All the samples show the signature hump of titania at 320 nm, with absorption extending throughout the visible region, typical to the pattern as observed for $AgBiSe_2$ (**Figure 68b**).[30]

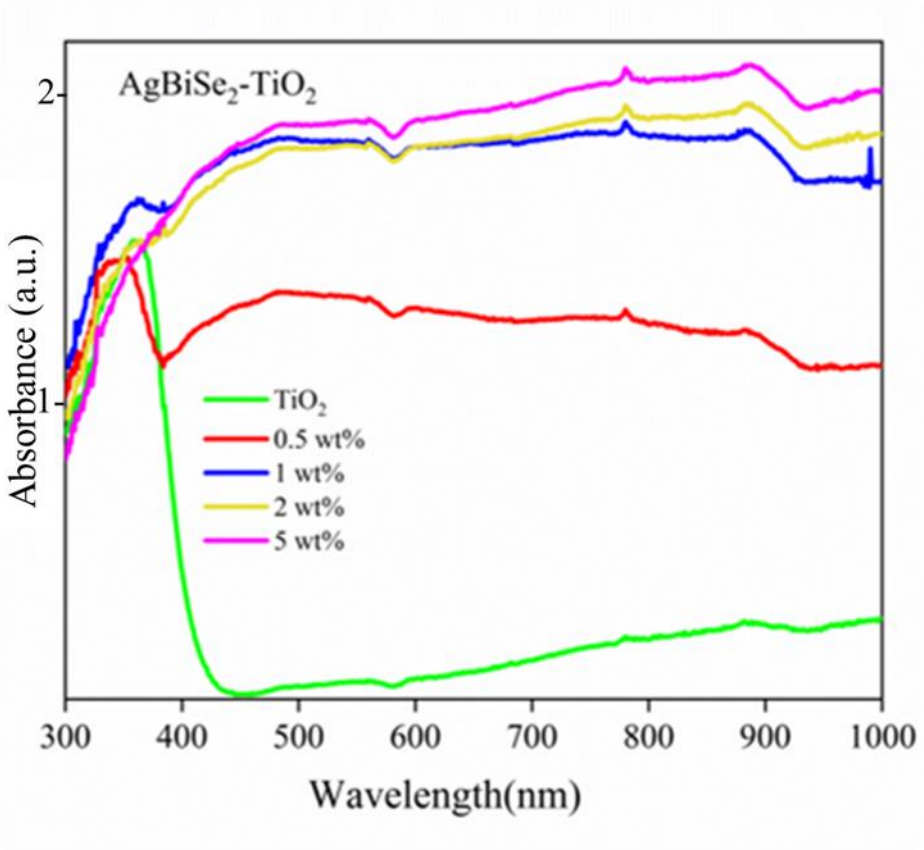

Figure 67. The absorption patterns of TiO_2, $AgBiSe_2$-TiO_2 composites.

Increase in the content of TC in the sample resulted in increased absorption in the visible region. This was further reflected in the change in the colour of the samples, varying from white to brown and further black. This demonstrated the coupling of TC with titania to construct $AgBiSe_2$-TiO_2 composites.

Band gap engineering of the semiconductors is the prime aspect of the heterojunction construction. Thus, the influence of the TC addition to TiO_2 could be further observed by the changes in the band gap of the composite sample. The Kubelka-Munk (K-M) function is utilised to convert the functionality to energy (**Figure 68a** and **68b**).[269]

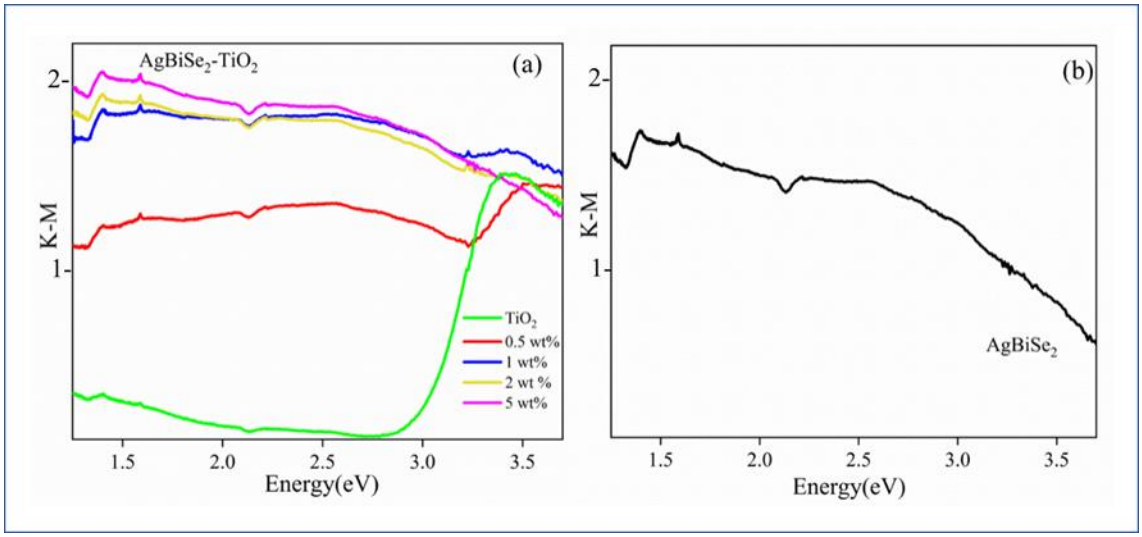

Figure 68. The Tauc plots of (a) TiO_2, $AgBiSe_2$-TiO_2 composites and (b) $AgBiSe_2$.

The extrapolation of the lines in the plots enables the evaluation of the absorption onset for these samples and further estimation of the band gap. The band gap of the pristine TiO_2 sample was estimated to be 3.2 eV, while the parent TC samples showed 1.23 eV. The values obtained are nearly close to the computationally calculated values, as explained in **section 5.2.2**. The band gap of the composite samples showed a decline in value with the increase in the content of TC (**Figure 69**). **Table 20** tabulates the band gap value of all the samples.

Table 20. Band gap values of TiO_2 and $AgBiSe_2$-TiO_2 composites.

Sample	**TiO_2**	**$AgBiSe_2$**	**0.5 wt%**	**1 wt%**	**2 wt%**	**5 wt%**
Band gap (eV)	3.20	1.23	1.30	1.32	1.28	1.25

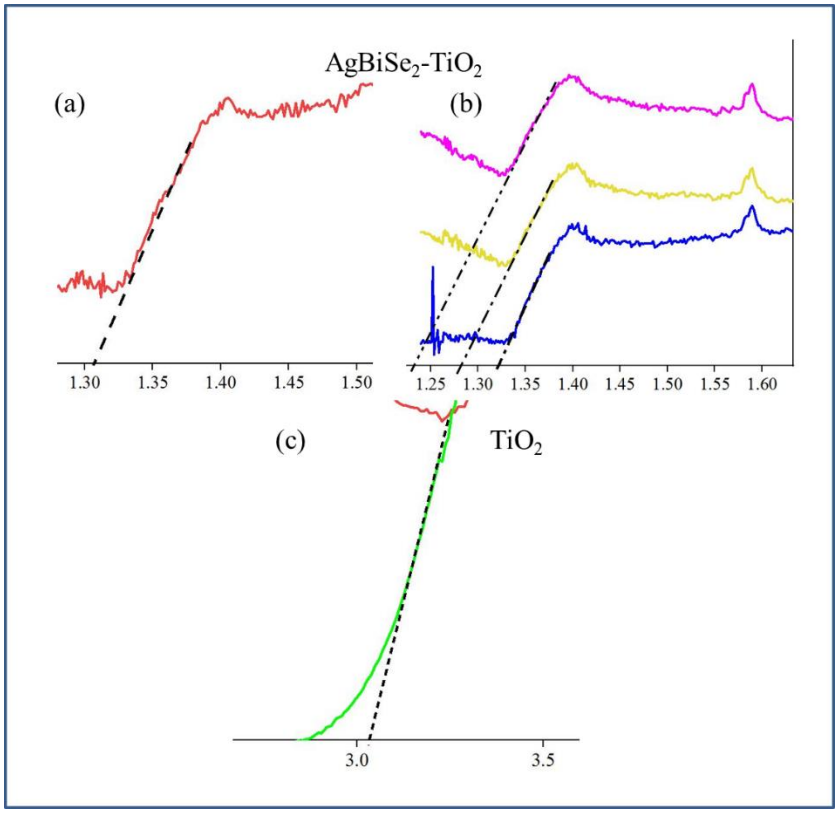

Figure 69. The Tauc plots of (a), (b) $AgBiSe_2$-TiO_2 composites and (c) TiO_2.

The strong interaction of the composite samples results in increased interfacial charge transfer and the decrease in the band gap. The computational analysis of the optical and the electronic properties of the parent samples shows that the band edge of the parent $AgBiSe_2$ is dominated by the contribution of Ag 4*d* and Se 4*p* states. The lower CB of $AgBiSe_2$ is dominated by the combination of Bi 6*p* and Se 4*p* states. Whereas TiO_2 displayed a contribution from Ti 3*d*-orbitals in the lower CB while the O 2*p*-orbitals are found to dominate the upper VB. Hence, the composite samples have a combined influence of the parent samples, which is observed experimentally in the enhanced absorption edge as well as the decreased band gap values. This infers the positive hybridisation of the parent samples and construction of heterostructure composites.[234, 270] The enhanced absorption properties and in turn the declined band gap proves to be effective in

multifunctional photocatalytic applications (**Section 5.3**). The 5 wt% composite displayed the best photocatalytic results, as discussed in **section 5.2.7.** Hence, here onward only this composite is assessed for their morphological and elemental analysis along with their pristine parent samples unless otherwise stated. **Table 21** summarises the experimentally attained band gap value and the reported values in literature.

Table 21. Band gap values of TiO_2 and $AgBiSe_2$-TiO_2 composites.

Sample	Band gap (eV)	From Literature	Band gap type	Ref
TiO_2	3.18	3.20	Indirect	248
$AgBiS_2$	1.23	1.68	Indirect	263

5.2.5 X-ray Photoelectron Spectroscopy (XPS)

The elemental states and the chemical composition of the prepared pristine parent and the composite samples were investigated by XPS measurements. The survey scans of TiO_2, $AgBiSe_2$ and $AgBiSe_2$-TiO_2 are displayed in **Figure 70**.

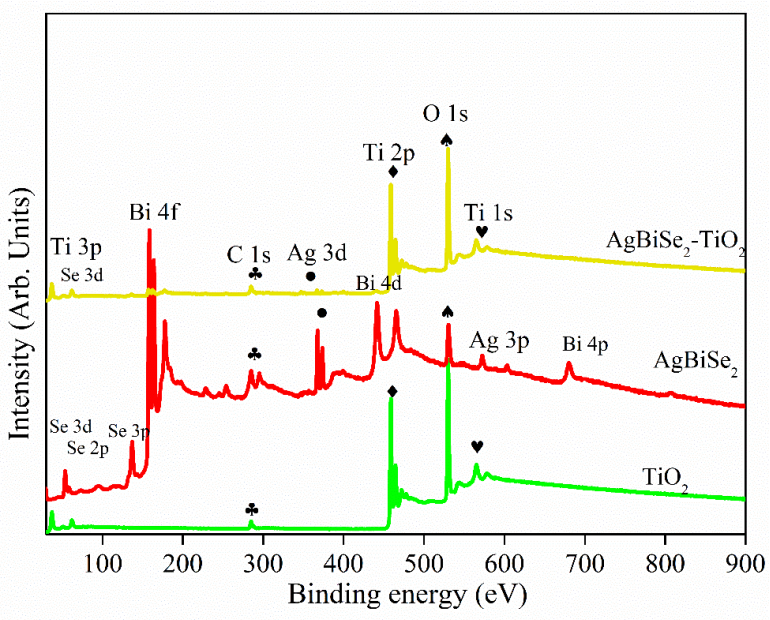

Figure 70. Survey scans of TiO_2, $AgBiSe_2$, and 5wt% $AgBiSe_2$-TiO_2. Data generated courtesy of Dr. Steven Hinder.

Peaks of Ti 2*p* and O 1*s* are found for TiO_2, while $AgBiSe_2$ sample displayed peaks of Ag 3*d* and Se 3*d* and Bi 4*f*. The composite samples showed all the combined peaks of the parent samples. In all the samples, a small percentage of C 1*s* and O 1*s* peaks were observed, these impurity peaks were acquired during the synthesis and the characterisation process. To further investigate the charge transfer at the heterojunction interface between TiO_2 and the TC nanoparticles, the high resolution XPS of the composites were also examined. **Figure 71(A)** displays the Ti 2*p* patterns of TiO_2 (a), $AgBiSe_2$-TiO_2 (b). The characteristic peaks at 458.84 eV (Ti $2p_{3/2}$) and 464. 60 eV (Ti $2p_{1/2}$), ascribed to Ti^{4+} state was observed for TiO_2 sample.[188]

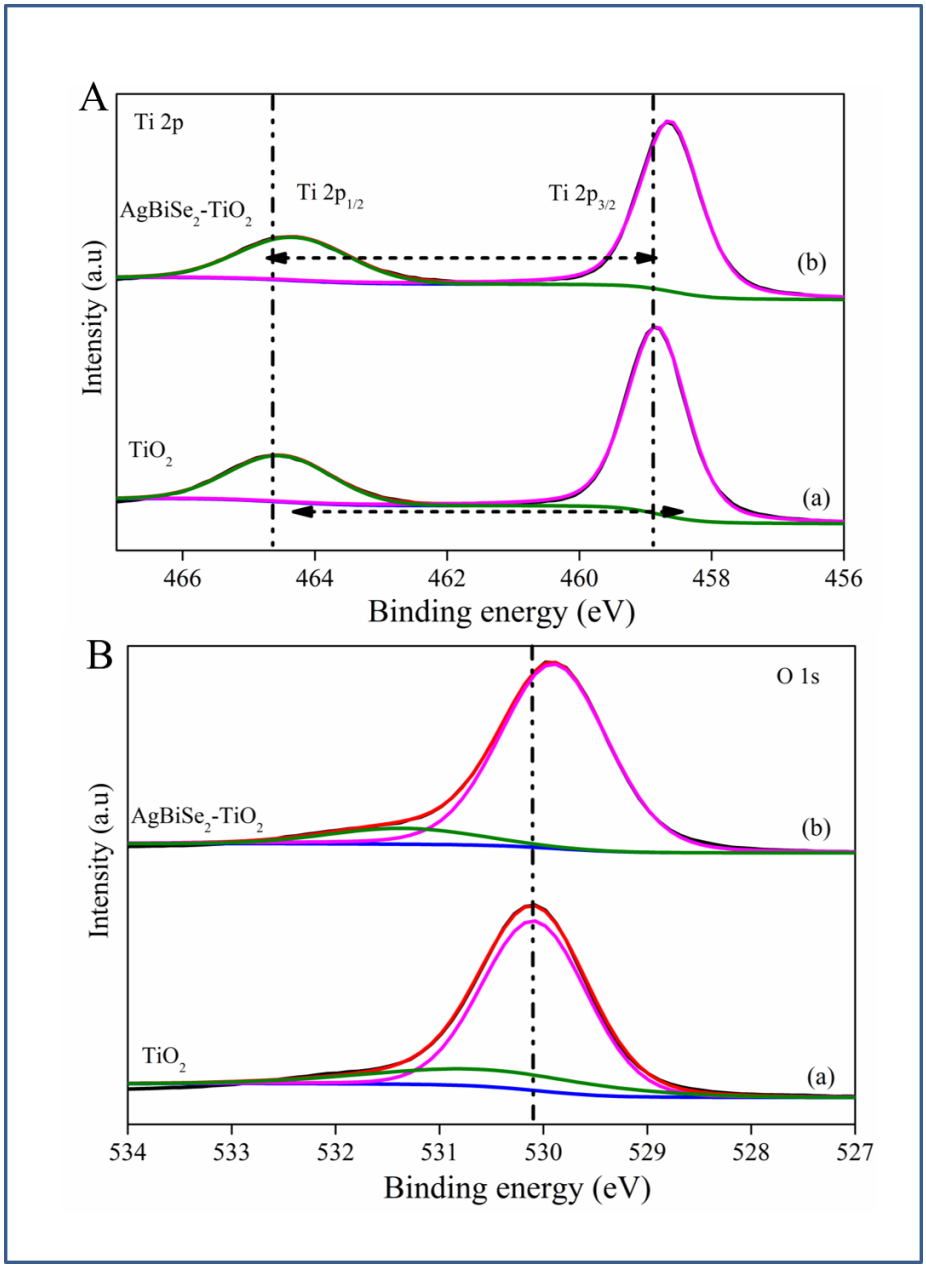

Figure 71. High resolution XPS spectra of (A) Ti 2*p* (a) TiO_2 (b) 5wt% $AgBiSe_2$-TiO_2; (B) O 1*s* (a) TiO_2 and (b) 5wt% $AgBiSe_2$-TiO_2. Data generated courtesy of Dr. Steven Hinder.

In the case of composite samples, the signature profile of Ti in the +4 state did not show any changes. However, both the doublets of Ti 2*p* in composite samples displayed a small shift in binding energy values. A shift of ~0.3 eV was observed for $AgBiSe_2$-TiO_2. This shift in the composite samples to lower

binding energy value compared to the parent sample constitutes the change in the chemical environment of TiO_2 nanoparticles in the due presence of the small amount of TC introduced. [234, 270] In the composite sample, the spin-orbit splitting difference for Ti 2*p* remained consistent (5.7 eV). **Figure 71(B)** displays the deconvoluted O 1*s* patterns of TiO_2 (a), $AgBiSe_2$-TiO_2 (b). The characteristic peak at 530.20 eV observed for pristine titania sample is assigned to Ti-O bonds.[184] As similar to the Ti 2*p* patterns, the peaks of O 1*s* also displayed a small shift for the composite sample (~0.3 eV for $AgBiSe_2$-TiO_2). Deconvoluted O 1*s* spectrum also displayed a peak above 531 eV for all the two samples, which is assigned to the hydroxyl molecules adsorbed or the water molecules.[271, 272]

Figure 72(A) displays the high-resolution spectra of Ag 3*d* patterns of $AgBiSe_2$ (a) and $AgBiSe_2$-TiO_2 (b). Sharp and symmetric peaks of Ag 3*d* were observed for both the samples. Characteristic peaks of Ag^+ were observed at 367.78 (Ag $3d_{5/2}$) and 373.80 (Ag $3d_{3/2}$) for $AgBiSe_2$ sample. The composite sample with titania displayed a shift (~0.8 eV) in both the peaks to 367.03 (Ag $3d_{5/2}$) and 373.05 (Ag $3d_{3/2}$).

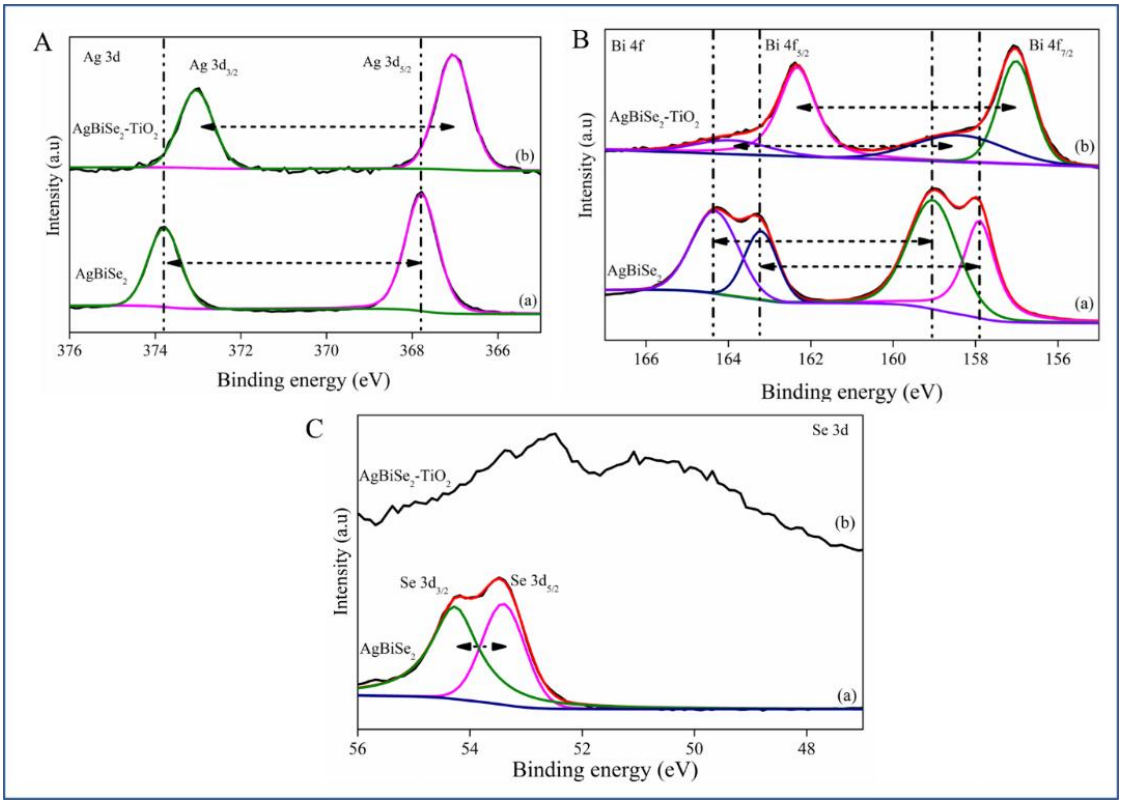

Figure 72. High resolution XPS spectra of (A) Ag 3*d* (a) $AgBiSe_2$ and (b) 5wt% $AgBiSe_2$-TiO_2; (B) Bi 4*f* (a) $AgBiSe_2$ and (b) 5wt% $AgBiSe_2$-TiO_2; (C) Se 3*d* (a) $AgBiSe_2$ and (b) 5wt% $AgBiSe_2$-TiO_2. Data generated courtesy of Dr. Steven Hinder.

The doublet separation remained consistent for the Ag 3d patterns for both the samples (6 eV). As shown**, Figure 72(B)** displays the deconvoluted high resolution spectra of Bi 4*f* patterns of $AgBiSe_2$ (a) and $AgBiSe_2$-TiO_2 (b). Peaks corresponding to Bi^{3+} state were observed at 159.03 eV (Bi $4f_{7/2}$) and 164.36 eV (Bi $4f_{5/2}$) for $AgBiSe_2$ sample. Moreover, doublets of Bi in the elemental state were also observed in the spectra (157.91 eV and 163.23 eV). In the case of the composite samples, the doublet peaks corresponding to the Bi^{3+} state showed a shift to lower binding energy (~0.6 eV). Apart from that, the peak intensity of elemental Bi reduced and displayed a similar shift in the peak values. In all the cases, the spin-orbit splitting difference of 5.31 eV remained constant. **Figure 72(C)** displays the deconvoluted high resolution spectra of

Se 3*d* patterns of $AgBiSe_2$ (a) and $AgBiSe_2$-TiO_2 (b). Peaks at 53.38 eV (Se $3d_{5/2}$) and 54.27 eV (Se $3d_{3/2}$) were observed for $AgBiSe_2$ sample attributed to Se^{2-} state. The doublet splitting difference was observed to be 0.86 eV, consistent to Se^{2-}. The composite sample did not show any symmetric peaks of Se; however, a small pattern is observed.[30, 273] **Table 22** summarises the peak position of all the samples. As observed from the above peak patterns displayed of the pristine parent sample and the composite structures.

Table 22. The summarised glance of all the peak position of different elements $AgBiS_2$ and $AgBiS_2$-TiO_2 (in eV)

Sample Name	**Ti $2p_{1/2}$**	**Ti $2p_{3/2}$**	**O 1s**	**Ag $3d_{3/2}$**	**Ag $3d_{5/2}$**	**Bi $4f_{5/2}$**	**Bi $4f_{7/2}$**	**Se $3d_{3/2}$**	**Se $3d_{5/2}$**
TiO_2	464.60	458.84	530.20 531.20	**X**	**X**	**X**	**X**	**X**	**X**
$AgBiSe_2$	**X**	**X**	**X**	373.80	367.78	164.36	159.03	54.58	53.50
$AgBiSe_2$-TiO_2	464.36	458.60	529.90 531.15	373.05	367.03	163.23	157.91		

All the composite patterns displayed a shift in the peak values to lower binding energy values. The change in the chemical environment by the introduction of TC nanoparticles showed the change in the Ti 2*p* and O 1*s* patterns. Similar changes were also observed for pristine $AgBiSe_2$ samples. The shift, above-mentioned manifests the efficient charge transfer at the heterojunction interface and demonstrates the creation of effective heterostructure for multifunctional applications.

5.2.6 TEM Analysis

Figure 73a and **73b** show typical TEM images of the as-prepared $AgBiSe_2$ with the particles being nanosheets of average width ranging 50-70 nm. The SAED pattern (**Figure 73c**, inset) is consistent with the XRD pattern with the major diffractions of (104), (012), (110) and (018) crystal planes of hexagonal

$AgBiSe_2$. Meanwhile, the HRTEM image (**Figure 73c**) showed high crystallinity for $AgBiSe_2$ nanocrystals, and the adjacent atomic lattice fringes showed a distance of about 0.293 nm, which is in agreement with the calculated fringe width of 0.291 nm for (104) planes of $AgBiSe_2$.[274] TEM and HRTEM (**Figure 73d**, **73e**, and **73f**) images of 5wt% $AgBiSe_2$-TiO_2 composite revealed that larger $AgBiSe_2$ particles are covered with smaller titania nanoparticles. HRTEM well matched with fringe width of 0.293 nm corresponding to (104) plane of hexagonal $AgBiSe_2$ for the larger particles in addition to a fringe width of 0.354 nm indicating (101) plane of anatase titania for the smaller particles. SAED pattern (**Figure 73f**, inset) again supports the presence of both nanoparticles and is also consistent with XRD obtained.

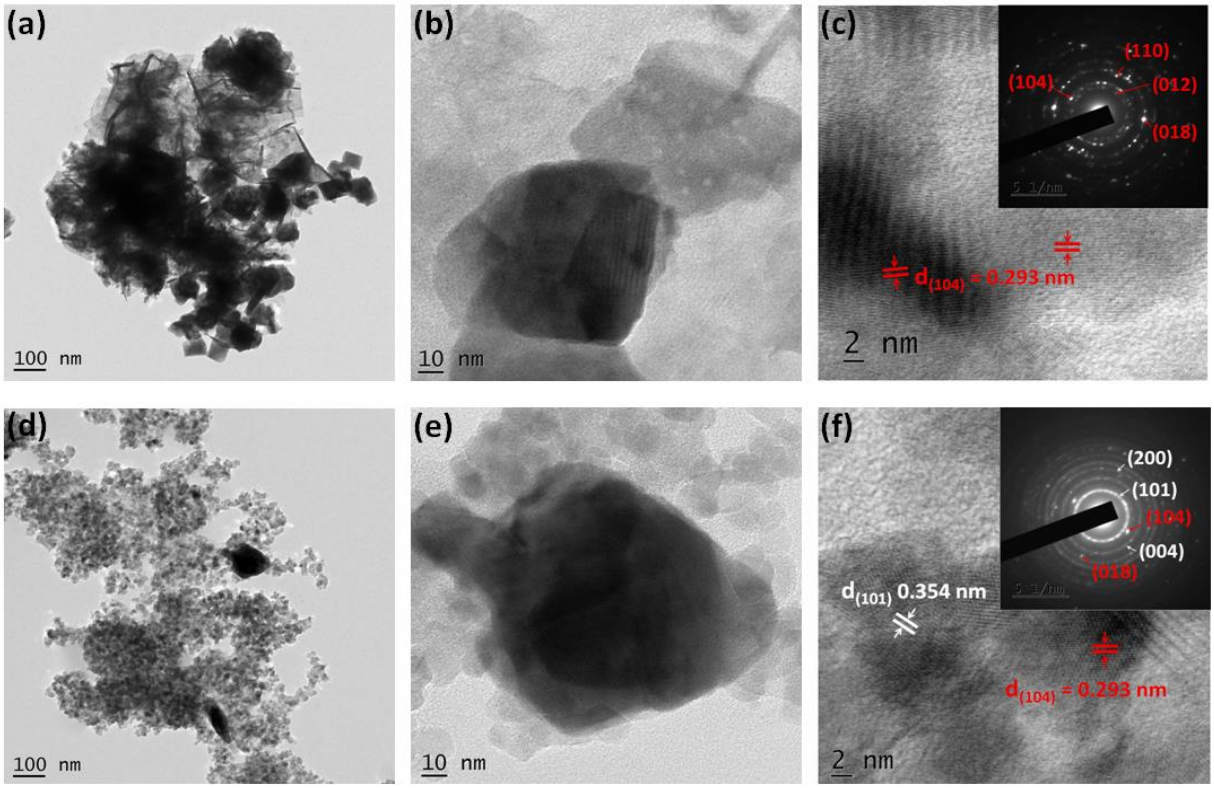

Figure 73. TEM and HRTEM images of $AgBiSe_2$ (a,b,c) and 5wt% $AgBiSe_2$-TiO_2 composite (d,e,f). Inset of (c) and (f) are the SAED patterns of the samples with red colour markings corresponding to TC and white to TiO_2. Data generated courtesy of Ms. Nisha Padmanabhan.

5.2.7 Photoluminescence Analysis

The photocatalytic efficacy is largely governed by the ability of the composite structure to migrate the photogenerated exciton to various reaction sites. **Figure 74** presents the mass normalized photoluminescence spectra of TiO_2 and its 5wt% composites with $AgBiSe_2$. The spectra clearly portray the effect of heterojunction formation on the recombination of excitons in parent TiO_2. The emission intensity of composite of TC with TiO_2 is quenched. Since PL emission has resulted from the recombination of photogenerated electron-hole pairs, the reduction in the PL intensity for the composite indicate that recombination rate is very much diminished, resulting in their high photocatalytic efficiencies compared to parent TiO_2. The emission peaks at 365 nm displayed a small red shift in the composite samples compared to the pristine parent sample. This is attributed to the change in the local chemical environment of the sample and this further validates the positive heterojunction creation. [275]

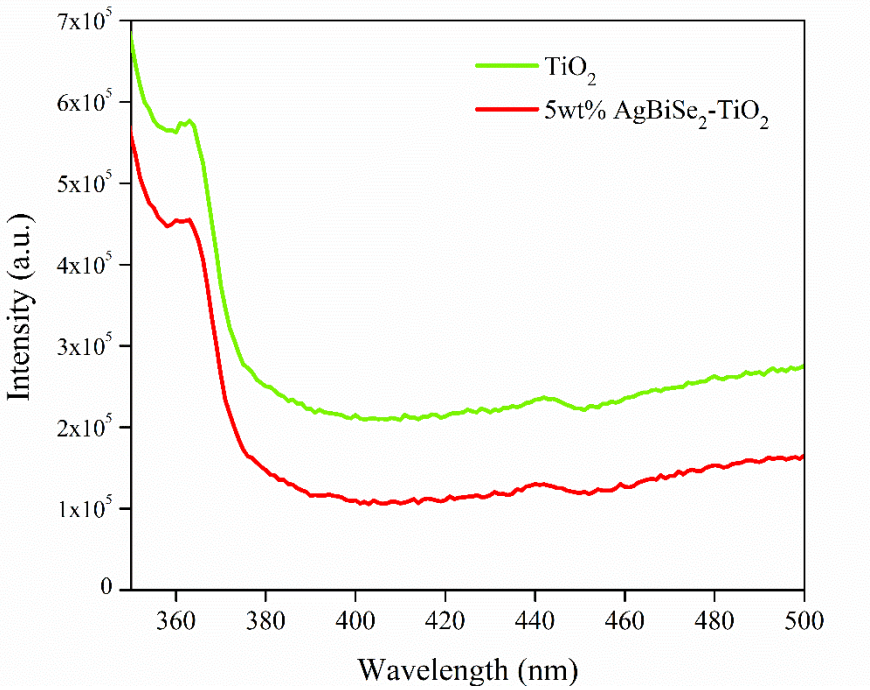

Figure 74. The photoluminescence spectra of TiO_2 and its 5wt% composites with $AgBiSe_2$. Data generated courtesy of Ms. Nisha Padmanabhan.

5.2.8 Photocatalytic H_2 production

In this following section, the results of photocatalytic hydrogen generated for $AgBiSe_2$-TiO_2 was examined at different weight percentage and compared to the results observed for their parent samples. In particular, the possibility to adapt the materials prepared to produce hydrogen through the photocatalytic reforming of an organic species was examined.

As it is clear from the figure displayed below (**Figure 75a**), no catalyst showed hydrogen production in the first 60 minutes of reaction, during which the UVA-component of the light source has been cut off utilizing a proper sodium nitrite filter, as reported in **section 2.6**. After removing the UVA-cut off the filter, the highest value of hydrogen production rate for the $AgBiSe_2$-TiO_2 materials was recorded over a co-catalyst weight percentage of 5 wt %. Overall, increasing values of hydrogen generation were observed with raising the co-catalyst weight percentage, with a remarkable lower value of hydrogen production over the 0.5 wt % $AgBiSe_2$-TiO_2 sample. No hydrogen production was detected at all by adopting bare $AgBiSe_2$ and TiO_2 samples.

As regards to the solution pH (**Figure 75b**), no significant changes have been recorded for the $AgBiSe_2$-TiO_2 samples throughout the reaction, with an average value of 8.5. A moderate decrease was observed as the photoreforming process occurred upon UV-A irradiation. The irradiance values (**Figure 75c**) recorded in the UV range (λ=315÷400 nm) on the external wall of the reactor in the first 60 minutes of reaction are almost negligible due to the presence of the UVA-cut off the filter. After removing the UVA-cut off the filter, an instant increase in the irradiance values has been recorded, which has been followed by a very slight lowering at T=120 min, probably due to the photocatalyst activation resulting into a higher suspension absorption. No significant changes before and after removing the UVA-cut off filter have been observed for the irradiance values collected on the external walls of the reactor in the visible range (λ=400÷1100 nm) at T=60

min (**Figure 75d**). Also, in such wavelength range, a slight reduction in irradiance at T=120 min was observed.

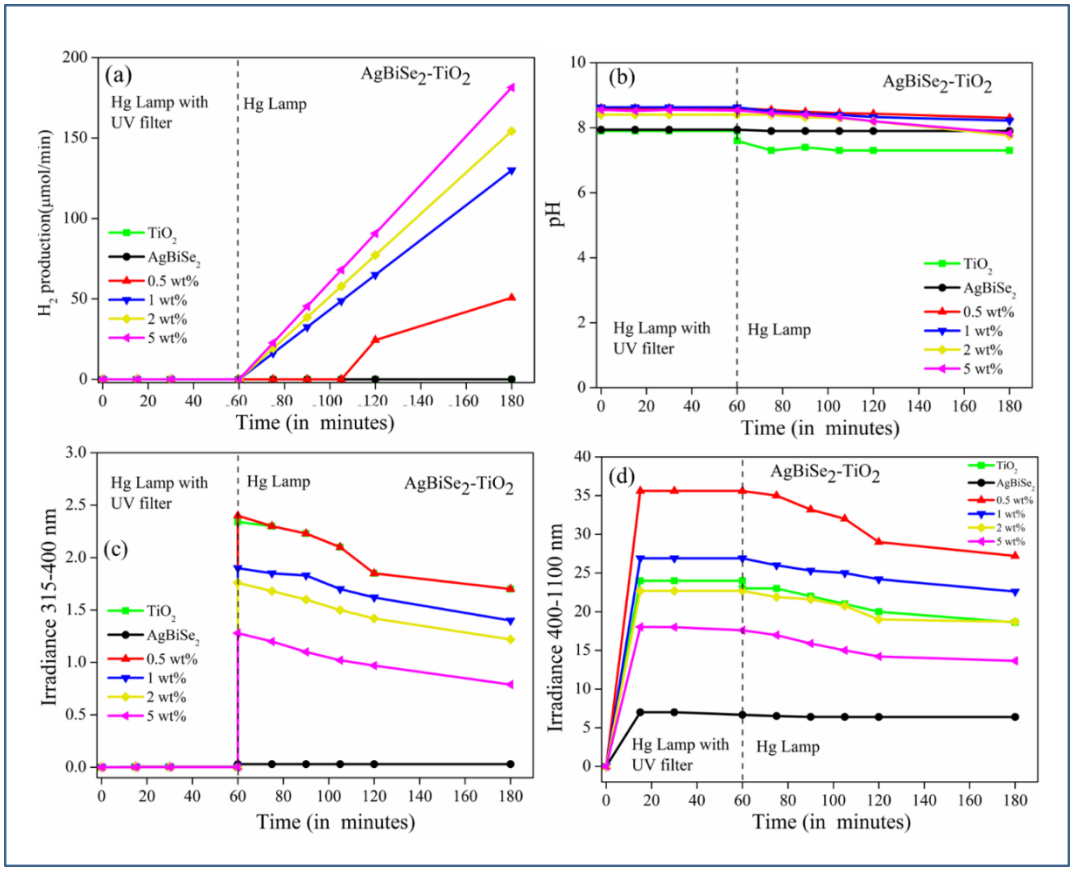

Figure 75. H_2 production rate (a); pH of the solution (b); Irradiance measured on the external walls of the reactor between 315-400 nm (c) and 400-1100 nm (d) at varying weight percentage of $AgBiSe_2$, TiO_2 and $AgBiSe_2$-TiO_2 catalysts. [CH_3OH] =10 vol.%; Catalyst load=500 ppm; T=25°C; P=1atm. Data generated courtesy of Dr. Laura Clarizia.

5.2.9 Photodegradation

Furthermore, to the hydrogen generation study, the composites of $AgBiSe_2$-TiO_2 were examined for Doxycycline degradation. Hence, in this study, the composites of $AgBiSe_2$-TiO_2 were considered for DC degradation at different weight percentage and compared to the results observed for their parent samples. **Figure 76a** displays the change in concentration of DC with time for

$AgBiSe_2$-TiO_2 samples. The samples kept in the dark for 30 minutes did not show any difference in concentration; this proves the significance of light irradiation. On exposure to solar light for a period of 180 minutes displayed a significant reduction in the initial concentration of DC by the composite samples.

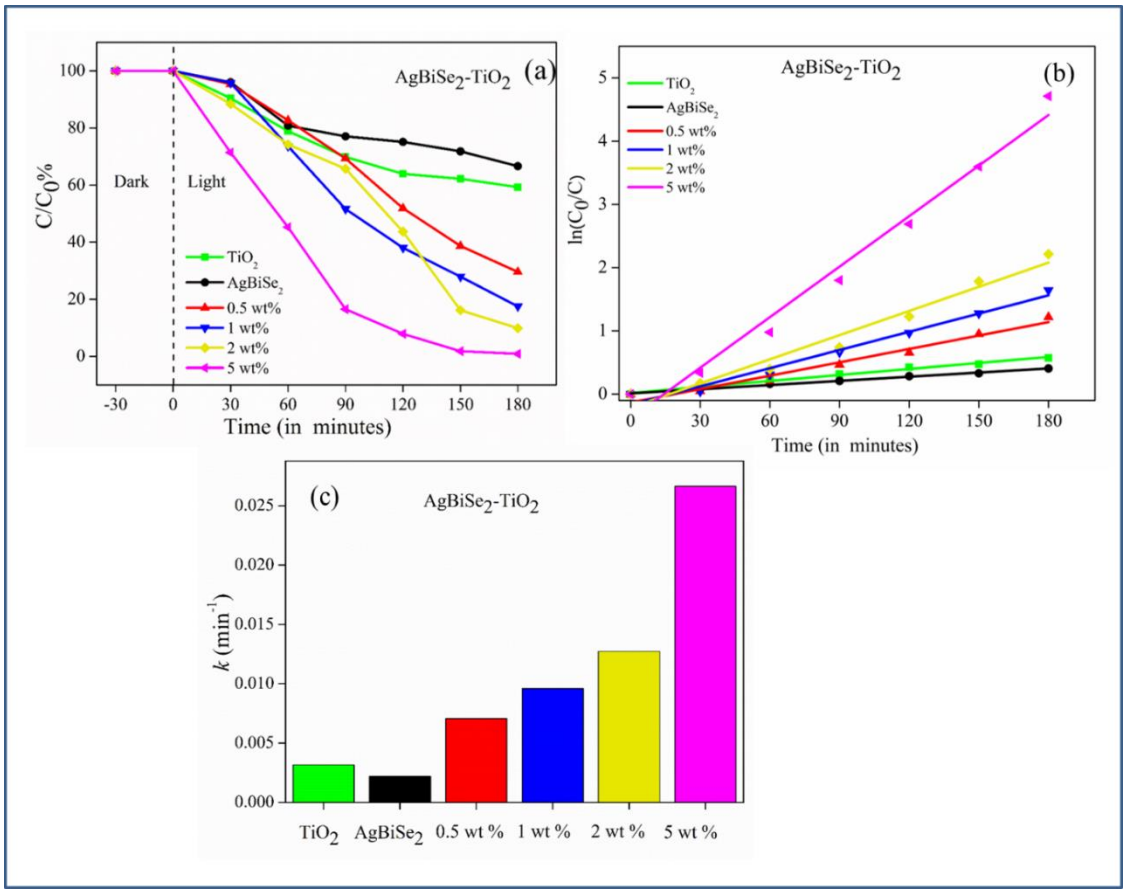

Figure 76. (a) Change in concentration (C/C_0 vs time) of DC; (b) pseudo-first-order kinetic study of DC degradation; (c) Summary of the calculated pseudo-first-order rate constants of $AgBiSe_2$, TiO_2 and $AgBiSe_2$-TiO_2 catalysts.

Parent samples, TiO_2 and $AgBiSe_2$, displayed a degradation percent less than 50%. The increase in the loading of TC in TiO_2 showed gradual improvement in the degradation process. Towards the end, the 2 wt% and the 5 wt% samples displayed a nearly similar trend of 98% degradation. Hence, this

proves the efficiency of the composite formation and the enhanced charge separation built up.

The DC degradation of $AgBiSe_2$-TiO_2 samples observed to follow pseudo-first-order kinetics and can be determined by **equation 39**.[269]

$$Log\frac{C_0}{C_t} = kt \qquad (Equation\ 39)$$

Where C_0 and C_t are the DC concentration (mg/L) at time zero and time '*t*' respectively. '*k*' in the equation is the kinetic rate constant (min^{-1}). **Figure 76b** and **76c** illustrate the kinetics for the DC degradation and summarise the kinetic constants calculated for all the samples, respectively. A straight line was observed for all the cases, and this confirms the presumed pseudo-first-order kinetics. The correlation coefficients (R^2) values for all the samples were found to be more than 0.98. The highest kinetic constant for 5wt % was observed to be 0.02663 min^{-1}, and the least was observed for $AgBiSe_2$ (0.00316 min^{-1}).

The recyclability of the catalyst and its effectiveness was evaluated through the cyclic studies (**Figure 77a**). The 5 wt% composite samples displayed similar results all the time with a slight decline in the degradation efficiency by the end of the fifth cycle. To ascertain the reactive oxygen species (ROS) participating in the degradation process, the scavenging experiments were performed (**Figure 77b**).

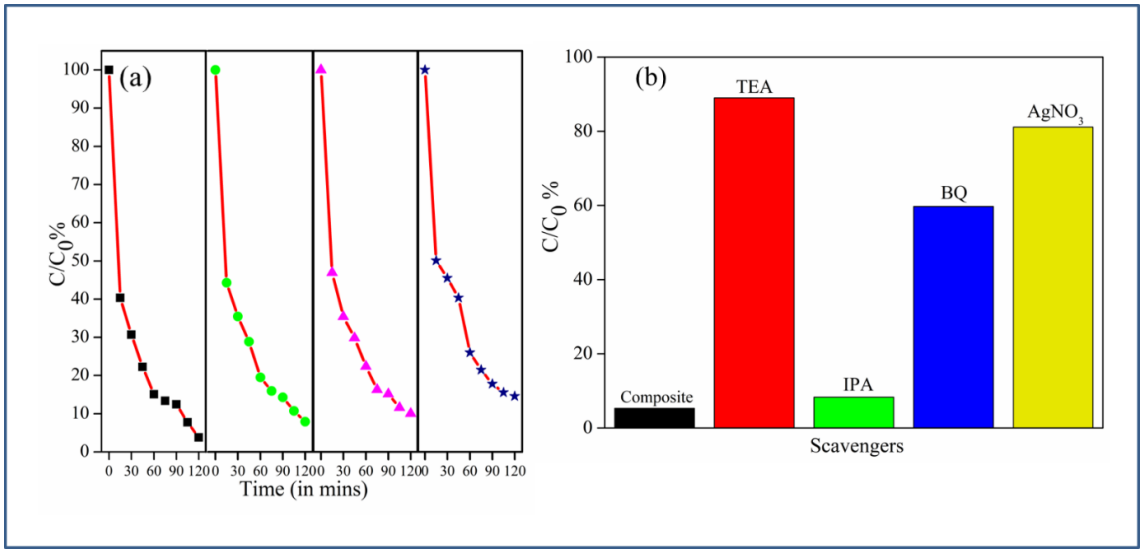

Figure 77. (a) Recyclability profile; (b) scavenging experiment results for 5 wt% $AgBiSe_2$-TiO_2.

The use of triethanolamine and silver nitrate showed a severe dampening of the degradation efficiency. Thus, holes and electrons were found to be the significant ROS in the DC degradation process. On the other hand, a small portion of the decline in activity was observed in the presence of benzoquinone. Thus, superoxide radicals also had an effective share in the degradation process. The hydroxyl radicals necessarily did not show any contribution, as observed by the addition of the IPA in the reaction mixture.

5.2.10 Photocatalytic antimicrobial studies

In this study, a gram-negative (*E. coli*) and a gram-positive (*S. aureus*) bacterium are chosen as a modal microorganism to evaluate the efficacy of the composites and compare their results with their parent samples. The best composite samples from the previous two applications (5 wt%) and the pristine samples of $AgBiSe_2$ and TiO_2 are studied. **Figure 78a** and **78b** display the change in the number of bacteria grown over 120 minutes of light irradiation. The log reduction profiles are shown in **Figure 78c**.

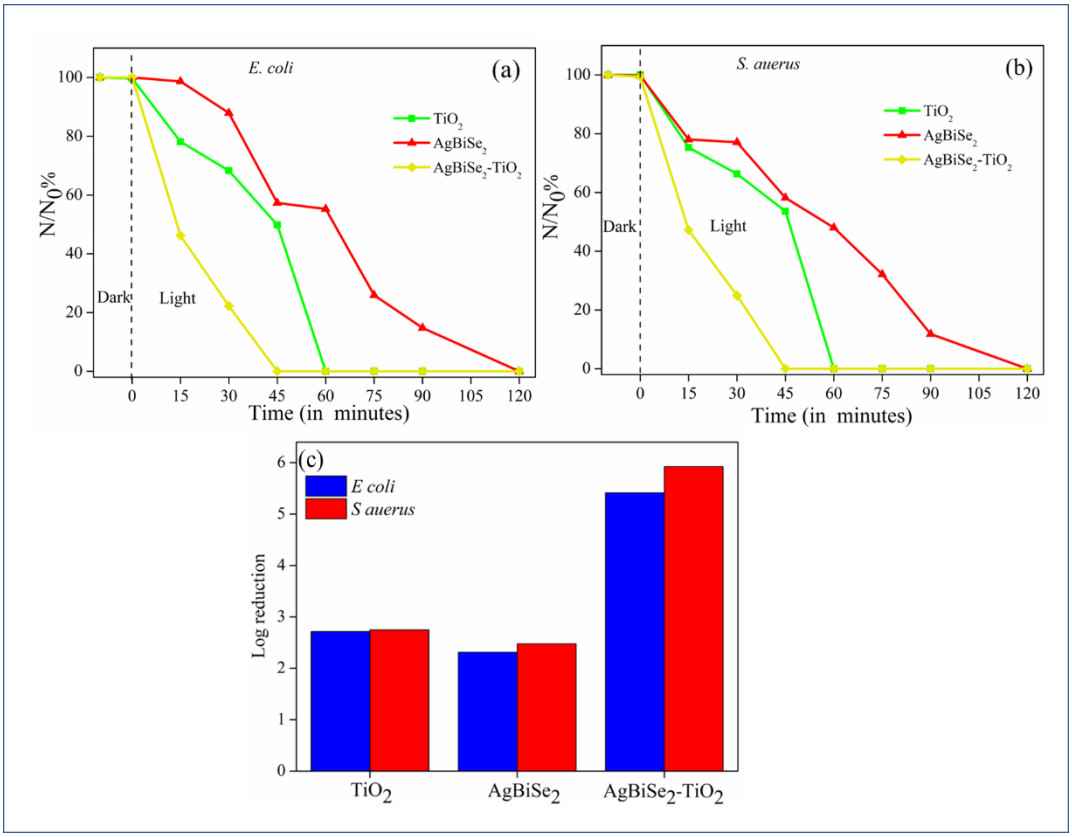

Figure 78. Photocatalytic inactivation of (a) *E. coli* and (b) *S. aureus* with TiO_2, $AgBiS_2$ and 5wt% $AgBiS_2$-TiO_2.

The dark experiment conducted displayed no change in the numbers, and this limits the possibility of dark inactivation caused due to the presence of a catalyst. In the case of *E. coli* inactivation, complete death of the bacteria was observed within 45 minutes of solar light illumination by $AgBiSe_2$-TiO_2 composite. A similar result was also displayed in the case of *S. aureus*, where all the colonies ceased to exist. An approximate log 6 and log 5 reduction in bacterial growth was observed in the case of $AgBiSe_2$-TiO_2 composite (**Figure 78c**). The pristine TC samples required nearly 120 minutes to display complete inactivation. The change in bacterial density grown on agar plates before and after illumination with $AgBiSe_2$-TiO_2 composite for both the bacterial strains are presented in **Figure 79**, respectively.

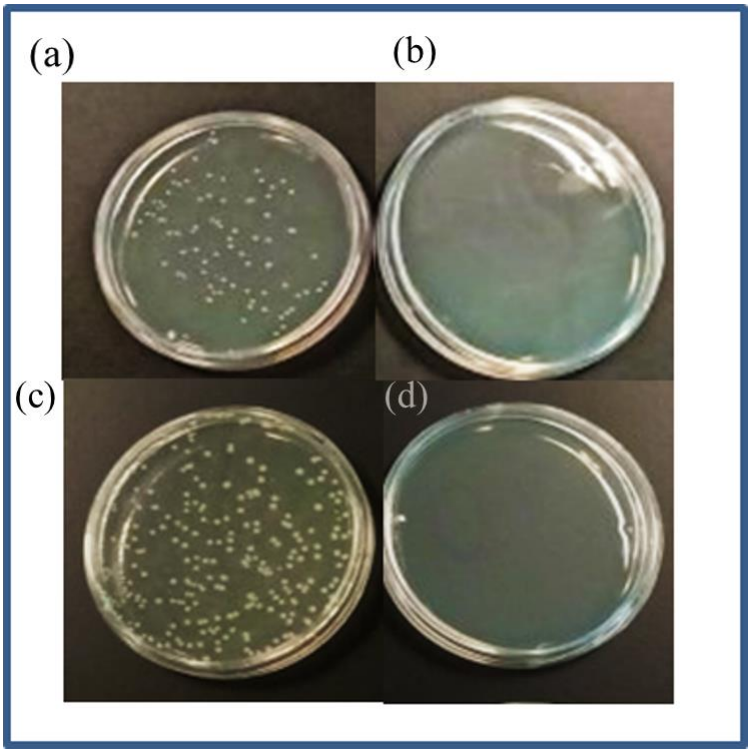

Figure 79. Images of (a) *S. aureus* colonies and (b) *E. coli* colonies change in bacterial density grown on agar plates before and after illumination with 5wt% $AgBiSe_2$-TiO_2.

Thus, the $AgBiSe_2$-TiO_2 composites displayed superior inactivation performance. The bacterial inactivation mechanism is established in previous other literature. Disruption of the cellular membrane due to potential attack by ROS generated during the irradiation process results in the leakage of cellular components and results to the cause of inactivation.[182]

5.3 PHOTOCATALYTIC MECHANISM

The photocatalytic results of the AgB**i**Se_2-TiO_2 displayed enhanced hydrogen generation, impressive degradation efficiency as well as antimicrobial properties compared to their pristine parent samples. The structural analysis displays the stability of the hexagonal phase of $AgBiSe_2$ and the tetragonal crystal structure of anatase, which corroborated to the experimental observations. The computational analysis of titania and TC were crucial to

comprehend the electronic and optical properties. The results from XPS analysis demonstrates the shift in the binding energies of both the composite structures to lower energies. This highlights the strong interaction between the pristine titania and TC.

On the other hand, the peaks of Ti^{4+} state displayed a small shift to lower binding energy, which is ascribed to the influence of TC. The peak value also confirms the absence of any oxygen vacancies and reiterates the anatase structure and positive heterojunction formation. The band gap estimation and the electronic properties aided in summarising the band edge values for $AgBiSe_2$ and TiO_2 (as given in **Table 20**). A prospective electron-transfer mechanism is proposed to understand the improved photocatalytic results displayed by the composites architectures.

Visible light irradiation on $AgBiSe_2$-TiO_2 composites results in the electrons to jump from the upper VB of Ag 4*d* and Se 4*p* states to the lower CB of Bi 6*p* and Se 4*p* states of $AgBiSe_2$ respectively and further travel to the O 2*p*-orbitals of titania. The improved photocatalytic activity by the $AgBiSe_2$-TiO_2 composites could be described *via* conjecturing the formation of *p*-*n* heterojunction.[276, 277] The band edge positions of TiO_2 and $AgBiSe_2$ before and after having contact are shown in **Figure 80**. The Fermi level (E_f) of *n*-type TiO_2 is present slightly below the E_{CB} of TiO_2, and the E_f of *p*-type $AgBiSe_2$ is slightly higher than the E_{VB} of $AgBiSe_2$ (**Figure 80a**).[272, 273] As the *p*-*n* junction is created, the Fermi levels of both the semiconductors align themselves to a new uniform level. Since the dopant amount in case of $AgBiSe_2$ is low, therefore the Fermi level of $AgBiSe_2$ bring into line with TiO_2 (-0.1 eV). This results in the formation of *p*-*n* heterojunction in the interface. The new band alignment as shown in **Figure 80b** displays the flow of the electrons present in the CB potential of $AgBiSe_2$, transfers to the more negative CB of TiO_2 resulting in a negative charge accumulation in the CB of TiO_2. Similarly, the diffusion of the holes from the VB of TiO_2 to the VB of $AgBiSe_2$ results in positive charge accumulation. Hence, the equilibration of the Fermi levels of both the

semiconductors results in the creation of an internal electric field.[269] Therefore, the resultant electric field prohibits the charge recombination in the junction and thereby improving the charge separation. The electrons and holes accumulated at the VB of $AgBiSe_2$ and CB of TiO_2 respectively participate in the oxidation and reduction processes.[276, 277] The scavenging results, as shown in **section 5.2.7**, shows the contribution of both electrons and holes to be dominant, which explains the improved photocatalytic results observed for all the three different applications.

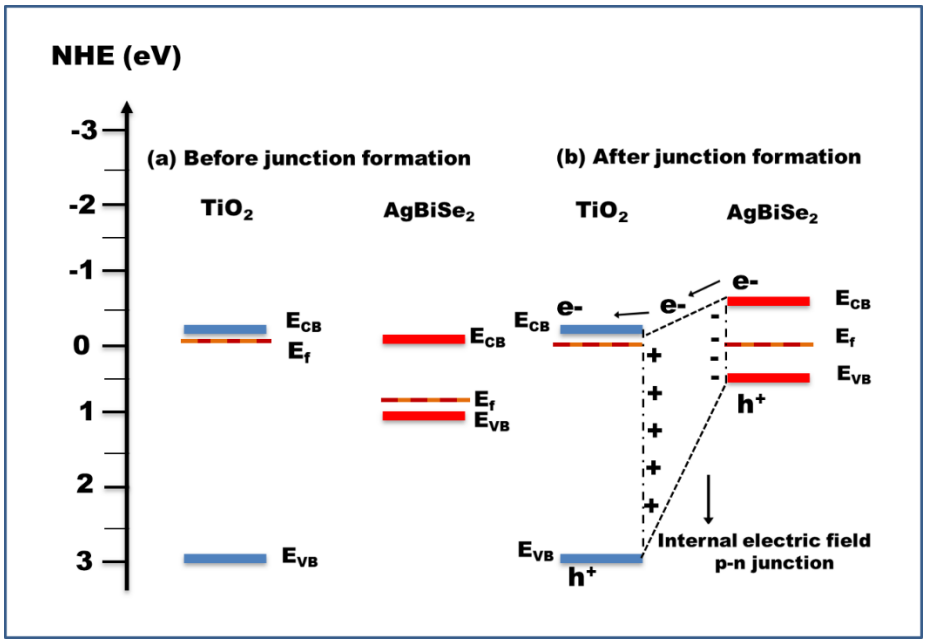

Figure 80. a) Band alignment of *p*-type $AgBiSe_2$ and *n*-type TiO_2 before junction formation and b) band alignment and the photocatalytic mechanism of $AgBiSe_2$-TiO_2 *p–n* nano-heterojunctions.

5.4 Conclusions

In this study, $AgBiS_2$-TiO_2 using a one-pot solvothermal technique was synthesised. The as prepared composite structure with a small dopant level was efficient in improved visible light absorption. The band gap of the composites decreased with the increase in the dopant levels. Moreover, the XPS analysis demonstrated the shift in the peaks corresponding to the change

in the local environment of the composite structure. The degradation results of the composites showed improved efficacy. Similarly, a significant improvement for the light induced hydrogen generation is also observed. A log 3 bacterial reduction was attained within 30 minutes of visible light illumination. A plausible mechanistic understanding is proposed based on computational analysis, scavenger experiments and the band gap values derived from the DRS plot. Thus, the present study demonstrated the successful formation of heterostructure and details the multifunctional applications.

CHAPTER 6

THEORETICAL AND COMPUTATIONAL INVESTIGATION OF VISIBLE LIGHT RESPONSIVE $AgInSe_2$-TiO_2 HETEROJUNCTIONS FOR PHOTOCATALYTIC APPLICATIONS

6.1 INTRODUCTION

Materials with semiconducting properties are not enough for photocatalytic applications. But modifying the design to efficiently improve the interfacial charge transfer and reducing the rate of recombination is the critical feature. Numerous measures such as band-gap modulation, defect formation, dimensionality alteration, pore texture alteration, surface sensitization, heterojunction creation *etc.* are attempted to reduce the recombination rate and enhance the visible light absorption.[91, 226]

Amid all, $AgInSe_2$ (I-III-VI), a ternary semiconductor crystallises exists mostly in 2 different crystalline phases. The thermodynamically stable tetragonal phase (space group I42D), which transitions into a metastable orthorhombic phase at a higher temperature (space group Pna21).[28, 278]

$AgInSe_2$ based composites have displayed numerous applications.[279, 280] Chen e*t al.* reported the deposition of $AgInSe_2$ nanoparticles onto TiO_2 films for solar cell application. The films of the composite displayed a significant increase in efficiency.[281] In a different study, Li *et al.* reported the synthesis of functionalised quantum dots with varying types of organic molecules. The functionalised quantum dots displayed potential applications as light harvesters in quantum dot sensitised solar cell (QSSC).[282] In a more recent report, Kshirsagar *et al*. reported the composite of $AgInSe_2$ nanoparticles with

TiO_2 for photocatalytic dye degradation. The $AgInSe_2$ nanoparticles were synthesised using microwave and thermal irradiation. The composite displayed enhanced degradation result compared to their parent samples.[283] Thus, this shows the enormous potential of these novel composites and ushers the importance of their untapped potential for various other applications.

Hence, in this study, a new novel composite of $AgInSe_2$-TiO_2 is prepared using a facile two-step synthesis technique. Compared to other synthesis procedure, the reported synthesis method is inexpensive and evades any kind of complicated deposition or precursor injection methods. This study provides a direction for optimising the process conditions such as the time and temperature of the solvothermal synthesis. Composites of titania with TC are formed at different weight ratios (0.5, 1, 2, 5 wt %). The as prepared composites are analysed using structural, elemental and morphological characterisation techniques. Furthermore, the efficiency of these composites is studied using three different photocatalytic applications; hydrogen generation, Doxycycline (DC) degradation and antimicrobial disinfection. The results of all the characterisations and the applications are compared to their parent nanostructures.

The synthesis process and the process optimisation of the composites are explained in **section 2.2**.

6.2 RESULTS AND DISCUSSION

6.2.1 Structural Properties

After the structural optimization, the space groups of anatase TiO_2 and $AgInSe_2$ were found to be $I4_1/amd$ (space group number: 141) and $I\bar{4}2d$ (space group number: 122). TiO_2 and $AgInSe_2$ were found to crystallize into a body centred tetragonal crystal system upon relaxation. The lattice parameters and volume of the two compounds obtained after structural optimization are tabulated in **Table 23**, and the optimized structures are

presented in **Figure 81** and **Figure 82**. The lattice parameters of these compounds obtained after structural optimization are consistent with the reported ones and are well within the expected error range when compared to the experimental values observed in **section 6.2.3**.[157, 263, 264] Octahedral molecular geometry connects Ti and O in the case of anatase TiO_2. These octahedra are connected to each other by edge sharing at the centre of the unit cell and corner sharing elsewhere in the unit cell. There are two different Ti-O bond lengths present in the compound. The in-plane Ti-O bond length was found to be 1.94 Å and the out-of-plane Ti-O bond length was 2.00 Å which are well consistent with the ones that could be obtained from the literature.[157, 262]

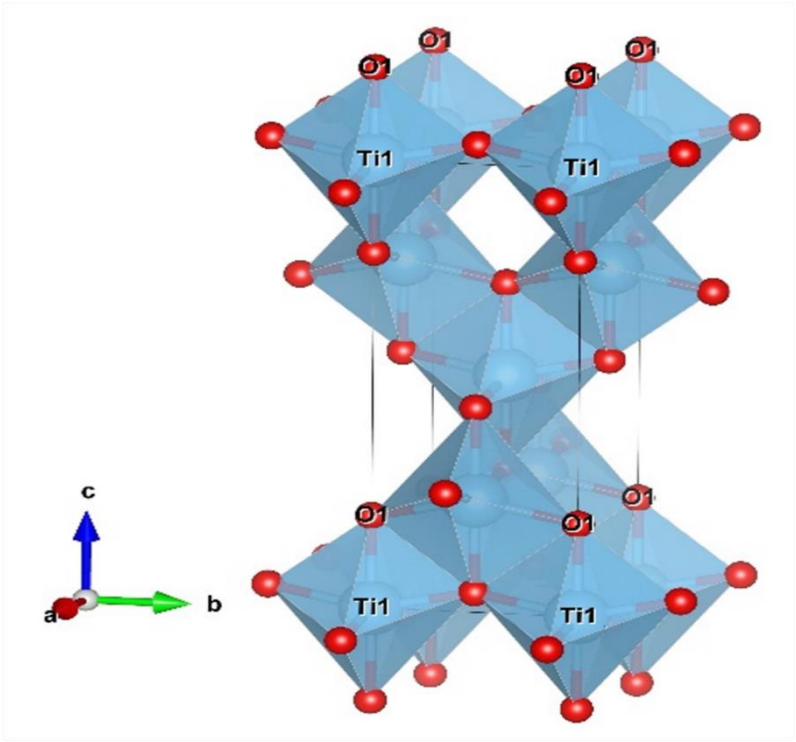

Figure 81. (Colour online) The optimised structures of TiO_2. Data generated courtesy of Dr. Syam Kumar.

In the case of $AgInSe_2$, In and Se are connected to each other in a tetrahedral molecular geometry. These tetrahedra are connected to each other through corner sharing, and Ag are found to occupy the interstitial sites of these

tetrahedra. In-Se bond lengths are isotropic in this compound and yields a value of 2.65 Å.

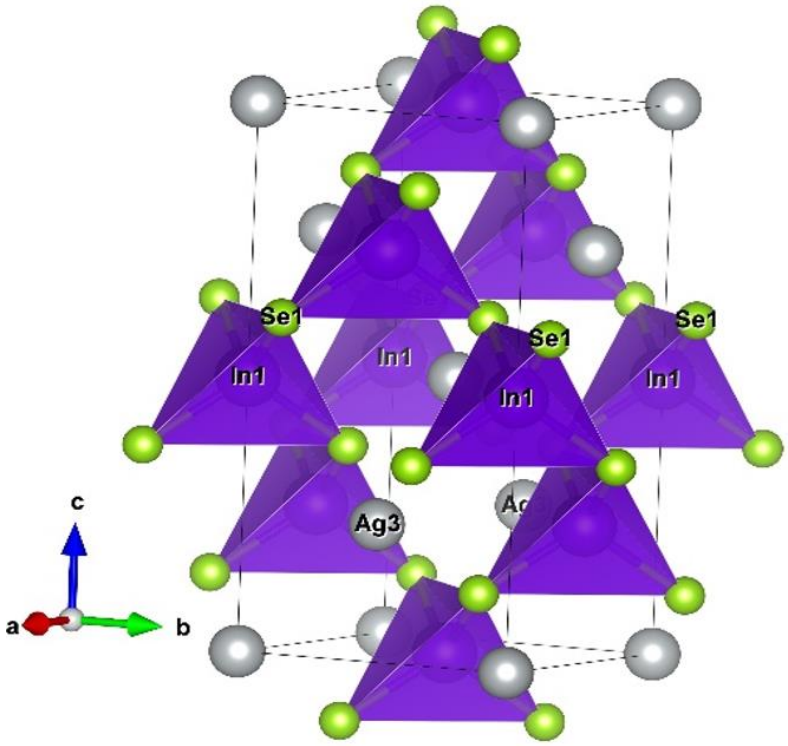

Figure 82. (Colour online) The optimised structure of $AgInSe_2$. Data generated courtesy of Dr. Syam Kumar.

Table 23: The DFT optimised lattice parameters of TiO_2 and $AgInSe_2$ and the percentage deviations from the observed experimental values.

Compound	Parameter	a(Å)	b(Å)	c(Å)	V(Å^3)	α(°)	β(°)	γ(°)
TiO_2	Experimental	3.78	3.78	9.43	135.06	90.00	90.00	90.00
	DFT	3.80	3.80	9.75	141.10	90.00	90.00	90.00
	Deviation (%)	0.53	0.53	3.26	4.47	0.00	0.00	0.00
$AgInSe_2$	Experimental	6.41	6.41	12.25	504.54	90.00	90.00	90.00
	DFT	6.21	6.21	12.04	465.07	90.00	90.00	90.00

	Deviation (%)	-3.16	-3.16	-1.72	-7.82	0.00	0.00	0.00

6.2.2 Electronic properties

The HSE has been used to study the electronic properties of materials. Anatase TiO_2, its band structure and its corresponding partial density of states (PDOS) are presented in **Figure 83**. Ti *d*-orbitals dominate the lower CB while the O *p*-orbitals are found to dominate the upper VB of TiO_2. The HSE06 calculation returns the bandgap of 3.35 eV for TiO_2, which is consistent with the experimentally observed value (**Section 6.2.4**) and in the reported literature.[157, 262] Anatase TiO_2 is an indirect bandgap material with its CBM positioned at the centre of the Brillouin zone, Γ and the VBM between P and Y.

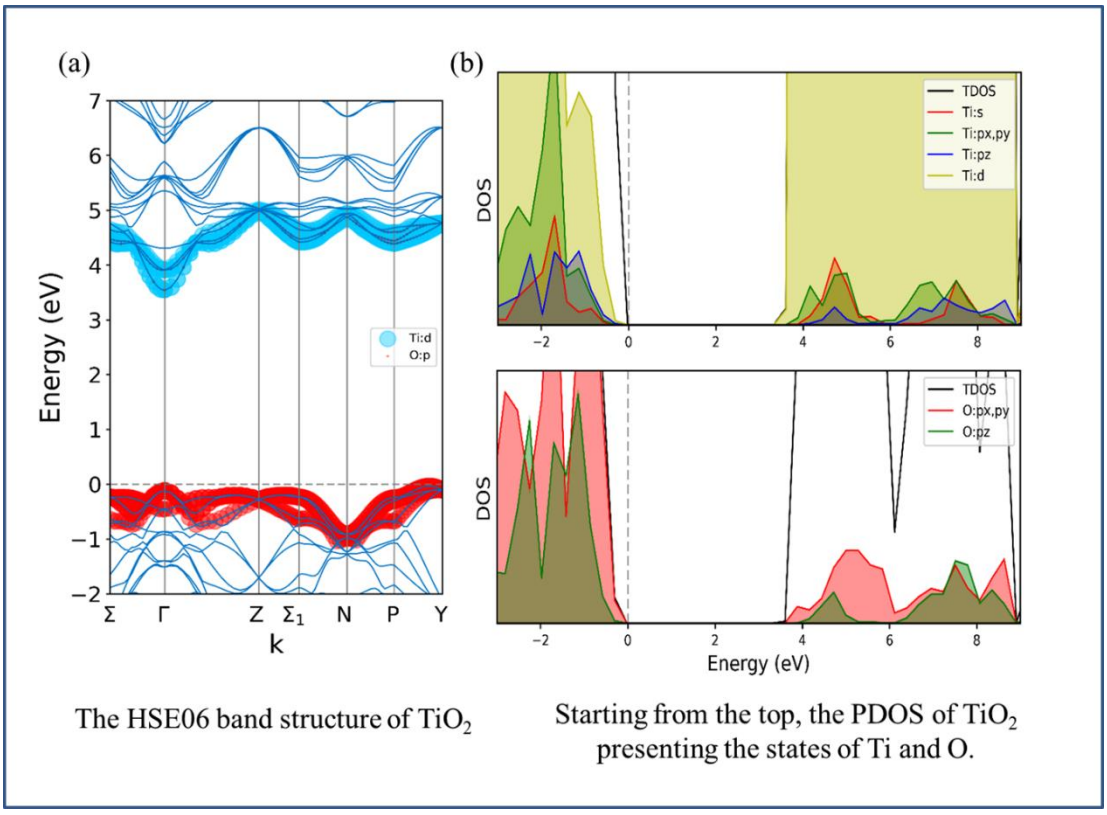

Figure 83: (Colour online) The HSE06 (a) band structure and (b) PDOS of anatase TiO_2. The PDOS plot is split into two to describe the Ti and O states

separately. Ti 3*d* states are clearly dominating the lower CB while the O $2p_x$ and $2p_y$ states are dominating the upper VB. Data generated courtesy of Dr. Syam Kumar.

$AgInSe_2$, in its tetragonal lattice, is found to have an HSE06 bandgap of 1.2 eV, which matches the reported values in the literature.[264, 284] The electronic structure and the PDOS of $AgInSe_2$ are shown in **Figure 84**. $AgInSe_2$ is a direct bandgap material at Γ. Interestingly, Ag 4*d* states and Se 4*p* states dominate the upper VB while In 5*s* and Se 4*p* states contribute to the lower CB of $AgInSe_2$.

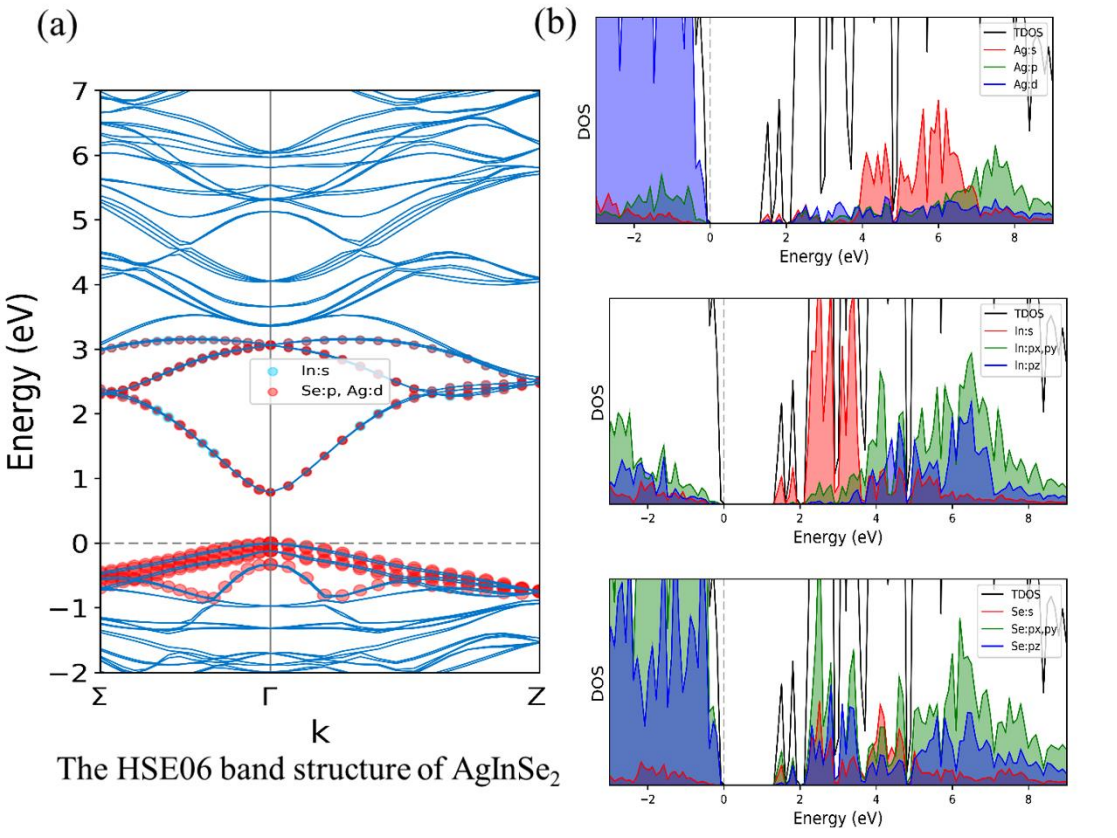

The HSE06 band structure of $AgInSe_2$

Starting from top, the PDOS of $AgInSe_2$ presenting the orbital contribution of Ag, In and Se.

Figure 84: (Colour online) The HSE06 (a) band structure and (b) PDOS of anatase $AgInSe_2$. The PDOS plot is split into two to describe the Ag, In and Se states separately. Ag 4*d* and Se 4*p* states dominate the upper VB while the Se 4*p* and In 5*s* states are dominating the lower CB. Data generated courtesy of Dr. Syam Kumar.

The band edge values of TiO_2, and $AgInSe_2$ are presented in **Table 18**. The reference scale was NHE which keeps the hydrogen evolution reaction (HER) potential at 0 eV and the oxygen evolution reaction (OER) potential at 1.23 eV. Looking into the band edge positions of the pristine compounds, it could be observed that $AgInSe_2$ could aid the HER and $AgBiSe_2$ as its own fails to aid either of the reaction paths.

Table 24. The band edge positions obtained experimentally and using HSE06 calculations for the pristine TiO_2 and $AgInSe_2$.

Compound	Determination	Valence Band Edge (eV)	Conduction Band Edge (eV)
TiO_2	HSE06	2.98	-0.36
	Experimental	2.90	-0.29
$AgInSe_2$	HSE06	0.772	-0.423
	Experimental	0.816	-0.514

6.2.3 Synthesis and structural analysis by X-ray diffraction

$AgInSe_2$ nanoparticles were synthesised using a solution-based technique. Ethanolamine was used as the solvent for the solvothermal synthesis. Amine based solvent usually lowers the temperature for thermal decomposition of the precursors and aid in the formation of nanoparticles at a lower temperature.[266] They are often used as a potential reagent for anisotropic growth of nanoparticles as well as surfactants for a possible stabilising

agent.[28] At the start, the Ag^{+} and In^{3+} ions react with the solvent molecules (ethanolamine) to form a covalent complex as given below (where x and y are positive integers).[190, 191]

$$AgNO_3 + xEA \rightarrow Ag(EA)_x^+ + NO_3^- \text{ (Equation 40)}$$

$$In(NO_3)_3 + yEA \rightarrow In(EA)_y^{3+} + 3NO_3^- \text{ (Equation 41)}$$

Furthermore, the silver complexes react with the Se^{2-} ions to form binary compound; [192]

$$Ag(EA)_x^+ + Se^{2-} \rightarrow Ag_2Se + xEA \text{ (Equation 42)}$$

Bai *et al.* had previously explained that the initial species formed in the process are the orthorhombic phase of Ag_2Se spherical nanoparticles.[267] The fluid-like nature of the silver and fast conducting behaviour of silver chalcogenides result in the creation of various cationic vacancies in the orthorhombic crystal structure. This results in fast diffusion of In^{3+} ions to form heterostructures of $AgInSe_2$-Ag_2Se, respectively. As the synthesis progresses, the diffusion phenomenon continues, until all the Ag_2Se seeds are exhausted. This could also be observed in the temperature and the time study graphs of the TC (**Figure 85**).

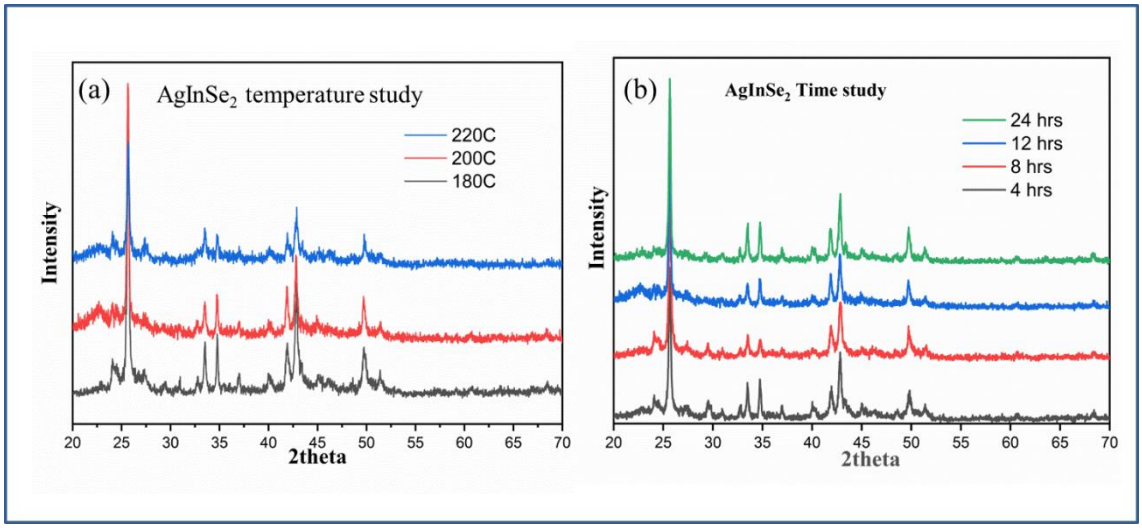

Figure 85. The XRD patterns of the solvothermal (a) temperature study for 12 h and (b) time study at 200 ˚C of $AgInSe_2$.

The peaks of Ag_2Se are present at lower reaction time and temperature, and as the reaction progresses the intensity of the peak starts to diminish, leaving a residue of a small percent of impurity.[28, 267, 268]

$$Ag_2Se + In(EA)_y^{3+} \rightarrow AgInSe_2 + yEA \quad \text{(Equation 43)}$$

Ethanolamine (EA), with a single amine and N-chelating atom, act as a potential structure directing agent.[189] The inbuilt pressure and the appropriate temperature supports the formation of unique phases and morphology.

$AgInSe_2$ nanoparticles and the composites with titania are examined using X-ray diffraction. Formation of tetragonal phase of $AgInSe_2$ nanoparticles are observed in **Figure 85a** and **85b** [ICDD card no: 04-010-1589 and 00-035-1099]. The influence of the solvothermal duration and the temperature to identify the optimised experimental parameters were also done (**Figure 85**). As observed, the intensity (100%) of the peaks at 25.68° for $AgInSe_2$ are found to be sharp and well defined. This infers the formation of crystalline structures at 200 °C and 12 h of solvothermal duration. Hence 200 °C and 12 h is the optimal temperature and time for the synthesis process and

henceforth used for composite preparation with titania nanoparticles. The sol-gel synthesis of TiO_2 and its further calcination at 500 °C leads in the formation of the anatase phase. Defined peaks at 25.1° corresponding to the tetragonal structure of the anatase phase are observed [ICDD card no: 00-021-1272]. The lattice parameter of the parent samples were estimated to be; tetragonal crystal structure of $AgInSe_2$ displayed a = b = 6.41 Å, c = 12.25 Å and α = β = γ = 90°. Pristine titania [tetragonal phase] have lattice parameter estimated to be a = b = 3.71 Å, c = 9.43 Å and α = β = γ = 90°. These values are similar to the values obtained through the computational study, as explained in **section 6.2.1**. **Table 25** summarises the lattice parameters experimentally calculated with the reported values in literature.

Table 25**.** Summarised lattice parameters of TiO_2 and $AgInSe_2$.

Compound	Parameter	a(Å)	b(Å)	c(Å)	α(°)	β(°)	γ(°)	**Ref**
TiO_2	Experimental	3.78	3.78	9.50	90.00	90.00	90.00	
	From Literature	3.80	3.80	9.60	90.00	90.00	90.00	188
$AgInSe_2$	Experimental	3.71	3.71	9.43	90.00	90.00	90.00	
	From Literature	3.79	3.89	9.48	90.00	90.00	90.00	31

Figure 86 further displays the composites prepared at various weight ratios. Peaks at 25.1° of titania in the anatase phase are observed for all the composite structures irrespective of the weight ratios. The broadening of the peaks demonstrates that the crystalline size of the sample is minimal. Peaks of TC are not observed prominently in any of the diffractograms. The incorporation of TC in minimal weight ratios and the crystalline nature of the titania nanoparticles makes it difficult to follow any distinct peaks of TC in the diffractograms. Furthermore, it also validates that the structure of TiO_2 remains unaltered even after the solvothermal reaction for the composite formation.

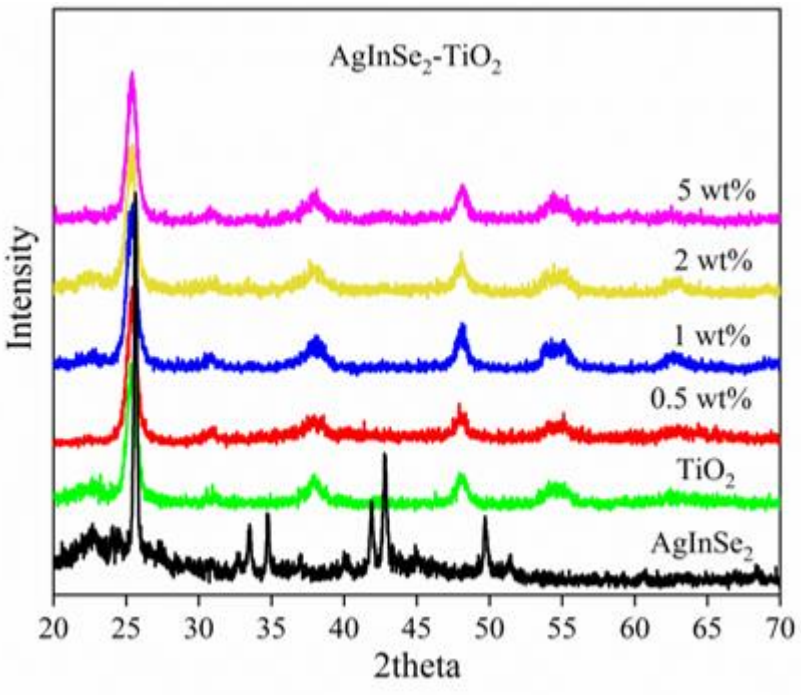

Figure 86. The XRD patterns of $AgInSe_2$, $AgInSe_2$-TiO_2 composites.

6.2.4 Absorption properties

UV-vis DRS measurements were taken of the as prepared samples to study their light absorption characteristics. As shown in **Figure 87**, the pristine TiO_2 displays its signature absorption at 320 nm in the UV region, and the absorption edge steeps at 400 nm. **Figure 87** also shows the absorption spectra of the $AgInSe_2$-TiO_2 composites. All the samples carried the signature profile of titania. In contrast, an increase in the content of the TC in the prepared sample, resulted in an increase in absorption in the visible region as defined by its parent $AgInSe_2$ (**Figure 88b**).[267] This was further reflected in the change in the colour of the samples, varying from white to brown and further black. This demonstrated the coupling of TC with titania to construct $AgInSe_2$-TiO_2 composites.

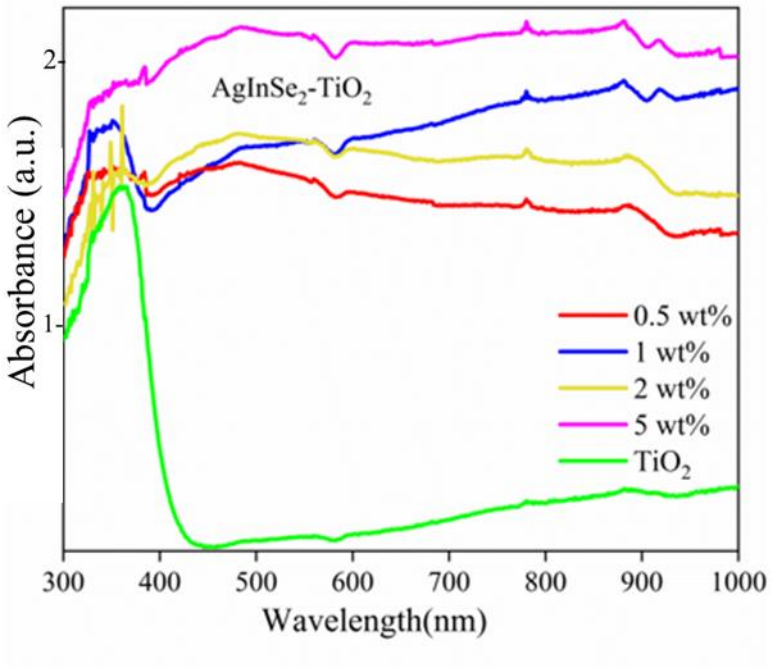

Figure 87. The absorption patterns of (a) TiO_2, and $AgInSe_2$-TiO_2 composites.

The effect of the TC addition to TiO_2 could be detected by the changes in the band gap of the composite sample. The Kubelka-Munk (K-M) function is utilised to convert the functionality to energy (**Figure 88a** and **88b**).[269]

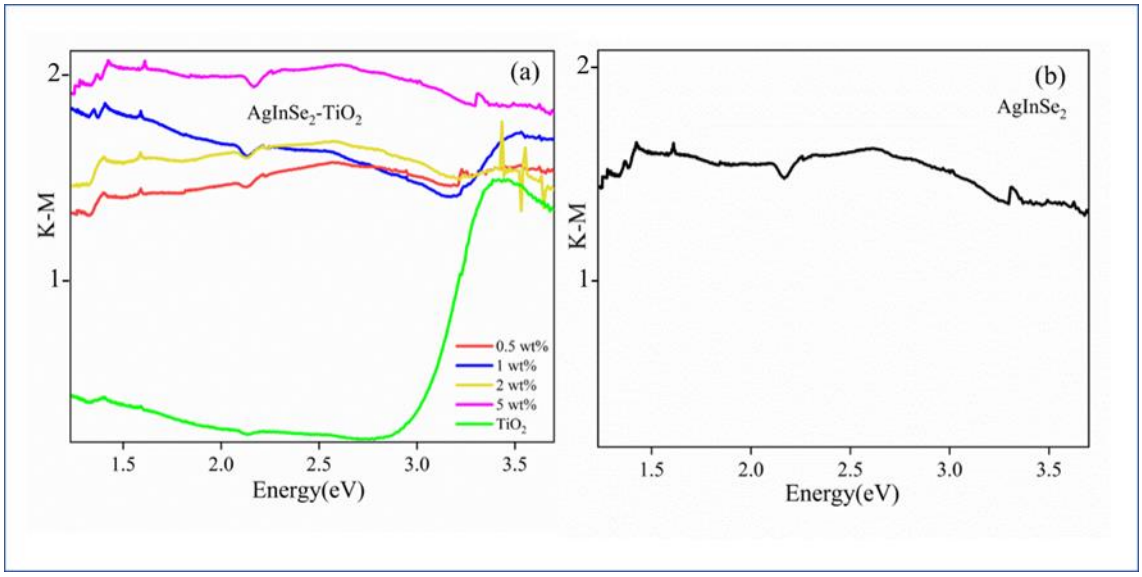

Figure 88. The Tauc plots of (a) TiO_2, $AgInSe_2$-TiO_2 composites and (b) $AgInSe_2$.

The band gap of the pristine TiO_2 sample was estimated to be 3.2 eV, while the parent TC samples showed 1.33 eV for $AgInSe_2$. The values obtained are very close to the computationally calculated values, as explained in **section 6.2.2**. The band gap of the composite samples showed minimal or even no changes in value with the increase in the content of TC (**Figure 89**). **Table 26** tabulates the band gap value of all the samples.

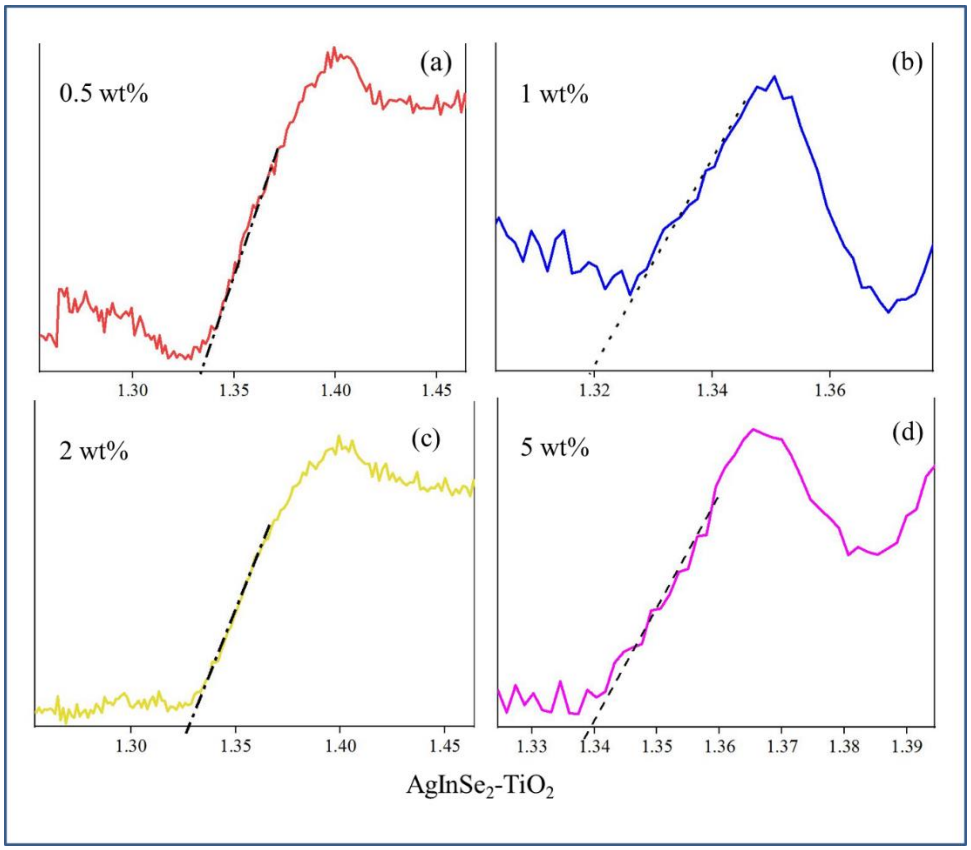

Figure 89. The Tauc plots of $AgInSe_2$-TiO_2 composites.

Table 26. Band gap values of TiO_2 and $AgInSe_2$-TiO_2 composites.

Sample	**TiO_2**	**$AgInSe_2$**	**0.5 wt%**	**1 wt%**	**2 wt%**	**5 wt%**

Band gap (eV)	3.20	1.33	1.34	1.32	1.32	1.34

The strong interaction of the composite samples results in increased interfacial charge transfer and the decrease in the band gap. The computational analysis of the optical and the electronic properties of the parent samples shows that the band edge of the parent $AgInSe_2$ displayed the contribution of Ag 4*d* states and Se 4*p* states which dominated the upper VB while In 5*s* and Se 4*p* states contributed to the lower CB of $AgInSe_2$. Whereas TiO_2 displayed a contribution from Ti 3*d*-orbitals in the lower CB while the O 2*p*-orbitals are found to dominate the upper VB. Hence, the composite samples have a combined influence of the parent samples, which is observed experimentally in the enhanced absorption edge as well as the decreased band gap values. This infers the positive hybridisation of the parent samples and construction of heterostructure composites.[234, 270] The 5 wt% composite of the TC displayed the best photocatalytic results. Hence, here onward only this composite is assessed for their morphological and elemental analysis along with their pristine parent samples unless otherwise stated. **Table 27** summarises the experimentally attained band gap value and the reported values in literature.

Table 27. Band gap values of TiO_2 and $AgInSe_2$-TiO_2 composites.

Sample	Band gap (eV)	From Literature	Band gap type	Ref
TiO_2	3.18	3.20	Indirect	[248]
$AgInSe_2$	1.33	1.25	Direct	[31]

6.2.5 XPS Analysis

The elemental states and the chemical composition of the prepared pristine parent and the composite samples were investigated by XPS measurements.

The survey scans of TiO_2, $AgInSe_2$ and $AgInSe_2$-TiO_2 are displayed in **Figure 90**. Peaks of Ti 2*p* and O 1*s* are found for TiO_2, while $AgInSe_2$ displayed peaks of Ag 3*d,* In 3*d* and Se 3*d*. The composite samples showed all the combined peaks of the parent samples. In all the samples, a small percentage of C 1*s* and O 1*s* peaks were observed, these impurity peaks were acquired during the synthesis and the characterisation process. To further investigate the charge transfer at the heterojunction interface between TiO_2 and the TC nanoparticles, the high resolution XPS of the composites were also examined.

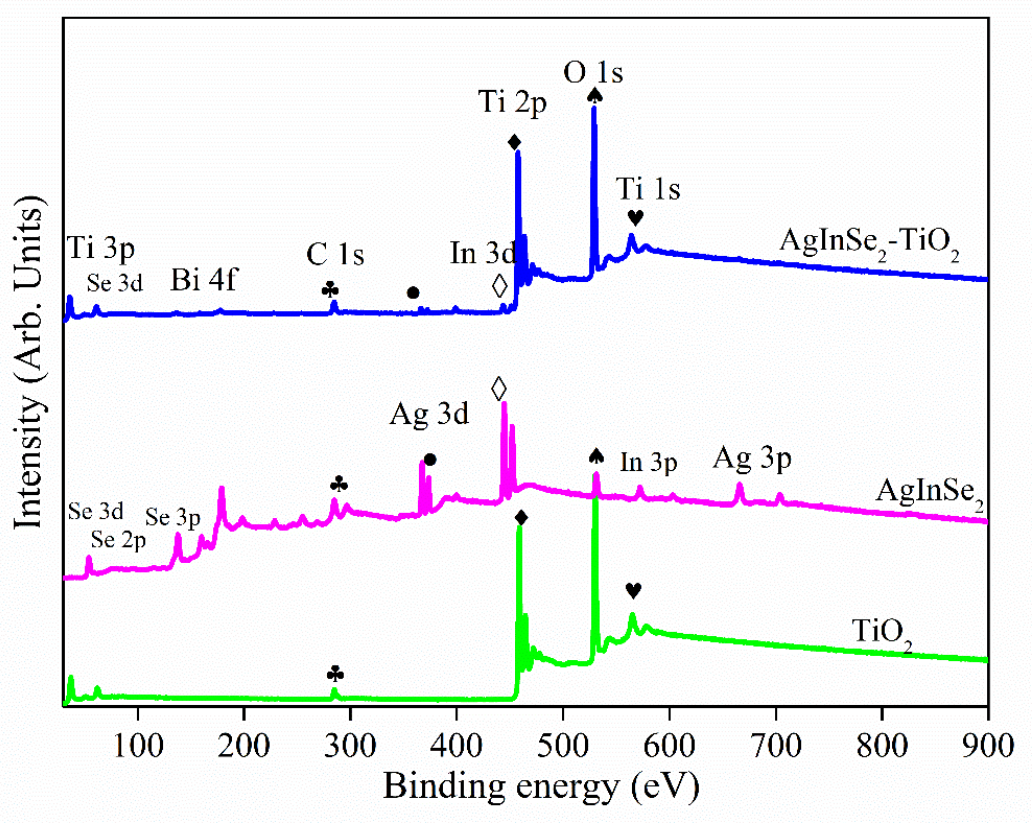

Figure 90. Survey scans of TiO_2, $AgInSe_2$ and 5 wt% $AgInSe_2$-TiO_2. Data generated courtesy of Dr. Steven Hinder.

Figure 91(A) displays the Ti 2*p* patterns of TiO_2 (a) and $AgInSe_2$-TiO_2 (b). The characteristic peaks at 458.84 eV (Ti $2p_{3/2}$) and 464. 60 eV (Ti $2p_{1/2}$), ascribed to Ti^{+4} state was observed for TiO_2 sample.[188] In the case of composite samples, the signature profile of Ti in the +4 state did not show any changes.

However, both the doublets of Ti 2*p* in composite samples displayed a small shift in binding energy values. A shift of ~0.4 eV was observed for $AgInSe_2$-TiO_2. This shift in the composite samples to lower binding energy value compared to the parent sample constitutes the change in the chemical environment of TiO_2 nanoparticles in the due presence of the small amount of TC introduced. [234, 270] In each of the two samples, the spin-orbit splitting difference for Ti 2*p* remained consistent (5.7 eV). **Figure 91(B)** displays the deconvoluted O 1*s* patterns of TiO_2 (a) and $AgInSe_2$-TiO_2 (b). The characteristic peak at 530.20 eV observed for pristine titania sample is assigned to Ti-O bonds.[184] As similar to the Ti 2*p* patterns, the peaks of O 1*s* also displayed a small shift for the composite sample (~0.4 eV). Deconvoluted O 1*s* spectrum also displayed a peak above 531 eV for all the two samples, which is assigned to the hydroxyl molecules adsorbed or the water molecules.[271, 272]

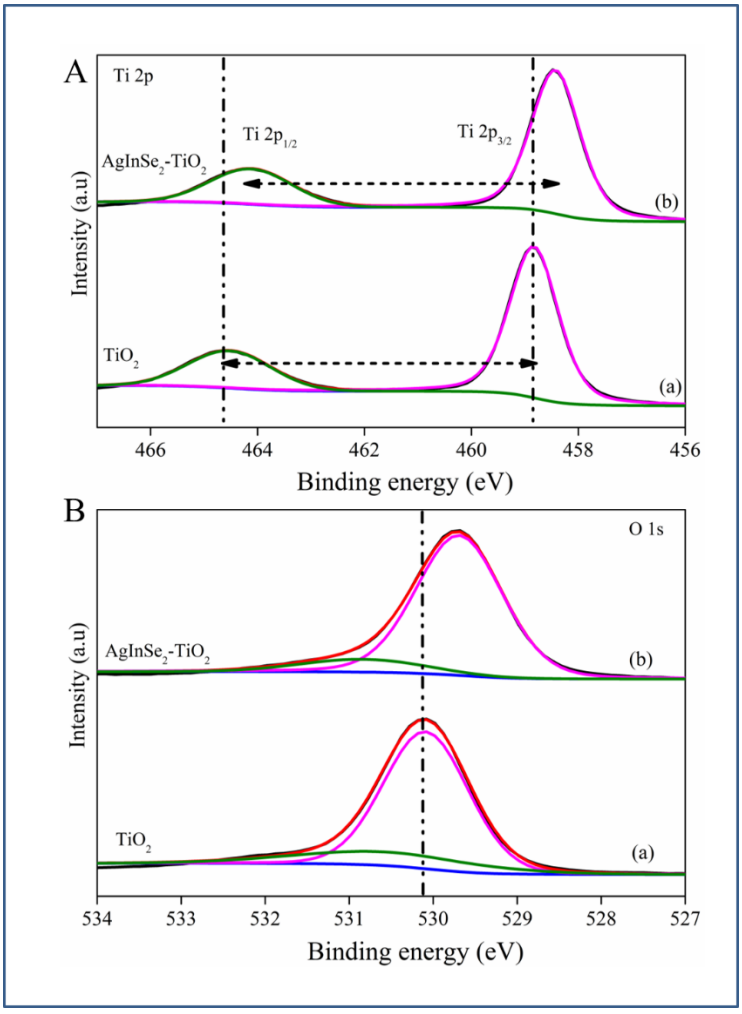

Figure 91. High resolution XPS spectra of (A) Ti 2*p* (a) TiO_2 and (b) 5 wt% $AgInSe_2$-TiO_2; (B) O 1*s* (a) TiO_2 and (b) 5 wt% $AgInSe_2$-TiO_2. Data generated courtesy of Dr. Steven Hinder.

Figure 92(A) displays the high-resolution spectra of Ag 3*d* patterns of $AgInSe_2$ (a) and $AgInSe_2$-TiO_2 (b). Well defined and symmetric peaks of Ag 3d were observed for both the samples. Characteristic peaks of Ag^+ were observed at 367.70 eV (Ag $3d_{5/2}$) and 373.70 eV (Ag $3d_{3/2}$) for $AgInSe_2$ sample. The composite sample with titania displayed a shift (~0.8 eV) in both the peaks to 366.96 eV (Ag $3d_{5/2}$) and 372.98 eV (Ag $3d_{3/2}$). The doublet separation remained consistent for the Ag 3*d* patterns for both the samples (6 eV). As given, **Figure 92(B)** displays the high-resolution spectra of In 3*d*.

Signature peaks of In^{3+} state was observed at 444.65 (In $3d_{5/2}$) and 452.24 eV (In$3d_{3/2}$) for $AgInSe_2$ sample. The composite sample, as similar to the other profiles, displayed a shift of ~0.3 eV to lower binding energy value. The spin-orbit splitting difference of 5.31 eV remained the same for both the samples. In case of Se $3d$ patterns, the high-resolution spectra of $AgInSe_2$ sample displayed deconvoluted peaks at 53.56 eV (Se $3d_{5/2}$) and 54.67 eV (Se $3d_{7/2}$) as shown in **Figure 92C(a)**. The peaks of Se 3d in the composite sample (**Figure 92C(b)**) are not so well defined.[266, 285, 286]

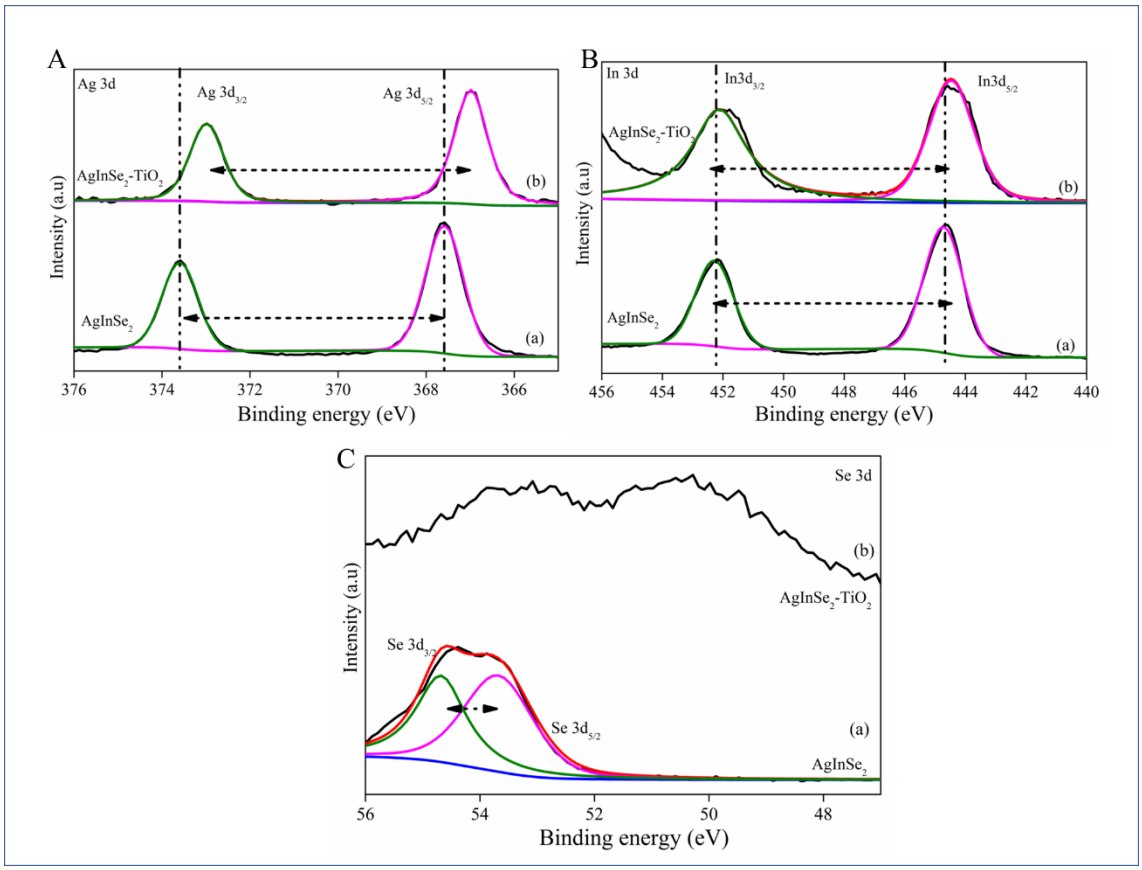

Figure 92. High resolution XPS spectra of (A) Ag $3d$ (a) $AgInSe_2$ and (b) 5 wt% $AgInSe_2$-TiO_2; (B) In $3d$ (a) $AgInSe_2$ and (b) 5 wt% $AgInSe_2$-TiO_2; (C) Se $3d$ (a) $AgInSe_2$ and (b) 5 wt% $AgInSe_2$-TiO_2.

Table 28 summarises the peak position of all the samples. As observed from the above peak patterns displayed of the pristine parent sample and the composite structures.

Table 28. The summarised glance of all the peak position of different elements in $AgInS_2$ and 5 wt% $AgInS_2$-TiO_2 (in eV).

Sample Name	**Ti $2p_{1/2}$**	**Ti $2p_{3/2}$**	**O 1s**	**Ag $3d_{3/2}$**	**Ag $3d_{5/2}$**	**In $3d_{3/2}$**	**In $3d_{5/2}$**	**Se $3d_{3/2}$**	**Se $3d_{5/2}$**
TiO_2	464.60	458.84	530.20 531.20	X	X	X	X	X	X
$AgInSe_2$	X	X	X	373.70	367.70	452.24	444.65	54.67	53.56
$AgInSe_2$ - TiO_2	458.43	464.16	529.70 530.90	372.98	366.96	451.95	444.42		

All the composite patterns displayed a shift in the peak values to lower binding energy values. The change in the chemical environment by the introduction of TC nanoparticles showed the shift in the Ti 2*p* and O 1*s* patterns. Similar changes were also observed for pristine $AgInSe_2$ sample. The shift, above-mentioned manifests the efficient charge transfer at the heterojunction interface and demonstrates the creation of effective heterostructures for multifunctional applications.

6.2.6 TEM Analysis

Figure 93a and **93b** showed $AgInSe_2$ nanoparticles exposing a quasi-spherical morphology. The HRTEM image (**Figure 93c**) showed clear and prominent lattice fringes of 0.34 nm width consistent with the calculated fringe width of 0.346 nm corresponding to (112) crystal plane of tetragonal AgInSe2 (at $2\theta = 25.68^{o}$ from XRD). 5wt% $AgInSe_2$-TiO_2 composite showed nano titania is well accumulated around $AgInSe_2$ having a good interaction between them. The presence of lattice fringe widths of 0.354 nm and 0.235 nm attributing to the (101) crystal planes and (004) planes respectively of

anatase titania, along with fringe width of 0.34 nm fitting to (112) plane of tetragonal $AgInSe_2$. Both HRTEM and SAED pattern reflected the high crystallinity of the sample. Both SAED patterns of $AgInSe_2$ and the composite (**Figure 93c** and **93f**, inset) obtained are again consistent with the XRD pattern of the samples.

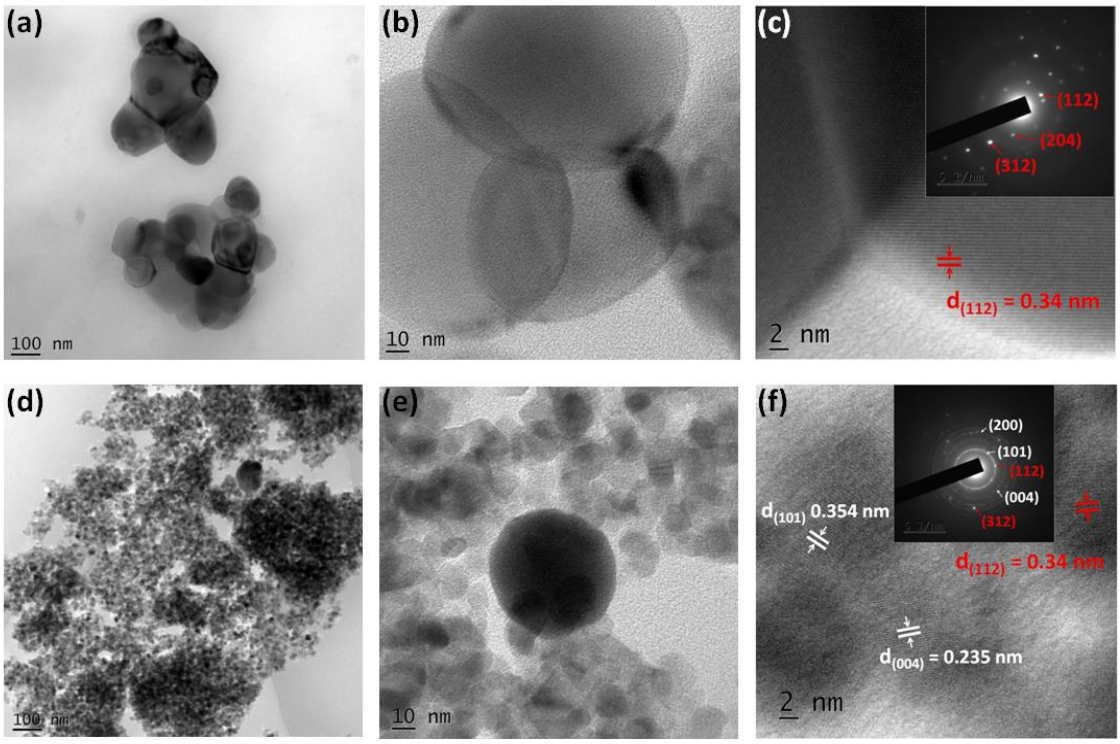

Figure 93. TEM and HRTEM images of $AgInSe_2$ (a,b,c) and 5wt% $AgInSe_2$-TiO_2 composite (d,e,f). Inset of (c) and (f) are the SAED patterns of the samples with red colour markings corresponding to TC and white to TiO_2. Data generated courtesy of Ms. Nisha Padmanabhan.

6.2.7 Photoluminescence Analysis

The photocatalytic efficiency is mainly ruled by the capability of the composite structure to migrate the photogenerated exciton to various reaction sites. **Figure 94** presents the mass normalized photoluminescence spectra of TiO_2 and its 5wt% composites with $AgInSe_2$. The spectra clearly portray the effect of heterojunction formation on the recombination of excitons in parent TiO_2. The emission intensity of the composites of $AgInSe_2$ with TiO_2 is quenched.

Since PL emission has resulted from the recombination of photogenerated electron-hole pairs, the reduction in the PL intensity for the composites indicates that recombination rate is very much diminished, resulting in their high photocatalytic efficiencies compared to parent TiO_2. The emission peaks at 365 nm displayed a small red shift in the composite samples compared to the pristine parent sample. This is attributed to the change in the local chemical environment of the sample and this further validates the positive heterojunction creation.[275]

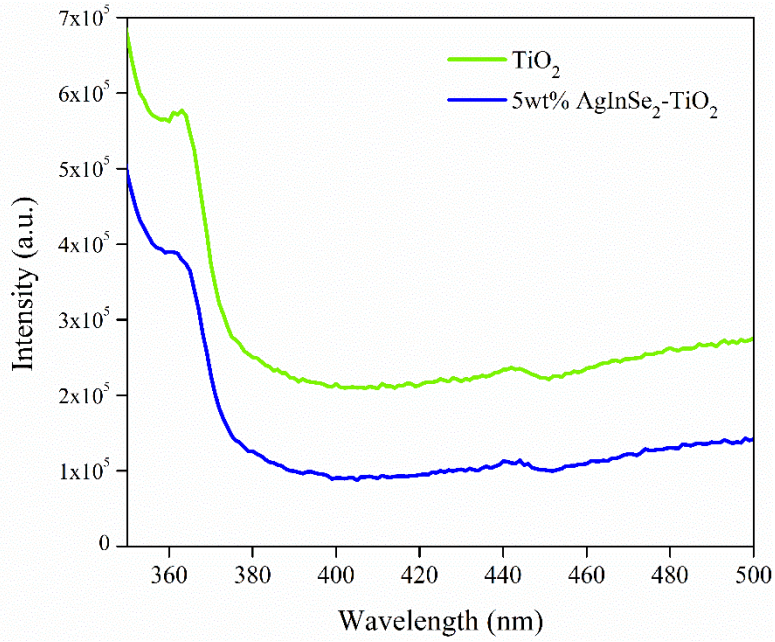

Figure 94. The photoluminescence spectra of TiO_2 and its 5wt% composites with $AgInSe_2$. Data generated courtesy of Ms. Nisha Padmanabhan.

6.2.8 Photocatalytic hydrogen generation

In this following section, the results of photocatalytic hydrogen generated for $AgInSe_2$-TiO_2 was examined at different weight percentages and compared to the results observed for their parent samples.

In the case of $AgInSe_2$-TiO_2, as shown in **Figure 95a**, all the catalysts tested displayed negligible hydrogen production under UV light irradiation only. As the UV cut-off filter was removed (T=60 min), increasing hydrogen production was observed, enhancing the co-catalyst weight percentage in the

range 1% to 5%. Scarce photoactivity for hydrogen evolution was recorded upon UV-A irradiation of the 0.5 wt.% $AgInSe_2$-TiO_2 composite. As regards to the solution, no significant changes concerning the starting pH values were recorded under visible light irradiation only (**Figure 95b**). A moderate decrease in solution pH occurred upon UV-A irradiation of $AgInSe_2$-TiO_2 samples at T=120 min.

The irradiance values recorded in the UV and the visible wavelength range on the external wall of the reactor for the various the $AgInSe_2$-TiO_2 samples tested are reported in **Figure 95c** and **95d**, respectively. After removing the UVA-cut off the filter, an instant increase in the UV irradiance values has been recorded. The higher irradiance values herein recorded for the 0.5 wt% $AgInSe_2$-TiO_2 material indicate a lower suspension absorption. No significant changes before and after removing the UVA-cut off filter have been observed for the irradiance values collected on the external walls of the reactor in the visible range (λ=400÷1100 nm) at T=60 min. Comparable irradiance values have been recorded in such range for 2 wt% and 5 wt% $AgInSe_2$-TiO_2 samples, which exhibited a higher visible light absorption with respect to samples with lower co-catalyst percentage.

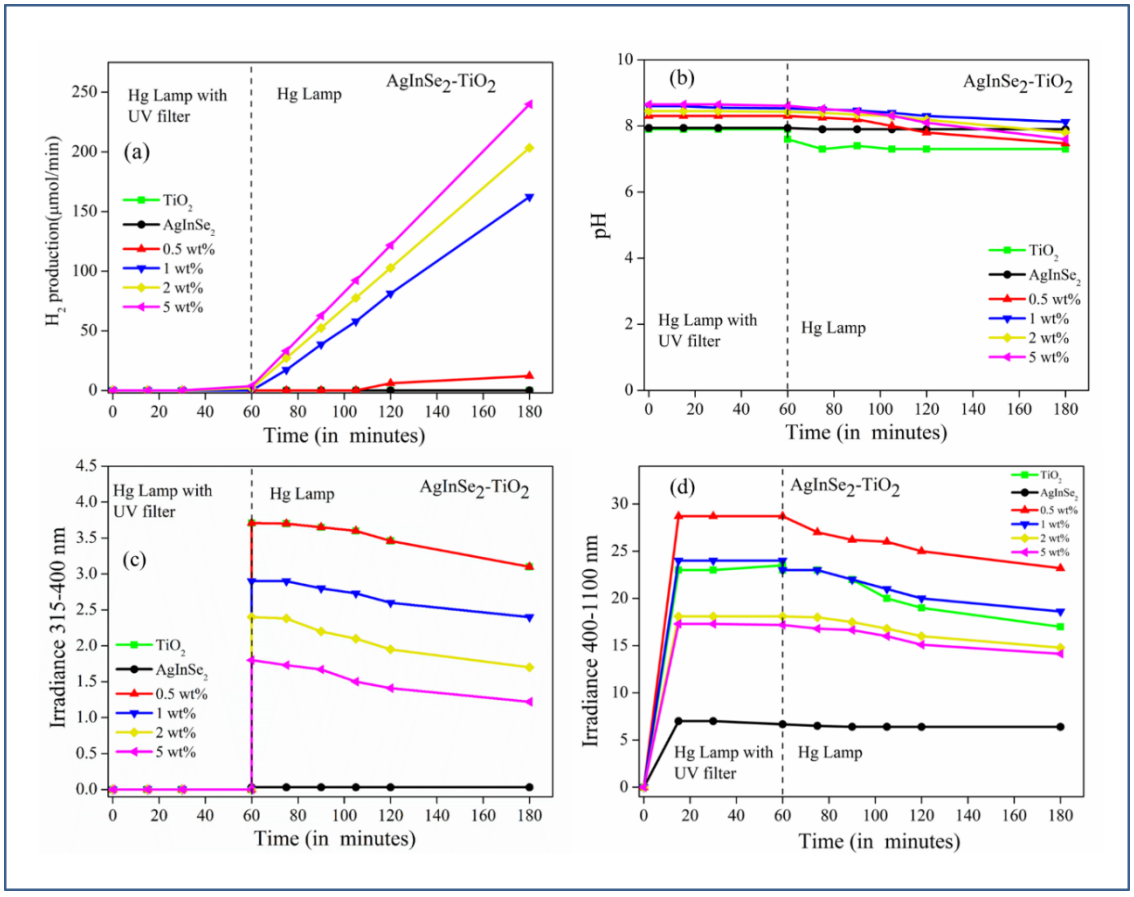

Figure 95. H_2 production rate (a); pH of the solution (b); Irradiance measured on the external walls of the reactor between 315-400 nm (c) and 400-1100 nm (d) at varying weight percentage of $AgInSe_2$, TiO_2 and $AgInSe_2$-TiO_2 catalysts. [CH_3OH] =10 vol.%; Catalyst load=500 ppm; T=25°C; P=1atm. Data generated courtesy of Dr. Laura Clarizia.

Thus, the composites displayed a relative hydrogen generation compared to their parent samples within 120 minutes of light irradiation. It can be therefore concluded that $AgInSe_2$-TiO_2 materials exhibited a more efficient absorption and use of the incident light irradiation over a co-catalyst weight percentage of 5 wt.%. At the same time, all the pristine samples displayed no hydrogen output. As explained in **section 6.2.2**, the band edge estimation shows the HER and OER potential for TiO_2 and $AgInSe_2$, displaying significant potential. However, the quick recombination and the values of the band gap

could be the potential causes for zero hydrogen generation. On the other hand, both the composite samples displayed enhanced H_2 generation, which portrays the significance of the heterojunction creation and the enhanced charge separation by delaying the rate of recombination.

6.2.9 Photocatalytic degradation of Doxycycline (DC)

Additionally, to the hydrogen generation study, the composites of $AgInSe_2$-TiO_2 were examined for Doxycycline degradation. Advanced oxidation processes (AOP), biological degradation and membrane filtration are some of the commonly utilised methods of DC removal. Photocatalytic degradation has lately turned out to be an effective alternative to alleviate the current problem.[287, 288]

Hence, in this study, the composites of $AgInSe_2$-TiO_2 was examined for DC degradation at different weight percentage and compared to the results observed for their parent samples. The composites of $AgInSe_2$-TiO_2 were also examined for DC degradation at different weight percentages and compared to the results observed for their parent samples. **Figure 96a** displays the change in concentration of DC with time for $AgInSe_2$-TiO_2 samples. In this case, also, the samples kept in the dark for 30 minutes did not show any variation in concentration; this reflects the consequence of light irradiation. Exposure to solar light irradiation for 180 minutes showed a substantial decrease in the initial concentration of DC by the composite samples. Parent samples, TiO_2 and $AgInSe_2$, showed a degradation percent less than 50%. Similar to the previous case, the increase in the amount of TC in TiO_2 presented a steady improvement in the degradation method. In the end, the 2 wt% and the 5 wt% samples exhibited a virtually similar trend of more than 92% degradation. Henceforth, this demonstrates the efficacy of the composite development and the improved charge separation created.

The DC degradation of $AgInSe_2$-TiO_2 samples was also observed to follow pseudo-first-order kinetics and can be determined by **equation 39**. **Figure**

96b and **96c** show the kinetics for the DC degradation and reviews the kinetic constants calculated for all the samples, respectively. The presumed pseudo-first-order kinetics was confirmed by observing the straight line for all the cases. The correlation coefficients (R^2) values for all the samples were found to be more than 0.97. The maximum kinetic constant for 5 wt % was calculated to be 0.02643 $min^{-1,}$ and the minimum was observed for $AgInSe_2$ (0.00317 min^{-1}).

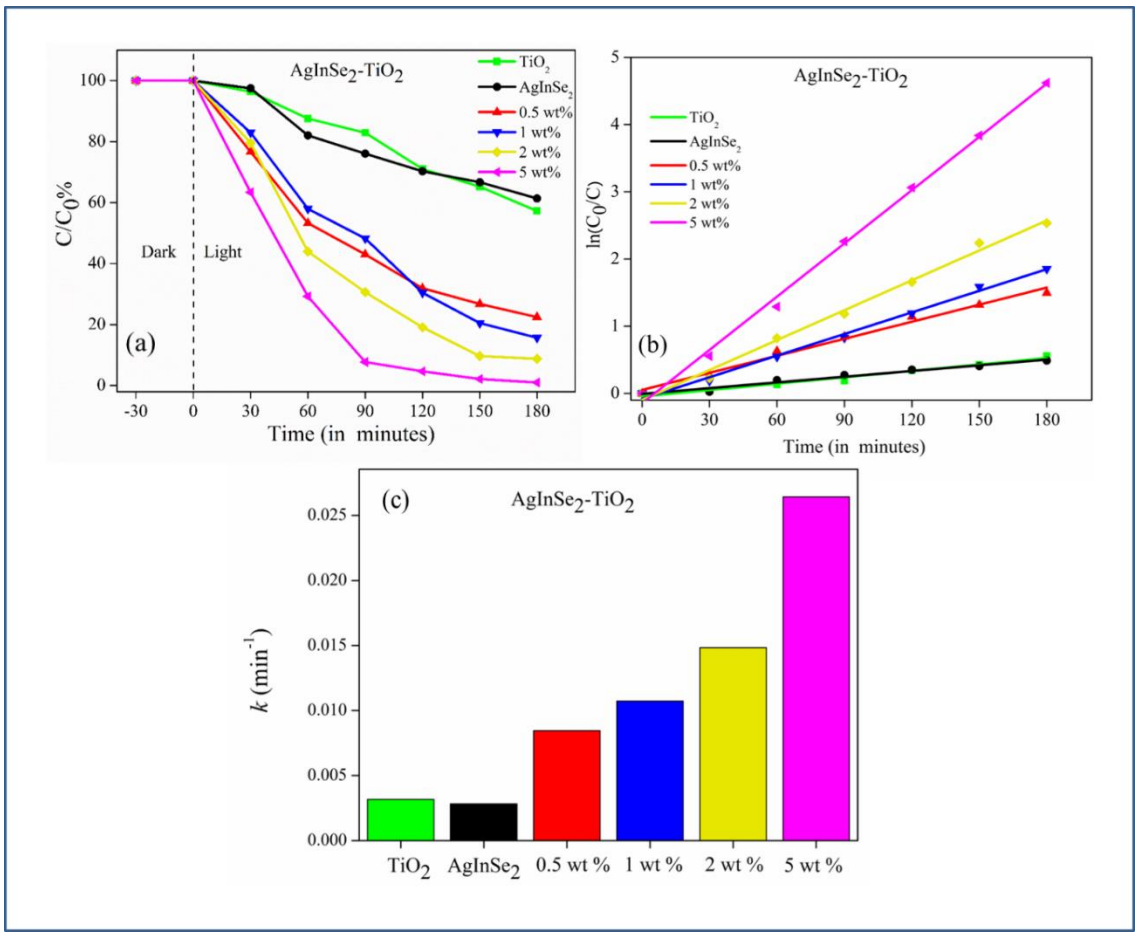

Figure 96. (a) Change in concentration (C/C_0 vs time) of DC; (b) pseudo-first order kinetic study of DC degradation; (c) Summary of the calculated pseudo-first order rate constants of $AgInSe_2$, TiO_2 and $AgInSe_2$-TiO_2 catalysts.

The cyclic studies of the catalyst were performed to evaluate the recyclability and its effectiveness (**Figure 97a**). The 5 wt% composite samples showed comparable results consistently with a small decrease in the degradation

efficacy by the end of the fifth cycle. The scavenging experiments were performed, with the purpose to ascertain the ROS contributing to the degradation procedure (**Figure 97b**). The use of triethanolamine and silver nitrate showed a quick reduction in the degradation efficacy; thus, holes and electrons were found to be the significant ROS in the DC degradation process. Instead, a small portion of decay in activity was observed in the presence of benzoquinone. Therefore, superoxide radicals also had an active part in the degradation process. The hydroxyl radicals necessarily did not demonstrate any influence, as detected by the adding of the IPA in the reaction mixture.[234]

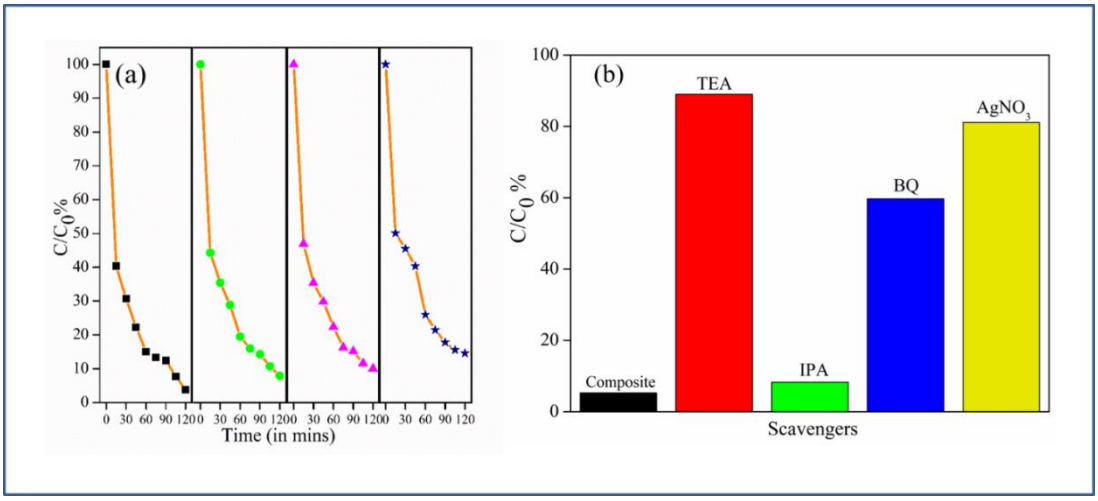

Figure 97. (a) Recyclability profile; (b) scavenging experiment results for 5 wt% $AgInSe_2$-TiO_2.

Thus, in this study of DC removal from aqueous environment, both the composites of titania displayed reasonable efficiency. According to the results observed, the 5 wt% composites of both the TC displayed more than 98% decline of initial DC concentration of 100 ppm for a catalyst dosage of 1 g/L. Pseudo-first order kinetics was observed for both the composites ($R^2 > 0.98$) with the highest rate constant of 0.026 min^{-1}. The efficiency did not change as observed through the recyclability and the stability test and therefore, the catalyst might be used regularly based on its possible retrieval. Thus, this

catalyst could be suitable for demineralisation of persistent pharmaceutical organic pollutants.

6.2.10 Photocatalytic antimicrobial disinfection

Microbially contaminated water could result in the cause of several infections and even death. Typical water treatment procedures include ozonation, UV disinfection technique, chlorination *etc*. Disadvantages of chlorination processes are not new, as the formation of carcinogens like trihalomethanes is reported widely. Thus, it is indeed necessary to find effective microbial inactivation processes. [287, 288]

The photocatalytic efficiency of the as prepared composites was already analysed by studying for hydrogen generation and DC degradation. In this study, a gram-negative (*E. coli*) and a gram-positive (*S. aureus*) bacterium are chosen as a modal microorganism to evaluate the efficacy of the composites and compare their results with their parent samples. The best composite samples from the previous two applications (5 wt%) and the pristine samples of $AgInSe_2$ and TiO_2 are studied. **Figure 98a** and **98b** display the change in the number of bacteria grown over 120 minutes of light irradiation. The log reduction profiles are shown in **Figure 98c**.

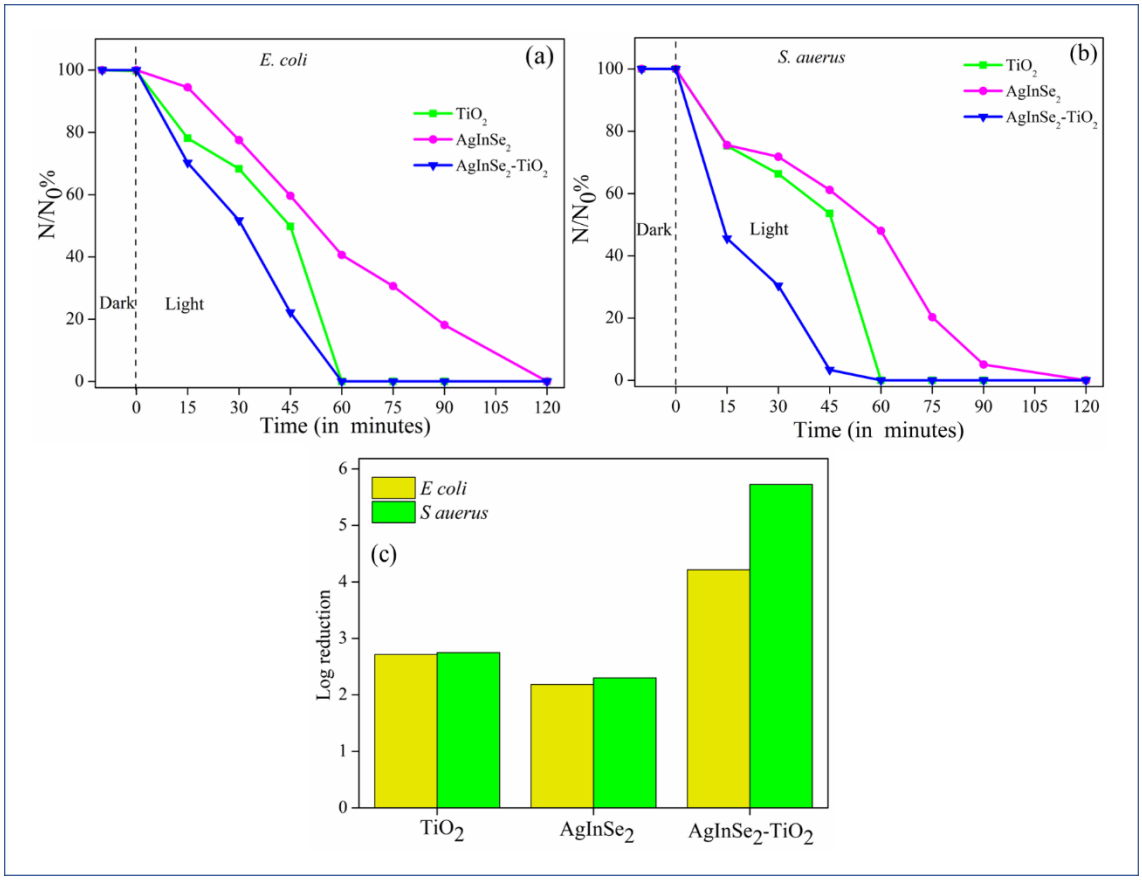

Figure 98. Change in bacterial density (N/N_0 vs time) by photocatalytic inactivation of (a*) E. coli* and (b) *S. aureus*; and (c) calculated log reductions of $AgInSe_2$, TiO_2 and 5 wt% $AgInSe_2$-TiO_2 catalysts.

The dark experiment conducted displayed no change in the numbers; this limits the possibility of dark inactivation caused due to the presence of a catalyst. The $AgInSe_2$-TiO_2 composite and TiO_2, both showed a complete inactivation within 60 minutes of illumination. The pristine TC samples required nearly 120 minutes to display complete inactivation. The change in bacterial density grown on agar plates before and after illumination with $AgInSe_2$-TiO_2 composite for both the bacterial strains are displayed in **Figure 99**.

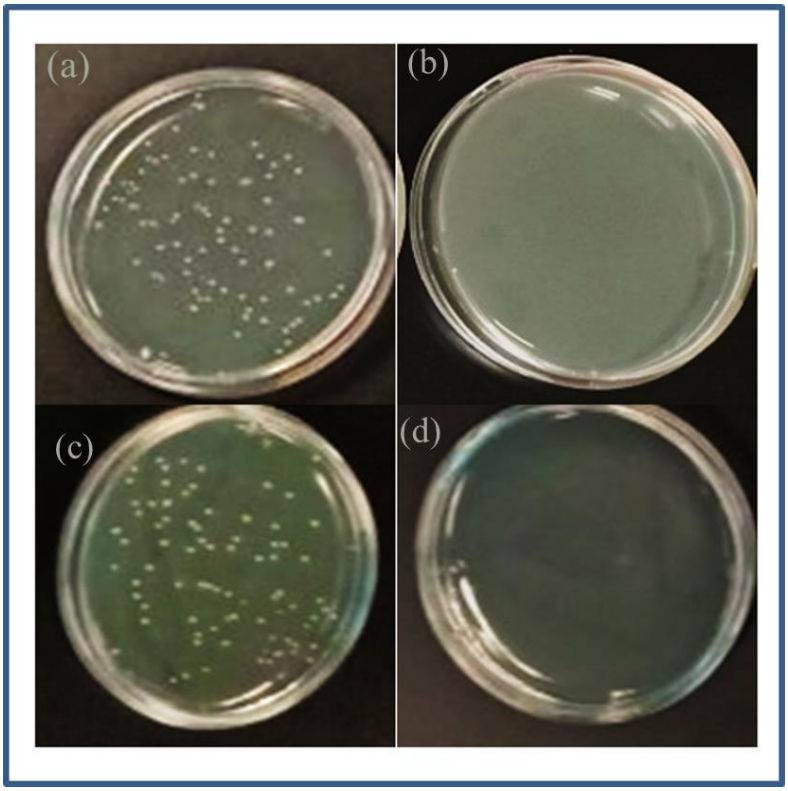

Figure 99. Images of (a) *S. aureus* colonies and (b) *E. coli* colonies change in bacterial density grown on agar plates before and after illumination with 5 wt% $AgInSe_2$-TiO_2.

The bacterial inactivation mechanism is established in previous other literature. Disruption of the cellular membrane due to potential attack by ROS generated during the irradiation process results in the leakage of cellular components and results to the cause of inactivation.[182]

6.3 PHOTOCATALYTIC MECHANISM

The photocatalytic results of the $AgInSe_2$-TiO_2 displayed enhanced hydrogen generation, impressive degradation efficiency as well as antimicrobial properties compared to their pristine parent samples. The structural analysis displays the stability of the tetragonal crystal structure of anatase and $AgInSe_2$, which corroborated to the experimental observations. The computational analysis of titania and TC were crucial to comprehend the electronic and optical properties. The results from XPS analysis demonstrates

the shift in the binding energies of both the composite structures to lower energies. This highlights the strong interaction between the pristine titania and TC. On the other hand, the peaks of Ti^{4+} state displayed a small shift to lower binding energy, which is ascribed to the influence of TC. The peak value also confirms the absence of any oxygen vacancies and reiterates the anatase structure and concrete heterojunction formation. The band gap estimation and the electronic properties aided in summarising the band edge values for $AgInSe_2$ and TiO_2 (as given in **Table 18**). A prospective electron-transfer mechanism is proposed to understand the improved photocatalytic results displayed by the composites architectures.

In case of $AgInSe_2$-TiO_2 composites, the visible light illumination results in the migration of electrons occur from the upper VB of Ag 4*d* states and Se 4*p* states of $AgInSe_2$ to the lower CB of In 5*s* and Se 4*p* states of $AgInSe_2$ and further migrate to the lower CB of titania contributed by Ti 3*d*-orbitals O 2*p*-orbitals. The improved photocatalytic activity by the $AgInSe_2$-TiO_2 composites could be defined *via* hypothesising the formation of type II heterojunction. The band edge positions of TiO_2 and $AgInSe_2$ before and after having contact are shown in **Figure 100**. The Fermi level (E_f) of TiO_2 is present slightly below the E_{CB} of TiO_2, and the E_f of $AgInSe_2$ is also lower than the E_{CB} of $AgInSe_2$ (**Figure 100a**). As the heterojunction is created, the Fermi levels of both the semiconductors align themselves to a new uniform level. Since the dopant amount in case of $AgInSe_2$ is little, therefore the Fermi level of $AgInSe_2$ bring into line with TiO_2 (-0.1 eV). The new band alignment, as shown in **Figure 100b**, displays the flow of the electrons from the CB potential of $AgInSe_2$ to the CB of TiO_2 resulting in a negative charge accumulation in the CB of TiO_2. The diffusion of the holes from the VB of TiO_2 to the VB of $AgInSe_2$, which results in positive charge accumulation. The heterojunction creation results in the delayed charge recombination in the junction and thereby improving the charge separation. The electrons and holes accumulated at the CB of TiO_2 and VB of $AgInSe_2$ respectively participate in the oxidation and reduction processes. The

experimental results of the scavenging process, as shown in **section 6.2.8**, displays the contribution of both the electrons and the holes for the improved photocatalytic results observed for all the three different applications.

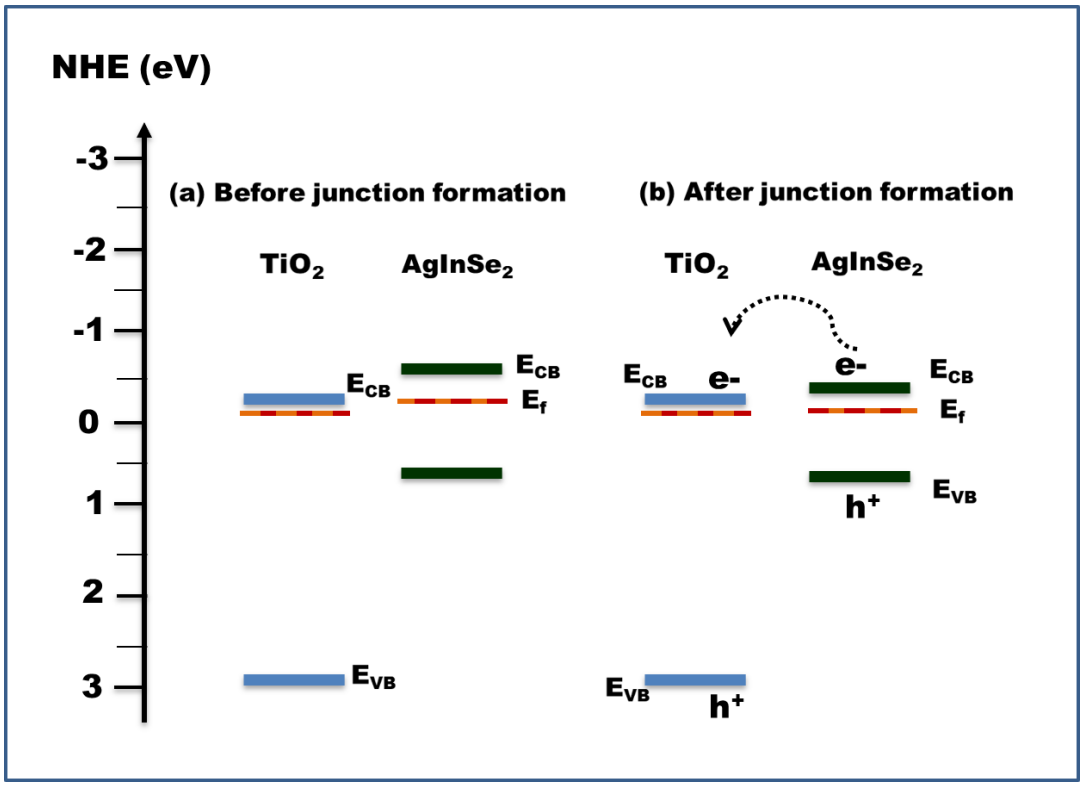

Figure 100. The photocatalytic mechanism for $AgInSe_2$-TiO_2 (a) before the junction and (b) after junction formation.

6.4 DISCUSSION AND CONCLUSIONS

Hence, the present study successfully demonstrates the synthesis of novel composites of $AgInSe_2$-TiO_2. As observed in this study, the In^{3+} cations result in the formation of body centred tetragonal crystal structure of $AgInSe_2$. The electronic properties of both the structures show a significant influence of the In orbitals. An indirect band gap was estimated for TiO_2 while direct band gap was observed for $AgInSe_2$. However, the synthesised nanoparticles displayed a narrow bang gap and effectively improved the visible light absorption of the composite architectures. The photocatalytic results observed for the composite structures for all the three different applications were impressive.

The band alignment of $AgInSe_2$ displayed a very different variation and the formation of type II heterojunction. The heterojunctions result in effective charge separation *via* delayed recombination of the charge carriers, which contributes to the enhanced photocatalytic results.

CHAPTER 7

SUMMARY AND FUTURE WORK

7.1 SUMMARY

In the present report, heterostructure nanocomposites of the Ag-based ternary chalcogenide family have been explored with a classical semiconductor such as titania. All the composites were prepared using a two-step synthesis route. The titania samples were prepared by a sol-gel synthesis and further calcined at 500 °C to attain an anatase phase. The as synthesised titania is added upon the precursor mixture of the ternary chalcogenide of different weight ratios and further solvothermally treated at varying time and temperature. The theoretical study of the pristine titania sample showed the formation of the tetragonal phase. The electronic and optical properties study displayed an indirect transition for TiO_2. Furthermore, these novel heterojunctions illustrated impressive photocatalytic applications. The major conclusions drawn are;

1. **Chapter 3** details the synthesis and process optimisation of $AgBiS_2$-TiO_2 using a one-pot solvothermal technique. The theoretical study of the pristine parent sample showed the formation of the trigonal phase of $AgBiS_2$; however, a metastable cubic phase was obtained experimentally. The choice of the solvothermal solvent and the use of Thiourea as a sulphur source, which acted as a capping agent, were attributed to the formation of the metastable phase. The composite structure with a small dopant level displayed improved visible light absorption and showed decreased band gap values with the increase in dopant levels. The electronic and optical property study of $AgBiS_2$ conferred to the experimentally observed

findings and calculated an indirect transition. The XPS analysis demonstrated the shift in the peaks corresponding to the change in the local environment of the composite structure. The degradation results of the composites showed improved efficacy. Similarly, a significant improvement for the light induced hydrogen generation (1300 μmole/min) is also observed. A log 3 bacterial reduction was attained within 30 minutes of visible light illumination. A plausible Type II heterojunction mechanistic understanding is proposed based on computational analysis, scavenger experiments and the band gap values derived from the DRS plot.

2. **Chapter 4** describes the study of $AgInS_2$-TiO_2 heterostructure nanocomposite. The theoretical study of the pristine parent sample showed the formation of the orthorhombic phase of $AgInS_2$, which confers to the crystal structure obtained experimentally. The composite material showcased a dramatic improvement in visible light absorption. The increase in the dopant percent in the composite ensued in narrowing of the band gap. The electronic and optical property study of $AgInS_2$ validated to the experimentally observed findings and calculated a direct transition. Furthermore, the shift in the peak signals of XPS suggested an alteration in the chemical surroundings of the heterostructure. The degradation results demonstrated the enhanced efficiency and comparable results were observed in the case of the light induced hydrogen generation. The composite structure displayed a 300 times enhanced hydrogen production output when matched with their bare sample materials (300 μmole/min). A log 5 microbial inactivation was accomplished in 30 minutes of light irradiance. A possible interfacial electron transfer and the photocatalytic mechanism is offered based on the computational analysis, species trapping experiment also the bandgap value estimation from the absorbance plot. The formation of a type II heterojunction is observed for this composite.

3. **Chapter 5** describes the process optimisation and the synthesis of $AgBiSe_2$-TiO_2 heterostructure composite. The theoretical study of the pristine parent sample showed the formation of the hexagonal phase of $AgBiSe_2$, which corroborates to the crystal structure obtained experimentally. The composites showcased enhanced visible light absorption and displayed a reduction in band gap values with an increase in the dopant value. The electronic and optical property study of $AgBiSe_2$ validated to the experimentally observed findings and calculated an indirect transition. The XPS results indicated a shift to lower binding energy values, which confirms the change in the chemical environment. The composite samples illustrated more than 95% degradation results within 180 minutes and showed more than 5 log reductions of bacterial strains within 30 minutes of irradiation. The hydrogen production outcomes were fascinating as the $AgBiSe_2$ based composites displayed an increase of about 180 folds (180 μmole/min). The enhanced photocatalytic efficiency displayed is attributed to the delayed charge recombination of the photogenerated electron-hole pairs in the $AgBiSe_2$-TiO_2 interface. Hence, a *p*-*n* nano heterojunction for $AgBiSe_2$-TiO_2 was postulated to explain the band edge alignment and the enhanced activity.
4. **Chapter 6** describes the synthesis and the process optimisation of $AgInSe_2$-TiO_2 heterostructure composite. The theoretical study of the pristine parent sample showed the formation of the tetragonal phase of $AgInSe_2$, which corroborates to the crystal structure obtained experimentally. The composites showcased enhanced visible light absorption and displayed a reduction in band gap values with an increase in the dopant value. The electronic and optical property study of $AgInSe_2$ validated to the experimentally observed findings and calculated a direct transition. The XPS results indicated a shift to lower binding energy values, which proves the change in the chemical environment. The composite samples illustrated more than 98% degradation results within

180 minutes and showed more than 6 log reductions of bacterial strains within 30 minutes of irradiation. The hydrogen production outcomes were fascinating as the $AgBiSe_2$ based composited displayed significant improvement for the light induced hydrogen generation (250 μmole/min). The formation of type II heterojunction is attributed to the enhanced photocatalytic efficiency and the delayed charge recombination of the photogenerated electron-hole pairs.

Table 29 provides a summarised glance of the composites developed and the type of heterojunction created. It also provides an overall comparison of the photocatalytic efficiency of these silver-based chalcogenides.

Table 29. The summarised glance of the composites developed, and the type of heterojunction created.

Composites	Heterojunction	Hydrogen generation ($\mu mol\ min^{-1}$)	Antimicrobial disinfection within 30 minutes	Degradation % (in 180 minutes)
$AgBiS_2$-TiO_2	Type II	1300	Log 3	>97%
$AgInS_2$-TiO_2	Type II	300	Log 4	>97%
$AgBiSe_2$-TiO_2	*p-n*	180	Log 5	>97%
$AgInSe_2$-TiO_2	Type II	250	Log 6	>97%

7.2 FUTURE WORKS

A great deal of research advancements has been made by the scientific community in the past decade on utilising solar power conversion to energy. Heterojunction creation with novel photocatalyst is an essential aspect to improve the catalytic activity, as explained in **section 1.3**. The prerequisite of this search is to identify materials with optimal band structure that promotes the charge separation, simultaneously remaining stable against photo-corrosion and structural stability after prolonged application. Apart from the

composition and the molecular arrangement, the morphological dimension of the material contributes to the critical aspect. Illuminating a photocatalytic surface with energy greater than or equal to its band gap leads to the creation of electron-hole pairs.[182] These photogenerated charge carriers produced within the nanostructure are required to react with water molecules existing on the surface. In this process, of reaching the surface, the charge carriers undergo recombination or get trapped at defect sites. Ida *et al.* effectually explained the importance of time and energy required by the nanomaterials of two different dimensions in the process of water splitting (**Figure 101**).[289] A nanocrystal to undergo water splitting to yield hydrogen requires 4 electron generations which further endures a reduction of water. Thus, to produce 4 electrons, the nanocrystal surface is required to impinge with 4 photons with appropriate energy at a short span of time. The solar photon flux density is estimated to be 2000 μmol s^{-1} m^{-2}.[182] Therefore, at least 4 ms of time is required by the photons to be absorbed by the nanoparticles and the lifetime of the charge carriers is estimated to be 1 μs.[182] Hence, it is extremely challenging to obtain a solar energy flux to complete the water splitting reaction. In order to reduce the recombination and shorten the travelling distance for the charge carriers, two-dimensional architecture nanomaterials can serve these requirements. The layered structure aids the process of light absorption even at a low flux density, and the charge carriers generated are only required to travel a minimal distance. [182] [289]

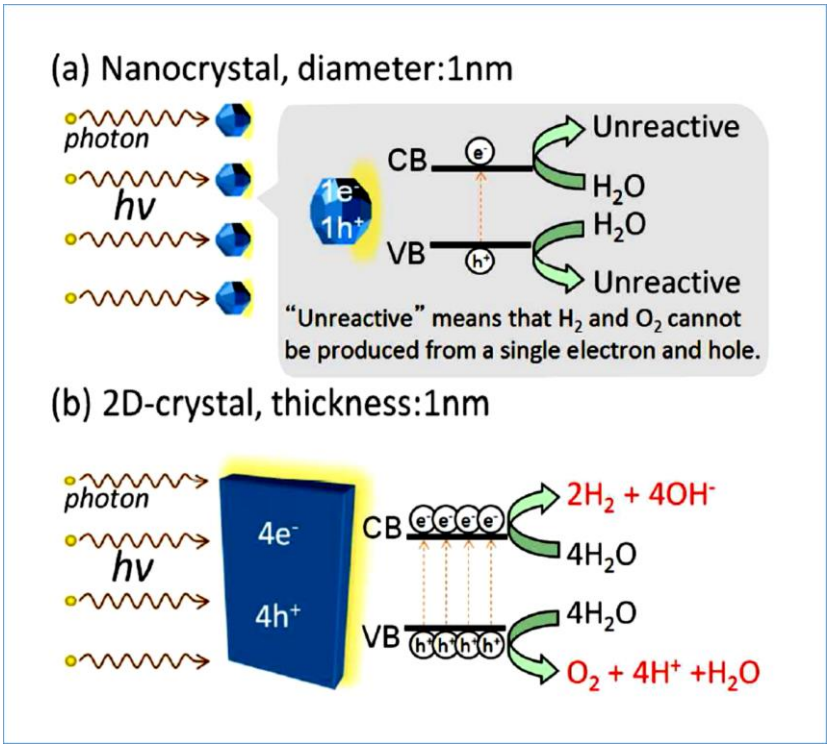

Figure 101. Schematic illustration of photocatalytic water splitting reaction under solar light illumination for (a) nanocrystal photocatalyst, and (b) two dimensional (2D) photocatalyst. Reproduced with permission of ref 16. Copyright 2014, American Chemical Society.[289]

The two-dimensional materials illustrate the unique ability of confinement of electrons in their ultrathin layer, resulting in exceptional optical and electronic properties. The strong in-plane covalent bonding offer sites for the formation of numerous heterojunctions and heterostructures. Moreover, the two-dimensional architecture boasts the high specific surface area, which enables surface reactions such as water splitting. Graphene is the first 2D material example to exhibit the unique electronic, mechanical and optical properties.[290, 291] The whole graphene revolution led to an entirely new domain of research of similar structures.[292-294]

All the four different kinds of ternary chalcogenides synthesised displayed unique structural and electronic properties. These narrow band gap materials hybridised with two-dimensional materials show promising scope for various

multifunctional applications. Apart from the opportunity for enhanced hydrogen generation, the high conductivity property displayed by the TC samples in conjecture with high surface area based 2D materials provides the opportunity to be explored for battery electrode (cathodic and anodic) materials and displays possibilities of use for charge storage (pseudocapacitive) applications.

2D nanomaterials

Since the revolution of graphene and its use for multifunctional applications has resulted in focus over nanomaterials on a two-dimensional scale. A great deal of attention is focussed on finding optimal materials that could be utilised for a broad range of interdisciplinary area of energy conversion and environmental applications.[295] In this section, different classes of 2D nanomaterials apart from graphene, used for various energy and environmental applications are detailed. Their major synthesis routes, electronic and optical properties as well as the disadvantages of these materials are also enlisted in this section.

7.2.1 Transition metal dichalcogenides (TMD)

The laminar sheet structure, which could be isolated from bulk materials, has always been an important aspect of the two-dimensional world. TMDs are semiconductors of the type MX_2, where M are transition metal such as Mo, W, *etc.* while, X is chalcogen atoms (S, Se, Te).[296] MoS_2 has always been an interesting layered structure worth for exploration amongst the material world, even before the graphene revolution. The TMDs are semiconductor in nature with band gap value in the range of 1-2 eV.[297] Thus, coupling these materials with wide band gap semiconductors to fabricate heterostructure catalysts results in various impressive applications. Moreover, the layered structure of these materials also serves as plausible anodic materials for lithium-ion batteries. The 2H hexagonal phase is the semiconducting and the stable phase amongst major TMDs.[298]

The issue again falls back to the synthesis of these 2D materials, as wet chemical synthesis is still one of the common routes of synthesis for these materials. Liquid exfoliation of bulk materials is also another common process to obtain a few layered thicknesses of TMDs. Lithiation is another alternate process, by doping the bulk material and being readily exfoliated to few layered thickness sheets. However, the lack of repeatability and the variation in the lateral size are the common issues that still pertains. Another technique of synthesis involves the growth of the TMD sheets using liquid phase routes and further filtering drying them over conducting substrates, which could be further used as electrodes for energy conversion and storage applications. Alternate techniques such as CVD are used to prepare high quality and uniform layers of TMDs. However, the cost and the scalability of such methods is remaining a challenge.[299]

The dependence of the layered thickness of the sheets to their electrochemical activity is a question which has conflicting inferences. Various applications tend to display activity due to the multiple zones of the layered sheets. The blunt edges of these sheets tend to display higher activity compared to the basal plane in the case of water splitting application. Whereas, the defects in the basal plane and engineering the creation of electron moieties along these sheets tend to improve the overall electron transfer kinetics for electrochemical applications; apart from random composition of 2D materials to create composites.[300] Another way is to fabricate van der Waals heterostructure, where deliberate attempts are made to arrange 2D structures at definite orientation.[301] The resulting sandwich layers contributes to enhanced electrochemical applications. Thus, thoughtful fabrication of heterostructures with defined geometrical contact of the materials offers a new dimension to evaluate the electrochemical applications of such complex nanostructured systems.[302]

7.2.2 Black Phosphorus

Black Phosphorus (BP) is a two-dimensional structure which is an allotrope of phosphorus. They are bounded by weak Van der Waal's attraction and few layers of these nanomaterials known as phosphorene.[303] Phosphorene sheets are commonly synthesised using top down approach of getting the phosphorus mechanically or chemically exfoliated. BP was first reportedly synthesised in 1914, by Bridgman. White phosphorus powder under high pressure and temperature (1.2 GPa and 200 °C) resulted in BP. However, alternative techniques such as Pulse layer deposition are used to grow the high quality of BP, but it's still economically unviable. Liquid exfoliation to produce a few layers of BP films is still the viable option in this regard.

This stable allotropic form of phosphorus has unique electronic and optical properties. It is an intrinsic p-type semiconductor, and the sheets display an anisotropic pattern for transport properties.[304] Hence, the strain applied in lattice direction can result in tuning the properties of the 2D materials. Reports of FET devices with high carrier mobility (1000 cm^2 V^{-l} s^{-1}) and materials for catalysis, sensors, batteries *etc.* have exploited this very feature of the material.[305]

Phosphorus has an electronic configuration of $3s^2$ $3p^3$. The sp^3 hybridisation results in three bonds of phosphorus with the adjacent atoms, leaving a lone pair electron. The sp^3 hybridisation in BP lead in 2D layers with puckered honey-comb structure.[306] These layered structures provide the opportunity to be cleaved down to single layer films from bulk material. The crystal structure of BP leads to a tunable direct band gap. The impressive crystal structure results in an anisotropic nature from few to mono layer of sheets with a band gap of 1.6 to 0.46 eV for 1 to 4 layers respectively.[307]

However, the challenge still pertains in synthesising high-quality, large-scale BP. Creation of intrinsic defects, which results in enhanced electron-hole recombination. The present top-down approach is commercially unviable.

Moreover, the stability of BP is a concern, as it is unstable in ambient nature. Surface functionalisation could be an effective process to enhance the stability as well as improve the intrinsic properties of the 2D sheets.[308]

7.2.3 2D Bismuth based layered materials

Bismuth based 2D materials have essentially turned an interesting class of layered materials. Bi-based layered materials display unique semiconducting behaviour. Doping of potential cation and anions in the layered structure influences the crystal structure and finally affects the band structure.[309] This results in band gap tuning from the range of infrared to UV (0.36 eV to 3.6 eV). The interesting electronic and optical properties contribute to their applications in energy conversion, storage devices, building blocks for electronic and optoelectronic components. These layered structures provide interlayer space for intercalation of ions, which could be effective for various energy storage devices.[310]

These 2D materials could be unitary binary (Bi_2Te_3, Bi_2Se_3) or ternary ($Bi_2O_2S/Se/Te$, $CuBiS_2$) or multinary [($MBiO_2X$) M= Ca, Sr, Ba and X= Br, Cl]. The unitary layer of Bi is a rhombohedral structure with the metallic property. These materials display high conductivity and high carrier mobility, while the binary structure is compounds of bismuth chalcogen and halides.[311] These materials also make up an extremely narrow band gap which displays intense infrared absorption and are often utilised for various thermoelectric applications.[312]

The ternary 2D structure of Bi is layered structures of Bismuth oxyhalides (BiOX) or chalcogens. The introduction of various halides (X=Cl, Br and I) results in tuning the electronic band structure. The decreased electronegativity contributes to the shift in the valence band maxima.[313] These structures are utilised for various photoconversion applications. The multinary system of 2D layered structures of Bi is extremely broad; the

presence of multiple elements results in broad composition and synthesis of such composition are extremely difficult.[314]

The common synthesis route of these types of 2D Bi layered materials is facile wet chemical methods. Sonochemical, solvothermal, electrochemical depositions, chemical reduction are some of the methods intensively used.

7.2.4 MXenes

Single element 2D materials such as graphene, silicene and germanium have been prepared and explored for these multiple applications. Transition metal carbides, carbonitrides and nitrides are the new entries to the world of 2D nanomaterials. MXenes are generally represented as $M_{n+1}X_nT_x$ (n= 1-3), where M is early transition elements. X is carbon or nitrogen, and Tx is surface terminations (OH, O or F).[315] Various combinations and the stoichiometric ratios of elements has fairly contributed to the rise of these materials. Titanium carbide was the first MXenes discovered and following several others were soon synthesised. Lately, a combination of introducing two transition metals has also been tried. Synthesising precursors for such MAX phases have been the exciting phase.[316] Extending two transition metal introduces various stoichiometric combination that results in the formation of a wide range of carbonitrides.[317]

These materials display excellent electrical conductivity, mechanical properties ability of surface functionalisation, which enables its usage in various applications. In general synthesising MXenes have been an interesting process. Surface etching of atomic layers from their MAX phase using concentrated acids like HF is one of the common routes. [317] The M-A bonds are metallic unlike to other 2D materials, where the layers are held up by van der Waals force. Hence getting metallic bonds scissored by any form of mechanical exfoliation is not possible. Use of concentrated HF acid or *in situ* formation of HF by the reaction of hydrochloric acid and fluoride salts such as LiF, ammonium fluoride *etc*. are some of the predominantly used methods.[318]

Use of these concentrated acids results in the formation of surface terminations. Defect free laminar sheets display high electrical conductivity and thus used for several energy storage applications.

7.2.5 Layered Double Hydroxide (LDH)

LDH is an interesting class of inorganic material which have gained intense attention in recent years. These ionic solids are made up of interlayers of cations with layers of anions and hydroxide ions. The positively charged metal cations from alternating stacking with interlayers of hydroxide and anions to form a sandwich structure.[319] The metal cations are bivalent, and trivalent (M^{2+}/M^{3+}) cations, which are the host layers and the anions present in the interlayers are bonded with ionic bonding, hydrogen bonding and Van der Waal's force. M^{2+} ion such as Mg^{2+}, Ca^{2+}, Zn^{2+} *etc*. while M^{3+} ions are Al^{3+}, Cr^{3+}, Fe^{3+} or Co^{3+}. While the anions are Cl^{-}, CO_3^{2-}, NO_3^{-}.[320, 321]

The ability to tailor the stoichiometric compositions allows tuning the chemical composition of the interlayer anions. The crystallite size *etc.* makes them an interesting functional material for various applications. Moreover, exfoliating these layered structures could result in a single layer which can result in improved surface area.[322]

LDH is typically synthesised using two routes: top down and bottom up approach. The top-down approach of exfoliating the layered materials is not an easy step. The high charge density in the layers makes these inorganic components difficult to exfoliate. In the exfoliation technique, an intercalating ion such as surfactants and amino acids are introduced in between the layers to enhance the distance between the layers and finally electrostatic repulsion of the layers by ultrasonication in a certain solvent.[322] Solvents commonly used are alcohols, formamide, toluene, and even water-based exfoliation has been reported. Apart from exfoliation, the most convenient technique is using laser ablation. This method results in controlling the lateral dimensions of the layered structures, within a few minutes of laser exposure. The bottom up

synthesis method includes facile co-precipitation, solvothermal techniques.[321, 323]

The presence of the wide range of metal cations and anions make them attractive candidates for energy applications. Hybrids of LDH with other carbon-based materials like graphene and CNT have displayed enhanced conductivity. The metal oxide precursor of the LDH contribute to the pseudocapacitance as their presence in the hybrid structure provide multiple oxidation states for reversible faradic reactions.[324]

7.3 FUTURE APPLICATIONS

7.3.1 Carbon dioxide reduction

The major cause of rise in global temperature is the heightened levels of CO_2 emission. Excess usage of fossil fuels and rise in deforestation has resulted in the curb of the carbon dioxide fixation cycle in our nature. Hence, in order to curtail the rising temperature, various renewable and sustainable strategies for energy production technologies are implemented. Conversion and recycling of CO_2 into fuel and several value-added products is a promising alternative. Conversion of CO_2 into useful products is certainly a challenging task. However, several methods such as electrocatalysis, thermocatalysis, photocatalysis, photoelectrochemical and biochemical *etc*. are some of the major routes. Amongst them, PEC conversion has been identified as an ideal technique to selectively convert CO_2 to methane, ethane, ethanol, methanol *etc*. under solar light irradiation. CO_2 being an extremely stable molecule, requires high amount of endothermic energy to break the strong dissociation energy. In nature, the photosynthesis process occurs via the aid of photosensitizer molecules such as chlorophyll. While, in case of photoelectrochemical process, the light and the electrical energy supplied helps to conduct the process. Apart from that the choice of the electrode and the electrolyte used governs the kind of product generated. The major design of the PEC cell is that the electron transfer reactions occur when the Fermi

level of the electrolyte and the electrode material are apart from each other. Later, in the reaction process the difference in the Fermi level is altered at the electrode/electrolyte interface *via* band bending process. Hence, the yield of the product formation is governed by the lifetime of the charge carriers generated and the light absorption ability of the electrode material. Therefore, fabrication of electrode material with essential surface properties and band edge position is crucial. Doping of metal atoms, morphological alterations, composite creation *etc.* are some of the methods to attain the essential stability, high turnover cycles. Fabrication of Z-scheme, *p-n* junctions composite heterojunctions with two dimensional materials and TC materials certainly aids in improving the product yield, product selectivity, avoid photocorrosion as well as maximise the overall performance.

7.3.2 Supercapacitor materials

Capacitors are simple electrical energy storage device which are being used extensively for various technologies. They utilise the electrical potential difference developed between two metal plates separated by a small distance and the kind of dielectric property of the material in between the plates. The overall capacitance of the overall energy stored in the device is proportional to the area of the plate and the dielectric constant of the material in between the 2 plates. While it is indirectly proportional to the distance of separation between the plates. Thus, reduction of the distance of separation, increase the area of the metal plates as well finding high dielectric constant overall contribute to the increased capacitance of the device. However, these conductive metallic devices have their own sets of disadvantages. Supercapacitors are the electrical devices with high power density and appreciable energy density. They are extremely useful in typical usage points where there is a sudden need of high energy flow. They are used nowadays in various electronic and electrical devices, industrial machines, and transportation, especially in public buses and tramways. They are particularly helpful in starting engines and can recharge by regenerative braking system.

Supercapacitor's cell comprises of two electrodes stuck to a current collector, which provides a link to the circuit and separated by separator and electrolyte. The electrodes could be made of identical material making up a symmetric cell, while a different electrode material makes up a asymmetric cell. The separator layer enables to reduce the volume of the supercapacitor cell, it also prevents from the short circuit of the device as well as enabling the flow of ions from the electrolytes. The active electrode materials could be further classified into 2 main categories; the materials for electric double-layer capacitors (EDLC) (non-faradic capacitors and EDLC) and pseudocapacitors (faradic capacitors). Thus, utilising both the faradic and non-faradic mechanism results in formation of various types of hybrid asymmetric supercapacitors. Thus, overall, each electrode behaves as a single supercapacitor and hence both the electrodes make up an arrangement of series connected capacitors. Hence, interesting combination of the two-dimensional materials and the TC materials could aid in creating various hybrid asymmetric supercapacitors.

7.3.3 Battery materials

Battery is an electrical device that converts chemical energy into electrical energy and vice versa. Rechargeable batteries are the most revolutionary device which has governed the entire 21'st century. Lead-acid batteries and Lithium-ion batteries are the most commercialised form of batteries used in various sectors of our livelihood. A basic battery design consists of a cathode and an anode, the two electrodes which store electrical energy as chemical energy. An electrolyte separates both the electrodes which aids the redox reaction process occurring on the surface of the electrode (exchange of electron) along with an external current circuit. The electrolyte used can be polymer or solid which is permeable to a liquid electrolyte. Wide range of materials are used as electrodes and various combinations of electrolytes are tried to increase the overall energy and power density. Design of battery materials which maximizes the energy density ensures lesser volume of

battery use, reduces the overall cost and the weight of the electronic products. Hence, interesting combination of the two-dimensional materials and the TC materials could aid in creating various hybrid of electrode materials.

7.4 OUTLOOK

In summary, the four different kinds of ternary chalcogenides synthesised displayed unique structural and electronic properties. These narrow band gap materials hybridised with two-dimensional materials show promising scope for various multifunctional applications. The intimate interfaces result in delayed recombination pathways. Moreover, the charge carrier transport was enhanced by multiple fabrication or introduction of a secondary component such as co-catalysts. The novel synthesis process of 2D/2D composite structures resulted in enhanced visible light absorption and improved the stability of the material against photocorrosion. Thus, these novel heterojunctions are a promising class of material for future use. Regardless of the significant progress achieved in the last decade, there remains a huge block of hurdles to cross with regards to photocatalytic water splitting reaction. Apart from materials synthesis and their core set of challenges, there lies another realm of concern related to hydrogen storage. It is indeed a critical issue of concern, which requires appropriate redress. The hydrogen with low volumetric energy can be compressed in liquid or gas state, which requires high amounts of energy and would finally sum up in the cost of production. The problem of commercialisation and the lack of technological support finally prevents consumers to purchase hydrogen vehicles until an adequate supply of fuel is guaranteed. However, the idea of integrating a photocatalytic hydrogen generation unit with storage entity can serve the realistic goals of solar to hydrogen energy utilisation.[325] The formation of photogenerated charge carriers and the charge separation is extremely important with respect to attaining an efficient hydrogen production system. At present, the separation relies on the charge migration length, which is typically around 10-50 nm. As explained by Yang and co-workers, the protons

generated in the oxidative sites, required to travel to the reductive sites of the material for hydrogen generation.[326] Subsequently, this leads to possible reverse reaction and contamination of hydrogen with oxygen. Thus, future research should primarily focus on effective electron transportation pathways to the oxidative sites. In the very same study, the author's proposed a multi-layered structure of carbon nitride and graphene sheets. The theoretical estimation demonstrated that the light generated holes migrate towards the exterior layers of graphene. The protons react with the inner electrons of the C_3N_4 sheets to form hydrogen. The H_2 generated is stored in between the sandwiched layers of graphene sheets, as the selective absorption does not allow the passage of any other molecules.[326] In a similar effort, DFT studies also predict the use of porous BN for hydrogen storage and generation.[327] The formation of defects in *h*-BN results in a porous structure which enhanced the specific surface area. Furthermore, doping with C, resulted in a decrease in bandgap from 3.98 eV to 1.8 eV. This curative architecture design of materials does necessarily define the upcoming innovative approach towards energy utilisation. The use of 2D nanomaterials like MXenes along with potential co-catalysts can also be worth designing for such hybrid applications. These heterojunction heterostructures have illustrated significant efficiency compared to their singular component. Mix and match of band structure alignment and utilising the pros and cons of multiple components has resulted in better hydrogen production output. However, caution must prevail in the selection of materials for heterostructure, heterojunction composites. Understanding of the singular component is still relevant for rational designing of the structure such as the morphology, composition, interface engineering *etc*.

7.5 CONCLUSIONS

Hence, the present thesis demonstrates the synthesis of novel composites of silver based ternary chalcogenides with TiO_2 and provides a detailed theoretical and experimental analysis. The optimal experimental parameters

are discussed thoroughly. The computational analysis aids in understanding the crystal structure, optical and electronic properties of these parent samples. It also validates the experimentally attained values and helps in defining the plausible transfer mechanism at the interface. The optical properties in aid to the electronic properties study provide more insights to the band alignment, that effectively illustrates the delayed recombination. The as prepared samples displayed efficient photocatalytic hydrogen generation, doxycycline degradation and antimicrobial disinfection. The reusability of the catalyst and the kinetics of the degradation process is also studied.

Even though there is an outpouring of research publications, less have converted into productive commercialise technologies. Publications communicating high production output of hydrogen often on closer analysis reveals the presence of sacrificial electron donor or acceptors in the reaction.[328] Yet, on the brighter side, the use of organic components as part of photo reforming and hydrogen generation has successfully been lead to different pilot scale projects. In the same way, with respect to 2D materials, there lacks a complete understanding of the mechanism behind the catalytic activity. These materials are more often semiconducting in nature and exhibit poor charge transfer. Apart from that, the catalytically active sites are located at the edges or around the defects. The in-plane atoms remain catalytically inert in the process. Thus, two dimensional surfaces with appreciable charge kinetic ability are of paramount interest. Considerable numbers of studies at present are based on trial-and-error stage and relays back to a first principle or DFT estimation. Synthesis of these materials has to date remained the single most challenging aspect for the whole scientific community. Therefore, the search for more efficient technologies for the bulk synthesis process is equally important. However, 2D materials and their composite architectures with the ternary chalcogenides do exhibit promising feature, but the careful rapport between theoretical and realistic approach would finally convert them into useful technology. In the near future, it is expected that these

material-based niche technologies will gradually transfer from the laboratory bench top experiment to industrial-scale applications.

REFERENCES

1. Hanaor, D. A.; Sorrell, C. C., Review of the anatase to rutile phase transformation. *Journal of Materials science* **2011,** *46* (4), 855-874.
2. Okasha, A.; Gomaa, F.; Elhaes, H.; Morsy, M.; El-Khodary, S.; Fakhry, A.; Ibrahim, M., Spectroscopic analyses of the photocatalytic behavior of nano titanium dioxide. *Spectrochimica Acta Part A: Molecular and Biomolecular Spectroscopy* **2015,** *136*, 504-509.
3. Pillai, S. C.; Periyat, P.; George, R.; McCormack, D. E.; Seery, M. K.; Hayden, H.; Colreavy, J.; Corr, D.; Hinder, S. J., Synthesis of high-temperature stable anatase TiO_2 photocatalyst. *The Journal of Physical Chemistry C* **2007,** *111* (4), 1605-1611.
4. Rao, K. K.; Kumar, G., Polymorphic phase transition among the titania crystal structures in solution based approach: From precursor chemistry to nucleation process. *Nanoscale* **2014** *6.20* 11574-11632.
5. Thamaphat, K.; Limsuwan, P.; Ngotawornchai, B., Phase characterization of TiO_2 powder by XRD and TEM. *Kasetsart J.(Nat. Sci.)* **2008,** *42* (5), 357-361.
6. Fisher, M. B.; Keane, D. A.; Fernandez-Ibanez, P.; Colreavy, J.; Hinder, S. J.; McGuigan, K. G.; Pillai, S. C., Nitrogen and copper doped solar light active TiO< sub> 2</sub> photocatalysts for water decontamination. *Applied Catalysis B: Environmental* **2013,** *130*, 8-13.
7. Hu, Y.; Tsai, H. L.; Huang, C. L., Effect of brookite phase on the anatase–rutile transition in titania nanoparticles. *Journal of the European Ceramic Society* **2003,** *23* (5), 691-696.
8. Carp, O.; Huisman, C. L.; Reller, A., Photoinduced reactivity of titanium dioxide. *Progress in Solid State Chemistry* **2004,** *32* (1), 33-177.
9. de Farias, R. F.; Silva, C. C.; Restivo, T. A., Thermal study of the anatase-rutile structural transitions in sol-gel synthesized titanium dioxide powders. *Journal of the Serbian Chemical Society* **2005,** *70* (4), 675-679.
10. Periyat, P.; Pillai, S. C.; McCormack, D. E.; Colreavy, J.; Hinder, S. J., Improved high-temperature stability and sun-light-driven photocatalytic activity of sulfur-doped anatase TiO2. *The Journal of Physical Chemistry C* **2008,** *112* (20), 7644-7652.
11. Heald, E. F.; Weiss, C. W., KINETICS AND MECHANISM OF ANATASE/RUTILE TRANSFORMATION, AS CATALYZED BY FERRIC OXIDE AND REDUCING CONDITIONS. *American Mineralogist* **1972,** *57* (1-2), 10-&.
12. Nolan, N. T.; Seery, M. K.; Pillai, S. C., Spectroscopic Investigation of the Anatase-to-Rutile Transformation of Sol− Gel-Synthesized TiO2 Photocatalysts. *The Journal of Physical Chemistry C* **2009,** *113* (36), 16151-16157.
13. Byun, C.; Jang, J. W.; Kim, I. T.; Hong, K. S.; Lee, B. W., Anatase-to-rutile transition of titania thin films prepared by MOCVD. *Materials Research Bulletin* **1997,** *32* (4), 431-440.
14. Markowska-Szczupak, A.; Ulfig, K.; Morawski, A., The application of titanium dioxide for deactivation of bioparticulates: an overview. *Catalysis Today* **2011,** *169* (1), 249-257.
15. Nolan, N. T.; Seery, M. K.; Hinder, S. J.; Healy, L. F.; Pillai, S. C., A systematic study of the effect of silver on the chelation of formic acid to a titanium precursor and the resulting effect on the anatase to rutile transformation of TiO2. *The Journal of Physical Chemistry C* **2010,** *114* (30), 13026-13034.
16. Pelaez, M.; Nolan, N. T.; Pillai, S. C.; Seery, M. K.; Falaras, P.; Kontos, A. G.; Dunlop, P. S.; Hamilton, J. W.; Byrne, J. A.; O'shea, K., A review on the visible light active

titanium dioxide photocatalysts for environmental applications. *Applied Catalysis B: Environmental* **2012,** *125*, 331-349.
17. Etacheri, V.; Seery, M. K.; Hinder, S. J.; Pillai, S. C., Oxygen rich titania: A dopant free, high temperature stable, and visible-light active anatase photocatalyst. *Advanced Functional Materials* **2011,** *21* (19), 3744-3752.
18. Gopal, M.; Chan, W. M.; De Jonghe, L., Room temperature synthesis of crystalline metal oxides. *Journal of Materials Science* **1997,** *32* (22), 6001-6008.
19. Pillai, S. C.; McGuinness, N. B.; Byrne, C.; Han, C.; Lalley, J.; Nadagouda, M.; Falaras, P.; Kontos, A. G.; Gracia-Pinilla, M. A.; OShea, K., Photocatalysis as an effective advanced oxidation process. *Advanced Oxidation Processes for Water Treatment: Fundamentals and Applications* **2017**, 333-381.
20. Padmanabhan, S. C.; Pillai, S. C.; Colreavy, J.; Balakrishnan, S.; McCormack, D. E.; Perova, T. S.; Gun'ko, Y.; Hinder, S. J.; Kelly, J. M., A simple sol-gel processing for the development of high-temperature stable photoactive anatase titania. *Chemistry of Materials* **2007,** *19* (18), 4474-4481.
21. Byrne, C.; Fagan, R.; Hinder, S.; McCormack, D. E.; Pillai, S. C., New Approach of Modifying the Anatase to Rutile Transition Temperature in TiO2 Photocatalysts. *RSC Advances* **2016**.
22. Wetchakun, N.; Phanichphant, S. J. C. A. P., Effect of temperature on the degree of anatase–rutile transformation in titanium dioxide nanoparticles synthesized by the modified sol–gel method. **2008,** *8* (3-4), 343-346.
23. Mahdy, M. A.; El Zawawi, I., The correlation of γ-irradiation, particle size and their effects on physical properties of $AgInSe_2$ nanostructure thin films. *Materials Science in Semiconductor Processing* **2016,** *56*, 43-51.
24. Yao, D.; Liu, H.; Liu, Y.; Dong, C.; Zhang, K.; Sheng, Y.; Cui, J.; Zhang, H.; Yang, B., Phosphine-free synthesis of Ag–In–Se alloy nanocrystals with visible emissions. *Nanoscale* **2015,** *7* (44), 18570-18578.
25. White, M. A.; Baumler, K. J.; Chen, Y.; Venkatesh, A.; Medina-Gonzalez, A. M.; Rossini, A. J.; Zaikina, J. V.; Chan, E. M.; Vela, J., Expanding the I–II–V Phase Space: Soft Synthesis of Polytypic Ternary and Binary Zinc Antimonides. *Chemistry of Materials* **2018,** *30* (17), 6173-6182.
26. Böcher, F.; Culver, S. P.; Peilstöcker, J.; Weldert, K. S.; Zeier, W. G., Vacancy and anti-site disorder scattering in AgBiSe 2 thermoelectrics. *Dalton Transactions* **2017,** *46* (12), 3906-3914.
27. Ghoshal, S.; Kumbhare, L. B.; Jain, V. K.; Dey, G. K., A facile synthesis of MInSe 2 (M= Cu, Ag) via low temperature pyrolysis of single source molecular precursors,[(R 3 P) 2 MIn (SeCOAr) 4]. *Bulletin of Materials Science* **2007,** *30* (2), 173-178.
28. Tappan, B. A.; Horton, M. K.; Brutchey, R. L., Ligand-Mediated Phase Control in Colloidal $AgInSe_2$ Nanocrystals. *Chemistry of Materials* **2019,** *32(7)*, 2935-2945.
29. Stroyuk, O.; Raevskaya, A.; Gaponik, N., Solar light harvesting with multinary metal chalcogenide nanocrystals. *Chemical Society Reviews* **2018,** *47* (14), 5354-5422.
30. Fan, X.; Zhang, J.; Yang, Y.; Xia, D.; Dong, G.; Li, M.; Qiu, L.; Zhang, Y.; Fan, R., Synthesis of AgBiSe2 via a facile low temperature aqueous solution route for enhanced photoelectric properties devices. *Journal of Solid State Chemistry* **2019,** *277*, 686-692.
31. Abazović, N. D.; Čomor, M. I.; Mitrić, M. N.; Piscopiello, E.; Radetić, T.; Janković, I. A.; Nedeljković, J. M., Ligand mediated synthesis of $AgInSe_2$ nanoparticles with

tetragonal/orthorhombic crystal phases. *Journal of Nanoparticle Research* **2012,** *14* (4), 810.
32. Yoshino, K.; Kinoshita, A.; Shirahata, Y.; Oshima, M.; Nomoto, K.; Yoshitake, T.; Ozaki, S.; Ikari, T. In *Structural and electrical characterization of $AgInSe_2$ crystals grown by hot-press method*, Journal of Physics: Conference Series, IOP Publishing: 2008; p 042042.
33. Dumortier, H.; Lacotte, S.; Pastorin, G.; Marega, R.; Wu, W.; Bonifazi, D.; Briand, J.-P.; Prato, M.; Muller, S.; Bianco, A., Functionalized carbon nanotubes are non-cytotoxic and preserve the functionality of primary immune cells. *Nano letters* **2006,** *6* (7), 1522-1528.
34. Lammel T, Boisseaux P, Fernandez-Cruz ML, Navas JM. Internalization and cytotoxicity of graphene oxide and carboxyl graphene nanoplatelets in the human hepatocellular carcinoma cell line Hep G2. Part Fibre Toxicol. **2013**, *10(1)*, 1-21.
35. Faria, A.; Moraes, A.; Marcato, P.; Martinez, D.; Durán, N.; Filho, A., Eco-friendly decoration of graphene oxide with biogenic silver nanoparticles: antibacterial and antibiofilm activity. *J Nanopart Res* **2014,** *16*(2), 1-16.
36. Teta, M.; Rankin, M. M.; Long, S. Y.; Stein, G. M.; Kushner, J. A., Growth and regeneration of adult β cells does not involve specialized progenitors. *Developmental cell* **2007,** *12* (5), 817-826.
37. Li, J.; Zhu, Y.; Li, W.; Zhang, X.; Peng, Y.; Huang, Q., Nanodiamonds as intracellular transporters of chemotherapeutic drug. *Biomaterials* **2010,** *31* (32), 8410-8418.
38. de Luna, L. A. V.; de Moraes, A. C. M.; Consonni, S. R.; Pereira, C. D.; Cadore, S.; Giorgio, S.; Alves, O. L., Comparative in vitro toxicity of a graphene oxide-silver nanocomposite and the pristine counterparts toward macrophages. *Journal of Nanobiotechnology* **2016,** *14* (1), 12.
39. Yue, H.; Wei, W.; Yue, Z. G.; Wang, B.; Luo, N. N.; Gao, Y. J., The role of the lateral dimension of graphene oxide in the regulation of cellular responses. *Biomaterials* **2012,** *33*.
40. Kroemer, G.; Galluzzi, L.; Vandenabeele, P.; Abrams, J.; Alnemri, E.; Baehrecke, E.; Blagosklonny, M.; El-Deiry, W.; Golstein, P.; Green, D., Classification of cell death: recommendations of the Nomenclature Committee on Cell Death 2009. *Cell Death & Differentiation* **2009,** *16* (1), 3-11.
41. Baehrecke, E. H., How death shapes life during development. *Nature Reviews Molecular Cell Biology* **2002,** *3* (10), 779-787.
42. Alkilany, A. M.; Nagaria, P. K.; Hexel, C. R.; Shaw, T. J.; Murphy, C. J.; Wyatt, M. D., Cellular Uptake and Cytotoxicity of Gold Nanorods: Molecular Origin of Cytotoxicity and Surface Effects. *Small* **2009,** *5* (6), 701-708.
43. Kerr, J. F.; Wyllie, A. H.; Currie, A. R., Apoptosis: a basic biological phenomenon with wide-ranging implications in tissue kinetics. *British journal of cancer* **1972,** *26* (4), 239.
44. Garrido, C.; Kroemer, G., Life's smile, death's grin: vital functions of apoptosis-executing proteins. *Current opinion in cell biology* **2004,** *16* (6), 639-646.
45. Galluzzi, L.; Joza, N.; Tasdemir, E.; Maiuri, M.; Hengartner, M.; Abrams, J.; Tavernarakis, N.; Penninger, J.; Madeo, F.; Kroemer, G., No death without life: vital functions of apoptotic effectors. *Cell Death & Differentiation* **2008,** *15* (7), 1113-1123.
46. Zhao, F.; Zhao, Y.; Liu, Y.; Chang, X.; Chen, C.; Zhao, Y., Cellular uptake, intracellular trafficking, and cytotoxicity of nanomaterials. *Small* **2011,** *7* (10), 1322-1337.

47. Etacheri, V.; Di Valentin, C.; Schneider, J.; Bahnemann, D.; Pillai, S. C., Visible-light activation of TiO 2 photocatalysts: Advances in theory and experiments. *Journal of Photochemistry and Photobiology C: Photochemistry Reviews* **2015,** *25*, 1-29.
48. Schneider, J.; Matsuoka, M.; Takeuchi, M.; Zhang, J.; Horiuchi, Y.; Anpo, M.; Bahnemann, D. W., Understanding TiO2 photocatalysis: mechanisms and materials. *Chemical reviews* **2014,** *114* (19), 9919-9986.
49. Abe, R., Recent progress on photocatalytic and photoelectrochemical water splitting under visible light irradiation. *Journal of Photochemistry and Photobiology C: Photochemistry Reviews* **2010,** *11* (4), 179-209.
50. Maeda, K.; Domen, K., Photocatalytic water splitting: recent progress and future challenges. *The Journal of Physical Chemistry Letters* **2010,** *1* (18), 2655-2661.
51. Fujishima, A.; Zhang, X.; Tryk, D. A., TiO 2 photocatalysis and related surface phenomena. *Surface Science Reports* **2008,** *63* (12), 515-582.
52. Peiró, A. M.; Colombo, C.; Doyle, G.; Nelson, J.; Mills, A.; Durrant, J. R., Photochemical reduction of oxygen adsorbed to nanocrystalline TiO2 films: A transient absorption and oxygen scavenging study of different TiO2 preparations. *The Journal of Physical Chemistry B* **2006,** *110* (46), 23255-23263.
53. Emeline, A.; Ryabchuk, V.; Serpone, N., Dogmas and misconceptions in heterogeneous photocatalysis. Some enlightened reflections. *The Journal of Physical Chemistry B* **2005,** *109* (39), 18515-18521.
54. Kamat, P. V., Photophysical, photochemical and photocatalytic aspects of metal nanoparticles. ACS Publications: **2002**, *106*(32), 7729-7744..
55. Fujishima, A.; Zhang, X., Titanium dioxide photocatalysis: present situation and future approaches. *Comptes Rendus Chimie* **2006,** *9* (5), 750-760.
56. Kamat, P. V.; Bedja, I.; Hotchandani, S., Photoinduced charge transfer between carbon and semiconductor clusters. One-electron reduction of C60 in colloidal TiO2 semiconductor suspensions. *The Journal of Physical Chemistry* **1994,** *98* (37), 9137-9142.
57. Yoshihara, T.; Katoh, R.; Furube, A.; Tamaki, Y.; Murai, M.; Hara, K.; Murata, S.; Arakawa, H.; Tachiya, M., Identification of reactive species in photoexcited nanocrystalline TiO2 films by wide-wavelength-range (400− 2500 nm) transient absorption spectroscopy. *The Journal of Physical Chemistry B* **2004,** *108* (12), 3817-3823.
58. Serpone, N.; Lawless, D.; Khairutdinov, R., Size effects on the photophysical properties of colloidal anatase TiO2 particles: size quantization versus direct transitions in this indirect semiconductor? *The journal of Physical Chemistry* **1995,** *99* (45), 16646-16654.
59. Lawless, D.; Serpone, N.; Meisel, D., Role of hydroxyl radicals and trapped holes in photocatalysis. A pulse radiolysis study. *The Journal of Physical Chemistry* **1991,** *95* (13), 5166-5170.
60. Bahnemann, D. W.; Hilgendorff, M.; Memming, R., Charge carrier dynamics at TiO2 particles: reactivity of free and trapped holes. *The Journal of Physical Chemistry B* **1997,** *101* (21), 4265-4275.
61. Furube, A.; Asahi, T.; Masuhara, H.; Yamashita, H.; Anpo, M., Charge carrier dynamics of standard TiO2 catalysts revealed by femtosecond diffuse reflectance spectroscopy. *The Journal of Physical Chemistry B* **1999,** *103* (16), 3120-3127.
62. Colombo, D. P.; Bowman, R. M., Does interfacial charge transfer compete with charge carrier recombination? A femtosecond diffuse reflectance investigation of TiO2 nanoparticles. *The Journal of Physical Chemistry* **1996,** *100* (47), 18445-18449.

63. Iwata, K.; Takaya, T.; Hamaguchi, H.-o.; Yamakata, A.; Ishibashi, T.-a.; Onishi, H.; Kuroda, H., Carrier Dynamics in TiO2 and Pt/TiO2 Powders Observed by Femtosecond Time-Resolved Near-Infrared Spectroscopy at a Spectral Region of 0.9–1.5 μm with the Direct Absorption Method. *The Journal of Physical Chemistry B* **2004,** *108* (52), 20233-20239.
64. Yamakata, A.; Ishibashi, T.-a.; Takeshita, K.; Onishi, H., Time-resolved infrared absorption study of photochemical reactions over metal oxides. *Topics in catalysis* **2005,** *35* (3), 211-216.
65. Colbeau-Justin, C.; Kunst, M.; Huguenin, D., Structural influence on charge-carrier lifetimes in TiO2 powders studied by microwave absorption. *Journal of Materials Science* **2003,** *38* (11), 2429-2437.
66. Martin, S. T.; Herrmann, H.; Choi, W.; Hoffmann, M. R., Time-resolved microwave conductivity. Part 1.—TiO 2 photoreactivity and size quantization. *Journal of the Chemical Society, Faraday Transactions* **1994,** *90* (21), 3315-3322.
67. Martin, S. T.; Herrmann, H.; Hoffmann, M. R., Time-resolved microwave conductivity. Part 2.—Quantum-sized TiO_2 and the effect of adsorbates and light intensity on charge-carrier dynamics. *Journal of the chemical society, Faraday transactions* **1994,** *90* (21), 3323-3330.
68. Furube, A.; Asahi, T.; Masuhara, H.; Yamashita, H.; Anpo, M., Direct observation of a picosecond charge separation process in photoexcited platinum-loaded TiO 2 particles by femtosecond diffuse reflectance spectroscopy. *Chemical physics letters* **2001,** *336* (5), 424-430.
69. Henglein, A., Small-particle research: physicochemical properties of extremely small colloidal metal and semiconductor particles. *Chemical Reviews* **1989,** *89* (8), 1861-1873.
70. Kolle, U.; Moser, J.; Gratzel, M., Dynamics of interfacial charge-transfer reactions in semiconductor dispersions. Reduction of cobaltoceniumdicarboxylate in colloidal TiO2. *Inorganic chemistry* **1985,** *24* (14), 2253-2258.
71. Szczepankiewicz, S. H.; Colussi, A.; Hoffmann, M. R., Infrared spectra of photoinduced species on hydroxylated titania surfaces. *The Journal of Physical Chemistry B* **2000,** *104* (42), 9842-9850.
72. Bahnemann, D.; Henglein, A.; Lilie, J.; Spanhel, L., Flash photolysis observation of the absorption spectra of trapped positive holes and electrons in colloidal titanium dioxide. *The Journal of Physical Chemistry* **1984,** *88* (4), 709-711.
73. Martin, S. T.; Morrison, C. L.; Hoffmann, M. R., Photochemical mechanism of size-quantized vanadium-doped TiO_2 particles. *The Journal of Physical Chemistry* **1994,** *98* (51), 13695-13704.
74. Yang, X.; Tamai, N., How fast is interfacial hole transfer? In situ monitoring of carrier dynamics in anatase TiO_2 nanoparticles by femtosecond laser spectroscopy. *Physical Chemistry Chemical Physics* **2001,** *3* (16), 3393-3398.
75. Tamaki, Y.; Furube, A.; Katoh, R.; Murai, M.; Hara, K.; Arakawa, H.; Tachiya, M., Trapping dynamics of electrons and holes in a nanocrystalline TiO_2 film revealed by femtosecond visible/near-infrared transient absorption spectroscopy. *Comptes Rendus Chimie* **2006,** *9* (2), 268-274.
76. Tamaki, Y.; Furube, A.; Murai, M.; Hara, K.; Katoh, R.; Tachiya, M., Dynamics of efficient electron–hole separation in TiO_2 nanoparticles revealed by femtosecond transient absorption spectroscopy under the weak-excitation condition. *Physical Chemistry Chemical Physics* **2007,** *9* (12), 1453-1460.

77. Tasdemir, E.; Galluzzi, L.; Maiuri, M. C.; Criollo, A.; Vitale, I.; Hangen, E.; Modjtahedi, N.; Kroemer, G., Methods for assessing autophagy and autophagic cell death. *Autophagosome and Phagosome* **2008**, 29-76.
78. Levine, B.; Kroemer, G., Autophagy in the pathogenesis of disease. *Cell* **2008,** *132* (1), 27-42.
79. González-Polo, R.-A.; Boya, P.; Pauleau, A.-L.; Jalil, A.; Larochette, N.; Souquère, S.; Eskelinen, E.-L.; Pierron, G.; Saftig, P.; Kroemer, G., The apoptosis/autophagy paradox: autophagic vacuolization before apoptotic death. *Journal of cell science* **2005,** *118* (14), 3091-3102.
80. Saptarshi, S. R.; Duschl, A.; Lopata, A. L., Interaction of nanoparticles with proteins: relation to bio-reactivity of the nanoparticle. *Journal of nanobiotechnology* **2013,** *11* (1), 26.
81. Chakravarthi, S.; Jessop, C. E.; Bulleid, N. J., The role of glutathione in disulphide bond formation and endoplasmic-reticulum-generated oxidative stress. *EMBO reports* **2006,** *7* (3), 271-275.
82. Stahl, W.; Junghans, A.; de Boer, B.; Driomina, E. S.; Briviba, K.; Sies, H., Carotenoid mixtures protect multilamellar liposomes against oxidative damage: synergistic effects of lycopene and lutein. *FEBS letters* **1998,** *427* (2), 305-308.
83. Apel, K.; Hirt, H., Reactive oxygen species: metabolism, oxidative stress, and signal transduction. *Annu. Rev. Plant Biol.* **2004,** *55*, 373-399.
84. Jornot, L.; Petersen, H.; JUNOD, A. F., Hydrogen peroxide-induced DNA damage is independent of nuclear calcium but dependent on redox-active ions. *Biochemical Journal* **1998,** *335* (1), 85-94.
85. Hajba, L.; Guttman, A., The use of magnetic nanoparticles in cancer theranostics: Toward handheld diagnostic devices. *Biotechnology advances* **2016,** *34* (4), 354-361.
86. Fu, J.; Yu, J.; Jiang, C.; Cheng, B., g-C3N4-Based heterostructured photocatalysts. *Advanced Energy Materials* **2018,** *8* (3), 1701503.
87. Wang, H.; Zhang, L.; Chen, Z.; Hu, J.; Li, S.; Wang, Z.; Liu, J.; Wang, X., Semiconductor heterojunction photocatalysts: design, construction, and photocatalytic performances. *Chemical Society Reviews* **2014,** *43* (15), 5234-5244.
88. Roul, B.; Kumar, M.; Rajpalke, M. K.; Bhat, T. N.; Krupanidhi, S., Binary group III-nitride based heterostructures: band offsets and transport properties. *Journal of Physics D: Applied Physics* **2015,** *48* (42), 423001.
89. Wang, Y.; Wang, Q.; Zhan, X.; Wang, F.; Safdar, M.; He, J., Visible light driven type II heterostructures and their enhanced photocatalysis properties: a review. *Nanoscale* **2013,** *5* (18), 8326-8339.
90. Ong, W.-J.; Tan, L.-L.; Ng, Y. H.; Yong, S.-T.; Chai, S.-P., Graphitic carbon nitride (g-C3N4)-based photocatalysts for artificial photosynthesis and environmental remediation: are we a step closer to achieving sustainability? *Chem. Rev* **2016,** *116* (12), 7159-7329.
91. Low, J.; Yu, J.; Jaroniec, M.; Wageh, S.; Al-Ghamdi, A. A., Heterojunction photocatalysts. *Advanced Materials* **2017,** *29* (20), 1601694.
92. Xu, C.; Anusuyadevi, P. R.; Aymonier, C.; Luque, R.; Marre, S., Nanostructured materials for photocatalysis. *Chemical Society Reviews* **2019,** *48*(14), 3868-3902.
93. Baranov, A.; Bertru, N.; Cuminal, Y.; Boissier, G.; Alibert, C.; Joullie, A., Observation of room-temperature laser emission from type III InAs/GaSb multiple quantum well structures. *Applied physics letters* **1997,** *71* (6), 735-737.

94. Li, Z.; Meng, X.; Zhang, Z., Recent development on MoS2-based photocatalysis: A review. *Journal of Photochemistry and Photobiology C: Photochemistry Reviews* **2018,** *35*, 39-55.
95. Moniz, S. J.; Shevlin, S. A.; Martin, D. J.; Guo, Z.-X.; Tang, J., Visible-light driven heterojunction photocatalysts for water splitting–a critical review. *Energy & Environmental Science* **2015,** *8* (3), 731-759.
96. Khan, M. R.; Chuan, T. W.; Yousuf, A.; Chowdhury, M.; Cheng, C. K., Schottky barrier and surface plasmonic resonance phenomena towards the photocatalytic reaction: study of their mechanisms to enhance photocatalytic activity. *Catalysis Science & Technology* **2015,** *5* (5), 2522-2531.
97. Teoh, W.; Scott, J.; Amal, R., Progress in Heterogeneous Photocatalysis: From Classical Radical Chemistry to Engineering Nanomaterials and Solar Reactors. *Journal of Physical Chemistry Letters* **2012,** *3* (5), 629-639.
98. Parsons, R., The rate of electrolytic hydrogen evolution and the heat of adsorption of hydrogen. *Transactions of the Faraday Society* **1958,** *54*, 1053-1063.
99. Hinnemann, B.; Moses, P. G.; Bonde, J.; Jørgensen, K. P.; Nielsen, J. H.; Horch, S.; Chorkendorff, I.; Nørskov, J. K., Biomimetic hydrogen evolution: MoS2 nanoparticles as catalyst for hydrogen evolution. *Journal of the American Chemical Society* **2005,** *127* (15), 5308-5309.
100. Rao, C.; Dey, S., Solar thermochemical splitting of water to generate hydrogen. *Proceedings of the National Academy of Sciences of the United States of America* **2017,** *114* (51), 13385-13393.
101. https://www.energy.gov/eere/fuelcells/hydrogen-production-thermochemical-water-splitting https://www.energy.gov/eere/fuelcells/hydrogen-production-thermochemical-water-splitting.
102. Wu, X.; Onuki, K., Thermochemical water splitting for hydrogen production utilizing nuclear heat from an HTGR. *Tsinghua Science and Technology* **2005,** *10* (2), 270-276.
103. Maness, P.-C.; Yu, J.; Eckert, C.; Ghirardi, M. L., Photobiological hydrogen production–prospects and challenges. *Microbe* **2009,** *4* (6), 659-667.
104. Poudyal, R.; Tiwari, I.; Koirala, A.; Masukawa, H.; Inoue, K.; Tomo, T.; Najafpour, M.; Allakhverdiev, S.; Veziroğlu, T., Hydrogen production using photobiological methods. In *Compendium of Hydrogen Energy*, Elsevier: 2015; pp 289-317.
105. Das, D.; Veziroğlu, T. N., Hydrogen production by biological processes: a survey of literature. *International journal of hydrogen energy* **2001,** *26* (1), 13-28.
106. Asada, Y.; Miyake, J., Photobiological hydrogen production. *Journal of Bioscience and Bioengineering* **1999,** *88* (1), 1-6.
107. FUJISHIMA, A.; HONDA, K., ELECTROCHEMICAL PHOTOLYSIS OF WATER AT A SEMICONDUCTOR ELECTRODE. *Nature* **1972,** *238* (5358), 37.
108. Bard, A. J., Photoelectrochemistry and heterogeneous photo-catalysis at semiconductors. *Journal of Photochemistry* **1979,** *10* (1), 59-75.
109. Xie, G.; Zhang, K.; Guo, B.; Liu, Q.; Fang, L.; Gong, J. R., Graphene-based materials for hydrogen generation from light-driven water splitting. *Advanced materials* **2013,** *25* (28), 3820-3839.
110. Ren, Y.; Xu, Q.; Zheng, X.; Fu, Y.; Wang, Z.; Chen, H.; Weng, Y.; Zhou, Y., Building of peculiar heterostructure of Ag/two-dimensional fullerene shell-WO3-x for enhanced photoelectrochemical performance. *Applied Catalysis B-Environmental* **2018,** *231*, 381-390.

111. Li, X.; Yu, J.; Low, J.; Fang, Y.; Xiao, J.; Chen, X., Engineering heterogeneous semiconductors for solar water splitting. *Journal of Materials Chemistry A* **2015,** *3* (6), 2485-2534.
112. Ibáñez, J. A.; Litter, M. I.; Pizarro, R. A., Photocatalytic bactericidal effect of TiO 2 on Enterobacter cloacae: comparative study with other Gram (−) bacteria. *Journal of Photochemistry and photobiology A: Chemistry* **2003,** *157* (1), 81-85.
113. Li, Y.; Zhang, W.; Niu, J.; Chen, Y., Mechanism of photogenerated reactive oxygen species and correlation with the antibacterial properties of engineered metal-oxide nanoparticles. *ACS nano* **2012,** *6* (6), 5164-5173.
114. Matsunaga, T.; Tomoda, R.; Nakajima, T.; Wake, H., Photoelectrochemical sterilization of microbial cells by semiconductor powders. *FEMS Microbiology letters* **1985,** *29* (1-2), 211-214.
115. Saito, T.; Iwase, T.; Horie, J.; Morioka, T., Mode of photocatalytic bactericidal action of powdered semiconductor TiO2 on mutans streptococci. *Journal of Photochemistry and Photobiology B: Biology* **1992,** *14* (4), 369-379.
116. Kikuchi, Y.; Sunada, K.; Iyoda, T.; Hashimoto, K.; Fujishima, A., Photocatalytic bactericidal effect of TiO 2 thin films: dynamic view of the active oxygen species responsible for the effect. *Journal of photochemistry and photobiology A: Chemistry* **1997,** *106* (1), 51-56.
117. Jacoby, W. A.; Maness, P. C.; Wolfrum, E. J.; Blake, D. M.; Fennell, J. A., Mineralization of bacterial cell mass on a photocatalytic surface in air. *Environmental Science & Technology* **1998,** *32* (17), 2650-2653.
118. Maness, P.-C.; Smolinski, S.; Blake, D. M.; Huang, Z.; Wolfrum, E. J.; Jacoby, W. A., Bactericidal activity of photocatalytic TiO2 reaction: toward an understanding of its killing mechanism. *Applied and environmental microbiology* **1999,** *65* (9), 4094-4098.
119. Bagchi, D.; Bagchi, M.; Hassoun, E.; Stohs, S., Detection of paraquat-induced in vivo lipid peroxidation by gas chromatography/mass spectrometry and high-pressure liquid chromatography. *Journal of analytical toxicology* **1993,** *17* (7), 411-414.
120. Sökmen, M.; Candan, F.; Sümer, Z., Disinfection of E. coli by the Ag-TiO 2/UV system: lipidperoxidation. *Journal of Photochemistry and Photobiology A: Chemistry* **2001,** *143* (2), 241-244.
121. Kiwi, J.; Nadtochenko, V., Evidence for the mechanism of photocatalytic degradation of the bacterial wall membrane at the TiO2 interface by ATR-FTIR and laser kinetic spectroscopy. *Langmuir* **2005,** *21* (10), 4631-4641.
122. Pigeot-Rémy, S.; Simonet, F.; Errazuriz-Cerda, E.; Lazzaroni, J.; Atlan, D.; Guillard, C., Photocatalysis and disinfection of water: identification of potential bacterial targets. *Applied Catalysis B: Environmental* **2011,** *104* (3), 390-398.
123. Wang, W.; Zhang, L.; An, T.; Li, G.; Yip, H.-Y.; Wong, P.-K., Comparative study of visible-light-driven photocatalytic mechanisms of dye decolorization and bacterial disinfection by B–Ni-codoped TiO 2 microspheres: the role of different reactive species. *Applied Catalysis B: Environmental* **2011,** *108*, 108-116.
124. Matai, I.; Sachdev, A.; Dubey, P.; Kumar, S. U.; Bhushan, B.; Gopinath, P., Antibacterial activity and mechanism of Ag–ZnO nanocomposite on S. aureus and GFP-expressing antibiotic resistant E. coli. *Colloids and Surfaces B: Biointerfaces* **2014,** *115*, 359-367.
125. Ventola, C. L., The antibiotic resistance crisis: part 1: causes and threats. *Pharmacy and therapeutics* **2015,** *40* (4), 277.

126. Perumal Samy, R.; Gopalakrishnakone, P., Therapeutic potential of plants as anti-microbials for drug discovery. *Evidence-based complementary and alternative medicine* **2010,** *7* (3), 283-294.
127. Hawkey, P., The growing burden of antimicrobial resistance. *Journal of antimicrobial chemotherapy* **2008,** *62* (suppl_1), i1-i9.
128. Laxminarayan, R.; Duse, A.; Wattal, C.; Zaidi, A. K.; Wertheim, H. F.; Sumpradit, N.; Vlieghe, E.; Hara, G. L.; Gould, I. M.; Goossens, H., Antibiotic resistance—the need for global solutions. *The Lancet infectious diseases* **2013,** *13* (12), 1057-1098.
129. Tasaki, S.; Nakayama, M.; Shoji, W., Self-organization of bacterial communities against environmental pH variation: Controlled chemotactic motility arranges cell population structures in biofilms. *PloS one* **2017,** *12* (3), e0173195.
130. Thanner, S.; Drissner, D.; Walsh, F., Antimicrobial resistance in agriculture. *MBio* **2016,** *7* (2), e02227-15.
131. Berendonk, T. U.; Manaia, C. M.; Merlin, C.; Fatta-Kassinos, D.; Cytryn, E.; Walsh, F.; Bürgmann, H.; Sørum, H.; Norström, M.; Pons, M.-N., Tackling antibiotic resistance: the environmental framework. *Nature Reviews Microbiology* **2015,** *13* (5), 310.
132. Malizos, K. N.; Kirketerp-Møller, K., Incidence and Socioeconomic Impact of Bone and Joint Infections (BJIs): The European Perspective. In *Periprosthetic Joint Infections*, Springer: 2016; pp 3-18.
133. Aslam, B.; Wang, W.; Arshad, M. I.; Khurshid, M.; Muzammil, S.; Rasool, M. H.; Nisar, M. A.; Alvi, R. F.; Aslam, M. A.; Qamar, M. U., Antibiotic resistance: a rundown of a global crisis. *Infection and drug resistance* **2018,** *11*, 1645.
134. Lundholm, K.; Hyltander, A.; Sandström, R., Nutrition and multiple organ failure. *Nutrition research reviews* **1992,** *5* (1), 97-113.
135. Organization, W. H. *WHO global strategy for containment of antimicrobial resistance*; Geneva: World Health Organization: 2001.
136. H. Jones, O.; Voulvoulis, N.; Lester, J., Human pharmaceuticals in wastewater treatment processes. *Critical Reviews in Environmental Science and Technology* **2005,** *35* (4), 401-427.
137. Chapman, D. V.; Organization, W. H., Water quality assessments: a guide to the use of biota, sediments and water in environmental monitoring. **1996**.
138. Rizzo, L.; Manaia, C.; Merlin, C.; Schwartz, T.; Dagot, C.; Ploy, M.; Michael, I.; Fatta-Kassinos, D., Urban wastewater treatment plants as hotspots for antibiotic resistant bacteria and genes spread into the environment: a review. *Science of the total environment* **2013,** *447*, 345-360.
139. Comninellis, C.; Kapalka, A.; Malato, S.; Parsons, S. A.; Poulios, I.; Mantzavinos, D., Advanced oxidation processes for water treatment: advances and trends for R&D. *Journal of Chemical Technology & Biotechnology: International Research in Process, Environmental & Clean Technology* **2008,** *83* (6), 769-776.
140. Zhu, X.-D.; Wang, Y.-J.; Sun, R.-J.; Zhou, D.-M., Photocatalytic degradation of tetracycline in aqueous solution by nanosized TiO_2. *Chemosphere* **2013,** *92* (8), 925-932.
141. Borghi, A. A.; Palma, M. S. A., Tetracycline: production, waste treatment and environmental impact assessment. *Brazilian Journal of Pharmaceutical Sciences* **2014,** *50* (1), 25-40.
142. Bolobajev, J.; Trapido, M.; Goi, A., Effect of iron ion on doxycycline photocatalytic and Fenton-based autocatatalytic decomposition. *Chemosphere* **2016,** *153*, 220-226.

143. Huang, H.; Feng, J.; Zhang, S.; Zhang, H.; Wang, X.; Yu, T.; Chen, C.; Yi, Z.; Ye, J.; Li, Z., Molecular-Level Understanding of the Deactivation Pathways during Methanol Photo-reforming on Pt-decorated TiO_2. *Applied Catalysis B: Environmental* **2020**, *272*, 118980.
144. Fu, J.; Xu, Q.; Low, J.; Jiang, C.; Yu, J., Ultrathin 2D/2D WO3/g-C3N4 step-scheme H2-production photocatalyst. *Applied Catalysis B: Environmental* **2019,** *243*, 556-565.
145. Zhang, Y.; Huang, Z.; Shi, J.; Guan, X.; Cheng, C.; Zong, S.; Huangfu, Y.; Ma, L.; Guo, L., Maleic hydrazide-based molecule doping in three-dimensional lettuce-like graphite carbon nitride towards highly efficient photocatalytic hydrogen evolution. *Applied Catalysis B: Environmental* **2020**, *272*,119009.
146. Sahu, A.; Qi, L.; Kang, M. S.; Deng, D.; Norris, D. J., Facile synthesis of silver chalcogenide (Ag2E; E= Se, S, Te) semiconductor nanocrystals. *Journal of the American Chemical Society* **2011,** *133* (17), 6509-6512.
147. Oluwafemi, O. S.; May, B. M.; Parani, S.; Tsolekile, N., Facile, large scale synthesis of water soluble $AgInSe_2$/ZnSe quantum dots and its cell viability assessment on different cell lines. *Materials Science and Engineering: C* **2020,** *106*, 110181.
148. Abdullaev, M.; Alhasov, A.; Magomedova, D. K., Fabrication and properties of $CuInSe_2$/$AgInSe_2$/CdS double heterojunction cascade solar cells. *Inorganic Materials* **2014,** *50* (3), 228-232.
149. Sun, W.; Dacek, S. T.; Ong, S. P.; Hautier, G.; Jain, A.; Richards, W. D.; Gamst, A. C.; Persson, K. A.; Ceder, G., The thermodynamic scale of inorganic crystalline metastability. *Science advances* **2016,** *2* (11), e1600225.
150. Samanta, M.; Ghosh, T.; Arora, R.; Waghmare, U. V.; Biswas, K., Realization of Both n-and p-Type GeTe Thermoelectrics: Electronic Structure Modulation by $AgBiSe_2$ Alloying. *Journal of the American Chemical Society* **2019,** *141* (49), 19505-19512.
151. Blum, V.; Gehrke, R.; Hanke, F.; Havu, P.; Havu, V.; Ren, X.; Reuter, K.; Scheffler, M., Ab initio molecular simulations with numeric atom-centered orbitals. *Computer Physics Communications* **2009,** *180* (11), 2175-2196.
152. Perdew, J. P.; Ernzerhof, M.; Burke, K., Rationale for mixing exact exchange with density functional approximations. *The Journal of chemical physics* **1996,** *105* (22), 9982-9985.
153. Tkatchenko, A.; Scheffler, M., Accurate molecular van der Waals interactions from ground-state electron density and free-atom reference data. *Physical review letters* **2009,** *102* (7), 073005.
154. Head, J. D.; Zerner, M. C., A Broyden—Fletcher—Goldfarb—Shanno optimization procedure for molecular geometries. *Chemical physics letters* **1985,** *122* (3), 264-270.
155. Kresse, G.; Furthmüller, J., Efficiency of ab-initio total energy calculations for metals and semiconductors using a plane-wave basis set. *Computational materials science* **1996,** *6* (1), 15-50.
156. Perdew, J. P.; Burke, K.; Ernzerhof, M., Generalized gradient approximation made simple. *Physical review letters* **1996,** *77* (18), 3865.
157. Zhang, J.; Zhou, P.; Liu, J.; Yu, J., New understanding of the difference of photocatalytic activity among anatase, rutile and brookite TiO_2. *Physical Chemistry Chemical Physics* **2014,** *16* (38), 20382-20386.
158. Blöchl, P. E., Projector augmented-wave method. *Physical review B* **1994,** *50* (24), 17953.

159. Kresse, G.; Joubert, D., From ultrasoft pseudopotentials to the projector augmented-wave method. *Physical review b* **1999,** *59* (3), 1758.
160. Monkhorst, H. J.; Pack, J. D., Special points for Brillouin-zone integrations. *Physical review B* **1976,** *13* (12), 5188.
161. Heyd, J.; Scuseria, G. E.; Ernzerhof, M., Hybrid functionals based on a screened Coulomb potential. *The Journal of chemical physics* **2003,** *118* (18), 8207-8215.
162. Heyd, J.; Scuseria, G. E., Efficient hybrid density functional calculations in solids: Assessment of the Heyd–Scuseria–Ernzerhof screened Coulomb hybrid functional. *The Journal of chemical physics* **2004,** *121* (3), 1187-1192.
163. Heyd, J.; Peralta, J. E.; Scuseria, G. E.; Martin, R. L., Energy band gaps and lattice parameters evaluated with the Heyd-Scuseria-Ernzerhof screened hybrid functional. *The Journal of chemical physics* **2005,** *123* (17), 174101.
164. Jain, A.; Ong, S. P.; Hautier, G.; Chen, W.; Richards, W. D.; Dacek, S.; Cholia, S.; Gunter, D.; Skinner, D.; Ceder, G., Commentary: The Materials Project: A materials genome approach to accelerating materials innovation. *Apl Materials* **2013,** *1* (1), 011002.
165. Panneri, S.; Ganguly, P.; Mohan, M.; Nair, B. N.; Mohamed, A. A. P.; Warrier, K. G.; Hareesh, U., Photoregenerable, Bifunctional Granules of Carbon-Doped g-C_3N_4 as Adsorptive Photocatalyst for the Efficient Removal of Tetracycline Antibiotic. *ACS Sustainable Chemistry & Engineering* **2017,** *5* (2), 1610-1618.
166. Zhou, B.; Song, J.; Xie, C.; Chen, C.; Qian, Q.; Han, B., Mo–Bi–Cd Ternary Metal Chalcogenides: Highly Efficient Photocatalyst for CO_2 Reduction to Formic Acid Under Visible Light. *ACS Sustainable Chemistry & Engineering* **2018,** *6* (5), 5754-5759.
167. Santra, P. K.; Kamat, P. V., Tandem-layered quantum dot solar cells: tuning the photovoltaic response with luminescent ternary cadmium chalcogenides. *Journal of the American Chemical Society* **2013,** *135* (2), 877-885.
168. Xie, R.; Rutherford, M.; Peng, X., Formation of high-quality I– III– VI semiconductor nanocrystals by tuning relative reactivity of cationic precursors. *Journal of the American Chemical Society* **2009,** *131* (15), 5691-5697.
169. Tang, X.; Ho, W. B. A.; Xue, J. M., Synthesis of Zn-doped AgInS2 nanocrystals and their fluorescence properties. *The Journal of Physical Chemistry C* **2012,** *116* (17), 9769-9773.
170. Chen, B.; Pradhan, N.; Zhong, H., From Large-Scale Synthesis to Lighting Device Applications of Ternary I–III–VI Semiconductor Nanocrystals: Inspiring Greener Material Emitters. *The journal of physical chemistry letters* **2018,** *9* (2), 435-445.
171. Zhong, J.; Xiang, W.; Xie, C.; Liang, X.; Xu, X., Synthesis of spheroidal $AgBiS_2$ microcrystals by L-cysteine assisted method. *Materials Chemistry and Physics* **2013,** *138* (2-3), 773-779.
172. Bryndzia, L. T.; Kleppa, O., Standard enthalpies of formation of sulfides and sulfosalts in the Ag-Bi-S system by high-temperature, direct synthesis calorimetry. *Economic Geology* **1988,** *83* (1), 174-181.
173. Wang, J.; Yang, X.; Hu, W.; Li, B.; Yan, J.; Hu, J., Synthesis of $AgBiS_2$ microspheres by a templating method and their catalytic polymerization of alkylsilanes. *Chemical Communications* **2007,** (46), 4931-4933.
174. Thongtem, T.; Jaroenchaichana, J.; Thongtem, S., Cyclic microwave-assisted synthesis of flower-like and hexapod silver bismuth sulfide. *Materials Letters* **2009,** *63* (24-25), 2163-2166.
175. Pejova, B.; Grozdanov, I.; Nesheva, D.; Petrova, A., Size-dependent properties of sonochemically synthesized three-dimensional arrays of close-packed

semiconducting AgBiS2 quantum dots. *Chemistry of Materials* **2008,** *20* (7), 2551-2565.
176. Liu, H.; Zhong, J.; Liang, X.; Zhang, J.; Xiang, W., A mild biomolecule-assisted route for preparation of flower-like $AgBiS_2$ crystals. *Journal of Alloys and Compounds* **2011,** *509* (27), L267-L272.
177. Bellal, B.; Berger, M.; Trari, M., Physical and photoelectrochemical properties of spherical nanoparticles of α-$AgBiS_2$. *Journal of Solid State Chemistry* **2017,** *254*, 178-183.
178. Han, J.; Liu, Z.; Guo, K.; Ya, J.; Zhao, Y.; Zhang, X.; Hong, T.; Liu, J., High-efficiency $AgInS_2$-modified ZnO nanotube array photoelectrodes for all-solid-state hybrid solar cells. *ACS applied materials & interfaces* **2014,** *6* (19), 17119-17125.
179. Liu, B.; Li, X.; Zhao, Q.; Ke, J.; Tadé, M.; Liu, S., Preparation of $AgInS_2/TiO_2$ composites for enhanced photocatalytic degradation of gaseous o-dichlorobenzene under visible light. *Applied Catalysis B: Environmental* **2016,** *185*, 1-10.
180. Li, Z.; Wang, B.; Deng, Z.; Fu, X., Photoreduction Obtained MoS_2/CQDs for Assembly of Ternary MoS_2/CQDs/$ZnIn_2S_4$ Nanocomposite for Efficient Photocatalytic Hydrogen Evolution under Visible Light. *Journal of Materials Chemistry A* **2018,** *6*(40), 19735-19742.
181. Banerjee, S.; Pillai, S. C.; Falaras, P.; O'shea, K. E.; Byrne, J. A.; Dionysiou, D. D., New insights into the mechanism of visible light photocatalysis. *The journal of physical chemistry letters* **2014,** *5* (15), 2543-2554.
182. Ganguly, P.; Byrne, C.; Breen, A.; Pillai, S. C., Antimicrobial Activity of Photocatalysts: Fundamentals, Mechanisms, Kinetics and Recent Advances. *Applied Catalysis B: Environmental* **2017,** *225*, 51-75.
183. Mac Mahon, J.; Pillai, S. C.; Kelly, J. M.; Gill, L. W., Solar photocatalytic disinfection of E. coli and bacteriophages MS2, ΦX174 and PR772 using TiO_2, ZnO and ruthenium based complexes in a continuous flow system. *Journal of Photochemistry and Photobiology B: Biology* **2017,** *170*, 79-90.
184. Etacheri, V.; Michlits, G.; Seery, M. K.; Hinder, S. J.; Pillai, S. C., A highly efficient TiO2–x C x nano-heterojunction photocatalyst for visible light induced antibacterial applications. *ACS applied materials & interfaces* **2013,** *5* (5), 1663-1672.
185. Panneri, S.; Ganguly, P.; Nair, B. N.; Mohamed, A. A. P.; Warrier, K. G.; Hareesh, U. N., Copyrolysed C_3N_4-Ag/ZnO Ternary Heterostructure Systems for Enhanced Adsorption and Photocatalytic Degradation of Tetracycline. *European Journal of Inorganic Chemistry* **2016,** *2016* (31), 5068-5076.
186. Zhou, S.; Yang, J.; Li, W.; Jiang, Q.; Luo, Y.; Zhang, D.; Zhou, Z.; Li, X., Preparation and Photovoltaic Properties of Ternary $AgBiS_2$ Quantum Dots Sensitized TiO_2 Nanorods Photoanodes by Electrochemical Atomic Layer Deposition. *Journal of The Electrochemical Society* **2016,** *163* (3), D63-D67.
187. Huang, P.-C.; Yang, W.-C.; Lee, M.-W., $AgBiS_2$ semiconductor-sensitized solar cells. *The Journal of Physical Chemistry C* **2013,** *117* (36), 18308-18314.
188. Etacheri, V.; Seery, M. K.; Hinder, S. J.; Pillai, S. C., Highly visible light active $TiO_{2-x}N_x$ heterojunction photocatalysts. *Chemistry of Materials* **2010,** *22* (13), 3843-3853.
189. Yao, H.-B.; Gao, M.-R.; Yu, S.-H., Small organic molecule templating synthesis of organic–inorganic hybrid materials: their nanostructures and properties. *Nanoscale* **2010,** *2* (3), 322-334.
190. Jiang, N.; Wu, R.; Li, J.; Sun, Y.; Jian, J., Ethanol amine-assisted solvothermal growth of wurtzite-structured ZnS thin nanorods. *Journal of Alloys and Compounds* **2012,** *536*, 85-90.

191. Chen, Z.; Qin, X.; Zhou, T.; Wu, X.; Shao, S.; Xie, M.; Cui, Z., Ethanolamine-assisted synthesis of size-controlled indium tin oxide nanoinks for low temperature solution deposited transparent conductive films. *Journal of Materials Chemistry C* **2015,** *3* (43), 11464-11470.
192. Wang, X.; Zhang, Q.; Wan, Q.; Dai, G.; Zhou, C.; Zou, B., Controllable ZnO architectures by ethanolamine-assisted hydrothermal reaction for enhanced photocatalytic activity. *The Journal of Physical Chemistry C* **2011,** *115* (6), 2769-2775.
193. Hu, J.; Deng, B.; Tang, K.; Wang, C.; Qian, Y., Preparation and phase control of nanocrystalline silver indium sulfides via a hydrothermal route. *Journal of Materials Research* **2001,** *16* (12), 3411-3415.
194. Tipcompor, N.; Thongtem, S.; Thongtem, T., Transformation of cubic $AgBiS_2$ from nanoparticles to nanostructured flowers by a microwave-refluxing method. *Ceramics International* **2013,** *39*, S383-S387.
195. Martina, I.; Wiesinger, R.; Jembrih-Simbürger, D.; Schreiner, M., Micro-Raman characterisation of silver corrosion products: instrumental set up and reference database. *E-Preservation Science: Morana RTD [Online]* **2012**, 1-8.
196. Guin, S. N.; Banerjee, S.; Sanyal, D.; Pati, S. K.; Biswas, K., Origin of the Order–Disorder Transition and the Associated Anomalous Change of Thermopower in $AgBiS_2$ Nanocrystals: A Combined Experimental and Theoretical Study. *Inorganic chemistry* **2016,** *55* (12), 6323-6331.
197. Byrne, C.; Fagan, R.; Hinder, S.; McCormack, D. E.; Pillai, S. C., New approach of modifying the anatase to rutile transition temperature in TiO_2 photocatalysts. *RSC Advances* **2016,** *6* (97), 95232-95238.
198. Zhu, Y.; Wang, Y.; Ling, Q.; Zhu, Y., Enhancement of full-spectrum photocatalytic activity over $BiPO_4/Bi_2WO_6$ composites. *Applied Catalysis B: Environmental* **2017,** *200*, 222-229.
199. Li, N.; Lv, T.; Yao, Y.; Li, H.; Liu, K.; Chen, T., Compact graphene/MoS_2 composite films for highly flexible and stretchable all-solid-state supercapacitors. *Journal of Materials Chemistry A* **2017,** *5* (7), 3267-3273.
200. Leyland, N. S.; Podporska-Carroll, J.; Browne, J.; Hinder, S. J.; Quilty, B.; Pillai, S. C., Highly Efficient F, Cu doped TiO_2 anti-bacterial visible light active photocatalytic coatings to combat hospital-acquired infections. *Scientific reports* **2016,** *6*.
201. Liu, D.; Cai, D.; Yang, Y.; Zhong, H.; Zhao, Y.; Song, Y.; Yang, S.; Wu, H., Solvothermal synthesis of carbon nanotube-$AgBiS_2$ hybrids and their optical limiting properties. *Applied Surface Science* **2016,** *366*, 30-37.
202. Sun, M.-H.; Huang, S.-Z.; Chen, L.-H.; Li, Y.; Yang, X.-Y.; Yuan, Z.-Y.; Su, B.-L., Applications of hierarchically structured porous materials from energy storage and conversion, catalysis, photocatalysis, adsorption, separation, and sensing to biomedicine. *Chemical Society Reviews* **2016,** *45* (12), 3479-3563.
203. Nyholm, R.; Berndtsson, A.; Martensson, N., Core level binding energies for the elements Hf to Bi (Z= 72-83). *Journal of Physics C: Solid State Physics* **1980,** *13* (36), L1091.
204. Muilenberg, G., Handbook of X-ray photoelectron spectroscopy. *Perkin-Elmer Corporation* **1979**, 64.
205. Zhang, Z.; Liu, K.; Feng, Z.; Bao, Y.; Dong, B., Hierarchical sheet-on-sheet $ZnIn_2S_4$/g-C_3N_4 heterostructure with highly efficient photocatalytic H_2 production based on photoinduced interfacial charge transfer. *Scientific reports* **2016,** *6*, 19221.
206. Yang, G.; Chen, D.; Ding, H.; Feng, J.; Zhang, J. Z.; Zhu, Y.; Hamid, S.; Bahnemann, D. W., Well-designed 3D $ZnIn_2S_4$ nanosheets/TiO_2 nanobelts as direct Z-scheme

photocatalysts for CO_2 photoreduction into renewable hydrocarbon fuel with high efficiency. *Applied Catalysis B: Environmental* **2017,** *219*, 611-618.
207. Xia, Y.; Li, Q.; Lv, K.; Tang, D.; Li, M., Superiority of graphene over carbon analogs for enhanced photocatalytic H_2-production activity of $ZnIn_2S_4$. *Applied Catalysis B: Environmental* **2017,** *206*, 344-352.
208. Yang, G.; Ding, H.; Chen, D.; Feng, J.; Hao, Q.; Zhu, Y., Construction of urchin-like $ZnIn_2S_4$-Au-TiO_2 heterostructure with enhanced activity for photocatalytic hydrogen evolution. *Applied Catalysis B: Environmental* **2018,** *234*, 260-267.
209. Sze, S. M.; Ng, K. K., *Physics of semiconductor devices*. John wiley & sons: 2006.
210. Davis, E.; Mott, N., Conduction in non-crystalline systems V. Conductivity, optical absorption and photoconductivity in amorphous semiconductors. *Philosophical Magazine* **1970,** *22* (179), 0903-0922.
211. Yablonovitch, E., Photonic band-gap structures. *JOSA B* **1993,** *10* (2), 283-295.
212. Kaowphong, S., Biomolecule-assisted hydrothermal synthesis of silver bismuth sulfide with nanostructures. *Journal of Solid State Chemistry* **2012,** *189*, 108-111.
213. Han, C.; Luque, R.; Dionysiou, D. D., Facile preparation of controllable size monodisperse anatase titania nanoparticles. *Chemical Communications* **2012,** *48* (13), 1860-1862.
214. Deng, M.; Shen, S.; Zhang, Y.; Xu, H.; Wang, Q., A generalized strategy for controlled synthesis of ternary metal sulfide nanocrystals. *New Journal of Chemistry* **2014,** *38* (1), 77-83.
215. Verdier, T.; Coutand, M.; Bertron, A.; Roques, C., Antibacterial activity of TiO_2 photocatalyst alone or in coatings on E. coli: the influence of methodological aspects. *Coatings* **2014,** *4* (3), 670-686.
216. Karakitsou, K. E.; Verykios, X. E., Effects of altervalent cation doping of titania on its performance as a photocatalyst for water cleavage. *The Journal of Physical Chemistry* **1993,** *97* (6), 1184-1189.
217. Yang, Y.; Li, X.-j.; Chen, J.-t.; Wang, L.-y., Effect of doping mode on the photocatalytic activities of Mo/TiO2. *Journal of Photochemistry and Photobiology A: Chemistry* **2004,** *163* (3), 517-522.
218. Kumar, R.; Umar, A.; Kumar, G.; Akhtar, M.; Wang, Y.; Kim, S., Ce-doped ZnO nanoparticles for efficient photocatalytic degradation of direct red-23 dye. *Ceramics International* **2015,** *41* (6), 7773-7782.
219. Nethercot Jr, A. H., Prediction of Fermi energies and photoelectric thresholds based on electronegativity concepts. *Physical Review Letters* **1974,** *33* (18), 1088.
220. Butler, M., Photoelectrolysis and physical properties of the semiconducting electrode WO2. *Journal of Applied Physics* **1977,** *48* (5), 1914-1920.
221. Trasatti, S., The absolute electrode potential: an explanatory note (Recommendations 1986). *Pure Appl. Chem* **1986,** *58* (7), 955-966.
222. Mousavi, M.; Habibi-Yangjeh, A.; Abitorabi, M., Fabrication of novel magnetically separable nanocomposites using graphitic carbon nitride, silver phosphate and silver chloride and their applications in photocatalytic removal of different pollutants using visible-light irradiation. *Journal of colloid and interface science* **2016,** *480*, 218-231.
223. Mulliken, R. S., A new electroaffinity scale; together with data on valence states and on valence ionization potentials and electron affinities. *The Journal of Chemical Physics* **1934,** *2* (11), 782-793.

224. Habibi-Yangjeh, A.; Shekofteh-Gohari, M., Novel magnetic Fe3O4/ZnO/NiWO4 nanocomposites: Enhanced visible-light photocatalytic performance through pn heterojunctions. *Separation and Purification Technology* **2017,** *184*, 334-346.
225. Bose, R.; Manna, G.; Jana, S.; Pradhan, N., Ag2S–AgInS2: p–n junction heteronanostructures with quasi type-II band alignment. *Chemical Communications* **2014,** *50* (23), 3074-3077.
226. Liu, X.; Iocozzia, J.; Wang, Y.; Cui, X.; Chen, Y.; Zhao, S.; Li, Z.; Lin, Z., Noble metal–metal oxide nanohybrids with tailored nanostructures for efficient solar energy conversion, photocatalysis and environmental remediation. *Energy & Environmental Science* **2017,** *10* (2), 402-434.
227. Lin, L.-H.; Wu, C.-C.; Lai, C.-H.; Lee, T.-C., Controlled deposition of silver indium sulfide ternary semiconductor thin films by chemical bath deposition. *Chemistry of Materials* **2008,** *20* (13), 4475-4483.
228. Mao, B.; Chuang, C.-H.; Wang, J.; Burda, C., Synthesis and photophysical properties of ternary I–III–VI AgInS2 nanocrystals: intrinsic versus surface states. *The Journal of Physical Chemistry C* **2011,** *115* (18), 8945-8954.
229. Hong, S. P.; Park, H. K.; Oh, J. H.; Yang, H.; Do, Y. R., Comparisons of the structural and optical properties of o-AgInS 2, t-AgInS 2, and c-AgIn 5 S 8 nanocrystals and their solid-solution nanocrystals with ZnS. *Journal of Materials Chemistry* **2012,** *22* (36), 18939-18949.
230. Liu, Z.; Tang, K.; Wang, D.; Wang, L.; Hao, Q., Facile synthesis of AgInS 2 hierarchical flowerlike nanoarchitectures composed of ultrathin nanowires. *Nanoscale* **2013,** *5* (4), 1570-1575.
231. Feng, Z.; Dai, P.; Ma, X.; Zhan, J.; Lin, Z., Monodispersed cation-disordered cubic AgInS 2 nanocrystals with enhanced fluorescence. *Applied Physics Letters* **2010,** *96* (1), 013104.
232. Cui, X.; Gu, H.; Guan, Y.; Ren, G.; Ma, Z.; Yin, Y.; Liu, J.; Cui, X.; Yao, L.; Yin, Y., Fabrication of AgInS2 nanoparticles sensitized TiO2 nanotube arrays and their photoelectrochemical properties. *Solar Energy Materials and Solar Cells* **2015,** *137*, 101-106.
233. Yin, J.; Jia, J.; Yi, G., Synthesis and photoelectric application of AgInS2 clusters. *Materials Letters* **2013,** *111*, 85-88.
234. Ganguly, P.; Mathew, S.; Clarizia, L.; R Kumar, S.; Akande, A.; Hinder, S.; Breen, A.; Pillai, C. S., Theoretical and experimental investigation of visible light responsive AgBiS 2 -TiO 2 heterojunctions for enhanced photocatalytic applications. *Applied Catalysis B: Environmental* **2019**.
235. Liu, J.; Chen, S.; Liu, Q.; Zhu, Y.; Lu, Y., Density functional theory study on electronic and photocatalytic properties of orthorhombic AgInS2. *Computational Materials Science* **2014,** *91*, 159-164.
236. Perdew, J. P.; Levy, M., Physical content of the exact Kohn-Sham orbital energies: band gaps and derivative discontinuities. *Physical Review Letters* **1983,** *51* (20), 1884.
237. Crowley, J. M.; Tahir-Kheli, J.; Goddard III, W. A., Resolution of the band gap prediction problem for materials design. *The journal of physical chemistry letters* **2016,** *7* (7), 1198-1203.
238. Saha, S.; Sinha, T.; Mookerjee, A., Electronic structure, chemical bonding, and optical properties of paraelectric BaTiO 3. *Physical Review B* **2000,** *62* (13), 8828.
239. Xie, C.; Lu, X.; Deng, F.; Luo, X.; Gao, J.; Dionysiou, D. D., Unique surface structure of nano-sized CuInS2 anchored on rGO thin film and its superior

photocatalytic activity in real wastewater treatment. *Chemical Engineering Journal* **2018,** *338*, 591-598.
240. Liu, M.; Li, G.; Chen, X., One-pot controlled synthesis of spongelike CuInS2 microspheres for efficient counter electrode with graphene assistance in dye-sensitized solar cells. *ACS applied materials & interfaces* **2014,** *6* (4), 2604-2610.
241. Xu, F.; Zhang, J.; Zhu, B.; Yu, J.; Xu, J., CuInS2 sensitized TiO2 hybrid nanofibers for improved photocatalytic CO2 reduction. *Applied Catalysis B: Environmental* **2018,** *230*, 194-202.
242. Yuan, Y.-J.; Fang, G.; Chen, D.; Huang, Y.; Yang, L.-X.; Cao, D.-P.; Wang, J.; Yu, Z.-T.; Zou, Z.-G., High light harvesting efficiency CuInS 2 quantum dots/TiO 2/MoS 2 photocatalysts for enhanced visible light photocatalytic H 2 production. *Dalton Transactions* **2018,** *47* (16), 5652-5659.
243. Tian, L.; Vittal, J. J., Synthesis and characterization of ternary AgInS2 nanocrystals by dual-and multiple-source methodsElectronic supplementary information (ESI) available: Experimental details, EDX analysis spectrum and XRPD patterns. See. **2007**.
244. Sugan, S.; Dhanasekaran, R. In *Synthesis of AgInS2 semiconductor nano crystals by solvothermal method*, IOP Conference Series: Materials Science and Engineering, IOP Publishing: 2015; p 012147.
245. Delgado, G.; Mora, A.; Pineda, C.; Tinoco, T., Simultaneous Rietveld refinement of three phases in the Ag-In-S semiconducting system from X-ray powder diffraction. *Materials research bulletin* **2001,** *36* (13-14), 2507-2517.
246. Borkovska, L.; Romanyuk, A.; Strelchuk, V.; Polishchuk, Y.; Kladko, V.; Raevskaya, A.; Stroyuk, O.; Kryshtab, T., Optical characterization of the AgInS2 nanocrystals synthesized in aqueous media under stoichiometric conditions. *Materials Science in Semiconductor Processing* **2015,** *37*, 135-142.
247. Ohrendorf, F.; Haeuseler, H., Lattice dynamics of chalcopyrite type compounds. Part I. Vibrational frequencies. *Crystal Research and Technology: Journal of Experimental and Industrial Crystallography* **1999,** *34* (3), 339-349.
248. Mathew, S.; Ganguly, P.; Rhatigan, S.; Kumaravel, V.; Byrne, C.; Hinder, S.; Bartlett, J.; Nolan, M.; Pillai, S., Cu-Doped TiO_2: Visible Light Assisted Photocatalytic Antimicrobial Activity. *Applied Sciences* **2018,** *8* (11), 2067.
249. Swamy, V.; Kuznetsov, A.; Dubrovinsky, L. S.; Caruso, R. A.; Shchukin, D. G.; Muddle, B. C., Finite-size and pressure effects on the Raman spectrum of nanocrystalline anatase Ti O 2. *Physical Review B* **2005,** *71* (18), 184302.
250. Bird, R.; Swift, P., Energy calibration in electron spectroscopy and the re-determination of some reference electron binding energies. *Journal of Electron Spectroscopy and Related Phenomena* **1980,** *21* (3), 227-240.
251. Ouchene, M.; Senemaud, C.; Belin, E.; Gheorghiu, A.; Theye, M.-L., Influence of disorder on the electronic distribution of InP by X-ray and photoelectron spectroscopies. *Journal of Non-Crystalline Solids* **1983,** *59*, 625-628.
252. Vesely, C., CJ Vesely and DW Langer, Phys. Rev. B 4, 451 (1971). *Phys. Rev. B* **1971,** *4*, 451.
253. Tian, L.; Vittal, J. J., Synthesis and characterization of ternary AgInS 2 nanocrystals by dual-and multiple-source methods. *New Journal of Chemistry* **2007,** *31* (12), 2083-2087.
254. Panneri, S.; Ganguly, P.; Nair, B. N.; Mohamed, A. A. P.; Warrier, K. G. K.; Hareesh, U. N. S., Role of precursors on the photophysical properties of carbon nitride and its application for antibiotic degradation. *Environmental Science and Pollution Research* **2017,** *24* (9), 8609-8618.

255. Zhang, M.; Li, X.; Zhao, Q.; Fan, S.; Jiang, Z.; Chen, G., AgInS 2 nanoparticles modified TiO 2 nanotube array electrodes: Ultrasonic-assisted SILAR preparation and mechanism of enhanced photoelectrocatalytic activity. *Molecular Catalysis* **2017,** *442*, 97-106.
256. He, W.; Jia, H.; Yang, D.; Xiao, P.; Fan, X.; Zheng, Z.; Kim, H.-K.; Wamer, W. G.; Yin, J.-J., Composition directed generation of reactive oxygen species in irradiated mixed metal sulfides correlated with their photocatalytic activities. *ACS applied materials & interfaces* **2015,** *7* (30), 16440-16449.
257. Nosaka, Y.; Nosaka, A. Y., Generation and detection of reactive oxygen species in photocatalysis. *Chemical reviews* **2017,** *117* (17), 11302-11336.
258. Barbieriková, Z.; Pližingrová, E.; Motlochová, M.; Bezdička, P.; Boháček, J.; Dvoranová, D.; Mazúr, M.; Kupčík, J.; Jirkovský, J.; Šubrt, J., N-doped titanium dioxide nanosheets: Preparation, characterization and UV/visible-light activity. *Applied Catalysis B: Environmental* **2018,** *232*, 397-408.
259. Gordienko, A.; Filippov, D., Electronic Structure of OR-AgInS 2 and TiO 2 Crystals and Its Differential Characteristics. *Physics of the Solid State* **2018,** *60* (5), 858-864.
260. Deng, F.; Zhong, F.; Lin, D.; Zhao, L.; Liu, Y.; Huang, J.; Luo, X.; Luo, S.; Dionysiou, D. D., One-step hydrothermal fabrication of visible-light-responsive AgInS2/SnIn4S8 heterojunction for highly-efficient photocatalytic treatment of organic pollutants and real pharmaceutical industry wastewater. *Applied Catalysis B: Environmental* **2017,** *219*, 163-172.
261. Wu, H.-J.; Wei, P.-C.; Cheng, H.-Y.; Deng, J.-R.; Chen, Y.-Y., Ultralow thermal conductivity in n-type Ge-doped AgBiSe2 thermoelectric materials. *Acta Materialia* **2017,** *141*, 217-229.
262. Landmann, M.; Rauls, E.; Schmidt, W., The electronic structure and optical response of rutile, anatase and brookite TiO2. *Journal of physics: condensed matter* **2012,** *24* (19), 195503.
263. Hameed, T. A.; Wassel, A. R.; El Radaf, I., Investigating the effect of thickness on the structural, morphological, optical and electrical properties of AgBiSe2 thin films. *Journal of Alloys and Compounds* **2019,** *805*, 1-11.
264. Aliyev, V.; Guseinov, G.; Mamedov, F.; Chapanova, L., Anomalous temperature dependence of the band gap in AgGaSe2 and AgInSe2. *Solid state communications* **1986,** *59* (11), 745-746.
265. Rajaji, V.; Malavi, P. S.; Yamijala, S. S.; Sorb, Y.; Dutta, U.; Guin, S. N.; Joseph, B.; Pati, S. K.; Karmakar, S.; Biswas, K., Pressure induced structural, electronic topological, and semiconductor to metal transition in AgBiSe2. *Applied Physics Letters* **2016,** *109* (17), 171903.
266. Ng, M. T.; Boothroyd, C. B.; Vittal, J. J., One-pot synthesis of new-phase AgInSe2 nanorods. *Journal of the American Chemical Society* **2006,** *128* (22), 7118-7119.
267. Bai, T.; Li, C.; Li, F.; Zhao, L.; Wang, Z.; Huang, H.; Chen, C.; Han, Y.; Shi, Z.; Feng, S., A simple solution-phase approach to synthesize high quality ternary AgInSe 2 and band gap tunable quaternary AgIn (S 1− x Se x) 2 nanocrystals. *Nanoscale* **2014,** *6* (12), 6782-6789.
268. Tian, L.; Ng, M. T.; Venkatram, N.; Ji, W.; Vittal, J. J., Tadpole-shaped AgInSe2 nanocrystals from a single molecular precursor and its nonlinear optical properties. *Crystal growth & design* **2010,** *10* (3), 1237-1242.
269. Suyana, P.; Ganguly, P.; Nair, B. N.; Mohamed, A. P.; Warrier, K.; Hareesh, U., Co 3 O 4–C 3 N 4 p–n nano-heterojunctions for the simultaneous degradation of a

mixture of pollutants under solar irradiation. *Environmental Science: Nano* **2017,** *4* (1), 212-221.
270. Ganguly, P.; Mathew, S.; Clarizia, L.; Kumar R, S.; Akande, A.; Hinder, S. J.; Breen, A.; Pillai, S. C., Ternary Metal Chalcogenide Heterostructure (AgInS2–TiO2) Nanocomposites for Visible Light Photocatalytic Applications. *ACS Omega* **2019**.
271. Mathew, S.; Ganguly, P.; Kumaravel, V.; Harrison, J.; Hinder, S. J.; Bartlett, J.; Pillai, S. C., Effect of chalcogens (S, Se, and Te) on the anatase phase stability and photocatalytic antimicrobial activity of TiO2. *Materials Today: Proceedings* **2020**.
272. Xiao, C., Two Metal Ion Exchange Realizing Efficient Thermoelectric Properties and p–n–p Conduction Type Transition. In *Synthesis and Optimization of Chalcogenides Quantum Dots Thermoelectric Materials*, Springer: 2016; pp 51-64.
273. Xiao, C.; Qin, X.; Zhang, J.; An, R.; Xu, J.; Li, K.; Cao, B.; Yang, J.; Ye, B.; Xie, Y., High thermoelectric and reversible pnp conduction type switching integrated in dimetal chalcogenide. *Journal of the American Chemical Society* **2012,** *134* (44), 18460-18466.
274. Shi, L.; Wu, C.; Ding, J., Effect of solvent on the synthesis of AgBiSe2 nanostructures. *Journal of Alloys and Compounds* **2016,** *684*, 112-115.
275. Nakata, M. M.; Mazzo, T. M.; Casali, G. P.; La Porta, F. A.; Longo, E., A large red-shift in the photoluminescence emission of Mg1− xSrxTiO3. *Chemical Physics Letters* **2015,** *622*, 9-14.
276. Sarkar, D.; Ghosh, C. K.; Mukherjee, S.; Chattopadhyay, K. K., Three dimensional Ag2O/TiO2 type-II (p–n) nanoheterojunctions for superior photocatalytic activity. *ACS applied materials & interfaces* **2013,** *5* (2), 331-337.
277. Chen, P., A novel synthesis of Ti3+ self-doped Ag2O/TiO2 (p–n) nanoheterojunctions for enhanced visible photocatalytic activity. *Materials Letters* **2016,** *163*, 130-133.
278. Langevin, M.-A.; Ritcey, A. M.; Allen, C. N., Air-stable near-infrared AgInSe2 nanocrystals. *ACS nano* **2014,** *8* (4), 3476-3482.
279. Che, D.; Zhu, X.; Wang, H.; Duan, Y.; Zhang, Q.; Li, Y., Aqueous synthesis of high bright and tunable near-infrared AgInSe2–ZnSe quantum dots for bioimaging. *Journal of colloid and interface science* **2016,** *463*, 1-7.
280. Kameyama, T.; Douke, Y.; Shibakawa, H.; Kawaraya, M.; Segawa, H.; Kuwabata, S.; Torimoto, T., Widely Controllable Electronic Energy Structure of ZnSe–AgInSe2 Solid Solution Nanocrystals for Quantum-Dot-Sensitized Solar Cells. *The Journal of Physical Chemistry C* **2014,** *118* (51), 29517-29524.
281. Chen, L.-C.; Ho, Y.-C.; Yang, R.-Y.; Chen, J.-H.; Huang, C.-M., Electrodeposited AgInSe2 onto TiO2 films for semiconductor-sensitized solar cell application: The influence of electrodeposited time. *Applied surface science* **2012,** *258* (17), 6558-6563.
282. Li, P.-N.; Ghule, A. V.; Chang, J.-Y., Direct aqueous synthesis of quantum dots for high-performance AgInSe2 quantum-dot-sensitized solar cell. *Journal of Power Sources* **2017,** *354*, 100-107.
283. Kshirsagar, A. S.; Khanna, P. K., Titanium dioxide (TiO 2)-decorated silver indium diselenide (AgInSe 2): novel nano-photocatalyst for oxidative dye degradation. *Inorganic Chemistry Frontiers* **2018,** *5* (9), 2242-2256.
284. Aquino Gonzalez, A. Physical and optoelectronic properties of copper silver indium diselenide thin films. University of Illinois at Urbana-Champaign, 2012.
285. Jin, Y.; Tang, K.; An, C.; Huang, L., Hydrothermal synthesis and characterization of AgInSe2 nanorods. *Journal of crystal growth* **2003,** *253* (1-4), 429-434.

286. Kang, X.; Yang, Y.; Huang, L.; Tao, Y.; Wang, L.; Pan, D., Large-scale synthesis of water-soluble CuInSe 2/ZnS and AgInSe 2/ZnS core/shell quantum dots. *Green Chemistry* **2015,** *17* (8), 4482-4488.
287. Ganguly, P.; Panneri, S.; Hareesh, U.; Breen, A.; Pillai, S. C., Recent Advances in Photocatalytic Detoxification of Water. In *Nanoscale Materials in Water Purification*, Elsevier: 2019; pp 653-688.
288. Mathew, S.; Ganguly, P.; Kumaravel, V.; Bartlett, J.; Pillai, S. C., Solar light-induced photocatalytic degradation of pharmaceuticals in wastewater treatment. In *Nano-Materials as Photocatalysts for Degradation of Environmental Pollutants*, Elsevier: 2020; pp 65-78.
289. Ida, S.; Ishihara, T., Recent progress in two-dimensional oxide photocatalysts for water splitting. *The journal of physical chemistry letters* **2014,** *5* (15), 2533-2542.
290. Novoselov, K.; Jiang, D.; Schedin, F.; Booth, T.; Khotkevich, V.; Morozov, S.; Geim, A., Two-dimensional atomic crystals. *Proceedings of the National Academy of Sciences of the United States of America* **2005,** *102* (30), 10451-10453.
291. Castro Neto, A.; Novoselov, K., Two-Dimensional Crystals: Beyond Graphene. *Materials Express* **2011,** *1* (1), 10-17.
292. An, X.; Yu, J., Graphene-based photocatalytic composites. *Rsc Advances* **2011,** *1* (8), 1426-1434.
293. Wei, Y.; Ma, Y.; Wei, W.; Li, M.; Huang, B.; Dai, Y., Promising Photocatalysts for Water Splitting in BeN2 and MgN2 Monolayers. *The Journal of Physical Chemistry C* **2018,** *122* (15), 8102-8108.
294. Makaremi, M.; Grixti, S.; Butler, K. T.; Ozin, G. A.; Singh, C. V., Band Engineering of Carbon Nitride Monolayers by N-Type, P-Type, and Isoelectronic Doping for Photocatalytic Applications. *ACS applied materials & interfaces* **2018,** *10* (13), 11143-11151.
295. Mannix, A. J.; Kiraly, B.; Hersam, M. C.; Guisinger, N. P., Synthesis and chemistry of elemental 2D materials. *Nature Reviews Chemistry* **2017,** *1* (2), 1-14.
296. Manzeli, S.; Ovchinnikov, D.; Pasquier, D.; Yazyev, O. V.; Kis, A., 2D transition metal dichalcogenides. *Nature Reviews Materials* **2017,** *2* (8), 17033.
297. Choi, W.; Choudhary, N.; Han, G. H.; Park, J.; Akinwande, D.; Lee, Y. H., Recent development of two-dimensional transition metal dichalcogenides and their applications. *Materials Today* **2017,** *20* (3), 116-130.
298. Rivera, P.; Yu, H.; Seyler, K. L.; Wilson, N. P.; Yao, W.; Xu, X., Interlayer valley excitons in heterobilayers of transition metal dichalcogenides. *Nature nanotechnology* **2018,** *13* (11), 1004-1015.
299. Zhang, H.; Chhowalla, M.; Liu, Z., 2D nanomaterials: graphene and transition metal dichalcogenides. *Chemical Society Reviews* **2018,** *47* (9), 3015-3017.
300. Lin, Z.; Carvalho, B. R.; Kahn, E.; Lv, R.; Rao, R.; Terrones, H.; Pimenta, M. A.; Terrones, M., Defect engineering of two-dimensional transition metal dichalcogenides. *2D Materials* **2016,** *3* (2), 022002.
301. Luo, Y.; Wang, S.; Ren, K.; Chou, J.-P.; Yu, J.; Sun, Z.; Sun, M., Transition-metal dichalcogenides/Mg (OH) 2 van der Waals heterostructures as promising water-splitting photocatalysts: a first-principles study. *Physical Chemistry Chemical Physics* **2019,** *21* (4), 1791-1796.
302. Peng, Q.; Wang, Z.; Sa, B.; Wu, B.; Sun, Z., Electronic structures and enhanced optical properties of blue phosphorene/transition metal dichalcogenides van der Waals heterostructures. *Scientific reports* **2016,** *6*, 31994.

303. Kang, J.; Wood, J. D.; Wells, S. A.; Lee, J.-H.; Liu, X.; Chen, K.-S.; Hersam, M. C., Solvent exfoliation of electronic-grade, two-dimensional black phosphorus. *ACS nano* **2015,** *9* (4), 3596-3604.
304. Qiao, J.; Kong, X.; Hu, Z.-X.; Yang, F.; Ji, W., High-mobility transport anisotropy and linear dichroism in few-layer black phosphorus. *Nature communications* **2014,** *5* (1), 1-7.
305. Long, G.; Maryenko, D.; Shen, J.; Xu, S.; Hou, J.; Wu, Z.; Wong, W. K.; Han, T.; Lin, J.; Cai, Y., Achieving ultrahigh carrier mobility in two-dimensional hole gas of black phosphorus. *Nano letters* **2016,** *16* (12), 7768-7773.
306. Chen, Y.; Ren, R.; Pu, H.; Chang, J.; Mao, S.; Chen, J., Field-effect transistor biosensors with two-dimensional black phosphorus nanosheets. *Biosensors and Bioelectronics* **2017,** *89*, 505-510.
307. Kim, J.; Baik, S. S.; Ryu, S. H.; Sohn, Y.; Park, S.; Park, B.-G.; Denlinger, J.; Yi, Y.; Choi, H. J.; Kim, K. S., Observation of tunable band gap and anisotropic Dirac semimetal state in black phosphorus. *Science* **2015,** *349* (6249), 723-726.
308. Mu, X.; Wang, J.; Sun, M., Two-dimensional black phosphorus: physical properties and applications. *Materials Today Physics* **2019**.
309. Pumera, M.; Sofer, Z., 2D monoelemental arsenene, antimonene, and bismuthene: beyond black phosphorus. *Advanced Materials* **2017,** *29* (21), 1605299.
310. Teweldebrhan, D.; Goyal, V.; Balandin, A. A., Exfoliation and characterization of bismuth telluride atomic quintuples and quasi-two-dimensional crystals. *Nano letters* **2010,** *10* (4), 1209-1218.
311. Coleman, J. N.; Lotya, M.; O'Neill, A.; Bergin, S. D.; King, P. J.; Khan, U.; Young, K.; Gaucher, A.; De, S.; Smith, R. J., Two-dimensional nanosheets produced by liquid exfoliation of layered materials. *Science* **2011,** *331* (6017), 568-571.
312. Beladi-Mousavi, S. M.; Pumera, M., 2D-Pnictogens: alloy-based anode battery materials with ultrahigh cycling stability. *Chemical Society Reviews* **2018,** *47* (18), 6964-6989.
313. Di, J.; Xia, J.; Li, H.; Guo, S.; Dai, S., Bismuth oxyhalide layered materials for energy and environmental applications. *Nano Energy* **2017,** *41*, 172-192.
314. Zhu, M.; Sun, Z.; Fujitsuka, M.; Majima, T., Z-Scheme Photocatalytic Water Splitting on a 2D Heterostructure of Black Phosphorus/Bismuth Vanadate Using Visible Light. *Angewandte Chemie-International Edition* **2018,** *57* (8), 2160-2164.
315. Anasori, B.; Lukatskaya, M. R.; Gogotsi, Y., 2D metal carbides and nitrides (MXenes) for energy storage. *Nature Reviews Materials* **2017,** *2* (2), 1-17.
316. Anasori, B.; Xie, Y.; Beidaghi, M.; Lu, J.; Hosler, B. C.; Hultman, L.; Kent, P. R.; Gogotsi, Y.; Barsoum, M. W., Two-dimensional, ordered, double transition metals carbides (MXenes). *ACS nano* **2015,** *9* (10), 9507-9516.
317. Naguib, M.; Mochalin, V. N.; Barsoum, M. W.; Gogotsi, Y., 25th anniversary article: MXenes: a new family of two-dimensional materials. *Advanced materials* **2014,** *26* (7), 992-1005.
318. Zhang, C. J.; Pinilla, S.; McEvoy, N.; Cullen, C. P.; Anasori, B.; Long, E.; Park, S.-H.; Seral-Ascaso, A. s.; Shmeliov, A.; Krishnan, D., Oxidation stability of colloidal two-dimensional titanium carbides (MXenes). *Chemistry of Materials* **2017,** *29* (11), 4848-4856.
319. Yu, L.; Zhou, H.; Sun, J.; Qin, F.; Yu, F.; Bao, J.; Yu, Y.; Chen, S.; Ren, Z., Cu nanowires shelled with NiFe layered double hydroxide nanosheets as bifunctional electrocatalysts for overall water splitting. *Energy & Environmental Science* **2017,** *10* (8), 1820-1827.

320. Wang, Q.; O'Hare, D., Recent advances in the synthesis and application of layered double hydroxide (LDH) nanosheets. *Chemical reviews* **2012,** *112* (7), 4124-4155.
321. Zhao, Y.; Jia, X.; Waterhouse, G. I.; Wu, L. Z.; Tung, C. H.; O'Hare, D.; Zhang, T., Layered double hydroxide nanostructured photocatalysts for renewable energy production. *Advanced Energy Materials* **2016,** *6* (6), 1501974.
322. Gu, P.; Zhang, S.; Li, X.; Wang, X.; Wen, T.; Jehan, R.; Alsaedi, A.; Hayat, T.; Wang, X., Recent advances in layered double hydroxide-based nanomaterials for the removal of radionuclides from aqueous solution. *Environmental pollution* **2018,** *240*, 493-505.
323. Zhang, J.; Yu, L.; Chen, Y.; Lu, X. F.; Gao, S.; Lou, X. W., Designed Formation of Double-Shelled Ni–Fe Layered-Double-Hydroxide Nanocages for Efficient Oxygen Evolution Reaction. *Advanced Materials* **2020**, 1906432.
324. Chen, H.; Hu, L.; Chen, M.; Yan, Y.; Wu, L., Nickel–cobalt layered double hydroxide nanosheets for high-performance supercapacitor electrode materials. *Advanced Functional Materials* **2014,** *24* (7), 934-942.
325. Liao, C.-H.; Huang, C.-W.; Wu, J., Hydrogen production from semiconductor-based photocatalysis via water splitting. *Catalysts* **2012,** *2* (4), 490-516.
326. Yang, L.; Li, X.; Zhang, G.; Cui, P.; Wang, X.; Jiang, X.; Zhao, J.; Luo, Y.; Jiang, J., Combining photocatalytic hydrogen generation and capsule storage in graphene based sandwich structures. *Nature Communications* **2017,** *8*, 16049.
327. Zhang, H.; Tong, C.-J.; Zhang, Y.; Zhang, Y.-N.; Liu, L.-M., Porous BN for hydrogen generation and storage. *Journal of Materials Chemistry A* **2015,** *3* (18), 9632-9637.
328. Serpone, N.; Emeline, A., Semiconductor Photocatalysis - Past, Present, and Future Outlook. *Journal of Physical Chemistry Letters* **2012,** *3* (5), 673-677.

APPENDIX: PUBLICATIONS OF THE CANDIDATE

Aspects of this thesis have been published previously in the following publications. Research containing major contributions from this thesis is indicated with *.

Published:

1) **Ganguly, P**., Mathew, S., Clarizia, L., Kumar R, S., Akande, A., Hinder, S., Breen, A., & Pillai, S. C. (2019). Theoretical and experimental investigation of visible light responsive $AgBiS_2$-TiO_2 heterojunctions for enhanced photocatalytic applications. *Applied Catalysis B: Environmental*, *253*, 401-418. ***Impact factor: 16.68*****
2) **Ganguly, P**., Kumar R, S., Muscetta, M., Padmanabhan, N. T., Clarizia, L., Mathew, S., Akande, A., Hinder, S., John, H., Breen, A., & Pillai, S. C. (2020). Experimental and DFT insights of ternary chalcogenides composites of TiO_2 for efficient charge transfer. *Applied Catalysis B: Environmental*, *282*, 119612. ***Impact factor: 16.68*****
3) **Ganguly, P**., Harb, M., Cao, Z., Cavallo, L., Breen, A., Dervin, S., Dionysiou, D.D., & Pillai, S. C. (2019). 2D Nanomaterials for Photocatalytic Hydrogen Production. *ACS Energy Letters*, 4, 1687–1709 ***Impact factor: 19.00*****
4) **Ganguly, P**., Byrne, C., Breen, A., & Pillai, S. C. (2017). Antimicrobial activity of photocatalysts: fundamentals, mechanisms, kinetics and recent advances. *Applied Catalysis B: Environmental*. ***Impact factor: 16.68*****
5) **Ganguly, P**., Breen, A., & Pillai, S. C. (2018). Toxicity of Nanomaterials: Exposure, Pathways, Assessment, and Recent Advances. *ACS Biomaterials Science & Engineering*, *4*(7), 2237-2275. ***Impact factor: 4.51***
6) **Ganguly, P**., Mathew, S., Clarizia, L., Kumar R, S., Akande, A., Hinder, S., Breen, A., & Pillai, S. C. (2020). Ternary Metal Chalcogenide Heterostructure ($AgInS_2$–TiO_2) Nanocomposites for Visible Light Photocatalytic Applications *ACS Omega*, 5, 1, 406–421. ***Impact factor: 2.584*****

7) **Ganguly, P**., Panneri, S., Hareesh, U. N. S., Breen, A., & Pillai, S. C. (2018). Recent advances in Photocatalytic Detoxification of water; Nanoscale Materials in Water Purification, *Elsevier*. **ISBN:** 9780128139264 (Book Chapter) **

8) **Ganguly, P**., Breen, A., & Pillai, S. C. (2019). Cytotoxicology studies of 2-D Nanomaterial; Toxicity of Nanomaterials in the Environment, *CRC Press*. **ISBN:** 9780429265471 (Book Chapter)

9) Nair. K., M., **Ganguly, P**., Mathew, S., Kumaravel, V., and Pillai, S.C. (2020) TiO_2 based Z-scheme photocatalysts for energy and environmental applications Solar Cell Engineering, Elsevier, 2021, 257-282 (Book Chapter) **

10) Suyana, P., **Ganguly, P**., Nair, B. N., Mohamed, A. P., Warrier, K. G. K., & Hareesh, U. S. (2017). Co_3O_4–C_3N_4 p–n nano-heterojunctions for the simultaneous degradation of a mixture of pollutants under solar irradiation. *Environmental Science: Nano*, *4*(1), 212-221. ***Impact factor: 7.70***

11) Panneri, S., **Ganguly, P**., Mohan, M., Nair, B. N., Mohamed, A. A. P., Warrier, K. G., & Hareesh, U. S. (2017). Photoregenerable, bifunctional granules of carbon-doped g-C3N4 as adsorptive photocatalyst for the efficient removal of tetracycline antibiotic. *ACS Sustainable Chemistry & Engineering*, *5*(2), 1610-1618. ***Impact factor: 6.97***

12) Bhamore, J. R., **Ganguly, P**., & Kailasa, S. K. (2016). Molecular assembly of 3-mercaptopropinonic acid and guanidine acetic acid on silver nanoparticles for selective colorimetric detection of triazophos in water and food samples. *Sensors and Actuators B: Chemical*, *233*, 486-495. ***Impact factor: 7.10***

13) Panneri, S., Thomas, M., **Ganguly, P**., Nair, B. N., Mohamed, A. P., Warrier, K. G. K., & Hareesh, U. S. (2017). C 3 N 4 anchored ZIF 8 composites: photo-regenerable, high capacity sorbents as adsorptive photocatalysts for the effective removal of tetracycline from

water. *Catalysis Science & Technology*, *7*(10), 2118-2128. ***Impact factor: 5.72***

14) Panneri, S., **Ganguly, P**., Nair, B. N., Mohamed, A. A. P., Warrier, K. G. K., & Hareesh, U. N. S. (2017). Role of precursors on the photophysical properties of carbon nitride and its application for antibiotic degradation. *Environmental Science and Pollution Research*, *24*(9), 8609-8618. ***Impact factor: 3.30***

15) Panneri, S., **Ganguly, P**., Nair, B. N., Mohamed, A. A. P., Warrier, K. G., & Hareesh, U. N. S. (2016). Copyrolysed C_3N_4-Ag/ZnO ternary heterostructure systems for enhanced adsorption and photocatalytic degradation of tetracycline. *European Journal of Inorganic Chemistry*, *2016* (31), 5068-5076. ***Impact factor: 2.57***

16) Mathew, S., **Ganguly, P**., Rhatigan, S., Kumaravel, V., Byrne, C., Hinder, S., ... & Pillai, S. (2018). Cu-Doped TiO2: Visible Light Assisted Photocatalytic Antimicrobial Activity. *Applied Sciences*, *8*(11), 2067. ***Impact factor: 2.21***

17) Byrne, C., Moran, L., Hermosilla, D., Merayo, N., Blanco, Á., Rhatigan, S., Hinder, S., **Ganguly, P**., Nolan, M. and Pillai, S.C., (2019). Effect of Cu Doping on the Anatase-to-Rutile Phase Transition in TiO_2 Photocatalysts: Theory and Experiments. *Applied Catalysis B: Environmental,* 266-276. ***Impact factor: 16.68***

18) Mathew, S., **Ganguly, P**., Kumaravel, V., Bartlett, J., and Pillai, S.C. (2019) Solar light-induced photocatalytic degradation of pharmaceuticals in wastewater treatment, **ISBN**: 978-0-12-818598-8 (Book Chapter)

19) Mathew, S., **Ganguly, P**., Rhatigan, S., Kumaravel, V., Byrne, C., Hinder, S., & Pillai, S. (2020). Effect of chalcogens (S, Se, and Te) on the anatase phase stability and photocatalytic antimicrobial activity of TiO_2. *Materials Today: Proceedings.*

20) Padmanabhan, N. T., **Ganguly, P.,** Pillai, S.C., John, H. (2021). Morphology Engineered Spatial Charge Separation in Superhydrophilic

TiO_2/graphene Hybrids for Hydrogen Production. *Materials Today Energy*, 17, 100447. ***Impact factor: 5.60***

21) Padmanabhan, N. T., Thomas, N., Louis, J., Mathew, D.T., **Ganguly, P.,** Pillai, S.C., John, H. (2021). Graphene coupled TiO_2 photocatalysts for environmental applications: A review. *Chemosphere*, 271, 129506. ***Impact factor: 5.77***

22) Seyedhosseini, E., Dervin, S., **Ganguly, P**., and Dahiya R., S., (2020) Biodegradable sensors for healthcare and body monitoring. *ACS Appl. Bio Materials.* 4, 163–194,

23) **Ganguly, P**., Clarizia, L., (2020). Photocatalytic hydrogen production over semiconductor-based materials: Book Chapter for Elsevier

24) Mukherjee, R., **Ganguly, P.,** and Dahiya R., Bioinspired Distributed Energy in Robotics and Enabling Technologies. *Advanced Intelligent Systems* (Just accepted)

25) Dervin, S., **Ganguly, P.,** and Dahiya R., Disposable electrochemical sensor using Graphene oxide – chitosan modified carbon-based electrodes for the detection of tyrosine. *IEEE Sensors* (Just accepted)

Manuscript under preparation

26) Byrne, C., **Ganguly, P.** Nolan, M. Hermosilla, D. Merayo, N., Blanco, A., Hinder, S., & Pillai, S.C. (2020) Gold doped TiO_2 for the Photocatalytic Degradation of 1,4-dioxane (Ready to be submitted)

27) Mathew, S., Nair. K., M., **Ganguly, P**., Dervin, S., Dowd, O. K., Kumaravel, V., and Pillai, S.C. (2020) 2D Membranes: Nanomaterials for energy and water treatment applications (Ready to be submitted)

28) Mathew, S., Nair. K., M., **Ganguly, P**., (2020) Fundamentals of Photocatalysis: Book Chapter for Elsevier (Under preparation)

29) **Ganguly, P**., Breen, A., & Pillai, S. C. (2020). XPS: A tool for surface analysis for 2D nanomaterials. (Under preparation)

30) Pillai, S.C. and **Ganguly, P**. (2020). 2D Materials for Energy Storage and Conversion (Book editors) for IOP Publishing Ltd.

31) Forouzandeh, P., **Ganguly, P**., Dahiya R., S. and Pillai, S.C. (2020) Synthesis approaches of electrode materials in supercapacitor applications. (Under preparation)

32) Panneri, S., **Ganguly, P**., Nair, B. N., Pillai, S. C. & Hareesh, U. N. S. (2021). C_3N_4 based photocatalysts for antibiotic degradation. *Chemical Engineering Advances*, (Ready to be submitted)